

PoroTomo Final Technical Report: Poroelastic Tomography by Adjoint Inverse Modeling of Data from Seismology, Geodesy, and Hydrology

Federal Agency and Organization: DOE EERE – Geothermal Technologies Program

Recipient Organization: University of Wisconsin System
DUNS Number: 161202122
Recipient Address: Research and Sponsored Programs
21 N. Park Street, Suite 6401
Madison, WI 53715-1218

Award Number: DE-EE0006760

Project Title: PoroTomo: Poroelastic Tomography by Adjoint Inverse Modeling of Data from Seismology, Geodesy, and Hydrology

Project Period: 1 October 2014 through **31 December 2018** (extended)

Principal Investigator: Kurt Feigl, Professor, feigl@wisc.edu, (608) 262 0176

Technical Contact: Kurt Feigl, Professor, feigl@wisc.edu, (608) 262 0176

Report Submitted by: Kurt Feigl, Professor, feigl@wisc.edu, (608) 262 0176

Date of Report Submission: **6 March 2019 (updated 1 July 2019)**

Project Partners:

University of Wisconsin-Madison (UW) Dept. of Geoscience	http://geoscience.wisc.edu
Temple University (TU)	http://astro.temple.edu/~davatzes
University of Nevada-Reno (UNR)	http://geodesy.unr.edu
Ormat Technologies, Inc.	http://www.ormat.com/
Silixa Ltd.	http://www.silixa.com/
Lawrence Berkeley National Laboratory (LBL)	http://www.lbl.gov/
Lawrence Livermore National Laboratory (LLNL)	https://www.llnl.gov/

Signature *Kurt L. Feigl* **Date** *2019/07/01*

*The Prime Recipient certifies that the information provided in this report is accurate and complete as of the date shown.

Acknowledgment: "This material is based upon work supported by the Department of Energy's Office of Energy Efficiency and Renewable Energy (EERE) under the Geothermal Technologies Office under Award Number DE-EE0006760."

Disclaimer: "This report was prepared as an account of work sponsored by an agency of the United States Government. Neither the United States Government nor any agency thereof, nor any of their employees, makes any warranty, express or implied, or assumes any legal liability or responsibility for the accuracy, completeness, or usefulness of any information, apparatus, product, or process disclosed, or represents that its use would not infringe privately owned rights. Reference herein to any specific commercial, process, or service by trade name, trademark, manufacturer, or otherwise does not necessarily constitute or imply its endorsement, recommendation, or favoring by the United States Government or any agency thereof. The views and opinions of authors expressed herein do not necessarily state or reflect those of the United States Government or any agency thereof."

Table of Contents

Section 1. Executive Summary	3
Section 2. Introduction.....	7
Section 3. Analysis of Existing Data.....	11
Section 4. Deployment	20
Section 5. Seismology	42
Section 6. Geodesy.....	72
Section 7. Hydrology.....	87
Section 8. Value of Information.....	95
Section 9. Fiber Optic Technologies	99
Section 10. Feasibility of Coupled Inversion of Three Data Types	115
Section 11. Conclusions and Recommendations	125
Section 12. Data Management Plan	128
Section 13. Project Output.....	133

Section 1. Executive Summary

This final technical report compiles the results of the PoroTomo project conducted between 1 October 2014 and 31 December 2018. The work presented herein has been funded in part by the Office of Energy Efficiency and Renewable Energy (EERE), U.S. Department of Energy, under Award Number DE-EE0006760. The report cites articles published in the peer-reviewed literature and indicates data sets submitted to the Geothermal Data Repository (GDR).

In the geothermal field at Brady Hot Springs, Nevada, subsidence occurs over an elliptical area that is ~4 km by ~1.5 km. Results from inverse modeling suggest that the deformation is a result of volumetric contraction in units with depth less than 600 m. Characterizing such structures in terms of their rock-mechanical properties is essential to successful operations of Enhanced Geothermal Systems (EGS). The goal of the PoroTomo project is to assess an integrated technology for characterizing and monitoring changes in the rock-mechanical properties of an EGS reservoir in three dimensions with fine spatial resolution.

In March 2016, the PoroTomo team deployed the integrated technology in a 1500-by-500-by-400-meter volume at Brady Hot Springs. The integrated technology analyzes data from multiple arrays of sensors, including: active seismic sources, fiber-optic cables for Distributed Acoustic Sensing (DAS) and Distributed Temperature Sensing (DTS) arranged vertically in a borehole to ~400 m depth and horizontally in a trench 8700 m in length and 0.5 m in depth, 246 three-component seismometers on the surface, three pressure sensors in observation wells, continuous geodetic measurements at three GPS stations, and seven satellite images using Synthetic Aperture Radar (SAR). The deployment consisted of four distinct time intervals (“stages”). During each measurement interval, the hydrological conditions were intentionally manipulated by modifying the rates of pumping in the injection and production wells.

To account for the mechanical behavior of both the rock and the fluids, the PoroTomo team has developed numerical models for the 3-dimensional distribution of the material properties via inverse modeling of the three data sets (seismology, geodesy, and hydrology) individually. The estimated values of the material properties are registered on a three-dimensional grid with a spacing of 25 meters between nodes. The results agree on the following points. The material is unconsolidated and/or fractured, especially in the shallow layers. The structural trends follow the fault system in strike and dip. The geodetic measurements favor the hypothesis of thermal contraction. Temporal changes in pressure, subsidence rate, and seismic amplitude are associated with changes in pumping rates during the four stages of the deployment in 2016. The modeled hydraulic conductivity is high in the damage zones surrounding the faults. All the observations are consistent with a conceptual model of highly permeable conduits along faults channeling fluids from shallow aquifers to the deep geothermal reservoir tapped by the production wells.

During the 51-month performance period, the PoroTomo project produced: 1 doctoral dissertation, 5 master's theses, 11 articles published in the international peer-reviewed literature, 48 presentations at conferences, and 73 data sets submitted to the GDR. The members of the PoroTomo team participated in a kick-off meeting, two stage gate reviews, and a final review, as well as two peer reviews conducted by the Department of Energy's Geothermal Technologies Office (GTO). Documents from each of these meetings were shared with all members of the PoroTomo team, its Technical Management Team (TMT), and GTO staff on a collaborative web

site. The PoroTomo team submitted 17 quarterly reports, which were consistently assessed with health indicators of either “blue”¹ or “green”².

Looking forward, the PoroTomo team makes the following recommendations that apply to other experiments, such as those planned for the Frontier Observatory for Research in Geothermal Energy (FORGE) site in Utah. A multi-disciplinary team, including researchers from universities, industry and national laboratories contributed to the success of the PoroTomo project at Brady Hot Springs, Nevada, and led to collaborations at other geothermal sites, including Raft River, Idaho; Coso California; San Emidio, Nevada; Fallon, Nevada; and Milford, Utah. Critical discussions, including fortnightly teleconferences and yearly reviews, as well as conferences such as the Stanford Geothermal Workshop, the Geothermal Resource Council, and the American Geophysical Union, were essential to integrating the three types of data. The PoroTomo team started the process of planning and permitting 18 months in advance of field operations. Communications in the field are required for both safety and efficiency.

Regarding seismology, the PoroTomo learned several lessons that lead to the following recommendations. To compute material properties such as Young’s modulus and Poisson’s ratio from seismic data, the PoroTomo team took advantage of pre-existing 3-dimensional models of density that were inferred from a combination of gravimetric surveys and geologic models. For the active-source seismology, a repeatable, accelerated weight drop, such as the HH Seismic Hammer, would generate signals more like a simple impulse than traditional sources with time-varying (“sweeping”) frequencies. Taking advantage of local and regional seismic activity would also enlarge the data set. Using a combination of recordings made by DAS and conventional geophones in a joint inversion would improve the spatial resolution of the resulting models of material properties. Horizontal DAS arrays would benefit from long, straight segments of cable that minimize corners. If future deployments include multiple wells with DAS and/or downhole geophone arrays, then cross-hole studies using 3-D vertical seismic profiling (VSP) with active sources and/or ambient noise tomography would provide additional information.

Regarding geodesy, the PoroTomo learned several lessons that lead to the following recommendations. A GPS station in the actively deforming area is required to reference the InSAR data as well as to illuminate transient deformation signals on time scales on the order of a day that InSAR cannot recover. SAR images provide the required spatial resolution for deformation modeling, with X-band (e.g., TerraSAR-X) data providing the clearest interferograms. Although C-band (e.g., ERS-1, ERS-2) signals are adequate, SCANSAR images (e.g., Sentinel-1) degrade the spatial resolution too much to be useful for analyzing geothermal processes in the subsurface. It is also useful to have a satellite with a short revisit time to capture transient signals. In addition, a large dataset of interferometric pairs is useful to analyze trends over years. The “multi-cube” parameterization can be adapted to different spatial scales. Spatial correlation and prior models corresponding to the Bayesian, geostatistical inversion can also be adapted to reflect conditions at other sites.

Regarding hydrology, the PoroTomo team learned several lessons that lead to the following recommendations. The hydraulic data set provides independent information on reservoir hydraulic and thermal properties as a baseline against which other geophysical inversion results

¹ “Blue, which is rarely selected, indicates DOE believes the project is significantly outperforming on its goals and performance measures.”

² “Green indicates DOE believes the project is generally on track, there are no major concerns, and the project continues to hold strong promise”.

can be assessed. The hydraulic data set allows investigation and explanation of “multi-physics” coupled processes that occur in geothermal reservoirs (e.g., thermal/hydraulic coupling associated with movement of heat in wellbores, and hydraulic/mechanical coupling associated with deformation). Indeed, any assessment of the value of geophysical information strongly benefits from detailed hydraulic characterization data be collected alongside to provide validation of geophysical imaging or predictions. In future investigations, the following actions are recommended in order to improve hydraulic characterization of geothermal reservoirs. Hydraulic monitoring of temporal changes would be improved by via continuously acquiring more numerous, more accurate and more detailed measurements, especially in observation wells that are not pumping for either production or injection. Similarly, deploying packers and DTS in boreholes would improve spatial resolution. Multi-frequency oscillating pumping tests would improve the resolution of hydraulic parameters.

Regarding the fiber-optic technologies of DAS and DTS, the PoroTomo learned several lessons that lead to the following recommendations. The fiber-optic cable deployed vertically inside the casing in Brady Well 56-1 in March 2016 was a 1/8"-diameter (3.2 mm) bare 316 stainless steel double tube containing both single-mode and multi-mode, high temperature acrylate-coated fibers rated to 150°C. The cable was left in place following the deployment. More than two years later, in August 2018, the same fiber recorded temperatures up to 165°C with no loss of signal quality. Coupling is the most important consideration for DAS deployments. The particle motion needs to be coupled through the (rock or soil) formation, to the cable structure, and into the fiber itself. When installing new infrastructure, it is straightforward to clamp the cable to the casing as it goes into the well and then cement both the cable and the casing in place. This provides significantly improved coupling when compared to frictional coupling alone. The DAS technology has advanced since the PoroTomo deployment in 2016. For example, data from the Carina DAS system developed by Silixa in 2018 has a signal-to-noise ratio (SNR) that is two orders of magnitude greater than that deployed at Brady Hot Springs. The sensitivity allows for measuring strain on the picostrain scale and can be sensitive enough to measure the dilation and contraction of fractures directly *in situ*.

To assess the usefulness of the various data sets, the PoroTomo Team used a mathematical theory known as the Value of Information (VOI). Applied to seismic imaging, this approach shows that forward modeling of wave fields in combination with classification by machine learning algorithms would optimize the locations of seismic sources and receivers in a proposed deployment.

Overall, the PoroTomo project achieved its objective of assessing “an integrated technology for characterizing and monitoring changes in an EGS reservoir in three dimensions”. The technology performance metric of (spatial) resolution was assessed using checkerboard tests, as shown in Table 1.1. For the material property of P-wave velocity estimated using body-wave, travel-time tomography, the spatial resolution of the model is 100 m over most of the study area at a depth of 200 m. The P-wave and S-wave velocity models estimated from sweep interferometry were combined with a model of density to calculate the material properties of Poisson’s ratio and Young’s modulus with the same level of resolution. The 100-meter resolution achieved using the data from seismology represents a 2-fold improvement over the models existing at Brady before the PoroTomo project began and meets the minimum requirement specified in the Statement of Project Objectives (SOPO).

Using data from geodesy, the PoroTomo team was able to estimate the volumetric strain rate in the shallow aquifer with a spatial resolution of 100 m in a layer at depths of 50-150 m, thus going beyond the target resolution of 250 m specified in the SOPO. The rate of volumetric strain rate $d\varepsilon/dt$ can be used to infer the rate of cooling dT/dt and the rate of change in thermal energy dE/dt in the shallow parts of the field.

Using data from hydrology, the PoroTomo team was able to estimate the hydraulic conductivity K with a spatial resolution of 500 m, thus meeting the minimum requirement specified in the SOPO. These estimates of hydraulic conductivity K have been used to simulate the flow paths within the geothermal field at Brady. If estimates of porosity were available, then they could be combined with the hydraulic conductivity K to calculate permeability and thus further constrain models of fluid flow.

Using the information from seismology, geodesy, and hydrology, the PoroTomo team achieved a spatial resolution of 100 m, thus meeting the minimum requirement specified in the SOPO.

	Seismology	Seismology	Geodesy	Hydrology	Combined
Estimated parameter	P-wave velocity Vp [m/s]	S-wave velocity Vs [m/s]	volumetric strain rate $d\varepsilon/dt = d(\Delta V/V)/dt$ [1/s]	hydraulic conductivity K [m/s]	
Resolution at Brady in 2014	200 m	200 m	~500 m		
Minimum requirement: improve resolution to	100 m ✓	100 m ✓	500 m ✓	500 m ✓	100 m ✓
Target: improve resolution to	50 m	50 m	250 m ✓	250 m	50 m
Beyond ("over") target: improve resolution to	25 m	25 m	100 m ✓	100 m	25 m
Combined with	Vs, Density	Vp	T, P, Q	porosity	geology
Useful for inferring	Poisson's ratio, Young's modulus	Poisson's ratio	cooling rate dT/dt Thermal dE/dt	fluid flow permeability	porosity permeability

Table 1.1. Spatial resolution achieved for estimating various parameters.

Section 2. Introduction

In the geothermal field at Brady Hot Springs, Nevada, subsidence occurs at a rate of the order of a centimeter per year over an elliptical area that is ~4 km by ~1.5 km, as measured by satellite interferometric synthetic aperture radar (InSAR) and mapped in Figure 2.1. Results from inverse modeling suggest that the deformation is a result of volumetric contraction in units with depth less than 600 m. [Ali *et al.*, 2016]. Highly permeable conduits along faults appear to channel fluids from shallow aquifers to the deep geothermal reservoir tapped by the production wells, as sketched in Figure 2.2.

The Statement of Project Objectives (SOPO) for the PoroTomo project includes the following five paragraphs that are quoted verbatim.

The objective of the project is to assess an integrated technology for characterizing and monitoring changes in an EGS reservoir in three dimensions with a resolution better than 50 meters. ***The targeted characteristics include: saturation, porosity, Young's modulus, Poisson's ratio, and density***, all of which are “critically important” to a viable EGS reservoir (DOE GTO, 2014). Estimating these parameters and their uncertainties will contribute to the overarching goal of characterizing the reservoir in terms of its effective permeability and/or fracture transmissivity. By performing inverse modeling with a Bayesian, adjoint-based approach, the integrated technology will analyze measurements from three data sets: (1) seismic waveforms recorded by seismometers and distributed acoustic sensors (DAS); (2) the deformation of the Earth’s surface recorded by satellite geodesy, including the Global Positioning System (GPS) and Interferometric Synthetic Aperture Radar (InSAR); and (3) time series of hydraulic pressure, flow, and temperature measured in wells for production, injection, or observation. Methods for analyzing each of the three types of data individually are currently at Technology Readiness Level (TRL) 2 or 3. The project will drive each of these technologies to TRL 4 or 5 and the integrated technology to TRL3.

The expected outcome of Phase I is a Proof of Concept. During the first year (Budget Period 1), the project will focus on validating innovative computational analysis techniques by adapting and applying them to existing data sets. To design the configuration for testing a prototype of the integrated technology, the project team will perform simulations to calculate the expected values of the technology performance metrics listed in Table 1 of the Technical Volume. At the end of Phase I (the first go/no-go decision point), the project will undergo a formal Stage Gate Review. If the expected values of the metrics are equal to or better than the minimum requirements, then the project will proceed.

Phase II will demonstrate a prototype of the proposed integrated technology at the EGS field at Brady Hot Springs, Nevada, operated by Ormat. In this natural laboratory, the project will seek to characterize a small shallow volume with length ~1500 m, width ~500 m, and depth ~400 m, where changes in material properties and/or hydrological conditions in response to ongoing field operations have been inferred (Ali *et al.*, 2014a). To do so, the project will deploy the proposed technology during four distinct time intervals, as sketched in Figure 1. Between each measurement interval, the hydrological conditions will be intentionally manipulated by modifying the rates of pumping in the injection and production wells. Comparison of the four sets of results will quantify temporal changes in the characteristics of the study volume. The comparison will also assess the statistical uncertainty and resolution of the results. ***The expected***

outcome of Phase II is a validated small-scale prototype that will provide the technical specifications required to deploy the technology in a deeper, full-scale EGS field.

The technical specifications of the proposed integrated technology include the: 3-dimensional location, temporal sampling rate, observing time interval, spatial density, and measurement precision of each of the sensor networks (e.g., seismometers, DAS, distributed temperature sensors, pressure gauges, InSAR), as well as the configuration of the active seismic sources. To ascertain the practical numerical values for these quantities will require completing all three of the 1-year intervals in the proposed project: (1) analyzing existing data and designing the deployment strategy, (2) deploying the prototype in the natural laboratory at Brady Hot Springs, and (3) analyzing the data to estimate the material properties in a small-scale subset of an EGS field. If the technology performance metric of resolution (realized at the end of the project) satisfies the criteria in Table 1 of the Technical Volume, then the technical specifications could be scaled from the small-scale prototype toward a full-scale EGS field in a subsequent project. For example, scaling up the conventional seismic component would involve either (a) a stronger source and a similar number of receivers and source points but a decrease in spatial resolution roughly in proportion to the increased spatial scale, or (b) a stronger source and an increase in the number of receivers and source points in proportion to the increased spatial scale to maintain a comparable spatial resolution.

The technology performance metric for the proposed project will be resolution in meters of a feature in the modeled 3-D distribution of a rock mechanical property (e.g., Poisson's ratio), as determined by the dimension of a visible checkerboard pattern at 200 m depth in a test using simulated data (Table 2.1). Resolution is controlled by: the number of parameters to be estimated in the inverse problem, the number of measurements, and the distribution of the sensors. For seismic data, the wavelength and distribution of the sources also play crucial roles.

	Resolution			
	Seismology	Geodesy	Hydrology	Combined
Current state of the art at Brady	200 m ^(a)	~500 m ^(b)	—	—
Minimum requirement: improve resolution to	100 m	500 m	500 m	200 m
Target: improve resolution to	50 m	250 m	250 m	50 m
Beyond ("over") target: improve resolution to	25 m	100 m	100 m	25 m

Table 2.1. Technology performance metric. (a) Approximate resolution of seismic reflection survey (Queen et al., 2010, Lin et al., 2011). (b) Inverse modeling of InSAR data includes a geometric description of sinks in a half-space with uniform elastic properties (Ali et al., 2014a).

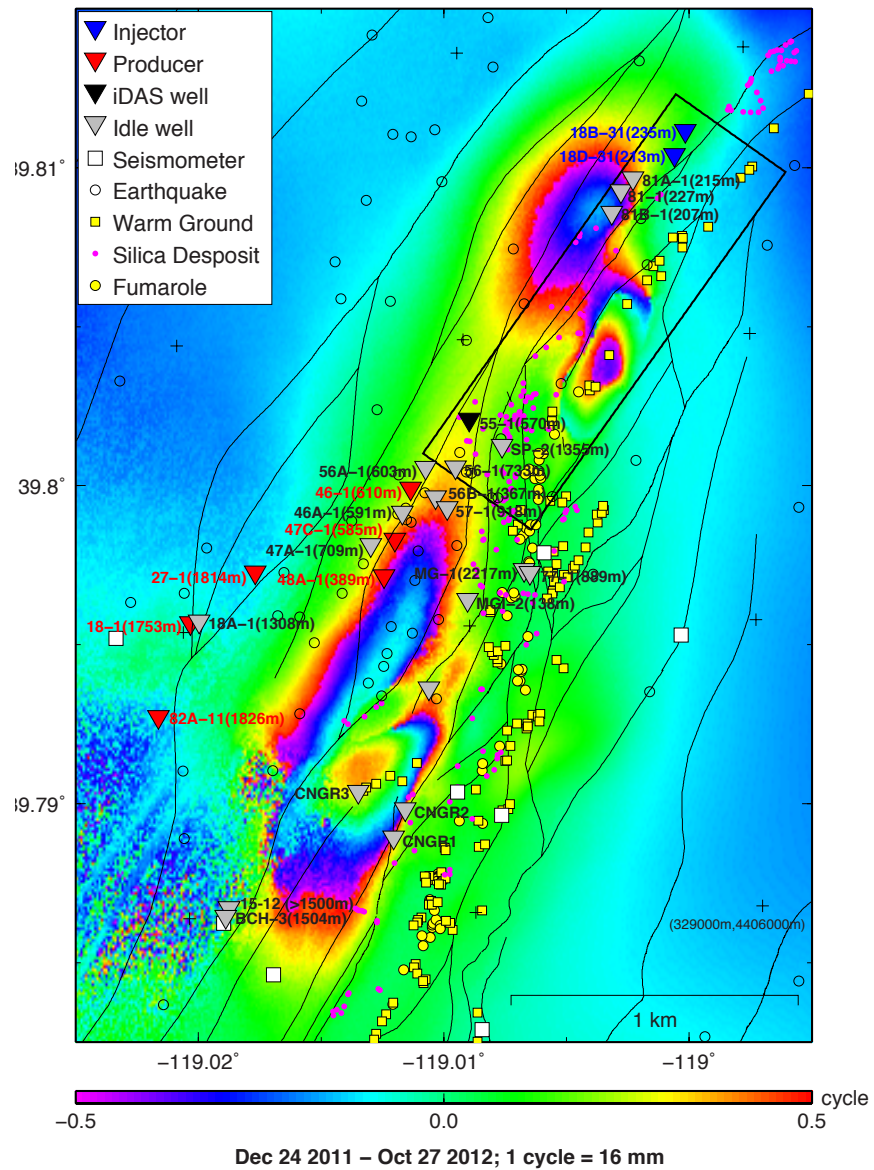


Figure 2.1. Map showing location of the Brady Hot Springs geothermal field, with faults (thin black lines, [Faulds et al., 2010]), surface hydrothermal activity, including fumaroles (yellow circles), warm ground (yellow squares), and silica deposits (magenta circles) from precise field mapping [Coolbaugh et al., 2004]. Injection wells are shown by blue triangles and producing wells are shown by red triangles. Fiducial crosses indicate 1000-meter grid in easting and northing of the Universal Transverse Mercator (UTM) projection (Zone 11). The SAR interferogram in the background shows the change in wrapped phase over the 308-day interval from December 24, 2011 to October 27, 2012. One colored fringe corresponds to one cycle of phase change, or 16 mm of range change. The black rectangle delimits the study area of the PoroTomo project. Circles denote seismicity from 2010 through 2016 recorded by the permanent seismic network (white squares) [LBL, 2016].

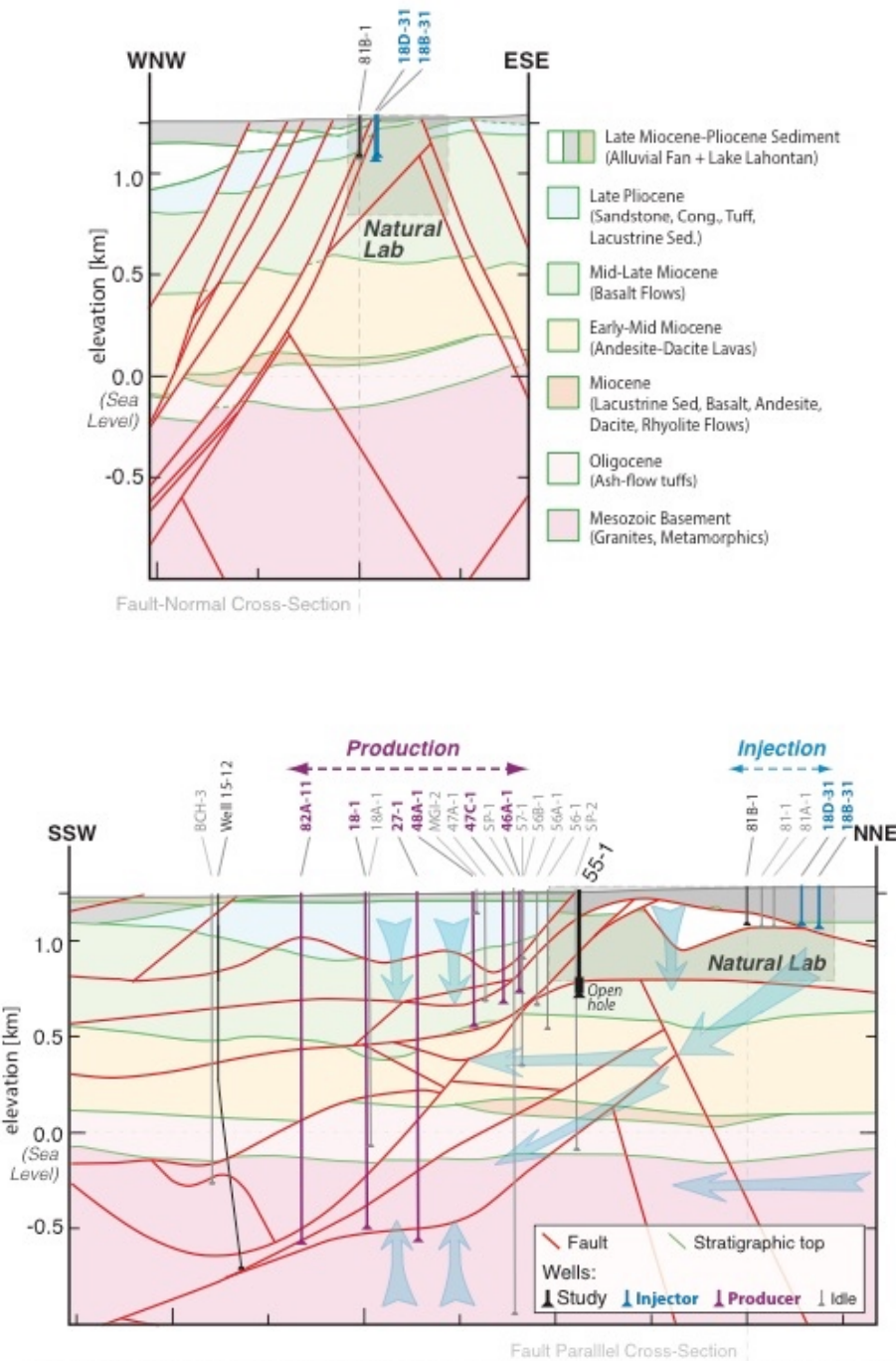


Figure 2.2. Sketches of vertical cross sections, showing the key idea that highly permeable conduits along faults channel fluids from shallow aquifers to the deep geothermal reservoir tapped by the production wells. Upper and lower vertical cross sections are perpendicular and parallel to the strike of the normal faulting system, respectively. These sketches are based on the geologic model of Jolie, Moeck and Faulds and geologic mapping by Faulds [Faulds et al., 2004; Faulds et al., 2006; Faulds et al., 2011; Shevenell et al., 2012; Jolie et al., 2015]. Elevation in km. V:H = 1:1.

Section 3. Analysis of Existing Data

Ambient Noise Tomography at Brady

We analyzed an existing passive seismic dataset recorded at the Brady site using ambient noise tomography and seismic interferometry, as has been successfully done for the EGS operation at Newberry (Matzel et al., 2014). We obtained continuous data from the current deployment of seismometers at the Brady site operated by the Lawrence Berkeley National Laboratory (LBNL). These data are continuous waveforms for 17 instruments, located just south of the PoroTomo natural lab boundary, and have been recording for several years.

A preliminary one-dimensional (1D) seismic velocity model (**Figure 3.1**) was derived from ambient noise correlation as part of a previously funded project (the INSAR-MEQ project led by Nick Davatzes of Temple University: EE0005510). This preliminary 1D model was based on continuous data from eight instruments deployed by LBNL at the Brady site, just south of the PoroTomo study area. Some 28 Green's functions were obtained and then filtered between 4-10 Hz. A 1D model of P-wave velocity (V_p), S-wave velocity (V_s), and P-wave quality factor (Q_p) was estimated for each path. The preliminary model is a median of those individual models. Due to the geometry of the instrumentation, resolution is best for the uppermost 1 km and poorly constrained with increasing depth.

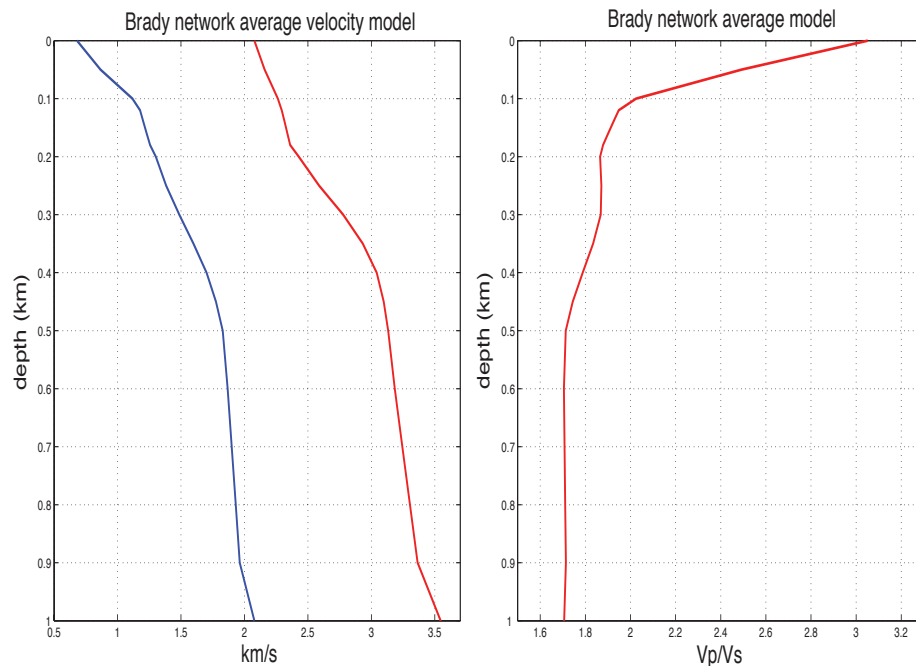


Figure 3.1. The updated average 1D velocity model for the Brady geothermal region, showing (left) V_s in blue, V_p in red, and (right) V_p/V_s in red. Note the sharp increase in V_p/V_s in the top 100 m.

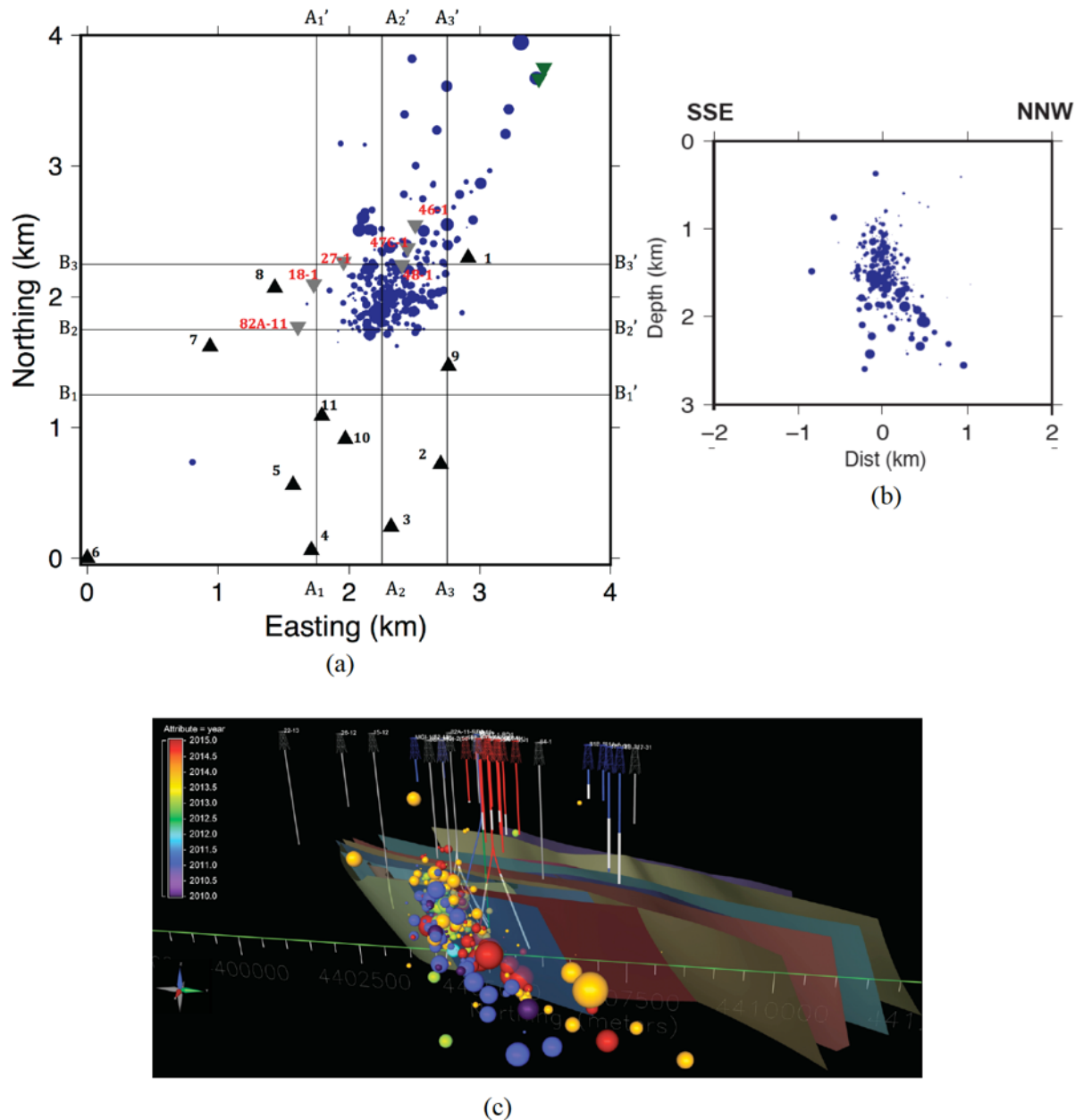


Figure 3.2. Microearthquake locations for the period December 2010 – March 2015, shown in map-view (a) and in a SSW-NNE along-strike vertical section (b). Blue circles show hypocenters with size scaled to magnitude; maximum magnitude is M 2.2. Black triangles, inverted grey triangles, and inverted green triangles show telemetered seismic stations, production wells, and injection wells, respectively. (c) Screen shot of EarthVision plot of microearthquake locations with respect to faults at Brady modeled by Drew Siler (LBNL) and Jim Faulds (UNR). Microearthquakes are color-coded according to date of occurrence. View is looking to the WSW.

Conventional Body-wave Seismology at Brady

We carried out simultaneous inversion for three-dimensional (3D) P- and S-velocity structures and microearthquake hypocenter locations using the program SimulCR developed at LBNL. Hand-picked arrival times from 476 events recorded by the Brady telemetered seismic network between November, 2010 and March, 2015 were used for the inversion, of which 347 are relocated. The remaining events were rejected by SimulCR, either because their location solutions provided poor fits to the data or they were outside the study area. Event magnitudes are from the routine LBL catalog.

Almost all of the events recorded at Brady since the network was installed in late 2010 have occurred as infrequent two- to three-day swarms, the largest of which occurred in April 2014 and March 2015. Each of these two swarms contained over 100 events. The bursts of activity appear to be correlated with geothermal field operations with increased seismic activity correlating with production shut downs. Microearthquakes that occurred during the April 2014 and March 2015 swarms appear to have initiated near the perforated interval of production well 27-1 and are located slightly to the East of the main NW-dipping fault zone (**Figure 3.2**). The microearthquakes are aligned along the general strike and dip directions of the faults.

Distributed Acoustic Sensing (DAS) Array at Garner Valley

A prototype Distributed Acoustic Sensing (DAS) array was deployed in September 2013 in a shallow trench at the site of the Garner Valley Downhole Array (GVDA) in southern California (Wang et al., 2014). The DAS was supplemented by a geophone array and active seismic sources included a vibroseis truck. Initial analysis included inventing a narrow-band, Time-Frequency Filter (TFF) to remove traffic noise and source harmonics (Lord et al., 2014), measuring directivity and sensitivity of the DAS response (Lancelle et al., 2014), and determining near-surface Rayleigh-wave velocity dispersion (Baldwin et al., 2014).

Follow-up studies were conducted to determine the usefulness of DAS for substituting or augmenting traditional geophone arrays. Software for the Source Synchronous Filter (formerly Time-Frequency Filter) was developed by Lord et al. (2016). Additional data analyses from DAS channels and PASSCAL geophones were used to add results to the subsurface dispersion profiles and an inversion of the dispersion profiles was made for the shear-wave velocity cross section at Garner Valley (Zeng et al., 2017). Group and phase velocity of Rayleigh waves along a segment of cable were obtained using the multichannel analysis of surface wave technique (MASW, Park et al., 2007) (**Figure 3.3**). The results are consistent with those obtained from seismometer records.

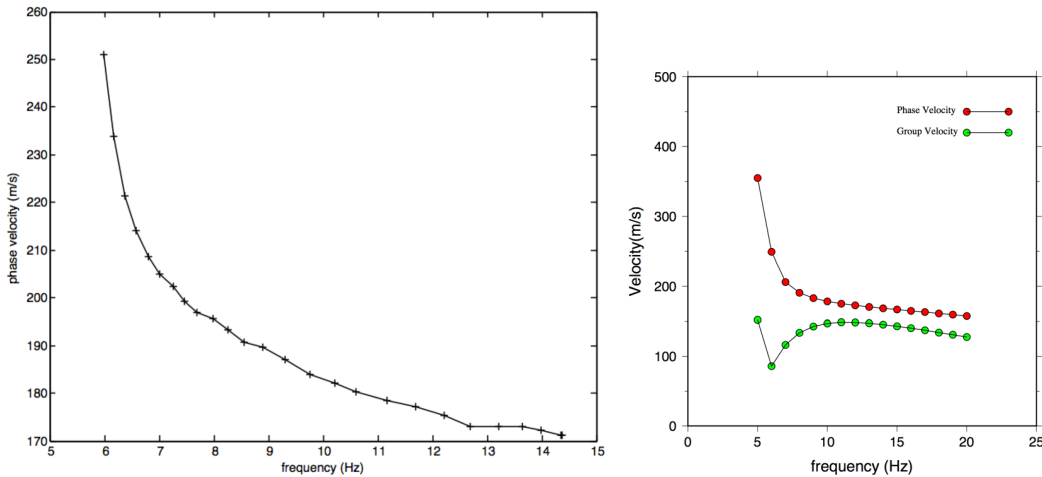


Figure 3.3. (a) Phase velocity measured with MASW method. (b) Group (green) and phase (red) velocities predicted by model in Steidl et al. (1996).

Applying Biot Theory

Based on the double porosity and dual permeability model presented in Berryman and Wang (1998) and Pride and Berryman (2003), we averaged the microscopic equations of constitutive relationships and of motion of three independent phases, solid, pore fluid and fracture fluid, which allows to accurately account for the intrinsic connection and coupling between the different phases. Doing so we derived a set of three equations for the solid phase displacement (\mathbf{u}_s), the pore fluid (\mathbf{w}^1), and fracture fluid (\mathbf{w}^2) displacements relative to the solid frame, as:

$$\rho \partial_t^2 \mathbf{u}_s + \rho_f \partial_t^2 \mathbf{w}^1 + \rho_f \partial_t^2 \mathbf{w}^2 = \nabla \cdot \mathbf{T} + \mathbf{f} \quad (3.1)$$

$$\rho_f \partial_t^2 \mathbf{u}_s + \rho_{22} \partial_t^2 \mathbf{w}^1 + \rho_{23} \partial_t^2 \mathbf{w}^2 - \mathbf{b}_{12}(t) \cdot (\partial_t \mathbf{w}^1 + \mathbf{b}_{23}(t) \cdot (\partial_t \mathbf{w}^1 - \partial_t \mathbf{w}^2)) = \nabla \cdot \mathbf{T}_f^1 + \mathbf{f} \quad (3.2)$$

$$\rho_f \partial_t^2 \mathbf{u}_s + \rho_{23} \partial_t^2 \mathbf{w}^1 + \rho_{33} \partial_t^2 \mathbf{w}^2 - \mathbf{b}_{13}(t) \cdot (\partial_t \mathbf{w}^2 - \mathbf{b}_{23}(t) \cdot (\partial_t \mathbf{w}^1 - \partial_t \mathbf{w}^2)) = \nabla \cdot \mathbf{T}_f^2 + \mathbf{f} \quad (3.3)$$

where ρ is the bulk density, ρ_f is the fluid density (assuming the same fluid flows in the pores and the fractures), ρ_{22} , ρ_{23} , and ρ_{33} are generalized as mass coefficients, dependent on the solid grain and fluid densities, porosity and tortuosity of the fracture and matrix pores, and the volume fraction of fractures. The dissipation parameters quantify dissipation solely triggered by the motion of pore and fracture fluid relative to the solid frame (\mathbf{b}_{12} and \mathbf{b}_{13}) and to the fluid flow in the matrix pore relative to the fracture (\mathbf{b}_{23}) – with \mathbf{b}_{12} , \mathbf{b}_{13} and \mathbf{b}_{23} related to the permeability tensor, fluid viscosity, porosity and tortuosity of the fracture and matrix pores and volume fraction. Finally, \mathbf{T} , \mathbf{T}_f , and \mathbf{f} refer to the total stress, pore fluid and fracture fluid stresses, and the source.

Note that when suppressing the fracture fluid displacement, these equations revert to the classical Biot equations. Building on the implementation of single porosity Biot theory already present in the spectral-element code SPECFEM (Morency and Tromp, 2008), this new set of equations can be readily added to the code.

We derived equations for wave propagation in a fractured porous medium. In doing so, we improved the homogeneous porous medium formalism from the Biot theory, by adding the coupled influence of fracture network, getting us closer to modeling Brady. The derivation of these equations shows three interfacial strains defined in terms of macroscopic quantities (e.g., solid, frame, pore fluid, fracture fluid moduli, porosity), which are measurable in the lab and

accessible in the literature to define a prior model. These interfacial strains help characterize the macroscopic constitutive relationships of the fractured porous system in terms of its three constituents: solid matrix, pore fluid, and fracture fluid. This allows us to differentiate these different mechanical properties for an adjoint inversion.

Analysis of Existing InSAR Data

We analyzed interferometric synthetic aperture radar (InSAR) pairs at Brady in order to better understand the deformation patterns prior to the deployment in March 2016. We started with SAR data from the ENVISAT ((McLeod et al., 1998), ALOS (Rosenqvist et al., 2007), and TerraSAR-X/TanDEM-X missions (Pitz & Miller, 2010). We also started ordering new TerraSAR-X (TSX) scenes, something to be continued through the end of the project. We explored using data from the Sentinel-1A satellite mission (Torres et al., 2012); however, we are unable to resolve a clear signal due to the coarse resolution degradation from the SCANSAR imaging mode.

Pairs were formed using SAR data to create deformation maps that span from 1994 to 2015. Spatial deformation is first modeled by representing the reservoirs as a combination of four dislocations embedded in a homogeneous half-space with uniform elastic properties (Okada, 1985). Best-fitting estimates of source parameters are found using simulated annealing with range change rate observables (Ali & Feigl, 2012; Ali et al., 2016). Time series analysis is then performed on volume change rate estimates derived from the best-fitting deformation source model parameters to test whether the deformation observed at Brady is related to geothermal activity. We find a positive correlation between the volumetric flow rates of water injected into shallow wells and volume change rates estimated from InSAR analysis. From this correlation, we infer that “highly permeable conduits along faults channel fluids to the reservoir tapped by the production wells” (Ali et al., 2016).

Results of this deformation analysis were presented at the American Geophysical Union Fall Meetings from 2013 through 2015 (Ali et al., 2013; Ali et al., 2014; Feigl et al., 2015) as well as the annual Stanford Geothermal Workshops in 2015 and 2016 (Ali et al., 2015; Ali et al., 2016a). In addition, this work led to a peer-reviewed publication in *Geothermics* entitled “Time-series analysis of surface deformation at Brady Hot Springs geothermal field (Nevada) using interferometric synthetic aperture radar” (Ali et al., 2016). An example interferogram from this work has been submitted to the GDR in Hierarchical Data Format (HDF-5) format (Ali & U. of Wisconsin, 2015b).

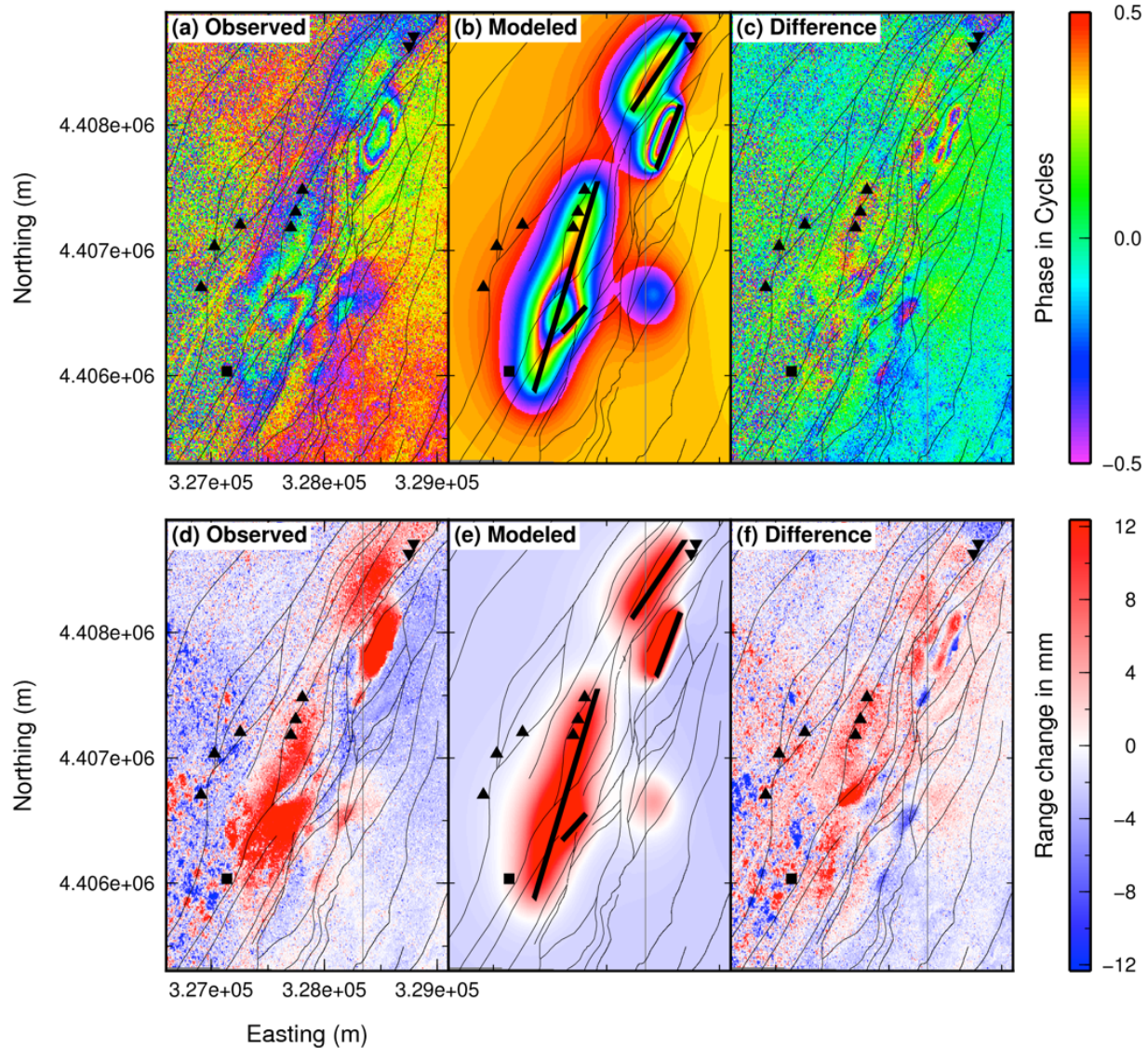


Figure 3.4. (a) Interferogram showing observed values of wrapped phase change for a pair of TerraSAR-X images in Track 53, spanning the 363-day interval from May-13-2013 to May-11-2014. One colored fringe corresponds to one cycle of phase change, or 16 mm of range change. (b) Modeled wrapped phase values calculated from the final estimate of the parameters in the elastic model. (c) Residual values of the phase, calculated by subtracting the modeled values from the observed values. (d) Observed unwrapped range change values in mm. (e) Modeled range change values in mm. (f) Residual values of the range change, calculated by subtracting the modeled values from the observed values. Thin solid lines represent the surface trace of faults, triangles represent producers, inverted triangles represent injectors and square represents the location of well 15-12. Thick solid lines represent the surface projections of the modeled sinks. Figure and caption from Ali et al., 2016.

GPS Data Analysis

GPS data from 2004/01/30 through 2014/09/15 have been downloaded from the two existing continuously operating GPS stations (BRAD and BRDY) (**Figure 3.5**) and analyzed to produce daily estimates of relative vector displacement. The data shows that we would be able to easily recognize changes in relative displacement of 5 mm in the horizontal and 10 mm in the vertical components (**Figure 3.6**). This uncertainty in position is better than that of InSAR and will help in using the InSAR in inferring subsurface volume changes.

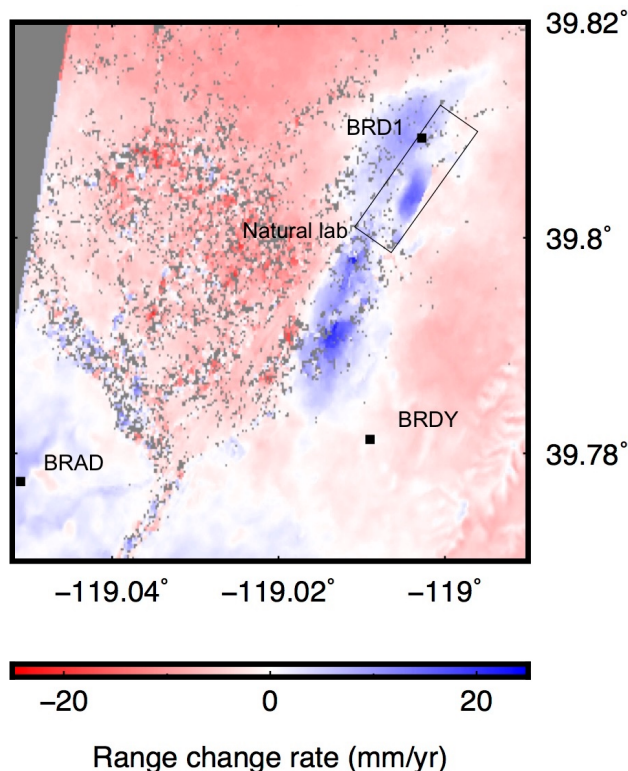


Figure 3.5. Interferogram showing the relative locations of GPS stations BRAD, BRDY, and BRD1 and the Brady natural lab.

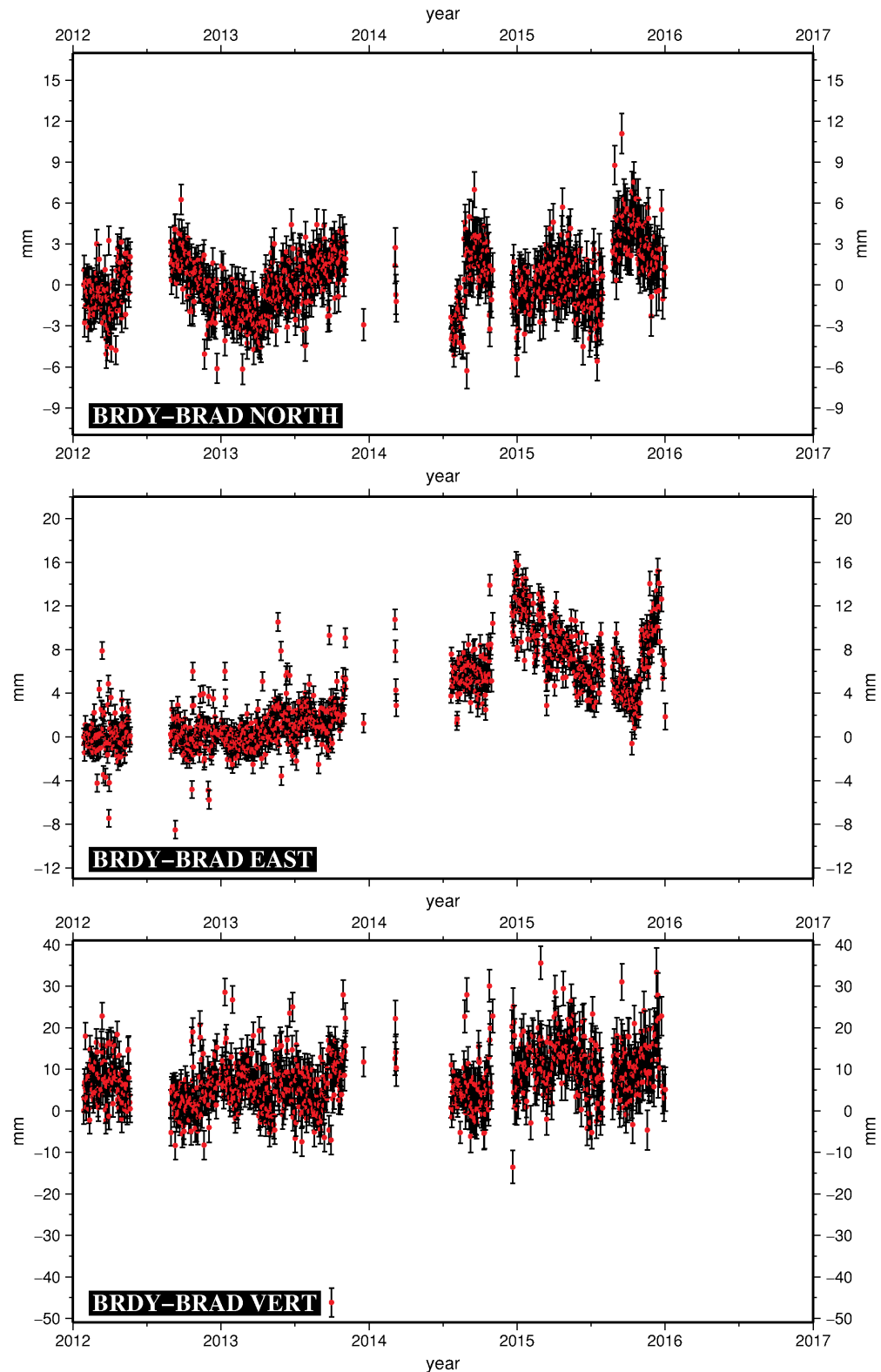


Figure 3.6. Time series of relative position between GPS stations BRDY and BRAD, referred to the NA12 reference frame.

Compilation of Pressure-Temperature Records at Brady

In an unprecedented release of temperature data by a private geothermal company, ORMAT made their pressure and temperature records from all wells including production, injection, stimulation, and observation wells, made between 1990 and 2015 available to us. These data were analyzed as part of Ali et al. (2016) and Cardiff et al. (2018).

DTS at Guelph, Ontario, Canada

DTS data from active heat-pulse injections in monitoring wells located in southern Ontario, Canada were identified for analysis to characterize flow through fractures under natural and/or forced gradient conditions (Coleman, 2013; Coleman et al., 2015). At Guelph, DTS data were collected during fluid injection in a shallow (78 m) borehole in fractured dolostone. The thermal response to active heating was used to identify the water level and inflow into the borehole. The temperature contrast of the injected fluid allowed for characterization of the flow distribution. In this case, most of the injected fluid leaves the borehole through a single zone with significant transmissivity.

The planned deployment at Brady did not include active heating methods or monitoring in the injection wells. Nonetheless, pumping and injecting fluids of varying temperature can create a thermal signature that could be monitored with DTS in an observation well (Johannesson et al., 2012). These data improved understanding of both the flow system and thermal response with depth due to geothermal energy production.

Development and Application of Hydraulic Tomography at Boise

Existing hydraulic tomography codes developed for transient hydraulic tomography (Cardiff et al., 2013b) and periodic hydraulic tomography (Cardiff et al., 2013a) were modified and tested on data collected from a shallow aquifer test in Boise, Idaho. Inversion results contain layerings and patches of heterogeneity that are consistent with prior investigations (Cardiff et al., 2011), though with somewhat lower resolution due to the small number of tests available. Still, heterogeneous features on the order of 7 m laterally or 3 m vertically are clearly visible, meaning that resolution of the Boise inversion is roughly comparable to the distances between observation locations (~2 m spacing vertically, ~7 m spacing laterally). The results were presented at the Fall Meeting of the American Geophysical Union (AGU) in a presentation entitled “Oscillatory Hydraulic Tomography at the Field Scale: Boise Hydrogeophysical Research Site” (Lim et al., 2015).

Section 4. Deployment

A. Results

Permitting

As the operator of the Brady geothermal field, Ormat handled all permits related to operations at the Brady natural laboratory. This process was important because the fieldwork in March 2016 could not move forward until the NEPA determination was made, as described in the award document (**Figure 4.1**).

The last day for public comments on the Notice of Intent (NOI) was October 18, 2015. After reviewing the Notice of Intent (NOI), the Winnemucca Office of the Bureau of Land Management (BLM) decided to perform an Environmental Assessment (EA).

Term 11. NEPA REQUIREMENTS

DOE must comply with the National Environmental Policy Act (NEPA) prior to authorizing the use of Federal funds. The Recipient is restricted from taking any action using Federal funds that would have an adverse effect on the environment or limit the choice of reasonable alternatives prior to DOE providing a final NEPA determination regarding this project.

DOE has made a conditional NEPA determination for this Award, and Federal funding for certain tasks under this Award is contingent upon the final NEPA determination.

The Recipient is restricted from taking any action using federal funds, which would have an adverse affect on the environment or limit the choice of reasonable alternatives prior to DOE/NNSA providing either a NEPA clearance or a final NEPA decision regarding the project.

Prohibited actions include the following phases and/or tasks as referenced in the SOPO approved by the Contracting Officer:

Task 6: Deployment including all subtasks.

This restriction does not preclude the Recipient from the following phases and/or tasks as referenced in the SOPO approved by the Contracting Officer:

All tasks and subtasks other than Task 6: Deployment and Task 6: Deployment subtasks.

Figure 4.1. Excerpt from PoroTomo award document.

The permitting process took longer than expected. A teleconference took place Thursday October 29, 2015 at 3:00 PM for a discussion of the permitting process at Brady. The teleconference included: Elisabet Metcalfe, Bill Vandermeer Casey Strickland, Mark Hanneman, and Janice Lopeman. A nominal timeline was developed.

On Tuesday, January 5, 2016, a BLM geologist from the Humboldt River Field Office (in Winnemucca, Nevada) sent an e-mail message indicating that the field deployment could occur in March 2016.

On January 13, 2016, a BLM geologist from Humboldt River Field Office (in Winnemucca, Nevada) sent an e-mail message indicating completion of the Environmental Assessment, Decision Record, and Finding of No Significant Impact.

On January 20, 2016, Kurt Feigl, Elisabet Metcalfe, Bill Vandermeer, and Casey Strickland agreed on the timeline on lifting restriction on deployment. By working quickly together, Kurt Feigl, Elisabet Metcalfe, Bill Vandermeer, and Casey Strickland were able to meet the timeline for lifting the restriction on deployment (Task 6), as shown in **Figure 4.2**.

Monday 2016/01/25:	Feigl submits Environmental Questionnaire (EQ-1)
Tuesday 2016/01/26:	Metcalfe submits (EQ-2) to Strickland
Friday 2016/01/29:	Strickland submits CX for legal review
Wednesday 2016/02/10:	Contract Officer provides updated award to UW
Tuesday 2016/02/16:	Feigl, Lord, Greer, Coleman commence trenching

Figure 4.2. Timeline for lifting restriction on deployment (Task 6).

In early February 2016, the process of permitting was completed.

The trenching for the horizontal fiber-optic cable was completed with the approval of the BLM. The seismometers near the California Trail were installed temporarily in shallow holes under the supervision of the BLM archeologist from Humboldt River Field Office (in Winnemucca, Nevada). **Figure 4.3** shows a Z-Land Fairfield Nodal seismometer as temporarily deployed at a typical station. In addition, several seismic stations included Reftek instrumentation, as shown in **Figure 4.4**. At six stations, both types of instrumentation were installed temporarily together, as shown in **Figure 4.5**.



Figure 4.3 Photograph showing a Fairfield Nodal Z-land seismometer temporarily deployed in the soil at Brady Hot Springs, Nevada, in March 2016.



Figure 4.4. Photograph showing a RefTek 130 datalogger with L-22 model 2-Hz three-component sensor (hidden under rocks) and power supply temporarily deployed at Brady Hot Springs, Nevada, in March 2016.



Figure 4.5 Photograph showing Fairfield Nodal Z-land seismometer, a RefTek 130 datalogger with L-22 model 2-Hz three-component sensor, and its power supply temporarily deployed in the soil at Brady Hot Springs, Nevada, in March 2016.

After the deployment, the Fairfield Nodal and Reftek seismic instruments were removed. Following the deployment's conclusion, Pioneer General Engineering was contracted for site reclamation. The contractor repaired the barbed wire fence in several locations. The contractor worked for two days raking over vibroseis stations and cable deployment paths. On Wednesday, April 13, 2016, a BLM archaeologist from the Humboldt River Field Office (in Winnemucca, Nevada) visited the site to view the results of reclamation activities and indicated approval.

Field Deployment

Deployment of the network of sensors at Brady Hot Springs geothermal field in Nevada (**Figure 4.6** and **Figure 4.7**) spanned four weeks in March 2016. Data were collected during four successive 3-day intervals with a goal of detecting temporal changes in material properties associated with changes in pumping operations (**Figure 4.8**). Stage 1 of the experiment was March 11-13 and consisted of normal well operations. Stage 2 was March 14-18 and corresponded to the shutdown of the power plant and cessation of pumping. Stage 3 was March 18-24 with increased in-field injection rate and pulsed pumping from March 21-23. Stage 4 was March 24-25 and was marked by a return to normal well operations. The deployment included both active and passive seismic monitoring, geodetic measurements using InSAR and GPS, and monitoring of the pressure in multiple observation wells.

A rotating staff of personnel were onsite before, during, and after active deployment of the array. A list of personnel appears in (Figure 4.9). All personnel working on site underwent safety training with ORMAT. Safety "toolbox" meetings were also held onsite every morning. Communications were facilitated by all personnel lodging at the same hotel. Lists of individuals arriving and departing were submitted by fax to ORMAT's operational control center daily. A minimum of two PoroTomo personnel were on site at all times between March 11 and 25. Two portable buildings (shipping containers with doors and windows) were temporarily installed. Electrical power was installed with a temporary junction box. Two portable toilets were rented for the deployment and were replaced once.

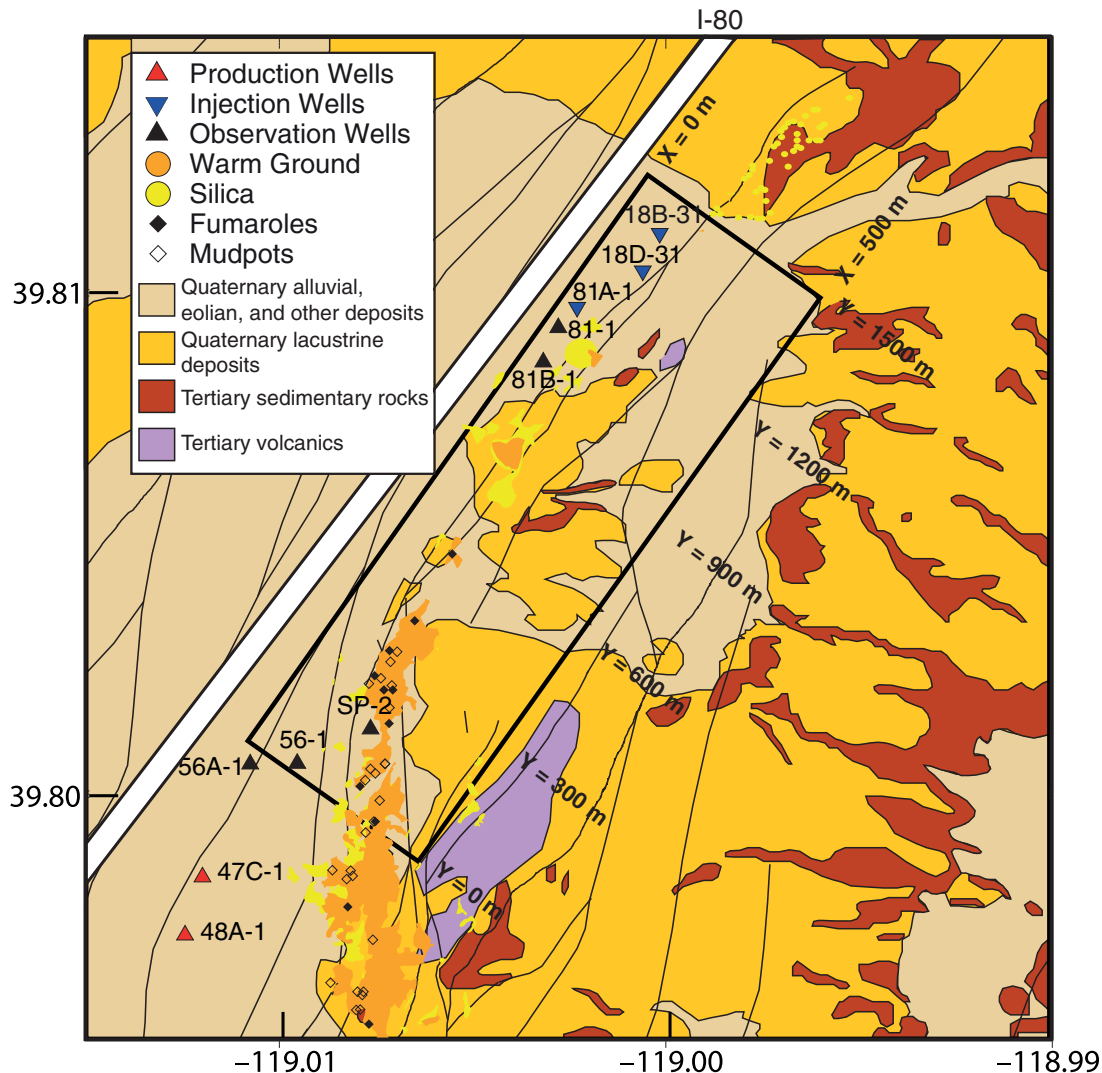


Figure 4.6. Geological map of Brady geothermal field from Parker et al. (2018). “Simplified geologic map of the Brady geothermal field modified from Faulds et al. (2017). The black rectangle corresponds to the target region where the seismic nodes were closely spaced. The surface geothermal features mapped by Coolbaugh et al. (2004) have been overlaid approximately. The white strip denotes the approximate location of Interstate highway 80.”

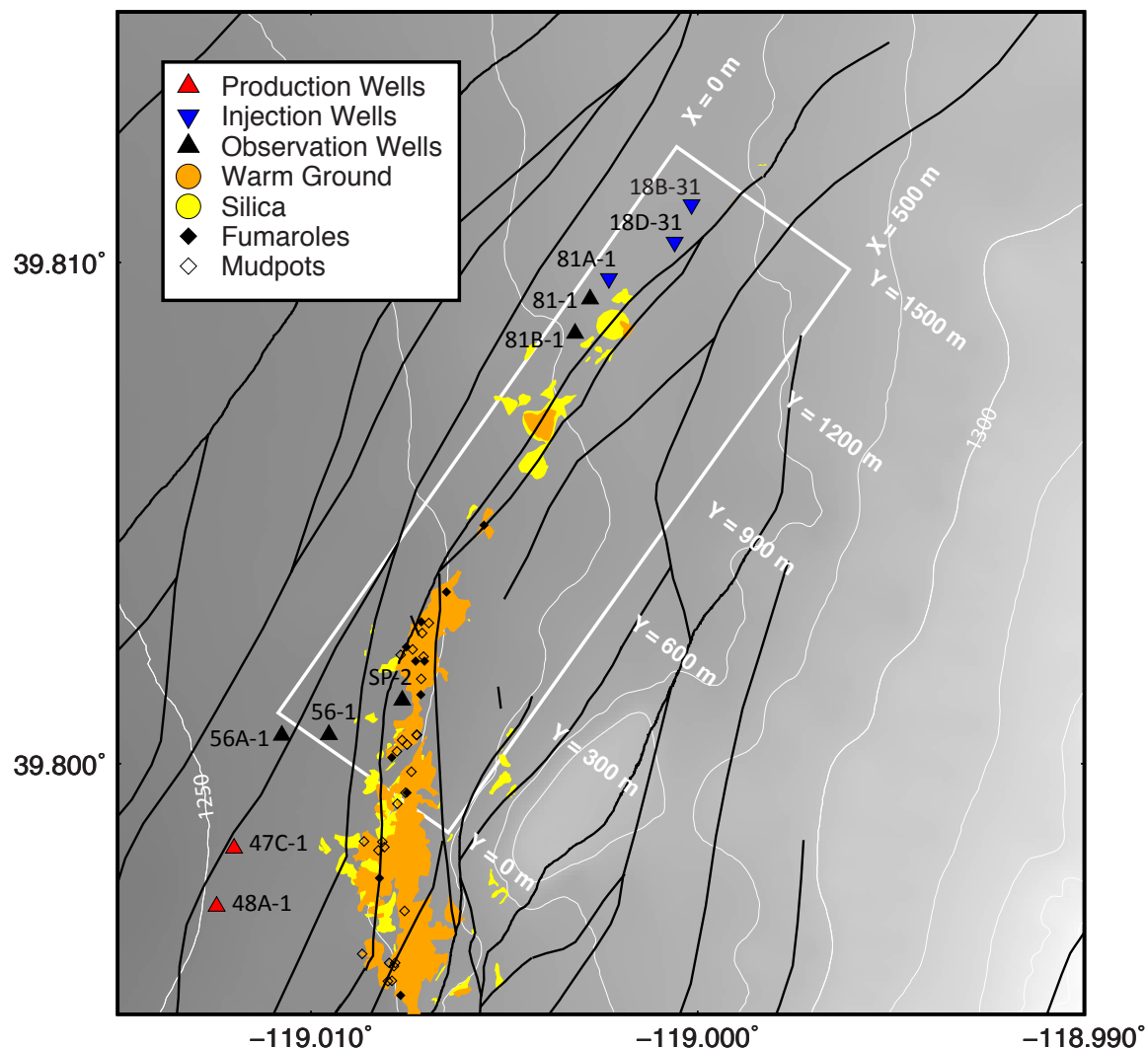


Figure 4.7. Map of geothermal surface features at Brady, from Parker, et al. (2018). Elevations are meters above the WGS84 ellipsoid with 10 m contour intervals. The box corresponds to the PoroTomo target area with labels of the rotated PoroTomo coordinate system.

Day of experiment	before	1	2	3	4	5	6	7	8	9	10	11	12	13	14	15	after
Calendar Date		2016-03-11	2016-03-12	2016-03-13	2016-03-14	2016-03-15	2016-03-16	2016-03-17	2016-03-18	2016-03-19	2016-03-20	2016-03-21	2016-03-22	2016-03-23	2016-03-24	2016-03-25	
day of week		Friday	Saturday	Sunday	Monday	Tuesday	Wednesday	Thursday	Friday	Saturday	Sunday	Monday	Tuesday	Wednesday	Thursday	Friday	
Normal operations																	
SHUTDOWN Stop injection and production																	
Divert injection to infield wells																	
Normal operations																	
Expected water level																	
Acquire SAR Image																	
Operate Active Seismic Source																	
Operate seismometers																	
Operate DAS and DTS																	
Operate Pressure Sensors																	

Figure 4.8. Plan for deployment schedule at Brady displayed as a Gantt chart.

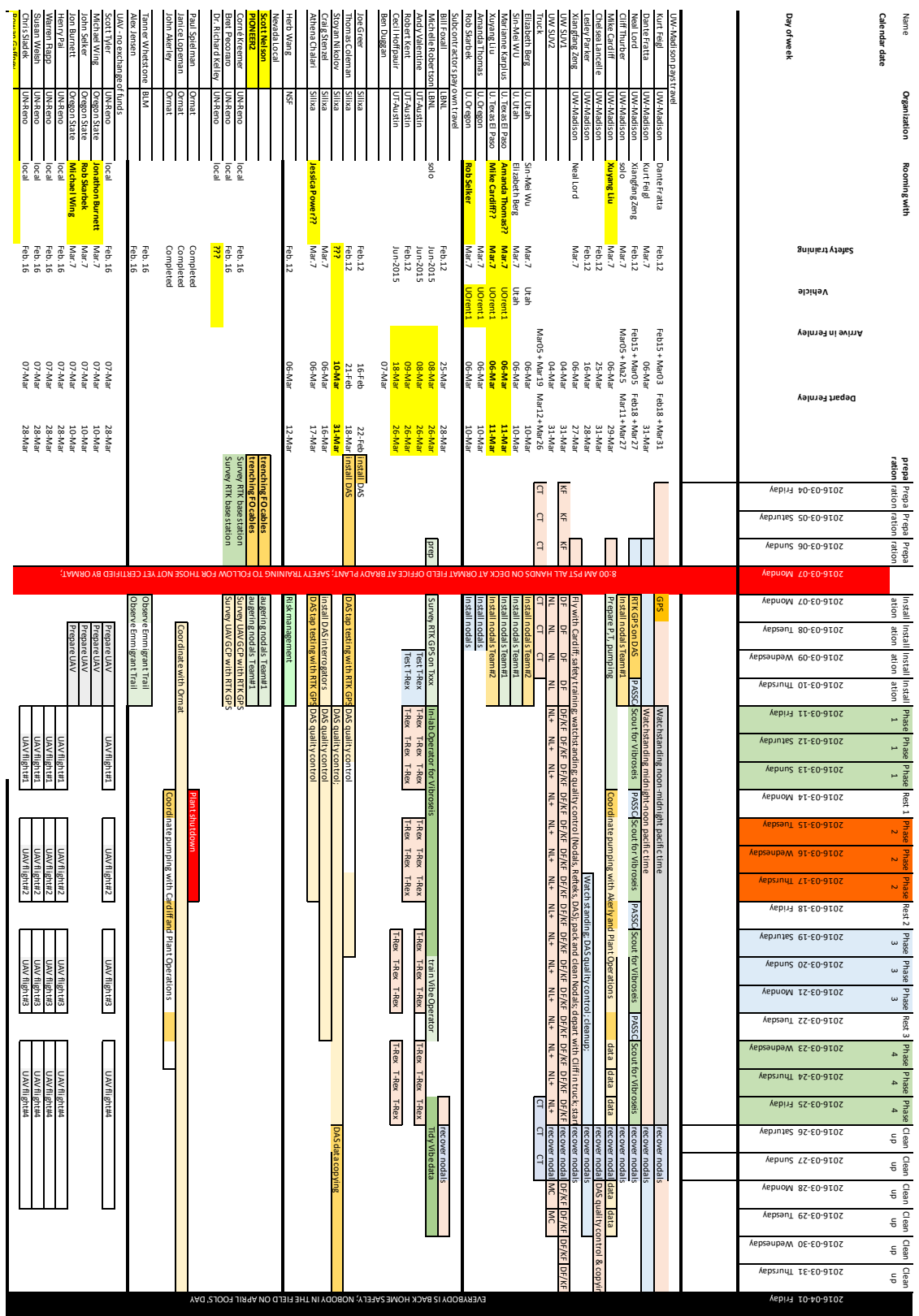


Figure 4.9. PERT diagram showing plans for deployment.

Seismology

A total of 248 seismic instruments were installed between March 7 and 10, 2016. Of these, 242 were Fairfield Nodal Zland 5-Hz three-component instruments (Figure 4.10) and six were RefTek 130 dataloggers with L-22 model 2-Hz three-component sensors. The geophone array had instrument spacing of approximately 60 m in the target zone (Figure 4.11). Two of the Zland units were removed on March 11 and sent to the University of Utah in order to check on proper instrument configuration and operation. This check proved satisfactory. Data from the six RefTek units were regularly downloaded and checked to assess vibroseis signal quality during the field experiment. All portable instruments were removed on March 26. Only two of the Zland units failed to record data. The nodal geophones were generously rented or loaned by the University of Utah (115 units), the University of Oregon (80 units), and the University of Texas at El Paso (47 units).



Figure 4.10. Z-land seismometer manufactured by Fairfield Nodal.

A real-time kinematic (RTK) GPS survey was carried out to determine positions of the instruments to within 10 cm. Two Zland sites were missed during the survey, so we use three other sources of location information (handheld GPS position at installation, handheld GPS position at removal, and the GPS location determined by the Zland instruments themselves) to provide a location estimate, which has poorer accuracy than RTK.

Fiber optic cables were installed both horizontally and vertically to collect distributed acoustic sensing (DAS) and distributed temperature sensing (DTS) data (Figure 4.11). Quality control was performed in the field. Approximately 9000 meters of fiber optic cable were deployed horizontally in a trench approximately 100 cm deep and began collection on March 11.

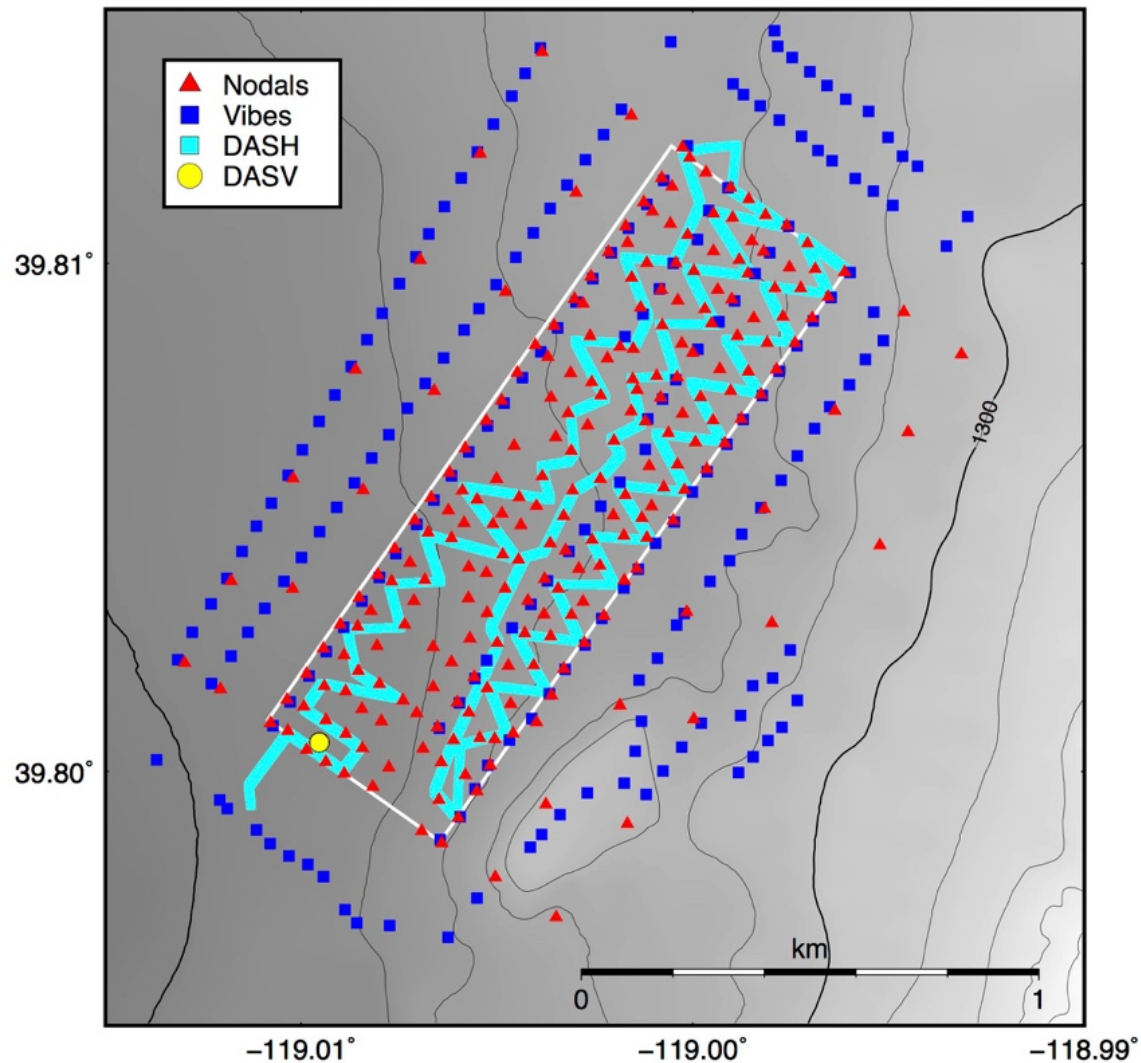


Figure 4.11. Map showing the seismic instrumentation deployment. Red triangles are nodal geophones, blue squares are vibroseis points, cyan line is the trenched fiber-optic cable, and the yellow circle is the borehole containing the vertical fiber-optic cable. From Parker et al. (2018).

The (horizontal) surface cable is a ruggedized polyurethane jacketed military type cable that is rodent-resistant with acrylate-coated fibers rated to 85°C. To install the cable, we dug a trench approximately 100 cm deep using a Ditch Witch-style trencher (**Figure 4.12**). The bottom surface of the trench was leveled and smoothed using a tool attached to the trencher and manually using a hoe. The trenching process took approximately two weeks. The cable was laid into the trench as five separate cable lengths spliced together using “direct-bury” enclosures.



Figure 4.12. Photo showing trenching for installation of fiber-optic cable at Brady. 2016/02/23 [Thomas Coleman].

The vertical fiber-optic cable in Well 56-1 was installed on March 17, in time to collect seismologic (DAS) and thermal (DTS) data continuously for the third and fourth stages of the deployment, through March 25. The vertical cable is a 1/8"-diameter (3.2 mm) bare 316 stainless

steel double tube containing both single-mode and multi-mode high temp acrylate-coated fibers rated to 150°C.

In total, four interrogators recorded DAS and DTS data from both the vertical and horizontal cables continuously. For the DAS data, the gauge length was set to 10 m. For timing, the sampling clock was phase locked to a GPS receiver. The UTC time stamp of the first sample was written with 1 microsecond accuracy in the text header of each Level-1 data file.

The DTS data, including raw Stokes and anti-Stokes measurements, were sampled once per minute. Quality control of the DAS data continued throughout the deployment. Optical signals were monitored hourly during acquisition using the DTS and DAS interrogators. No attenuation of the signal was identified. Copies of the data files were made in the field. The number and size of the DTS and DAS data files was verified hourly. Using the horizontal DAS array, we were able to record a moderate-sized earthquake with local magnitude 4.3 on March 21, as shown in **Figure 4.13**. As described by Wang et al. (2018), at the end of the deployment, both cables were terminated in steel splice boxes to allow future temperature and seismic measurements to be carried out at Brady.

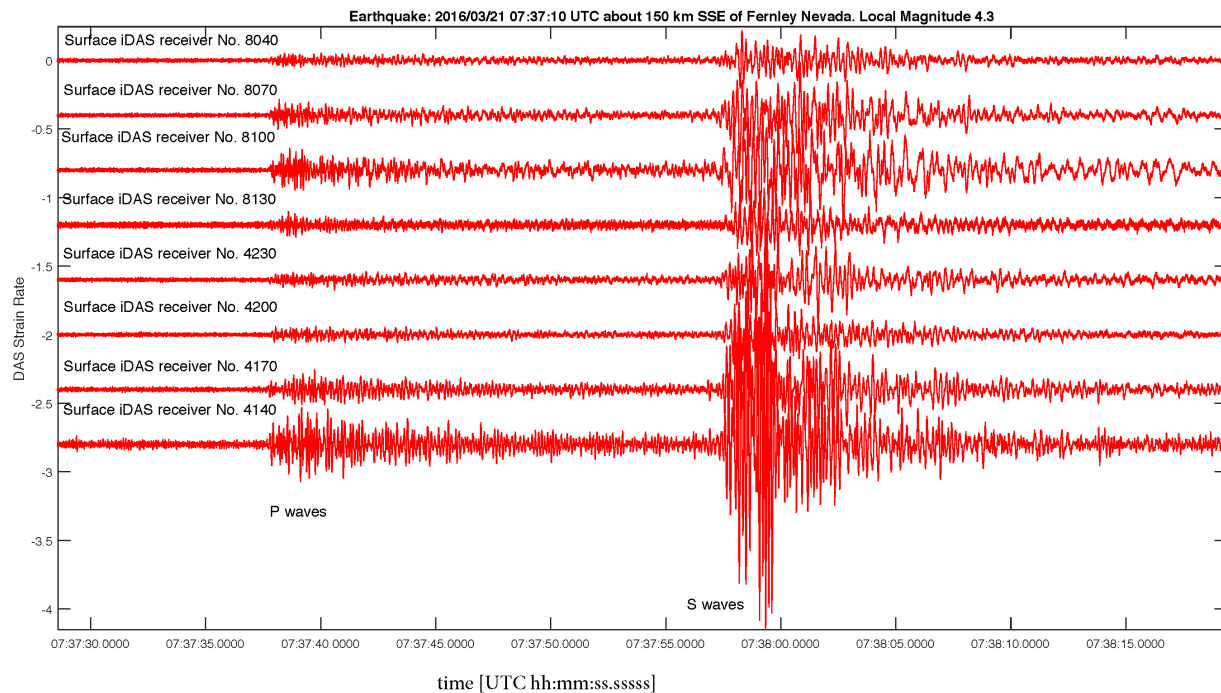


Figure 4.13. Strain rate (in arbitrary units) as recorded by DAS in the horizontal fiber optic cable, showing P- and S-waves from an earthquake on March 21, 2016 located about 150 km SSE of Fernley Nevada with local magnitude 4.3.

In addition, Lawrence Berkeley National Laboratory (LBNL) operated the existing seismic network, consisting of 8 borehole seismometers equipped with Nanometrics instruments and 6 Reftek stations deployed on the surface. This network operated and recorded data continuously during the month of March 2016. The waveform data and catalogs of seismic events derived from them are available from the Northern California Earthquake Data Center³. The permanent

³ <http://www.ncedc.org/egs/>

network of seismometers operated by LBNL has been described by Cardiff et al. (2018) as follows.

"In 2010, a network of seismometers was installed at Brady (Foxall, 2014; Nathwani et al., 2011). Microseismic events are automatically detected by this array using automated triggering and are then manually reviewed. Initial hypocenter estimates for these events are automatically estimated using a 1-dimensional velocity model. The events recorded between 2010 and 2015 have been re-analyzed by scientists at Lawrence Berkeley National Laboratory (LBL), who carried out simultaneous inversion to estimate event times and relocated hypocenters, along with 3-dimensional P- and S-wave velocity models (Foxall, 2016). The first event in this re-located long-term catalog is dated 2010 November 13, and the last event analyzed using this approach occurred on 2015 March 24. None of the events in this catalog were felt by humans. With the exception of a single moment magnitude (M_w) 2.2 event in November 2010, no event in this re-analyzed catalog exceeded magnitude M_w 2.0. The detection threshold within the array is estimated at about $M_w \sim -1.0$. Based on Gutenberg–Richter plots, this catalog is estimated to be complete to approximately $M_w \sim 0.5$. All event hypocenters from this catalog are shown spatially in Fig. 3, along with the locations of site wells. Absolute location errors for these events have been determined statistically, and are estimated to be less than 500 m for 95% of the epicentral locations and less than 500 m for 80% of the depth estimates. Location errors are associated with error in arrival time picks as well as with sensitivity to the starting velocity model used during simultaneous inversion. In Fig. 3, the open intervals of wells at the Brady site are highlighted as sections of thicker black lines – we note that these intervals appear to have similar depths to the location of event hypocenters, suggesting that a zone tapped for geothermal heat is associated with faulting at this interval. The apparent dip of the seismic event cloud also agrees with interpretations of subsurface fault geometry produced by Jolie et al. (2015)."'

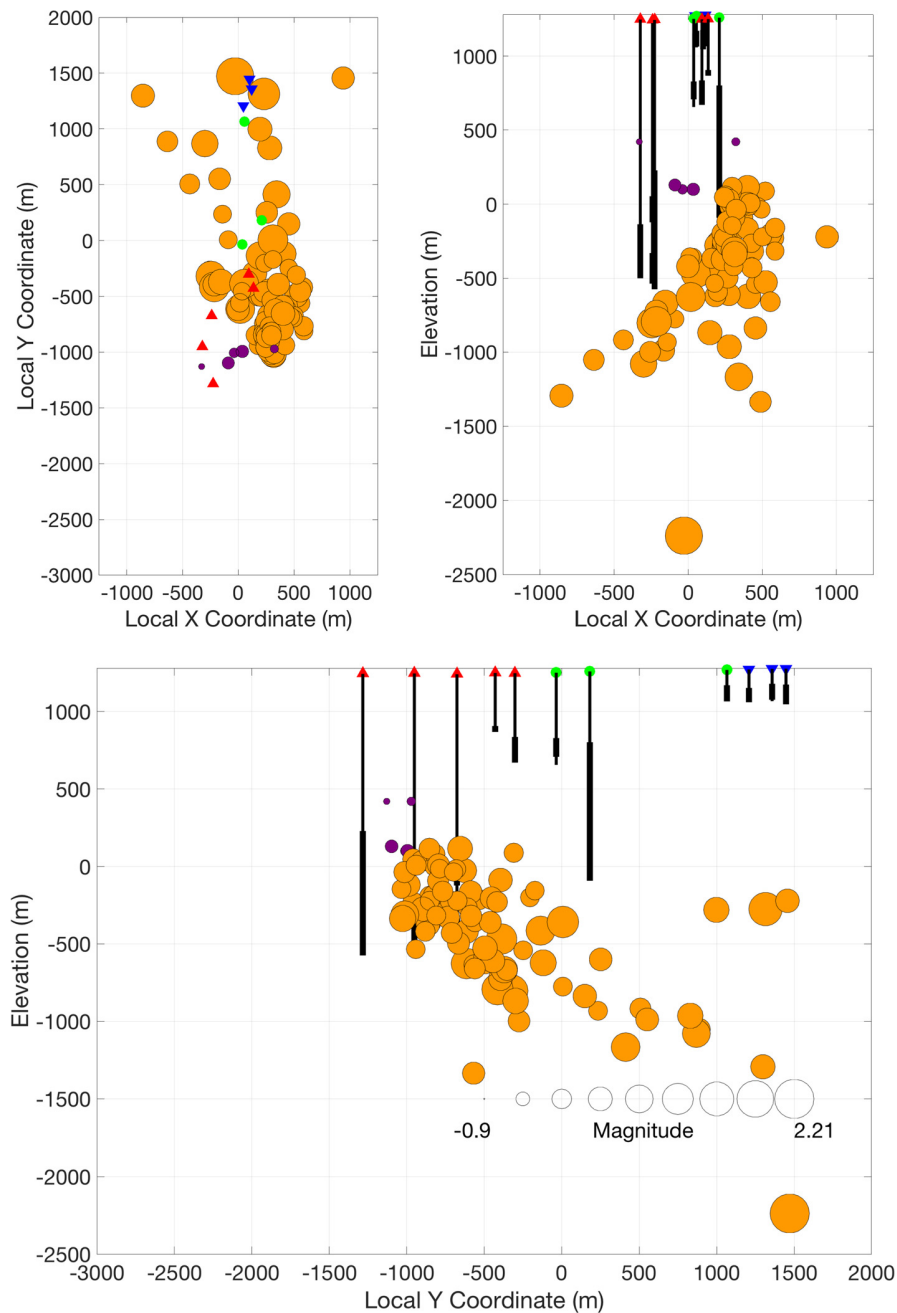


Figure 4.14. Fig. 3 from Cardiff et al. (2018): “Views of Brady subsurface, showing horizontal map view (top left), projection to a vertical plane striking NE (top right), and projection to a vertical plane striking NW (bottom). Orange circles show hypocentral locations in the long-term catalog, spanning dates from November 2010 to March 2015 (Foxall, 2016). Purple disks show hypocentral locations from the short-term catalog, spanning March 2016 dates of the PoroTomo experiment. Black lines show wells, with thicker segments representing intervals that are open to the surrounding formation. Red triangles denote production wells; blue, injection wells; green, observation wells. All elevations are represented as height above WGS84 ellipsoid.”

We chose a vibrating triaxial seismic source named “T-Rex” for the PoroTomo field deployment (Figure 4.15). Owned by the University of Texas at Austin, T-Rex is a 64,000-pound vibroseis (“vibe”) source. It is the only source in the western hemisphere that is capable of transforming between three orthogonal shaking directions without moving the vibe or its baseplate:

- P-wave compressional energy (vertical shaking)
- S-wave shear energy in the longitudinal direction (nose-to-tail horizontal shaking)
- S-wave shear energy in the transverse direction (side-to-side horizontal shaking)

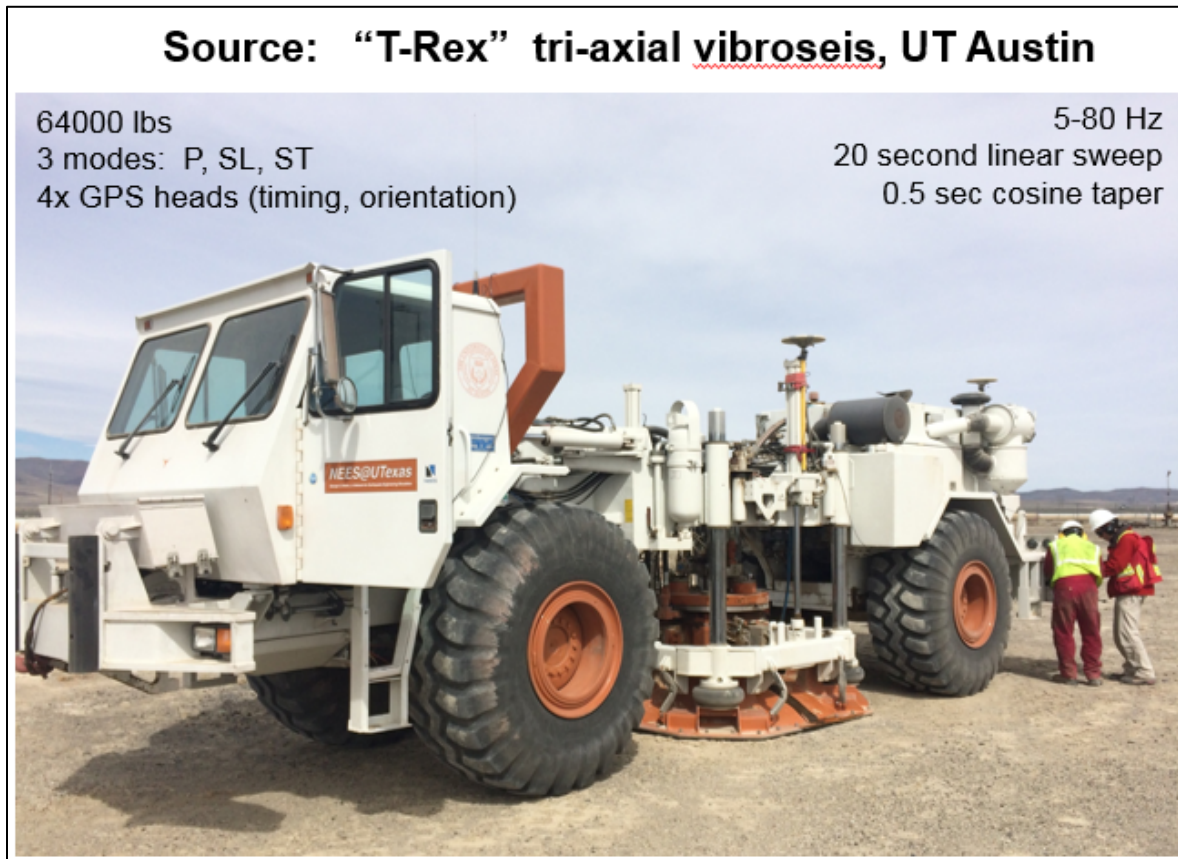


Figure 4.15. Tri-axial vibroseis vehicle “T-Rex”

The T-Rex tri-axial vibroseis source was successfully deployed for all four stages of the field deployment at Brady in March 2016. An engineering team from the University of Texas at Austin, including Andrew Valentine, Robert Kent, and Cecil Hoffpauir, served as vibe operators for T-Rex. Michelle Robertson of Lawrence Berkeley National Lab (LBNL) acted as the sole vibe observer.

At each vibration point (VP), the vibration protocol included a total of nine sweeps: three sweeps of P, three sweeps of transverse S, and three sweeps longitudinal S. Each sweep was composed of a linear progression from 5 to 80 Hz in frequency over a 20 second duration with a 0.5-second cosine taper at the start and end of the sweep. This protocol was repeated at each VP for each of the four stages of the field deployment. Additional sweeps were occasionally acquired at selected vibration points for quality control.

Out of the 216 VPs initially planned for each acquisition stage, three points were determined to be in areas too soft for the vibe truck and were removed from the list. An additional 17 VPs were removed due to tight time constraints. Acquisition downtime resulting from mechanical and other operational issues further reduced the total number of source points to a maximum of 190 VPs per stage. Overall, we recorded 6633 sweeps of 7668 planned, i.e. 86% (Figure 4.16).

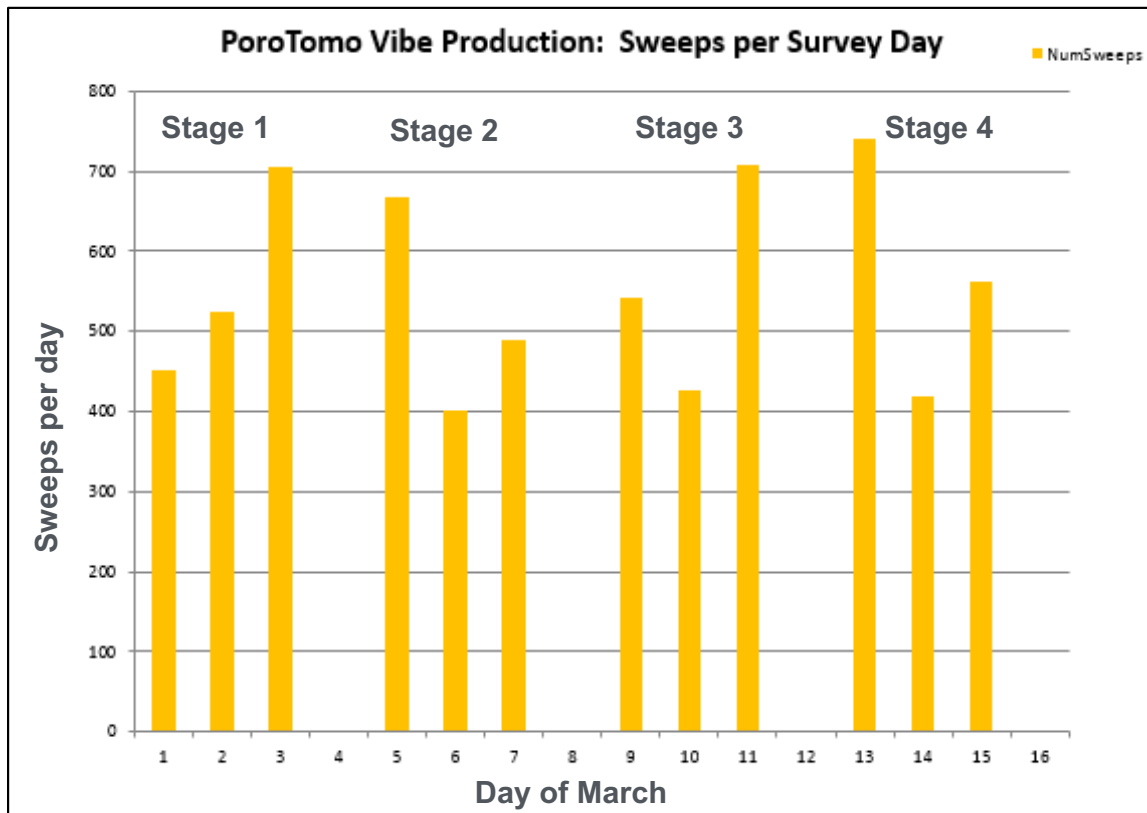


Figure 4.16. Bar graph showing number of sweeps per survey day.

Using associated coder/decoder telemetry units, the source operated in synchronization with the DAS array and the conventional seismometers. Time synchronization of the T-Rex electronics, the source encoder electronics, the DAS recorders and surface geophone recorders was set with a Time Zero box at the start of the survey and source-receiver timing was verified to better than half of a millisecond delay between the T-Rex and DAS recorder systems.

GPS-timed accelerometer data from the T-Rex baseplate and the actuator mass were recorded separately on a digital acquisition (DAQ) system in the T-Rex cab. A second DAQ independently recorded the zero-time generated by the source encoder for each sweep.

A spotter walking on foot visually verified the position and orientation of the T-Rex baseplate on the ground at each VP. The T-Rex baseplate makes a unique mark; ground conditions at the site allowed for easy re-occupation with good confidence of position. The orientation of the nose of the vibe at each VP was initially set by compass during Stage 1 to be either parallel or orthogonal to the long axis of the study area. The orientations were repeated for each phase. As shown in Figure 4.15, two GPS recorders were mounted on the T-Rex truck, one over the baseplate and one at the back of the vehicle, to verify its position and orientation for

each sweep at each vibration point. In addition to the GPS antennas mounted over the cab for timing and approximate position, the post-processed data from the Madison GPS antennas provide positioning for each P- and S-sweep without the need for resurveying the baseplate marks on the ground.

Hydrology

We installed pressure sensors capable of performing monitoring with one sample per minute in three observation wells reaching the “shallow aquifer” (**Figure 4.7**). At two sites (wells SP-2 and 81B-1), the pressure monitoring system consists of a pressure recorder on the surface, a 1/8” diameter stainless steel tube from surface to below the water level filled with nitrogen, and a 1-1/2” diameter by 10-foot chamber to maintain constant water level below the nitrogen. The pressure monitoring system deployed at the third site (well 56A-1) is a down-hole tool. Additional hydraulic data, including flow rates in production and injection wells, have been recorded by Ormat personnel. Reservoir pressure was monitored for the duration of the deployment in a total of eight wells distributed throughout the Brady wellfield.

Working with the operational staff in Ormat’s control rooms, we downloaded recordings of flow rate (in gallons per minute) and downhole pressure (in pounds per square inch) for the primary production and injection wells at Brady. The sampling rate is once per minute. These records span all four stages of the field deployment, from March 11 through March 26. These data were submitted to the GDR in raw (submission 844) and cleaned (submission 917) forms.

Geodesy

To gather geodetic information, we planned to acquire 12 scenes from 3 TerraSAR-X (TSX) tracks (T53, T91, T167). As shown in **Figure 4.17**, two of those scenes were cancelled leaving 10 scenes during the deployment in March 2016. To help supplement and provide quality control for the InSAR data, we collected GPS data for regional stations BRAD and BRDY. We also installed a GPS station named BRD1 on the wellhead of Well 18-1 on March 10, 2016.

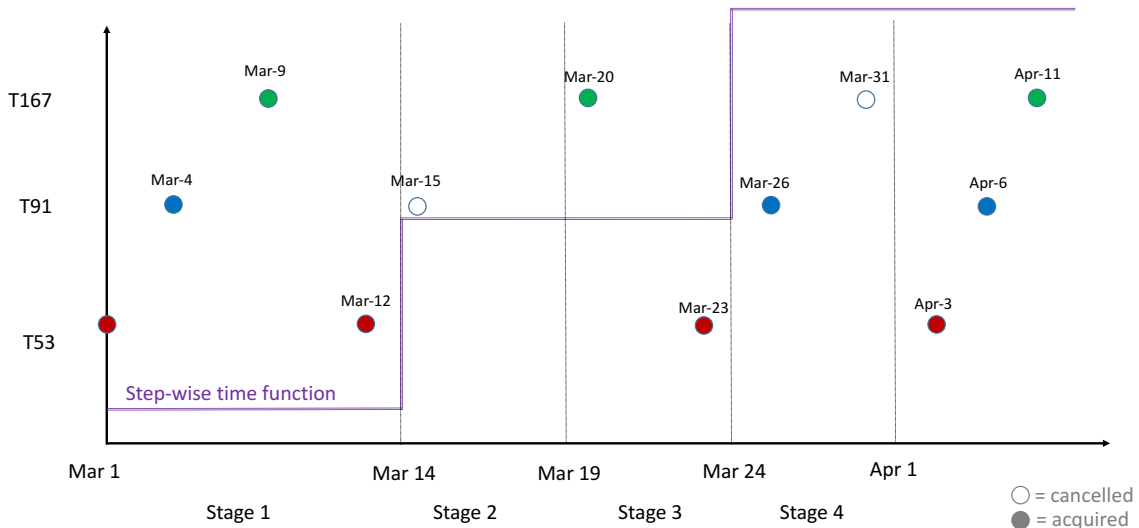


Figure 4.17. Schematic of the InSAR coverage over the deployment interval, showing dates in 2016.

Demobilization

Following deployment, the horizontal fiber optic cables were left in place with a junction box (**Figure 4.18**). The photographs in . The vertical fiber optic cable was left in place with a junction box near Brady Well 56-1, as shown in the following photographs (**Figure 4.21**).

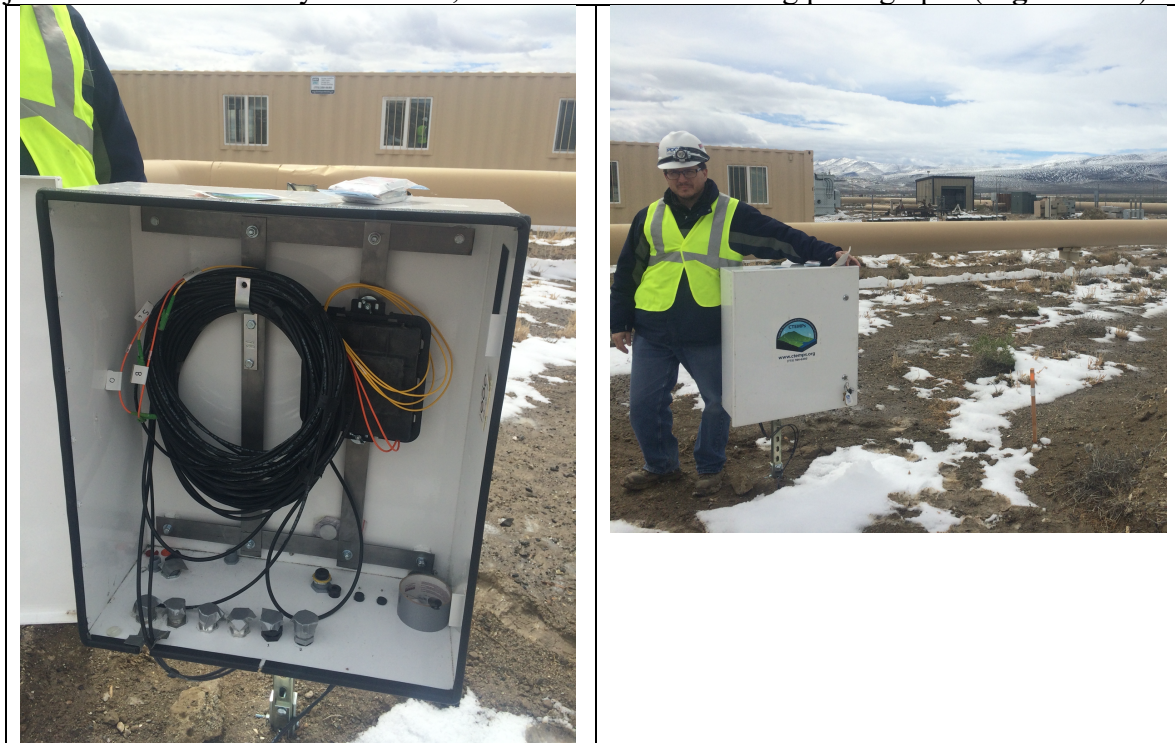


Figure 4.18. Post-deployment state of the horizontal fiber-optic cable junction box. Photos taken March, 2016. The temporary container building with windows has since been removed.

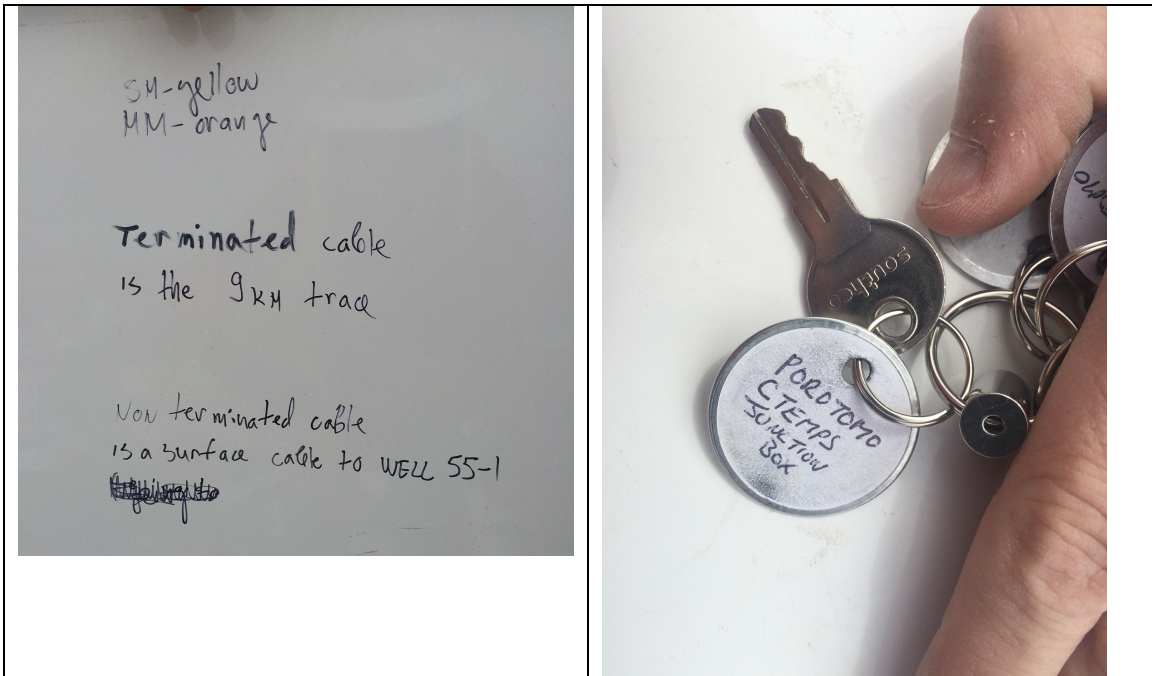


Figure 4.19. (Left) Field notes for the routing of the horizontal fiber-optic cable at Brady. (Right) Key for the junction box.



Figure 4.20. Post-deployment state of the junction box for the vertical fiber-optic cable. Photos taken March, 2016.

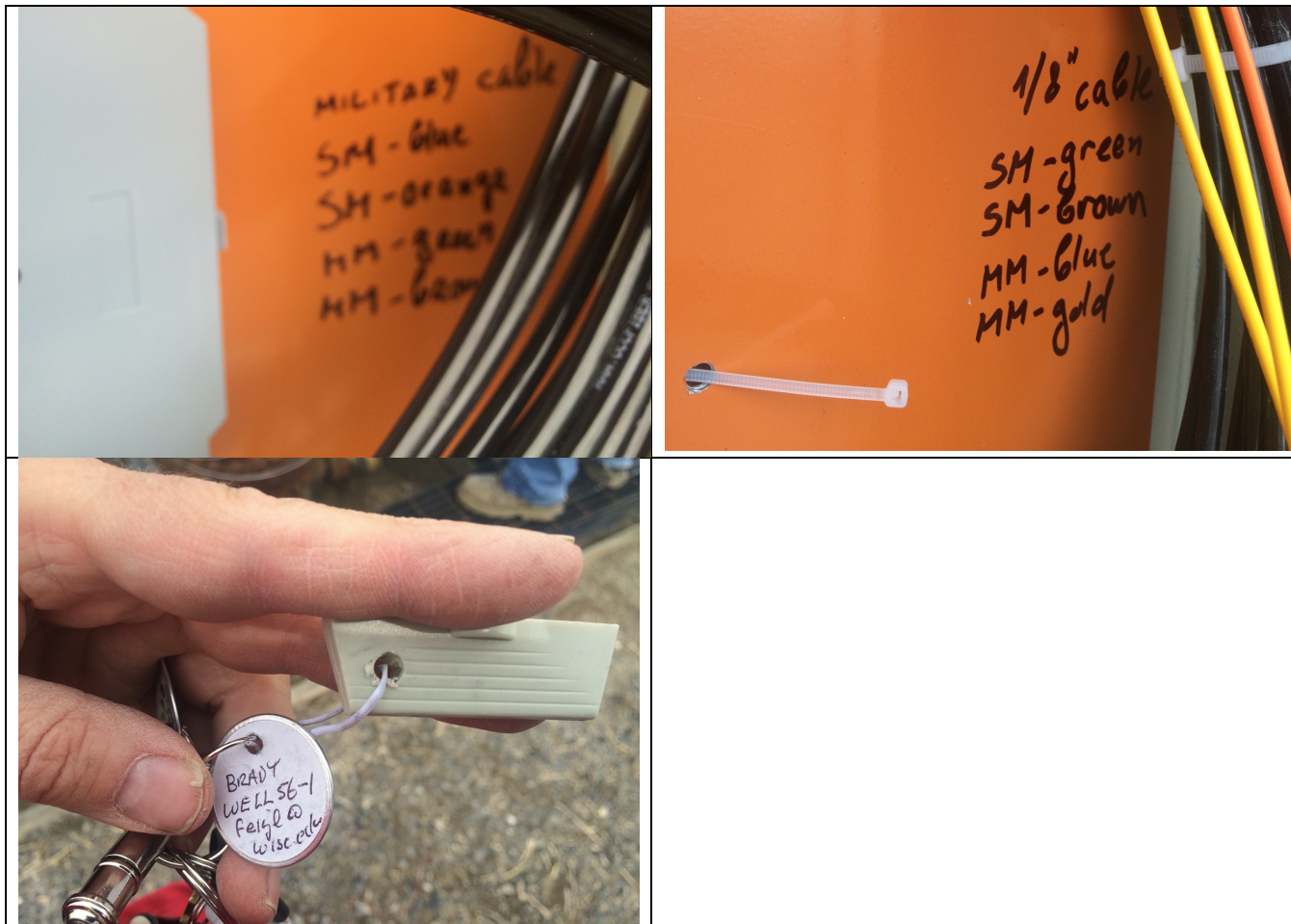


Figure 4.21. (Top) Routing notes for the vertical fiber optic cable. (Bottom) Key for the junction box near Brady Well 56-1.

B. Discussion

The greatest success of this project was the strength of the collaboration and cooperation between all of the various team members and organizations. By having a large multidisciplinary team, we were able to collect data efficiently. The differences in expertise resulted in fewer blind spots. In particular, this project could not have succeeded without the invaluable cooperation of ORMAT. They not only allowed us access to their site, but readily coordinated their efforts with us including by adjusting their operating procedure to augment our experiment.

However, sometimes the breadth of collaboration proved challenging. Traveling to and from the field area was accomplished predominately by rental vehicles. This necessitated careful coordination of personnel as most of the team members were from organizations that placed limitations on who could drive those vehicles.

The greatest challenge we faced during the deployment was when we attempted to install a fiber optic cable vertically in the borehole in Brady Well 55-1. The well was cooled using water and a stainless steel fiber optic cable installed. The target installation depth was 400 m; however, the cable could only be installed to 370 m due to a blockage ("bridge") in the well. The plan was to improve the mechanical and acoustic coupling between the cable and the borehole by filling it

with sand. However, pouring sand into the well increased the stress on the bridge, causing it to collapse. The friction between the sand and the cable dragged the cable downward and broke the cable at the lip of the well. Fortunately, no one was hurt. Most of the original cable was lost.

We considered several alternative plans to procure a new cable and deploy it in a different borehole: Brady Well 56-1. The new cable was purchased and delivered to the site. Prior to installation, a blockage (“bridge”) was discovered at about 370 m. We decided that filling the well with sand would risk repeating the events of 55-1. On Thursday March 17, 2016, we installed the cable into the borehole to a depth of approximately 370 meters, where it touched the bridge at the (false) bottom of the well. We left approximately 2 m of slack in the cable in Well 56-1, such that the cable forms a slight helix. No sand was added to the borehole. Presumably, the cable touches the wall of the borehole in several locations. The cable is coupled to the formation by the water in the well below a depth of approximately 80 m. Above that depth, the cable is surrounded by air where it is not touching the wall of the borehole.

Some changes to the deployment plans that happened during the planning stage proved to be auspicious. Installing the GPS station on an abandoned wellhead rather than on a deep-drilled braced monument saved time, money, and simplified permitting. The Zland nodal geophones that we used proved to be more advantageous than the IRIS PASSCAL instruments (either Texan or standard Reftek instruments) in the original plan proposed in the Technical Volume submitted in 2014. The Zland units were simpler and faster to install and were able to operate independently for the duration of the deployment with no need for changing batteries or downloading data.

One challenge with the DAS interrogators was that they are very sensitive to vibrations. If the interrogator units experienced vibration, it would create noise in the data across the entire DAS array. We housed the interrogators in a portable building and had to take precautionary measures to disturb them as little as possible. This included purchasing carpeting for the floor to minimize noise from people walking and chairs dragging. We also implemented protocols for gently closing the door on the portable building and created an alternate location for lunch and break time activities so that fewer people needed to access the building with the instruments.

On three occasions, the electrical power supplied by Ormat was shut off. On two of these occasions, we were able to use a gasoline generator. In total, less than three hours of data were lost during the power outages. The third occasion corresponded with a fire alarm and, as a result, the wells stopped operating for a couple hours. Since we were able to continue recording data during this time, we can observe the resulting pressure change in the observation wells.

One unexpected challenge we encountered was when we discovered part way through the experiment that the Nevada Department of Transportation (NDOT) had road work scheduled for the frontage road that ran through our target area. We were able to negotiate with the construction workers so that they started working on the part of the road farthest from our study area and so delayed working near the study area for as long as possible. If we had contacted NDOT ahead of time, the situation might have been avoided. As it was, the roadwork didn’t noticeably interfere with our deployment of the vibroseis source.

Communication on site was complicated by limited service for cellular telephones. We utilized handheld communication devices (walkie-talkies) but found that their range was also limited by topographic relief, even within our relatively small field area. Even with what we were expecting to be redundant forms of communication, we still ended up having no way of

notifying some team members of the fire alarm and that we had been instructed to relocate to the emergency meeting point. An airhorn might have been useful in that situation.

C. Recommendations

The most important recommendation we can make to future projects is to start the permitting process as early as possible. Even with an extra six months head start compared to the recommended lead-time, we still only got permits approved just in time. The extensive experience of Mark Hanneman at Ormat's Land Office was essential in the regard. To ease the permitting requirements, we advise avoiding locations with heritage sites.

It is also important to have as many means of communication as possible in the field. Having multiple backup systems of communication means that there is a better chance that at least one of them will work during an emergency situation. Being safety conscious also helps personnel act with confidence during emergencies and help prevent them.

Section 5. Seismology

A. Results

Data Collection

As described in Section 2, seismic data were collected in March 2016 on two main systems, a set of 240 5-Hz, 3-component nodal geophones and about 9 km of fiber-optic cable for a distributed acoustic sensing (DAS) system, including both surface-trenched and down-hole sections of cable. In addition, 6 RefTek dataloggers with 4.5 Hz 3-component geophones were deployed, co-sited with 6 nodal instruments, to provide a quick ability to check the quality of waveform data. Only two of the Fairfield Nodal geophones failed to record data. Difficulties with the initial attempt to install DAS cable in a borehole resulted in down-hole recording for only the second half of the planned recording interval, with non-ideal coupling of the cable. The geophone array had about 60-m instrument spacing in the target zone, whereas DAS channel separations were about 1 m with an averaging (gauge) length of 10 m. The acquisition systems provided 15 days of continuous records.

The recorded data can be divided into three main categories in terms of usage: vibroseis time segments, continuous data, and earthquake time segments. The University of Texas at Austin vibroseis truck, T-Rex, was utilized to generate repeatable swept-frequency signals, from 5 to 80 Hz, in three modes of vibration at nearly 200 source points in each of the four stages of power plant operation during the field experiment (normal pumping operations, plant shut-down, accelerated pumping operations, return to normal pumping operations). T-Rex was chosen for generating controlled-source data due to its triaxial capability - it can rapidly shift from vertical vibration to horizontal-longitudinal vibration to horizontal-transverse vibration. The hope was that the horizontal shaking would yield clearer S-wave arrivals, but that proved not to be the case. Continuous data were used for ambient noise analyses, and exploratory analyses were done with data from earthquakes recorded during the deployment period.

Data Analysis - Vibroseis Time Segments

Our work on this task concentrated on extracting first P- and S-wave arrival times corresponding to the surface-to-surface direct wave propagation from the vibroseis source to the geophone and DAS instrumentation. Because the vibroseis is a swept-frequency source and not an impulsive source, data processing is required to extract waveforms that are approximately equivalent to what would have been observed from an impulsive source (in effect, an estimate of the Green's function between source and receiver). We found that cross-correlating the source signal recorded on the vibroseis with the observed signals produced adequate results for picking first-P arrivals typically to a distance of 1,000 m. **Figure 5.1** shows an example.

The next step was picking the P-wave arrival times using automated methods. Automated methods were essential due to the vast amount of data to be picked, over 2.5 million traces just of vertical mode vibroseis data. Two methods were used, both from the paper by Akram and Eaton (2016): an Akaike Information Criteria (AIC) algorithm and a standard Short-Term-Average to Long-Term-Average ratio (STA/LTA). The STA/LTA picks were used for distances up to 150 m where the AIC picker performed poorly, and the AIC picks were used at greater distances.

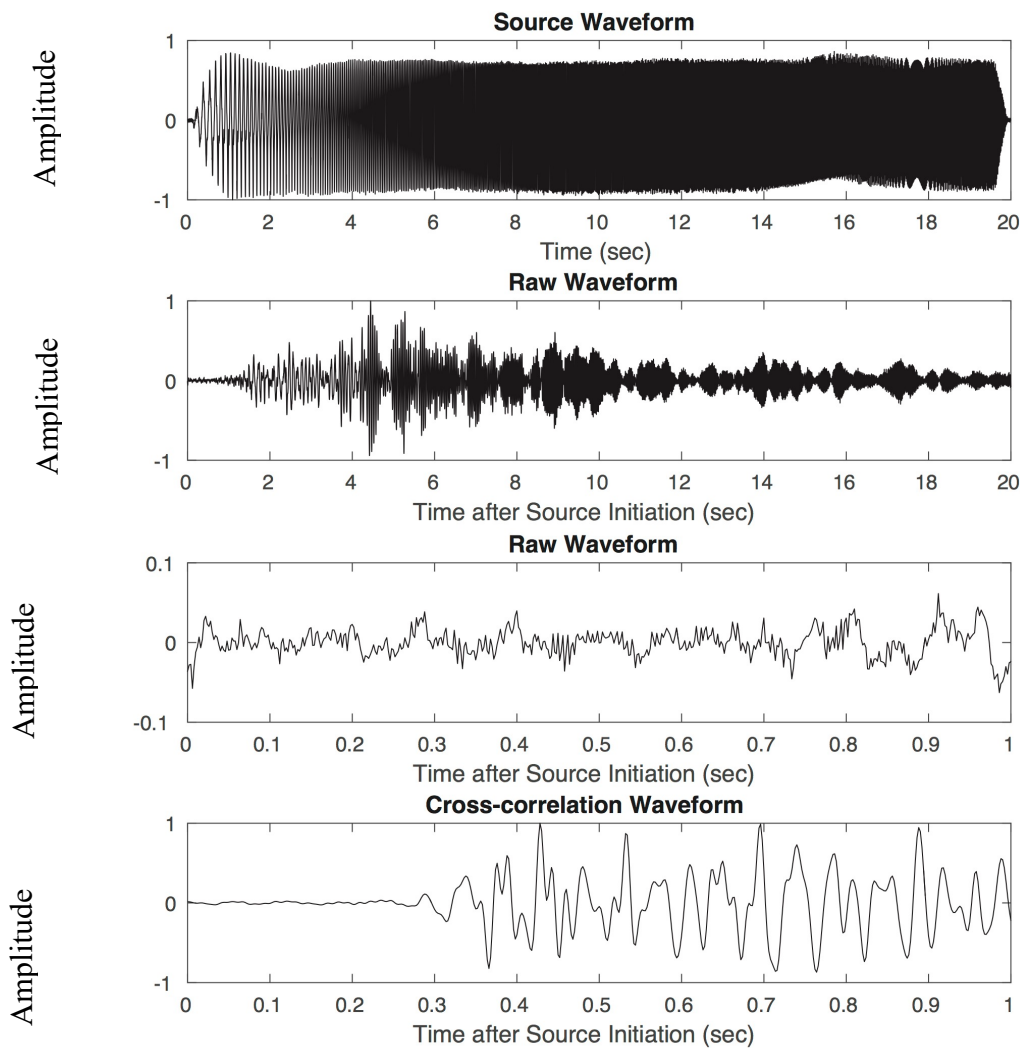


Figure 5.1. An example of the cross-correlation procedure for (top panel) the vibroseis sweep signal with (second panel) an observed seismogram (raw waveform), then (third panel) zooming in on the first second of the raw waveform, and (bottom panel) the result of the cross-correlation showing the P-wave arrival at around 0.28 seconds. From Parker et al. (2018).

We also determined a revised set of P-wave picks for the vertical-mode vibroseis records on all sensors (geophone, horizontal DAS, vertical DAS) in order to attempt further improvement of the velocity model obtained through tomography. Green's functions were obtained from sweep records in raw data using band-limited (5-75 Hz) frequency-domain deconvolution of the sweep source signal. For each vibe point and each sensor, we stacked data of all available vertical mode sweeps of all 4 stages using phase-weighted stacking, based on the phase coherence in the time-frequency domain, calculated using S-Transform (Schimmel and Gallart, 2007). This substantially improved the signal-to-noise ratio (SNR) of many records. We also revised our automatic picking procedure. Using the first version of the velocity model, we chose time windows of -0.1 to 0.1 s centered on predicted picks. The characteristic functions were AIC (Maeda, 1985) and its time-derivative. In the absence of a clear and strong global minimum on

the AIC curve, a weighted average of times corresponding to the minima of the AIC curve and the maxima of its time-derivative was chosen as the pick. The waveforms used in decreasing order of preference are: the raw phase-weighted stack (PWS), PWS filtered in a ~2.3-octave-wide passband in the range ~15-75 Hz and a weighted average of picks on the PWS filtered in multiple narrow (1-octave wide) passbands between ~15 and 75 Hz. All candidate picks were required to have SNR > 3.7 measured for a 0.08-s-wide time window following the pick and good phase coherence (>0.6) for at least 7% of the frequency range and 0.04 s in time within ± 0.1 s around the pick. The phase-weighted stacking, the revised picking procedure and the revised quality-control criteria helped in getting more P-wave picks for some candidate vibe points that had returned poor number of picks previously.

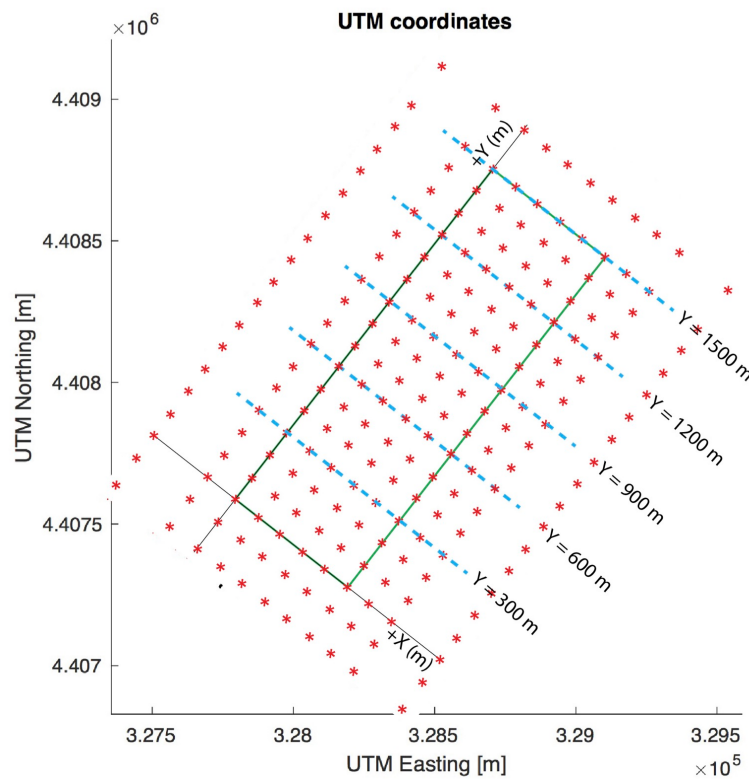


Figure 5.2. Map view of the nodes of the Cartesian grid for the preferred tomographic inversion.

A substantial effort was also made to pick S-wave arrivals. Most of the work focused on polarization analysis, taking advantage of the difference in particle motion for the P wave (longitudinal, that is, polarized in the direction of wave propagation) compared to the S wave (transverse, that is, polarized perpendicular to the direction of wave propagation). S waves could be tentatively identified in a small fraction of the analyzed waveforms.

Travel-Time Tomography

To obtain a 3D Vp model, we used the simul2000 tomography code (Thurber and Eberhart-Phillips, 1999). Source and receiver locations were transformed into a Cartesian coordinate system centered on the southwest corner of the inner portion of the nodal geophone array at

39.8010°N and 119.0108°W, with the Y axis oriented at about 36° azimuth to be parallel to the average north-northeast strike of the normal faults and the long axis of the study area (Figure 5.2). Sources and receivers were modeled at their true elevations above the WGS84 ellipsoid. The inversion grid for the final model is 2,000 m long in the X direction and 1,300 m wide in the Y direction, with horizontal spacing of the grid nodes of 100 m except for the outside edges where the spacing is 200 m. Grid nodes in the Z direction were positioned at 1,250 m (close to the surface), 1,230 m, 1,210 m, 1,190 m, 1,150 m, 1,100 m, 1,050 m, 1,000 m, 900 m, 800 m, and 600 m, with 0 m elevation corresponding to the WGS84 ellipsoid.

The simul2000 code (Thurber and Eberhart-Phillips, 1999) uses the pseudo-bending method of Um and Thurber (1987) for ray tracing and employs a damped least-squares inversion. A damping parameter governs the trade-off between data misfit and model perturbations. The code also provides complete information on model resolution and uncertainty. We constructed a trade-off curve to compare the model results for final misfit versus total model perturbation (variance) for damping values of 0.02, 0.1, 0.5, 2, 8, and 40. The "knee" of the trade-off curve was found at a damping value of 2. Based on the diagonal elements of the model resolution matrix (Aster et al., 2012) that are computed by the simul2000 algorithm, we find that model resolution is reasonably good above ~1,000 m elevation (~250 m below surface) in the 1,500 m by 500 m target area. A checkerboard test with 100 m size anomalies supports this result (**Figure 5.3**). The velocity anomalies were recovered within 1% for nearly 70% of the grid. A checkerboard test with 50-m grid spacing in the target region performed less well, with velocity anomalies recovered within 1% for only about 35% of the grid. We note that tomographic inversions including the DAS data provided substantially improved model resolution compared to ones without the DAS data, although the resulting velocity model values themselves were not very different (typically within 1-2%).

Figure 5.4 shows horizontal slices and **Figure 5.5** shows northwest-to-southeast oriented cross-sections of the V_p model for the tomographic inversion using the initial set of P-wave picks from the nodal geophones, DASH, and DASV (Parker et al., 2018). In the near-surface slices, low-velocity zones dominate the model. These velocities are consistent with the expected values of the alluvial deposits found near the surface. Based on well-log lithologies (**Figure 5.6**), the alluvial deposits extend to greater depths in the northern part of the study area compared to the southern part. In the southern well (**Figure 5.6f**), an alluvium thickness of ~50 m (Z ~ 1200 m) is consistent in depth with a transition from slower (< 1,500 m/s) to faster (> 2,000 m/s) velocities, a transition that is present in much of the southern part of the model (**Figure 5.4** and **Figure 5.5**). In the northern well logs, the Quaternary alluvial deposits extend to greater depths, and the depth of this velocity transition zone is fairly uniform, but transition depth in the velocity model does not occur at the same depth as boundaries in the logs **Figure 5.6**. This may be due to the presence of the water table perched just above the Tertiary deposits, which would place the water table at a shallower depth than the reported value of approximately 100 m found in pressure surveys of wells(Patterson et al., 2018).

In the rest of the study area, the faster velocities at greater depths fall within the reported seismic velocities for tuff (Wohletz and Heiken, 1992) and sedimentary deposits (Bourbié and Coussy, 1987). We interpret the abrupt lateral changes in velocity visible in the cross-sections (**Figure 5.5**) as faults juxtaposing rocks with different seismic velocities. In particular, the high-V_p at depth in the Y = 300 m cross-section in the central part of the model (**Figure 5.5e**) is approximately bounded by faults with much lower velocities on either side. This structure is

consistent with the sense of motion for normal faults. Similar structures can also be seen in the $Y = 1200$ m and 1500 m cross-sections at depth on the SE side of the model (**Figure 5.5 a and b**).

The other main feature that is apparent at shallow depths, particularly in the $Z = 1,200$ m slice (**Figure 5.4a**, ~50 m below the surface) is the zone of low velocities that strikes northeast, roughly parallel to and along the northwest edge of the long (Y) axis of the study area. The low velocities extend to greater depth (**Figure 5.4b**), and are closely aligned with the trend of the major faults and the trend of fumaroles and mudpots (**Figure 5.4b**, **Figure 5.5e**).

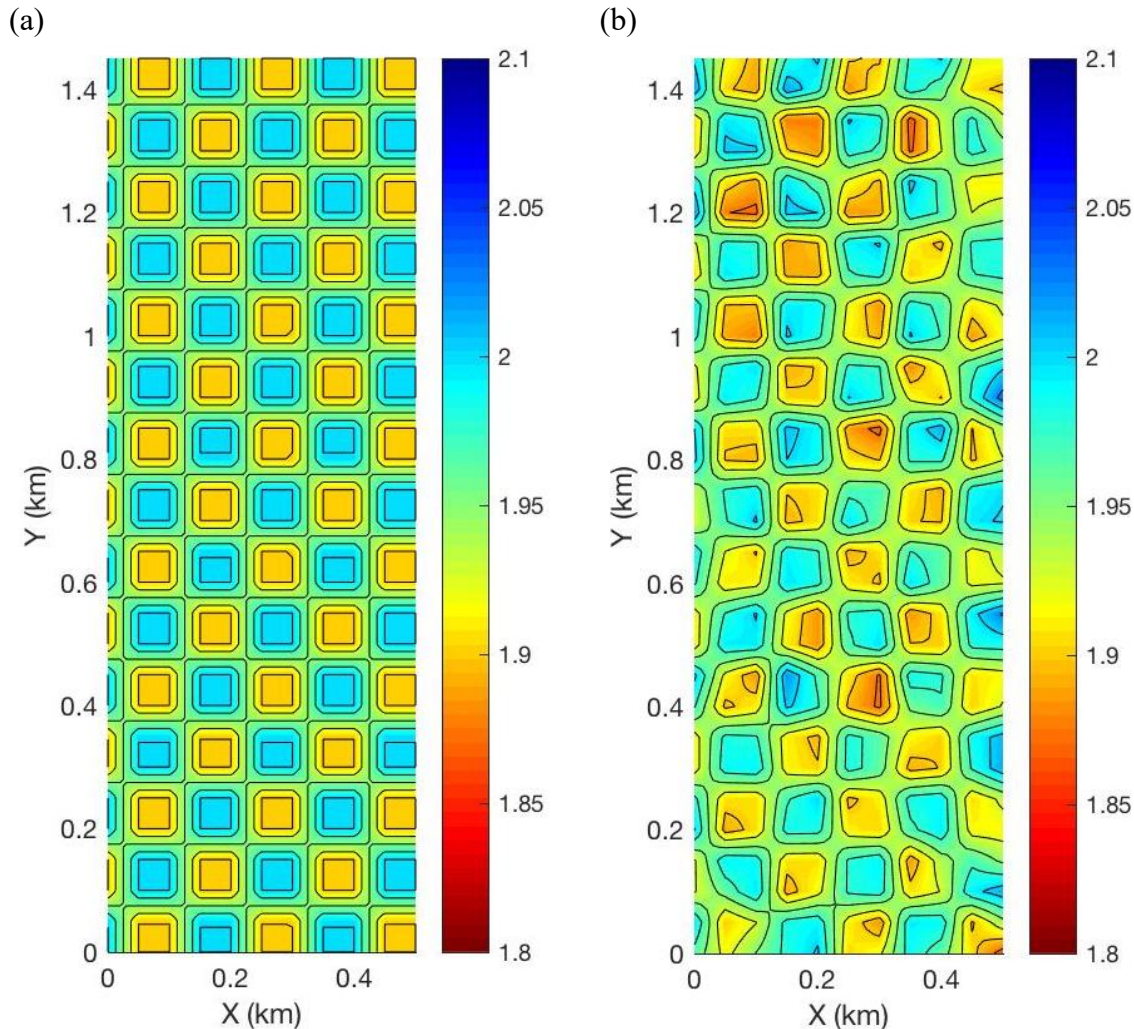


Figure 5.3. Checkerboard test results for 100 m grid spacing. (a) True model. (b) Recovered model. From Parker et al. (2018).

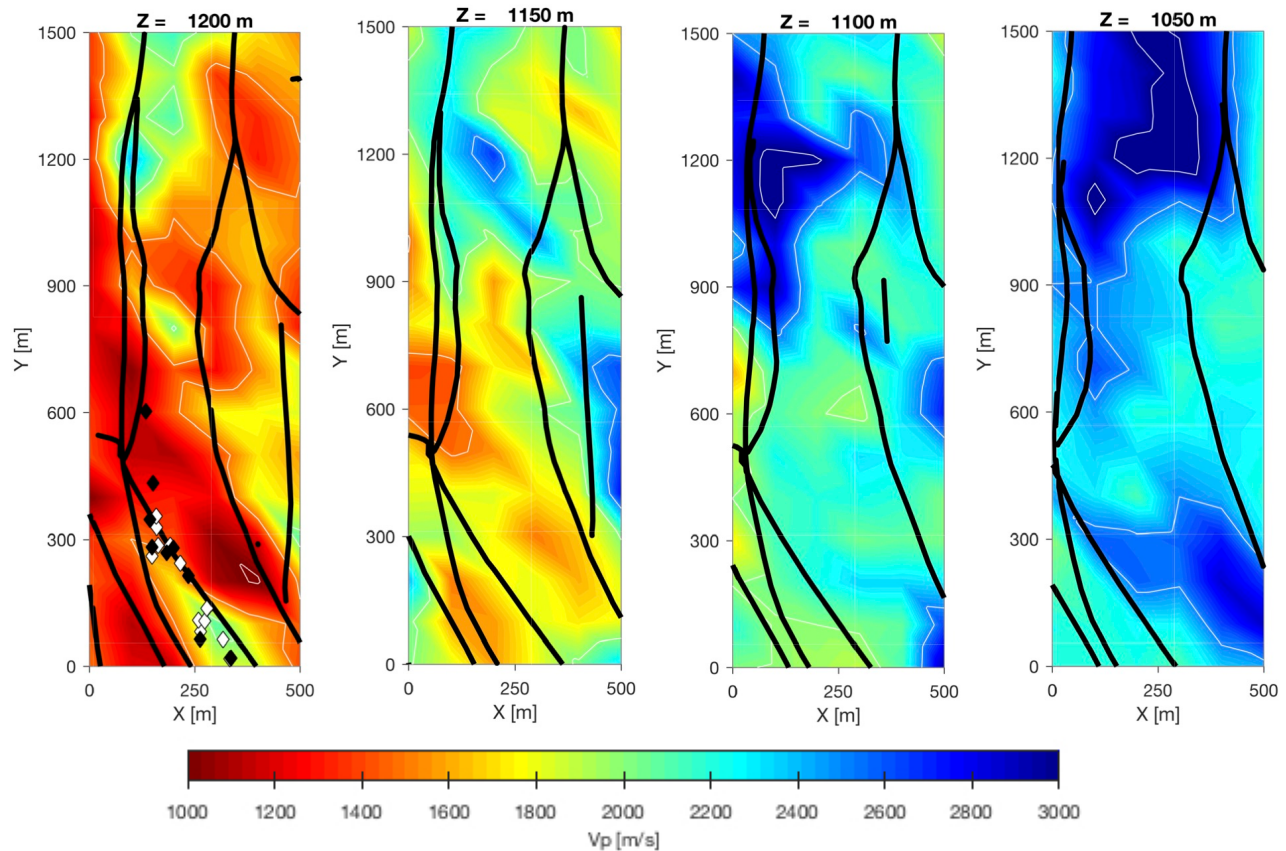


Figure 5.4. Representative depth slices through the 3D V_p model for the target region, at elevations Z with respect to the WGS84 ellipsoid of 1,200 m, 1,150 m, 1,100 m, and 1,050 m, respectively from left to right. Contours are at 1,000 m/s intervals. Thick lines are intersections of faults (from Siler et al. (2016)) with each depth slice. From Parker et al. (2018).

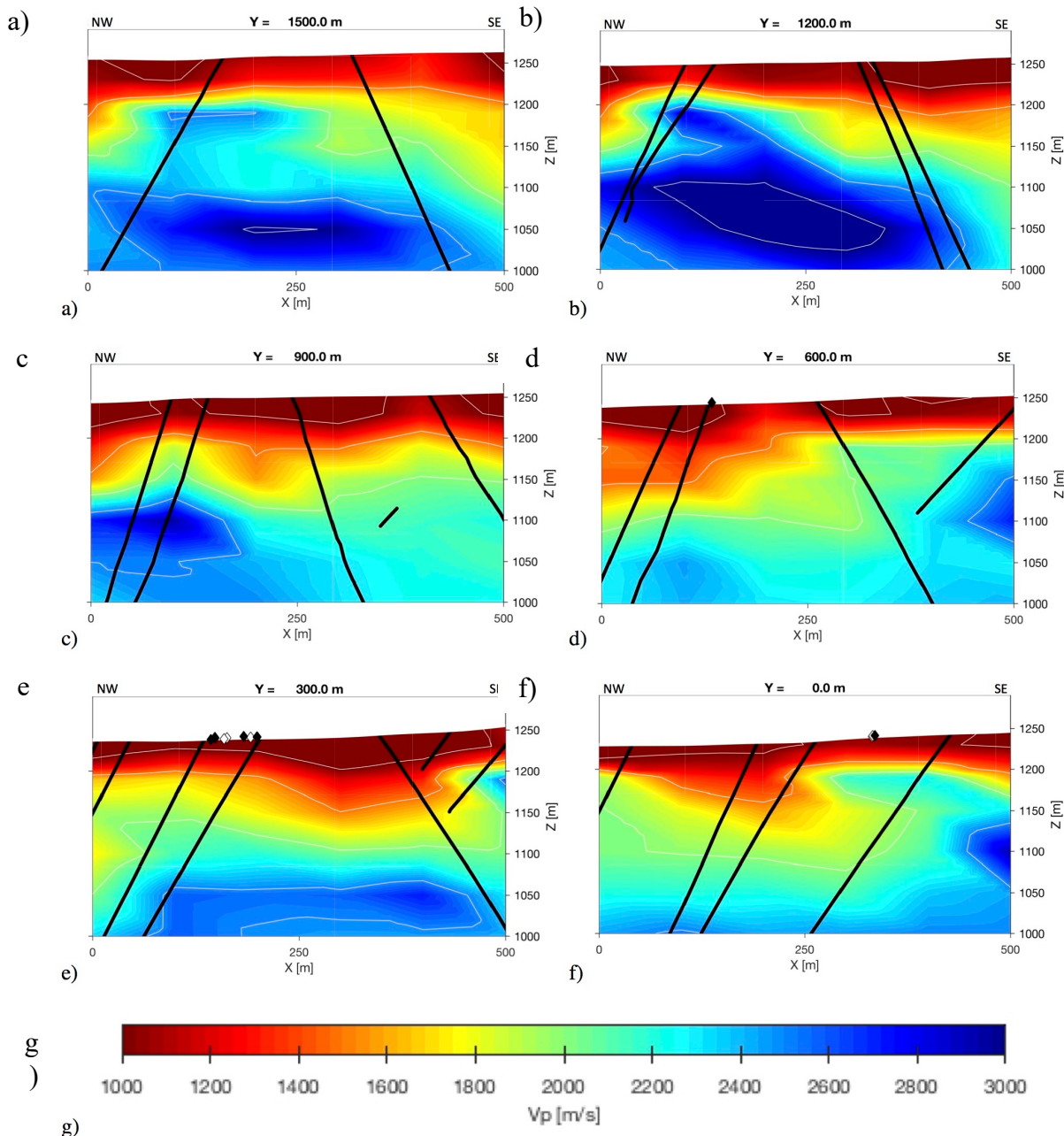


Figure 5.5. Representative northwest to southeast cross-sections through the 3D V_p model, at Y coordinates of (a) 1,500 m (northeast edge of the target region), (b) 1,200 m, (c) 900 m, (d) 600 m, (e) 300 m, and (f) 0 m (southwest edge of the target region). Contours are at 1,000 m/s intervals. Elevations, Z , are with respect to the WGS84 ellipsoid. Thick lines are intersections of faults (from Siler et al. (2016)) with each cross-section. Fault dips are generally $\sim 50\text{--}60^\circ$. (g) V_p legend. From Parker et al. (2018).

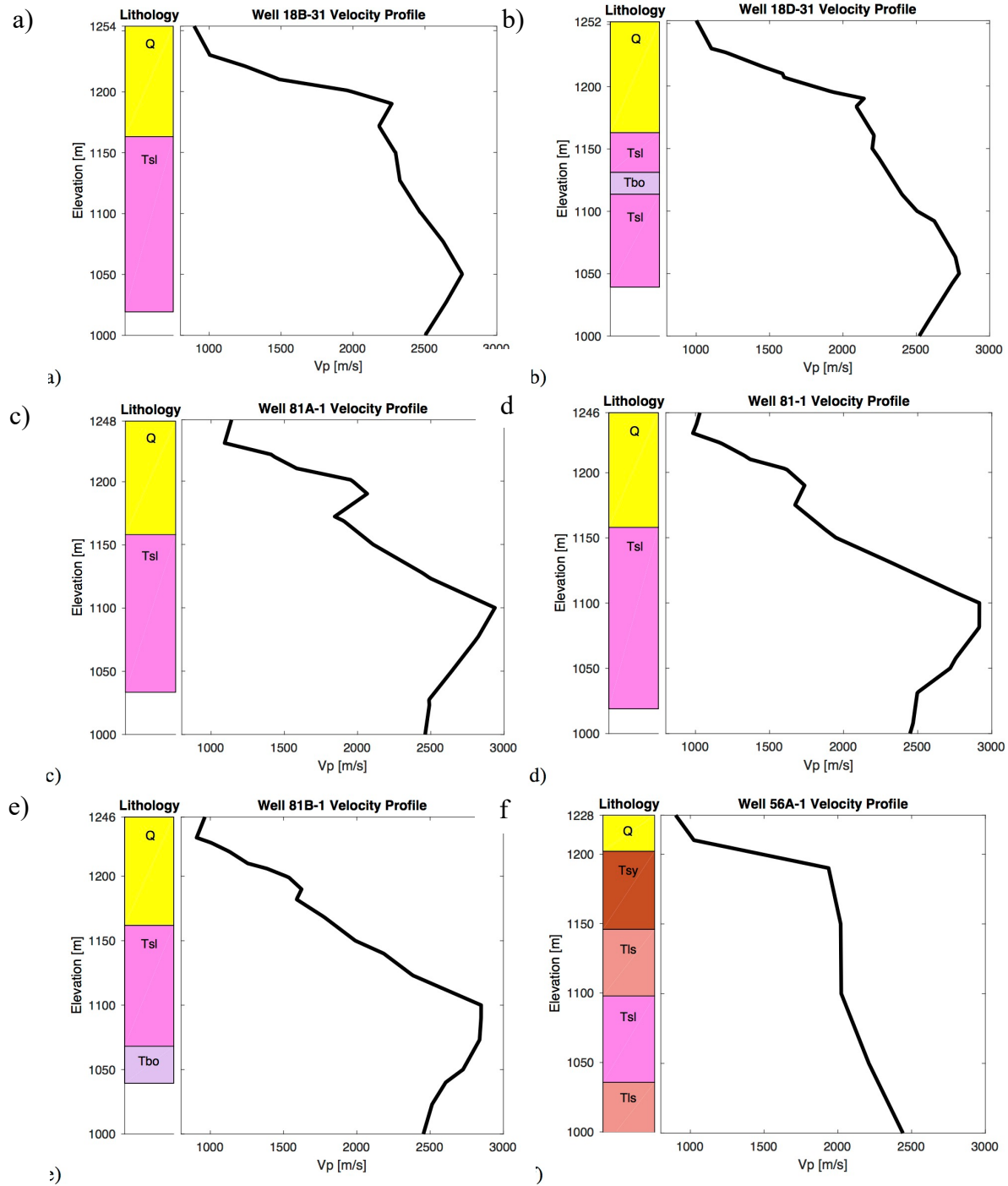


Figure 5.6. Comparisons of lithology from well logs (Siler et al., 2016) and V_p from each well's location in the 3D V_p model. See Figure 2.1 for location of the wells. Q is Quaternary sediments, Tsl is lacustrine sediments, Tbo is Tertiary basalts, Tls is limestone, and Tsy is sandstone and conglomerate. From Parker et al. (2018).

We also show representative cross-sections through the 3D V_p model derived from the revised set of picks in **Figure 5.7**. The main features are similar, but the model is slightly faster

overall, the sharp vertical gradients are generally closer to the surface, and sharp horizontal gradients are more closely aligned with the faults.

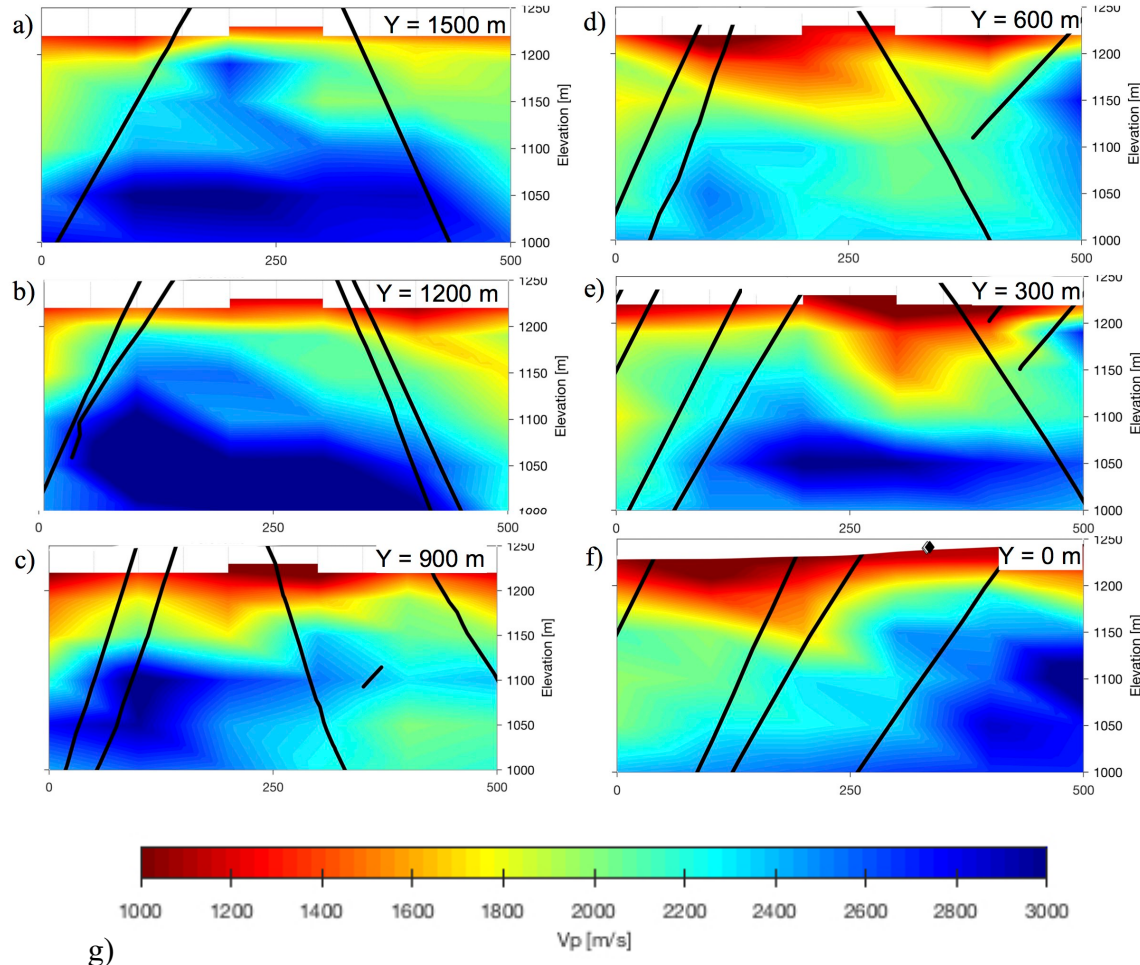


Figure 5.7. Representative northwest to southeast cross-sections through the 3D V_p model derived from the new set of picks, at Y coordinates of (a) 1,500 m (northeast edge of the target region), (b) 1,200 m, (c) 900 m, (d) 600 m, (e) 300 m, and (f) 0 m (southwest edge of the target region). Contours are at 1,000 m/s intervals. Elevations, Z , are with respect to the WGS84 ellipsoid. Thick lines are intersections of faults (from Siler et al. (2016)) with each cross-section. Fault dips are generally $\sim 50\text{--}60^\circ$. (g) V_p legend.

Data Analysis - Continuous Data

We used continuous records from the horizontal DAS array at the surface to compute high-quality noise cross-correlation functions of channel-pairs on the same linear segment and on two in-line linear segments. Several standard processing steps are applied to the raw data. The shaking of interrogator caused coherent noise signal across the whole array. Thus, the array mean and segment mean are subtracted at first. The strong transient signals (e.g. earthquake) are reduced with temporal and frequency domains normalization (Bensen et al., 2007). Then the processed waveforms from two receivers in a short time window (30 seconds) are used to compute individual noise cross-correlation functions (NCFs). The NCFs are stacked over 4 hour

periods to improve signal-to-noise ratio. The surface wave signal dominates the NCFs, and its dispersion curve can be used as observational data in our seismic imaging. The MASW method, based on slant stacks in frequency domain, is utilized to measure phase velocity between channels along

the same linear segment of fiber-optic cable. The group velocity is also measured, using the frequency time analysis (FTAN) method that has been widely used since the 1960s (Dziewonski et al., 1969). A series of narrow bandpass filters that are defined as Gaussian functions in the frequency domain are applied to the waveform and then the arrival times of maximum energy for each frequency are picked. The group velocity is the channel separation divided by the relative difference in respective travel times. The dispersion curves obtained from these steps are used to determine layered shear wave velocity structures beneath each segment using two linearized inversion method, and the final 3D model is interpolated from the multiple layered models.

The Rayleigh wave signal can be observed on both vertical-vertical and radial-radial component NCFs, where the radial direction is same as parallel to the linking two receivers. Since each DAS channel is equivalent to a horizontal single-component geophone, there are two possible channel-pairs that could be used: two channels on the same linear segment or channels on two in-line segments with cable orientations that are same as the path between the two channels. The first case includes 61 segments, whereas the second case includes 51 segments in total.

One example of channel-pairs on one linear segment is shown in **Figure 5.8**. The NCF shows strong asymmetry that reflects more energy coming from the highway (NW) side. The Rayleigh wave signal clearly emerges and the strongest energy propagates with a velocity of ~ 300 m/s. For the cross-segment channel-pairs, the greater offset makes it difficult to extract a clear signal. Therefore, the array interferometry technique, which has been successfully used to extract weak signals from NCFs (Lin et al., 2013; Nakata et al. 2015), is adopted to improve signal quality. This method requires computing NCFs of all possible receiver-pairs across arrays (segments in our case), and then stacking NCFs of receiver-pairs in particular distance bins. To reduce computational cost, only 10 percent of the channel-pairs between two inline segments are computed and the NCFs in 10 m distance bins are stacked. **Figure 5.9** shows NCFs of 13 channel-pairs with offsets ranging from 419.4 to 420.1 m, and the stacked traces. The Rayleigh wave signals on both negative and positive lags are enhanced while the random noise is significantly suppressed. Cross-segment NCFs in the southeast part of the study area are shown in **Figure 5.10**. The Rayleigh wave signal can be traced up to 600 m, making it possible to measure dispersion in a lower frequency band.

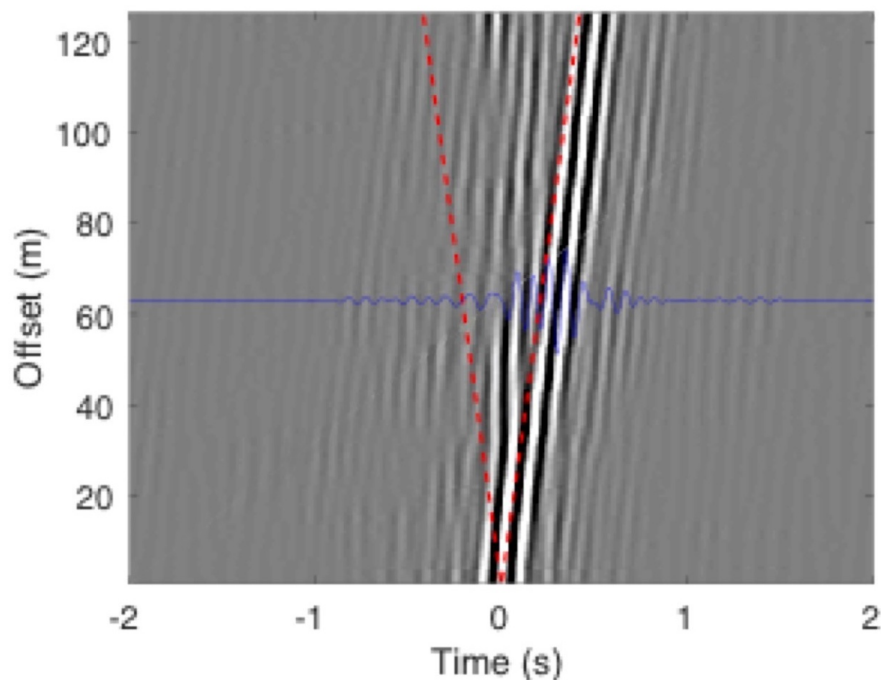


Figure 5.8. Record-section of NCFs between channel-pairs along one segment. The dashed red lines denote a velocity of 300 m/s and one example trace is shown in blue.

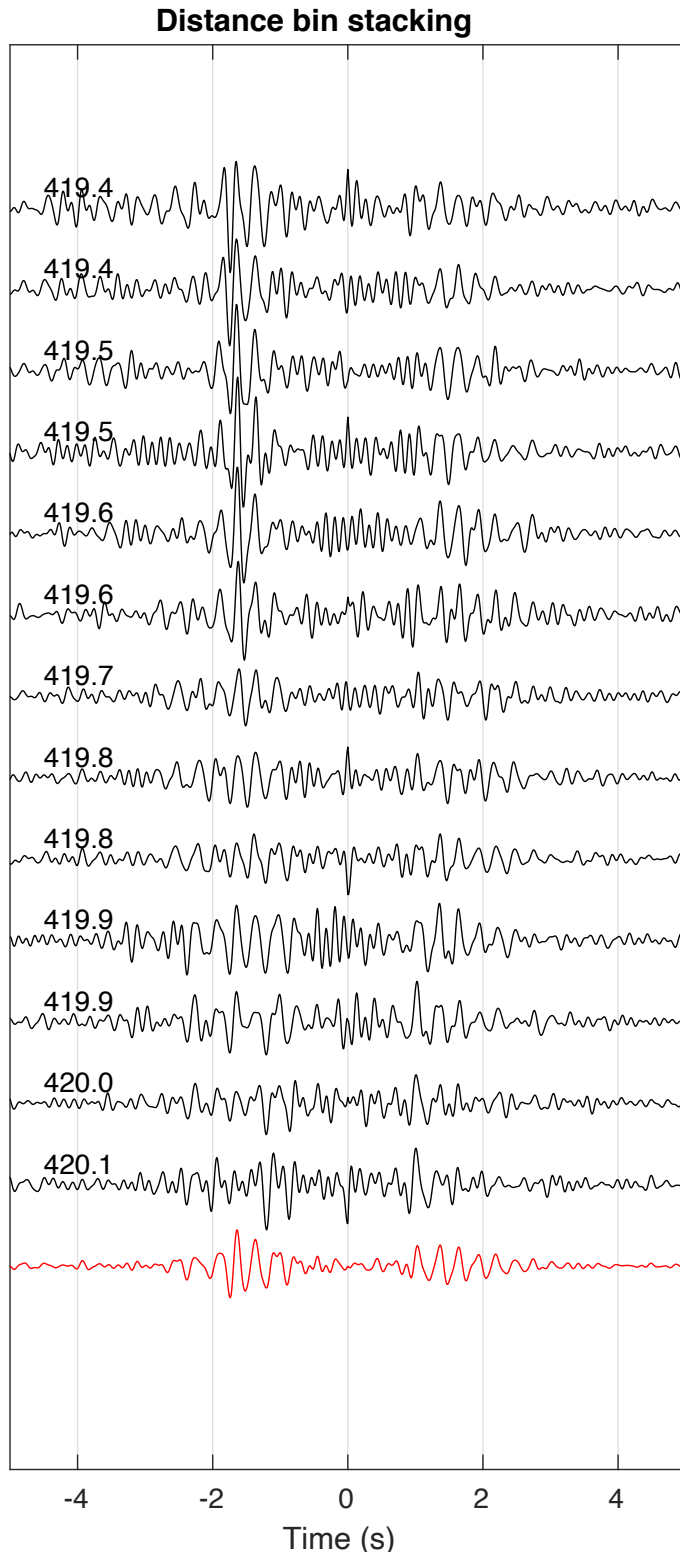


Figure 5.9. Individual NCFs (black) in a distance bin and the stacked trace (red). The number on each trace indicates offset in meters.

The MASW method is used to measure phase velocities of the Rayleigh wave for NCFs along one linear segment. Since the MASW method measures the phase difference between receivers, the phase velocity is mainly controlled by the seismic structure beneath the segment (array). The denser spacing theoretically reduces aliasing in the wavenumber domain, meaning it is possible to see relatively high-frequency components. On the other hand, the length of the segment also limits both the resolution in the wavenumber domain and the maximum wavelength that controls the maximum depth of investigation. An empirical criterion is that the maximum wavelength is approximately twice the segment length, whereas the maximum depth of investigation is very close to the segment length (Park and Carnevale, 2010). One MASW picking example is shown in **Figure 5.11**. The statistics show that the picking number reaches a peak around 10 Hz, corresponding to a wavelength of about 30 m.

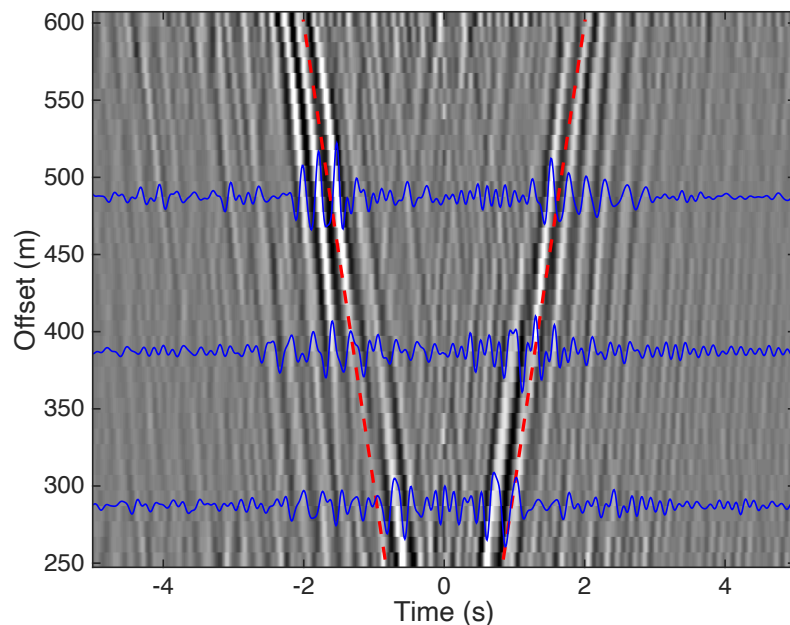


Figure 5.10. Record-section of NCFs between channel-pairs on two segments. The dashed red lines denote a velocity of 300 m/s and sample traces are shown in blue.

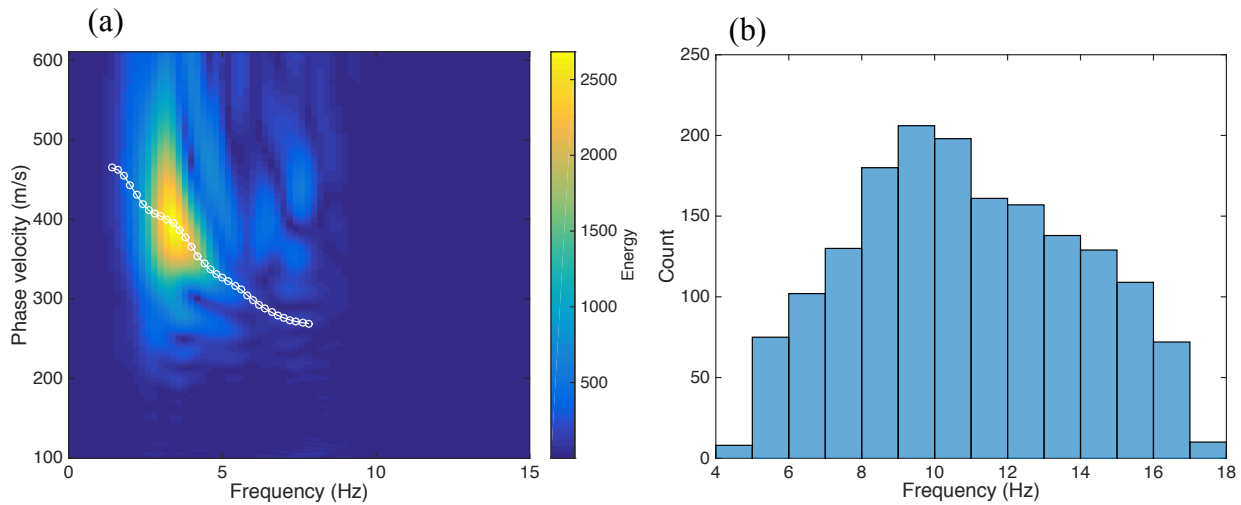


Figure 5.11. One MASW measurement example. The color represents stacking energy and the picked velocities are marked with white circles; (b) Histogram of MASW measurements.

The distance-bin-stacked NCFs mainly reflect average seismic structure of the whole path rather than the structure beneath a given segment, so the phase velocity measured with the MASW method might be affected by the structures beneath both segments. Therefore, the FTAN method is used to measure group velocities. Similar to the MASW method, the greater offset makes it possible to measure dispersion in a lower frequency band (Bensen et al., 2007). As **Figure 5.12** shows, the peak frequency of FTAN measurements is around 5 Hz, much lower than the peak frequency of MASW measurements. A total of 1,409 phase velocities and 768 group velocities are measured and used in the next inversion step. A typical layered Vs model is used to compute sensitivity kernels of our data set (**Figure 5.13**). The group velocity is more sensitive than phase velocity and the maximum depth of meaningful sensitivity is about 30-40 m in this model.

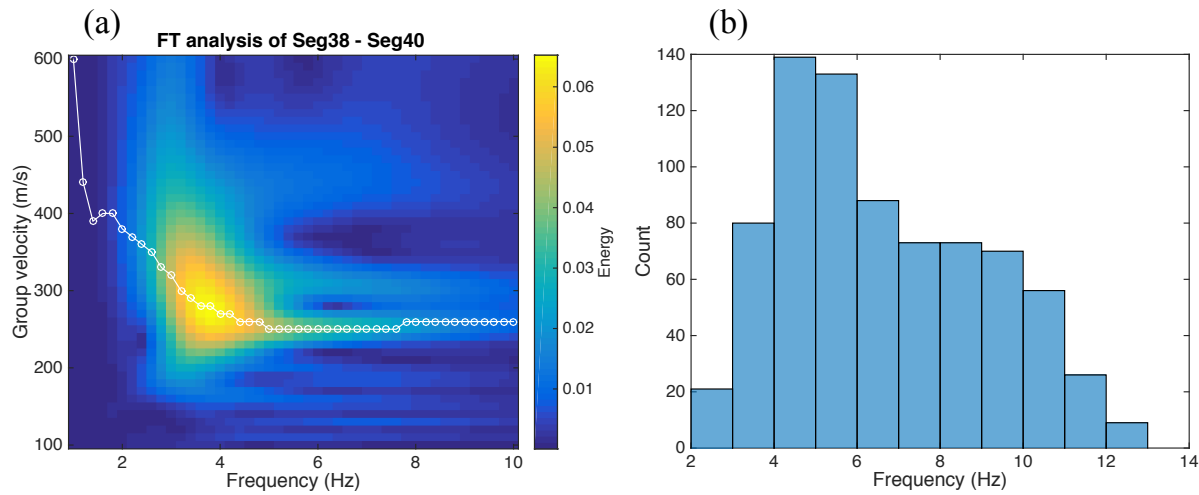


Figure 5.12. (a) One FTAN measurement example. The color represents stack energy and the picked velocities are marked with white circles. (b) Histogram of the number of FTAN measurements as a function of frequency.

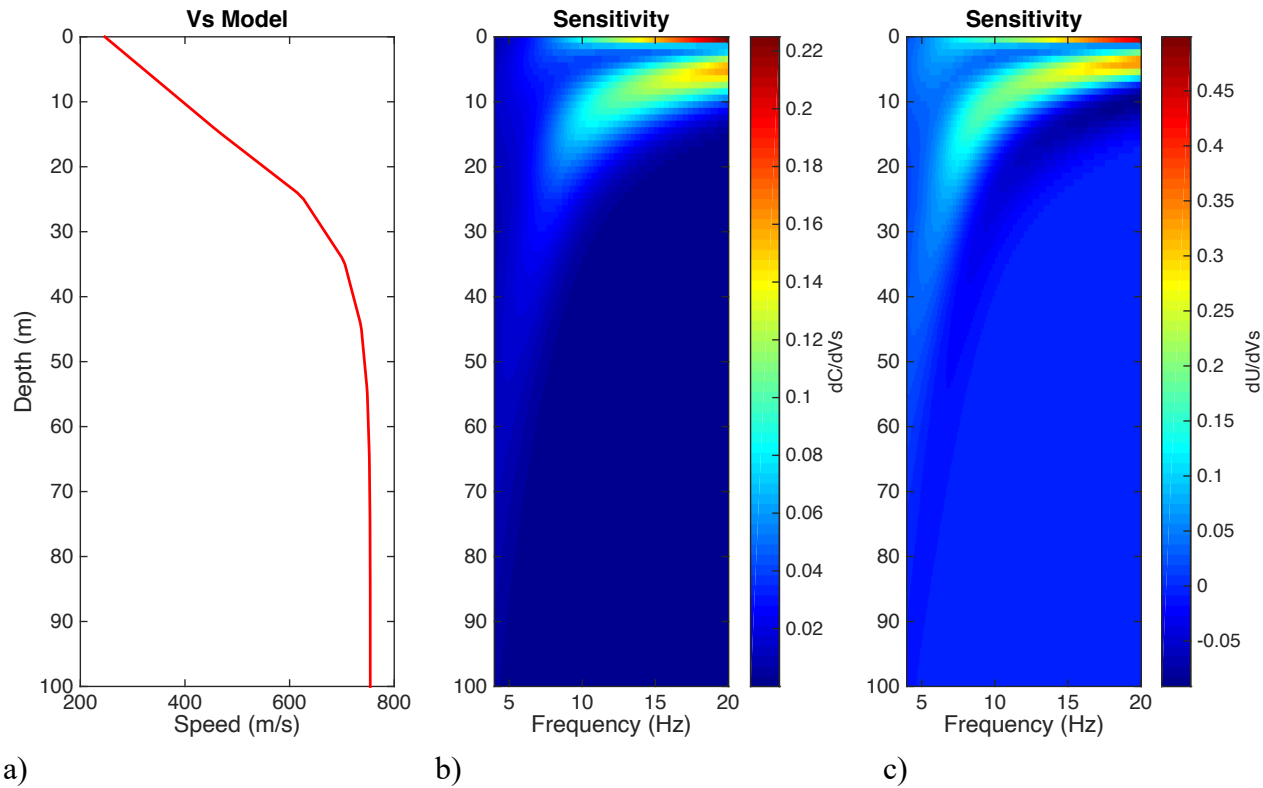


Figure 5.13. (a) The layered model used in sensitivity kernel computation. (b) Sensitivity kernels of Rayleigh wave phase velocity. (c) Sensitivity kernels of Rayleigh wave group velocity.

The last step is inversion to construct layered models at the sampled points. The sample point is defined as the center point of a segment for the same-segment dataset and as the middle point

of two segments for the cross-segment dataset. The cross-segment NCFs sample the warm ground zone where it was not possible to install the DAS cable (**Figure 5.14a**). Two inversion methods are utilized to solve for shear wave velocity profiles at the sampled points. The SWAMI code (Constable et al., 1987; Lai 1998), based on Occam's inversion, is used to invert phase velocities, whereas the group velocities are inverted with a linearized inversion code from the Computer Programs in Seismology software suite (Hermann, 2013). The pseudo 3D shear wave velocity model is interpolated from all the layered models (**Figure 5.14**).

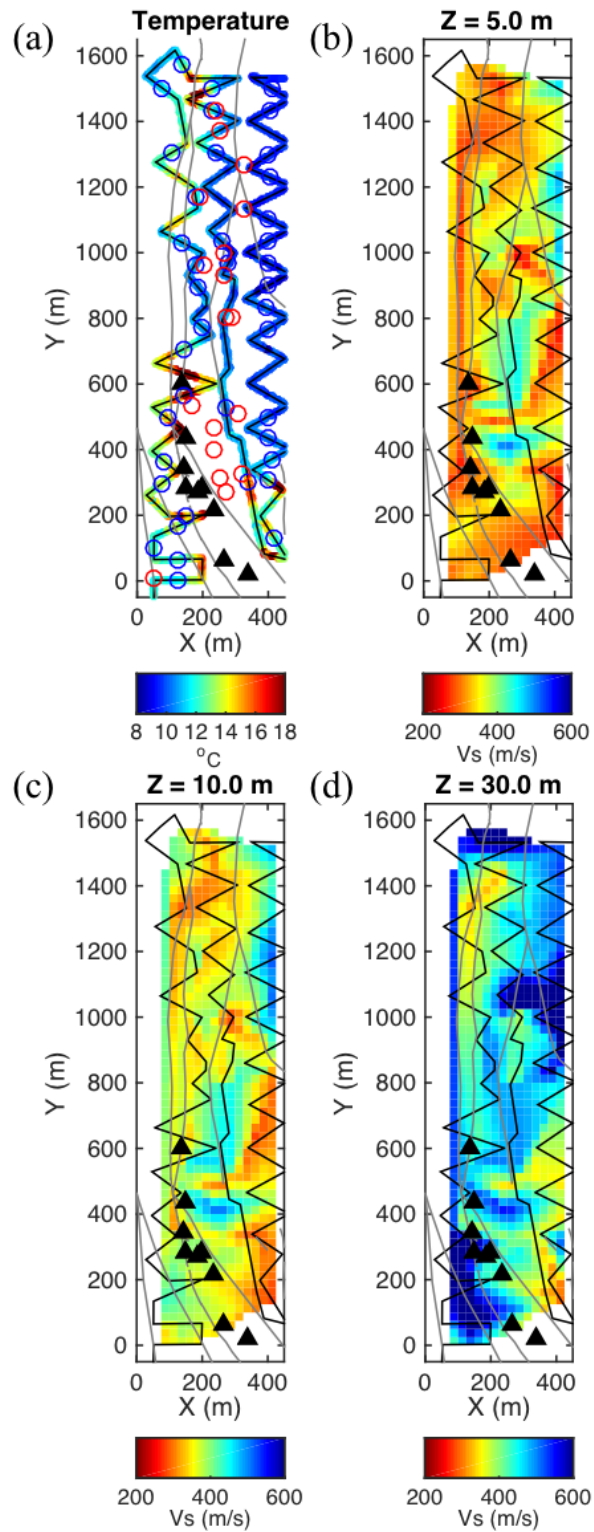


Figure 5.14. (a) Daily average surface temperature on March 14, 2016. (b) Shear wave velocity at 5 m depth. (c) Shear wave velocity at 10 m depth. (d) Shear wave velocity at 30 m depth. The fumaroles are shown as black triangles and the gray lines denote faults. Open circles in (a) denote sampled points (red: cross-segment, blue: same segment).

At very shallow depth (5 to 10 m), the low velocity zone (LVZ) is observed in the area covered by the Quaternary lacustrine deposits (Faulds et al., 2017) and warm ground (**Figure 5.14 b, c**). The area around the injection wells 18-31 and 18D-31 also shows relatively low velocity. Slightly deeper part, a velocity contrast emerges across the fault zone in southern part. Other tomography techniques are also used to image 3D seismic structure at Brady. The shot-interferometry (SI) technique with geophone array data provides 3D Vp and Vs models (Matzel et al., 2017). Parker et al. (2018) used the P-wave arrival times of DAS and geophone arrays to invert 3D Vp model. **Figure 5.15** shows comparison between these three models at 20 m depth. Generally, the SI Vs model show a higher velocity that might be due to a different initial model and/or inversion strategy. The LVZ near the injection wells is imaged in the two Vs models, whereas it is not clear in the Vp model. The other LVZ in the southwest part ($x \sim 400$, $y \sim 100-400$) is shown in our model and the Vp model.

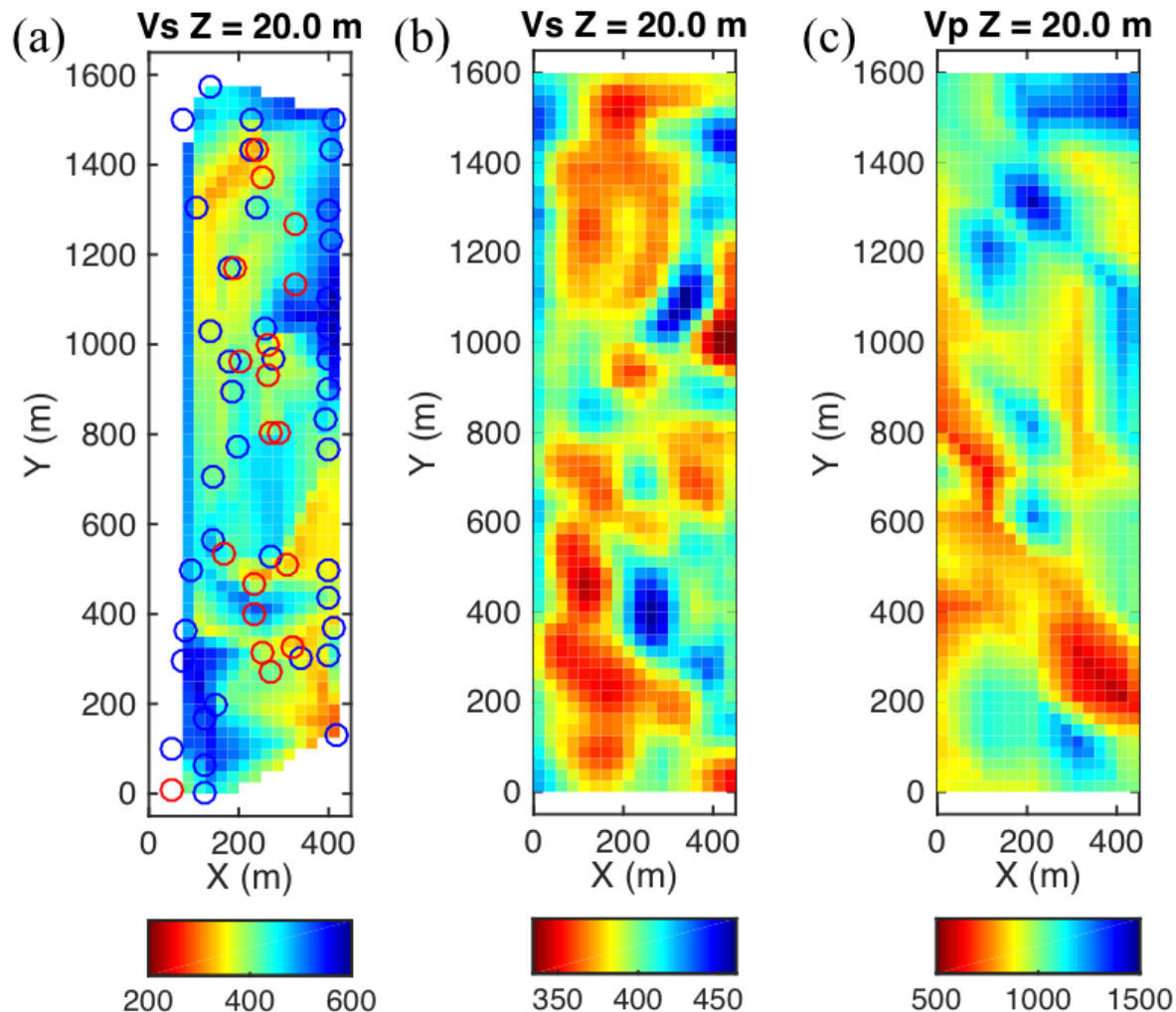


Figure 5.15. Comparison of velocity models at 20 m depth. (a) Vs model from this study. (b) Vs model from Matzel et al. (2017). (c) Vp model from Parker et al. (2018).

Data Analysis - Earthquake Data

Given the lack of success in picking S-wave arrivals in order to perform a tomographic inversion for 3D shear-wave velocity (Vs) structure, we attempted to use shear wave data from the earthquakes recorded during the field deployment (Cardiff et al., 2018) on both the nodal geophones and the Brady seismic network. P- and S-wave arrivals were picked on the nodal geophones and were combined with catalog P and S picks from the Brady seismic network and with the active-source data used for the Vp tomography (Parker et al., 2018) and a tomographic inversion was carried out. Unfortunately, the data were inadequate to resolve 3D structure under the target region because the earthquakes were outside the geophone array.

Sweep Interferometry

Sweep interferometry operates similarly to ambient noise tomography but relies on cross-correlating vibroseis signals recorded at different geophones (Matzel et al., 2017a; 2017b). Using the vibroseis sweep source as the energy source rather than ambient noise utilizes shorter record sections to produce high-frequency waveforms. Particular focus was on data with vibroseis locations outside of the main array (**Figure 4.11**). Figure 5.16 shows the moveout apparent when comparing cross correlation results that have a common station.

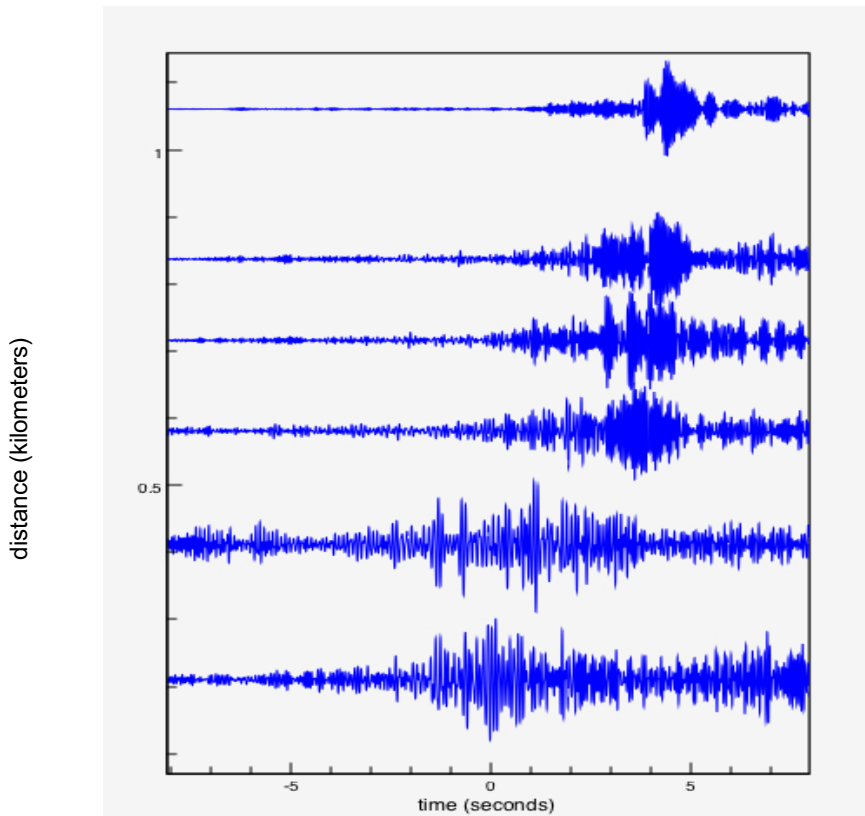


Figure 5.16. Example cross-correlation waveforms from sweep interferometry.

Multiple material properties were inverted for such as Vp, Vs, and attenuation of P-waves (parameterized by quality factor Qp) and S-waves (parameterized by quality factor Qs). **Figure 5.17** shows the near-surface inversion results for Vp, Vp/Vs, and Qs/Qp. Trends in the anomalies align with mapped faults and thermal surface features. This provides evidence in the models of fault bounding. Since Vp and Qp have different sensitivities than Vs and Qs to different material properties, such as saturated or free pore space, the ratios of Vp/Vs and Qs/Qp provide more refined information that the individual parameters. For the ratio Qs/Qp of the quality factors, higher ratio values are associated with higher saturation and less compaction while lower ratio values are associated with lower saturation and more compaction.

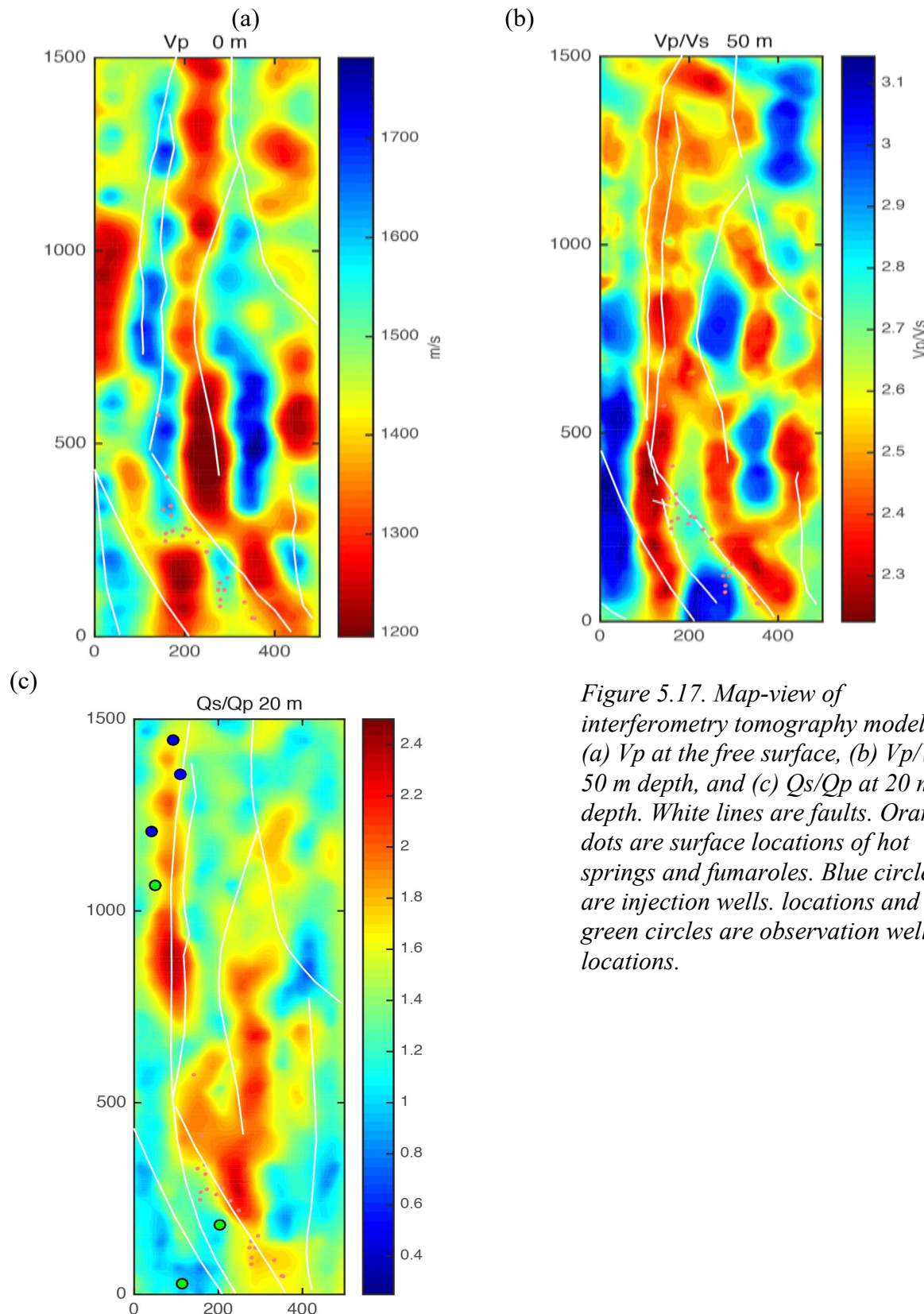


Figure 5.17. Map-view of interferometry tomography models: (a) V_p at the free surface, (b) V_p/V_s at 50 m depth, and (c) Q_s/Q_p at 20 m depth. White lines are faults. Orange dots are surface locations of hot springs and fumaroles. Blue circles are injection well locations and green circles are observation well locations.

Figure 5.18 shows the attenuation results in horizontal slices for different depths. At the surface there are relatively high values of Qs/Qp along the fault system and along the fumaroles. At deeper depths we see lower values of Gs/Qp that we interpret as more compact material. This is consistent with what we know about the natural laboratory structure, with unconsolidated sediment overlying more consolidated units at depth. Higher fluid saturation along the faults is consistent with our hypothesis that the faults act as conduits for fluid flow.

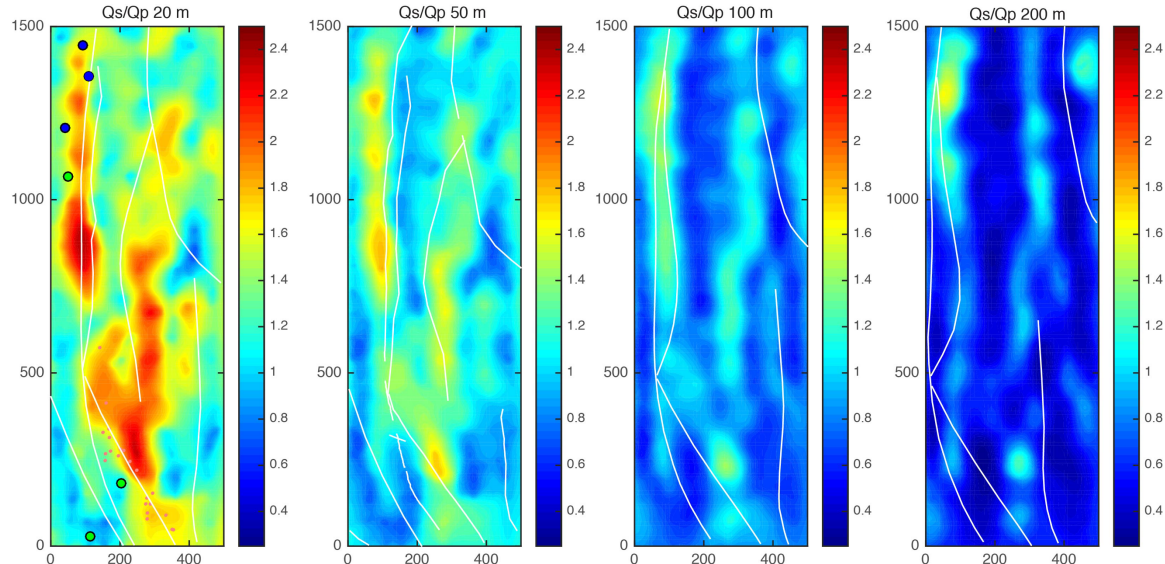


Figure 5.18. Map-view sections of the sweep interferometry Qs/Qp model.

The two Vp models estimated using travel-time tomography (**Figure 5.4**) or sweep interferometry (**Error! Reference source not found.a**) follow the same trends. While the interferometry model is smoother, they both show strong increasing velocity from the surface to the 100 m depth and display similar structures. Since these models were derived using independent methods, their similarity provides confidence in the results.

Lastly, we were able to track dynamic changes in seismic amplitudes, while the seismic phase arrivals remain nearly identical, as operations changed. These changes in seismic amplitudes lead to variations in the inverted attenuation. These variations can then be mapped, here at 20 m depth (**Figure 5.19**). Such mapping highlights areas of efficient wave propagation, i.e., more compacted medium, and of attenuated and less efficient wave propagation, i.e., less compacted medium.

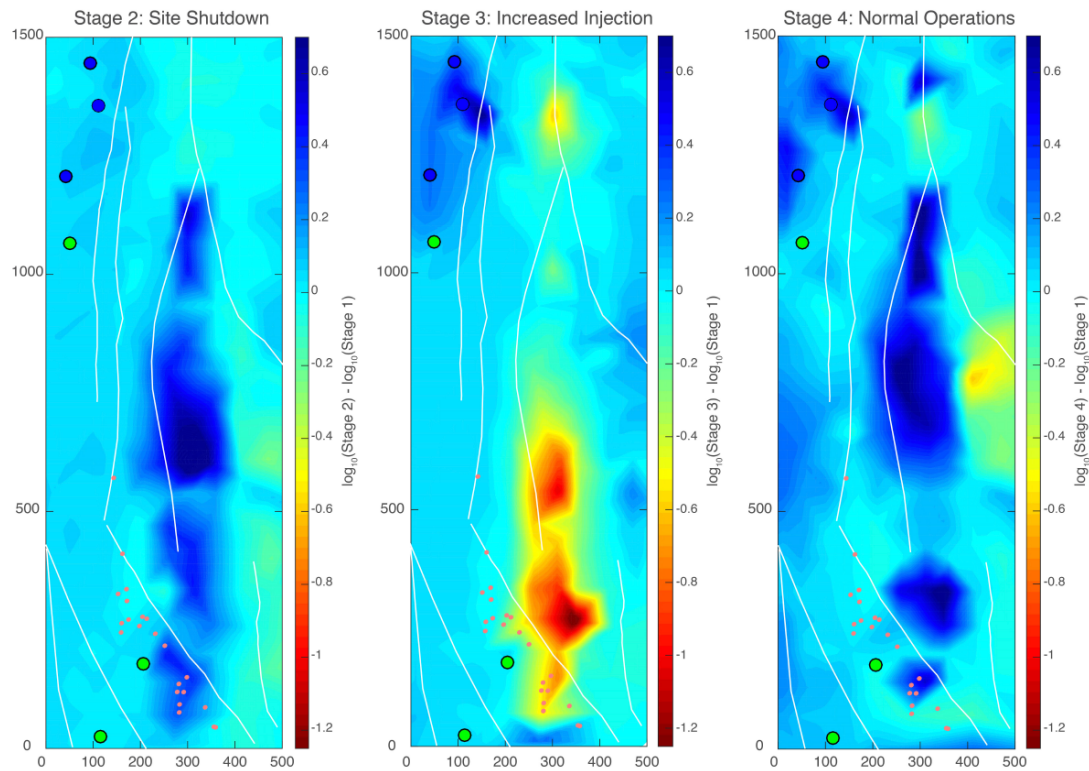


Figure 5.19. Map-view sections of the variation in attenuation at 20 m depth related to seismic amplitude changes between each operation. Blue translates into an area of efficient wave propagation, i.e., more compacted medium, and Red into an area of attenuated and less efficient wave propagation, i.e., less compacted medium. Note that at stage 4, the system does not return to what it was at stage 1.

3D Seismic Wave Modeling

By using V_p , V_s , and a 3D density model it is possible to generate synthetic seismic waveforms. Our mesh has 82,080 elements of 25 meter cubes that incorporate surface topography (**Figure 5.20**). For this modeling, we use the theoretical vibroseis signal at the location of each vibe point to calculate a source term. This signal is then propagated through the prior model of seismic velocities V_p and V_s and convolved with the instrument response of the Fairfield Nodal geophone to generate a synthetic waveform. We performed this simulation using two different prior models for the 3-dimensional structure of the seismic velocities V_p and V_s .

The first model (named “travel-time” and labelled M05) uses the V_p values estimated by travel-time tomography (Parker et al. 2018). To find values of V_s , we assume the following empirical relationship:

$$V_s = V_p/2.75 \text{ for } V_p < 1.8 \text{ km/s}$$

$$V_s = V_p/2.00 \text{ for } V_p \geq 1.8 \text{ km/s}$$

The 3D density model used values interpolated from a gravity model labelled M00 [*Witter et al.*, 2016].

The second model (named “sweep interferometry” and labelled M01 and M02), was calculated using sweep interferometry [*Matzel et al.*, 2017; *Matzel et al.*, 2018]. We used the same density model M00.

Using each of the two models, we calculate simulated waveforms and compare them to the observed waveforms recorded by the Fairfield Nodal geophones in **Figure 5.21**. Both models capture the pronounced beating pattern (interpreted as complex surface waves) observed in the raw data, but still have noticeable differences (**Figure 5.22**). Phase arrivals were picked using FLEXWIN (Maggi et al., 2009), a semi-automated time-window picker (**Figure 5.23** and **Figure 5.24**). In the case where the arrival time is not well constrained, the correlation coefficient between the data and synthetic is low, and no pick is made.

Figure 5.25 shows a statistical comparison between the pick results of waveforms from the inverted models and the data. Cross-correlating the simulated waveforms with the observed values quantifies the quality of the fit. The sweep-interferometry model shows slightly higher cross-correlation coefficients, i.e., a better fit to the data, but also has a systematic lag in the travel times. Amplitudes were analyzed using the logarithmic value of the amplitude ratio between observed and synthetic seismograms within the picking time windows, per equation 11 of Maggi et al. (2009).

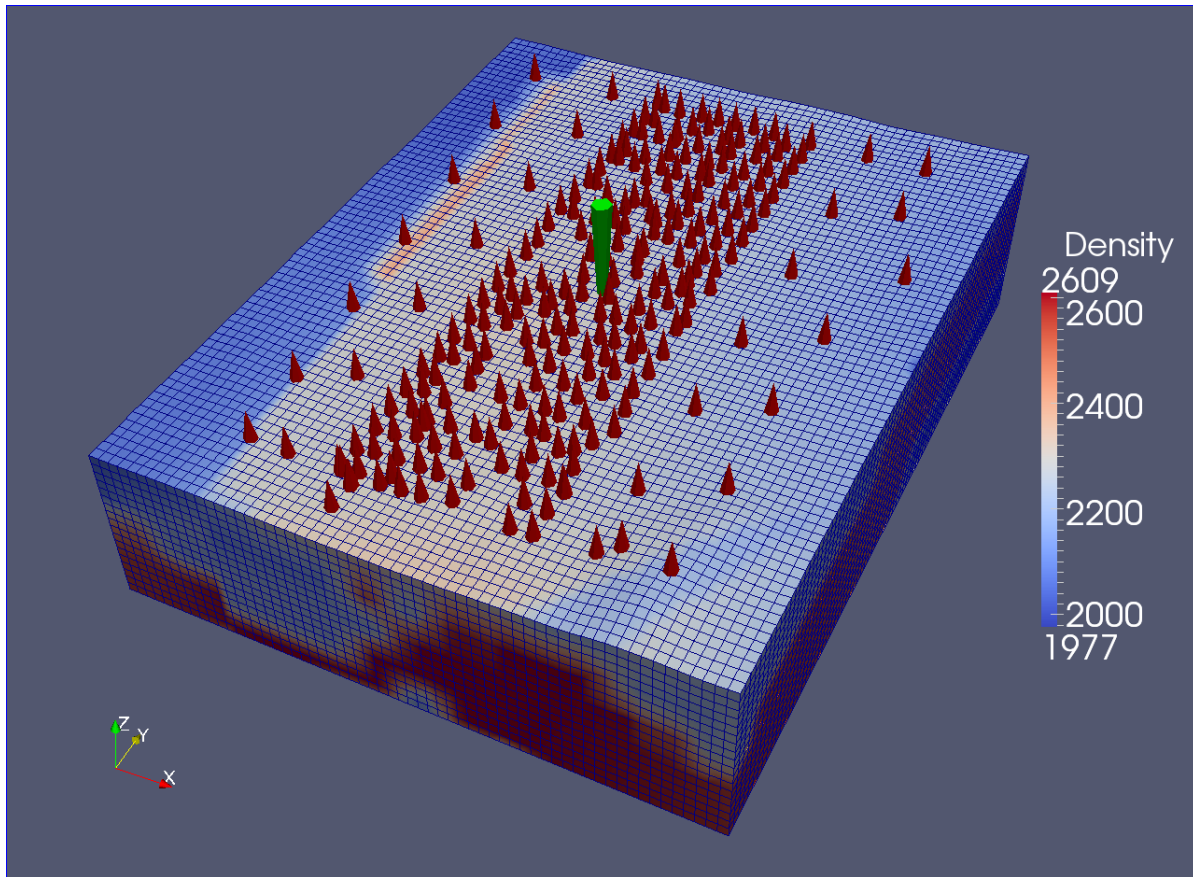


Figure 5.20. 3D density model after Witter et al. (2016) in SPECFEM3D mesh. Red cones are the nodal geophone locations.

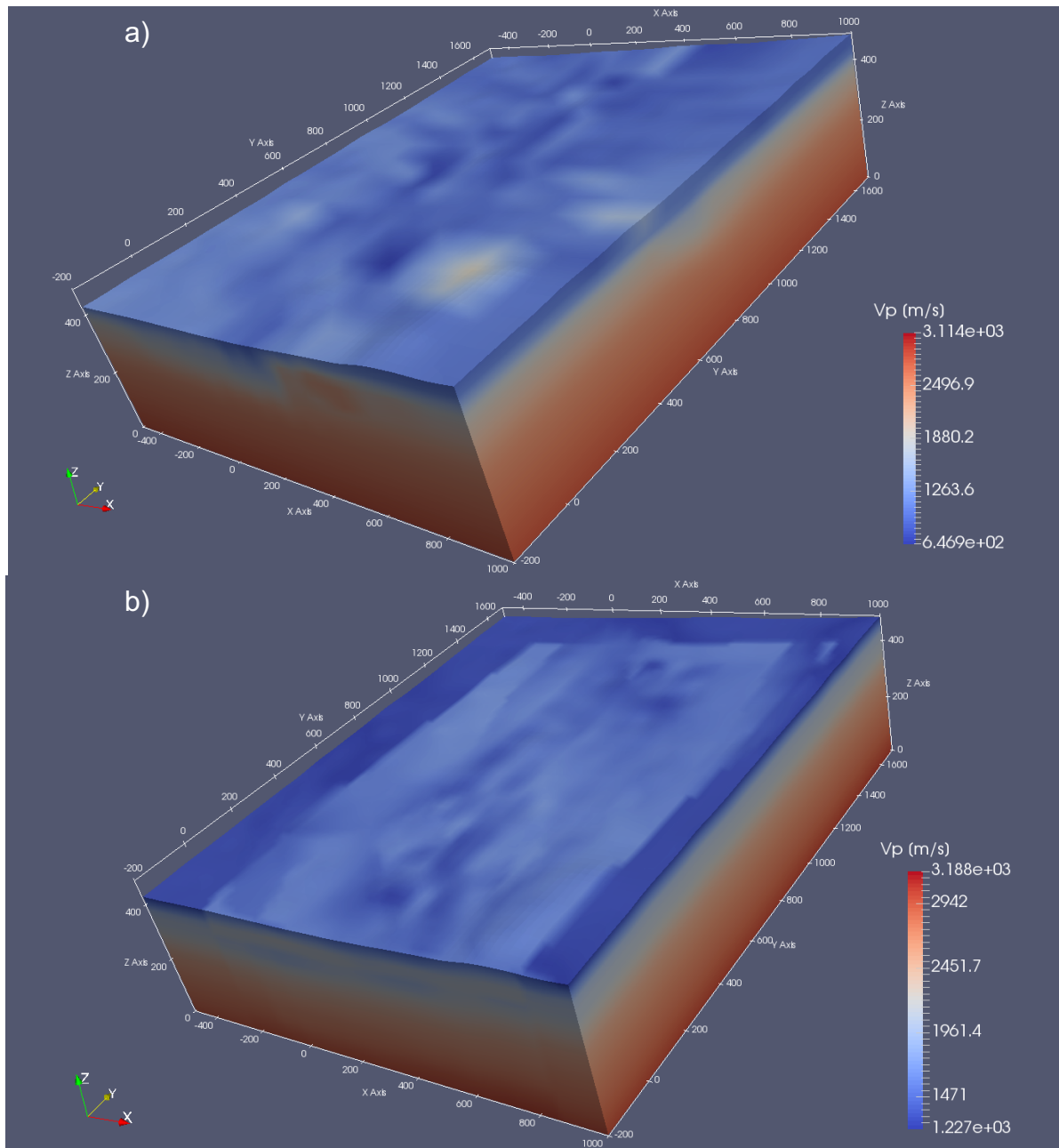


Figure 5.21. V_p models in *SPECFEM3D* mesh. (a) Travel time inversion model. (b) Sweep interferometry model.

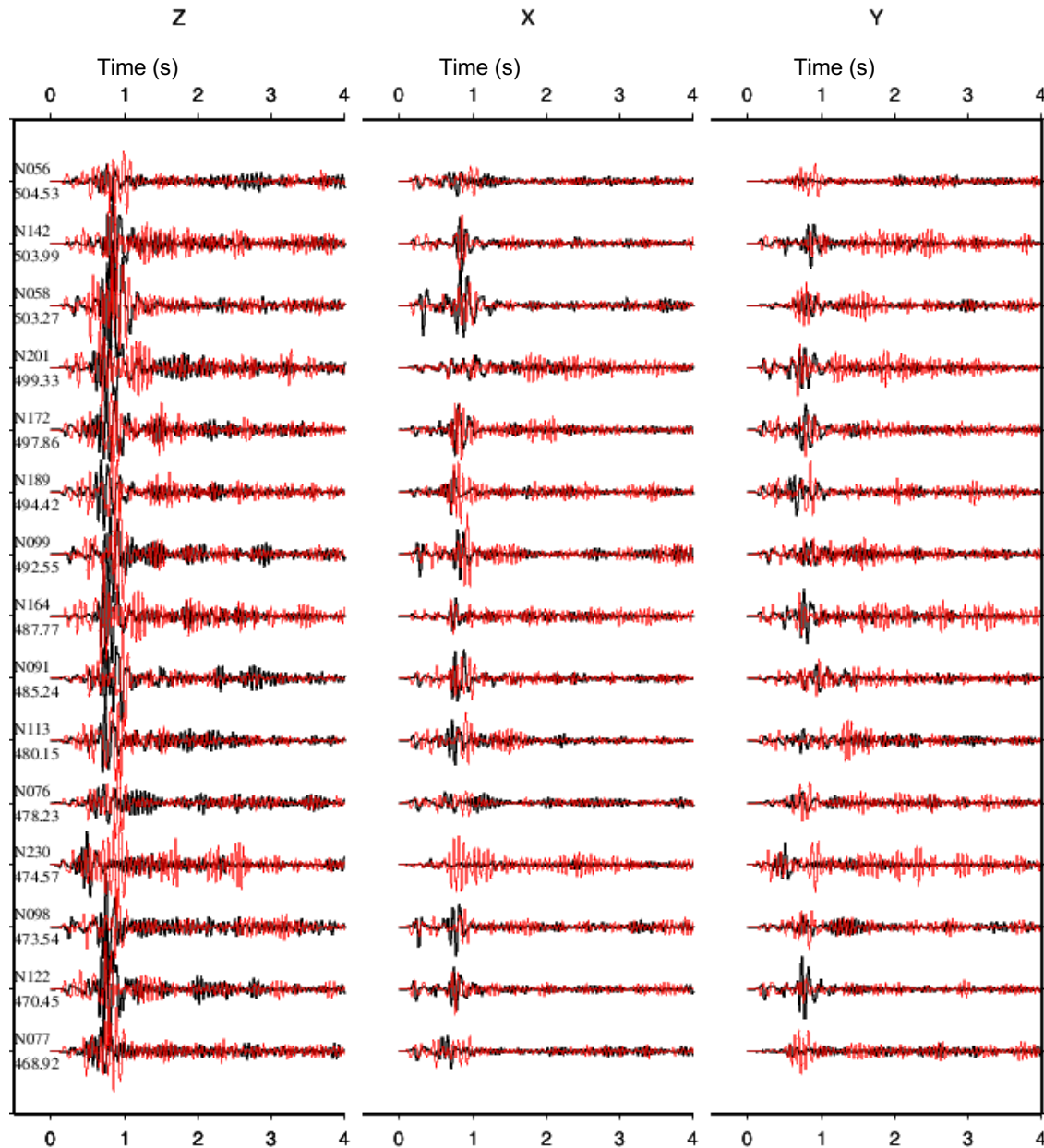


Figure 5.22. Waveform comparisons for modeled three component results after band-pass filtering between 3 and 20 Hz. Black waveforms are the travel time model results. Red waveforms are the sweep interferometry model results. Distance in meters from source to receiver is listed below the station number. Coordinates X,Y,Z correspond to the rotated PoroTomo frame.

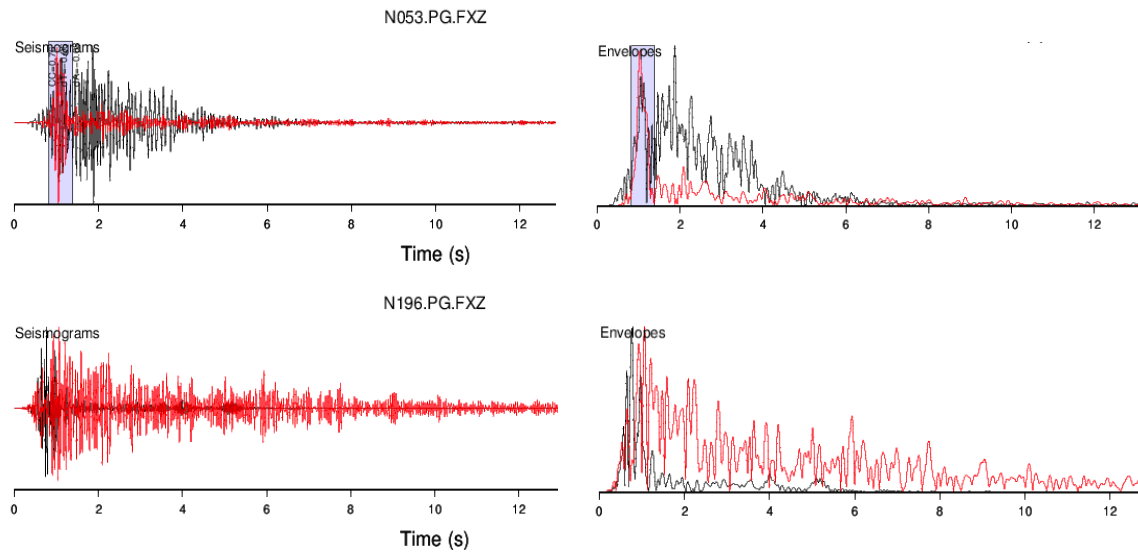


Figure 5.23. Vertical component of travel time model results (red) compared to the actual data (black) for two nodal stations. Waveforms filtered between 10 and 25 Hz. Shaded bars show phase arrival windows picked by FLEXWIN.

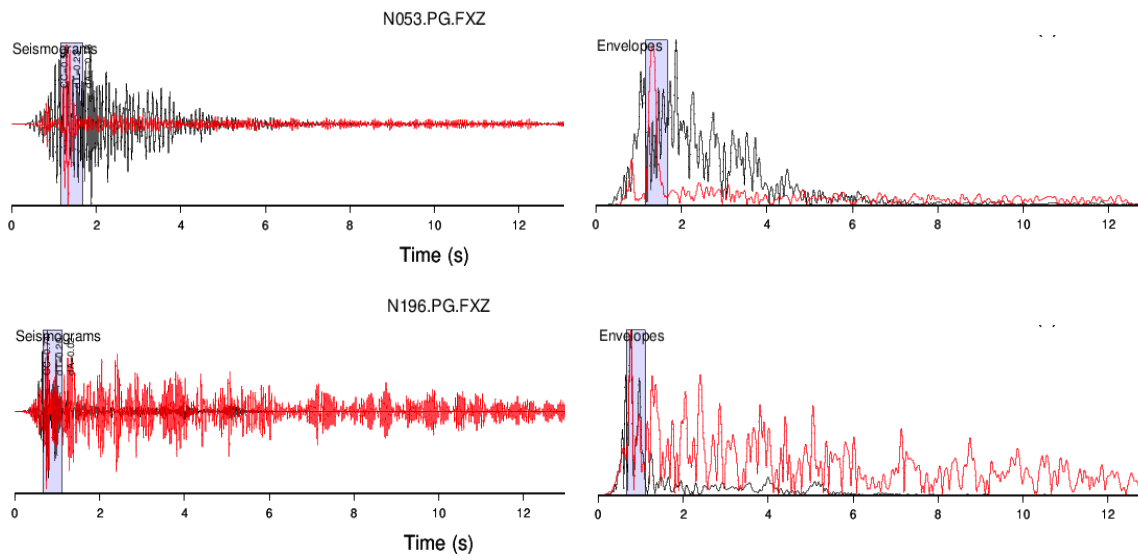


Figure 5.24. Vertical component of sweep interferometry results (red) compared to the actual data (black) for two nodal stations. Waveforms filtered between 10 and 25 Hz. Shaded bars show phase arrival windows picked by FLEXWIN.

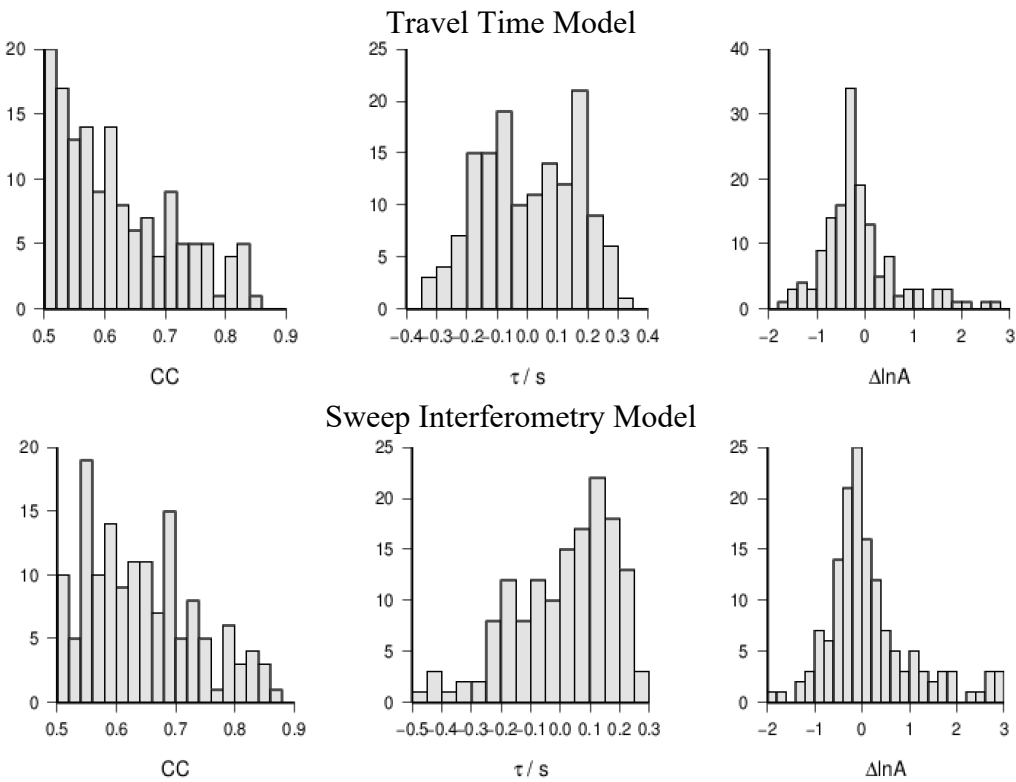


Figure 5.25. Histograms for 147 windows picked by FLEXWIN. (Left) Cross-correlation between the data showing results for 50% and above. (Middle) Time lag between the data and synthetic. (Right) Natural log of the amplitude.

B. Discussion

We achieved the goal of being able to resolve seismic velocity structure in 3D at a scale of 100 m at a depth of 200 m using the experiment design we adopted for P-wave structure from active-source body-wave observations. Using interferometry also allowed us to image V_p, V_s, Q_p, and Q_s at high resolution, showing that Brady geothermal field is highly heterogeneous in the top 100 m. The features of the 3D V_p travel-time tomography model are consistent with information from borehole logs. We did not attain similar success with shear waves and V_s structure due to the difficulty of identifying S-wave arrivals in the active source data. For our surface-to-surface experiment design, the vibroseis source was not the optimal choice.

The DAS cable was laid out in a zigzag fashion in order to provide a more varied orientation of the cable considering the known directional sensitivity limitations of the DAS system. This decision limited the length of straight segments of cable, which inhibited the surface wave analyses. A layout with more long, straight segments of cable would have benefitted the surface-wave analyses.

The earthquake analysis was limited by the location of the earthquakes outside the geophone and DAS arrays. If the dense arrays had encompassed the zone of seismicity near the extraction wells, the opportunity for successful use of earthquake data would have been enhanced.

One major unexpected result was the analysis of the Q_s/Q_p ratio, which showed a strong sensitivity to fluid saturation, with high ratios correlating with high fluid saturation. A second

interesting result was our ability to correlate changes in seismic amplitude with changes in pressure during operation changes.

C. Recommendations

One of our primary recommendations for future full-scale studies is to use a different active seismic source. The non-impulsive nature of the vibroseis source proved to be a challenge for our active-source analysis. One option for a repeatable, impulse-like source would be an accelerated weight drop source such as the HH Seismic Hammer (Hampshire and O'Donnell, 2013; Jones, 2014). The HH Seismic Hammer is not a pure impulse source and does have a complex source signal, but it is much simpler than that for vibroseis. An example field project using the HH Seismic Hammer was recently reported by Onyango et al. (2018).

Having a location with more seismic activity than Brady would benefit future studies. Our Vs modeling was limited by a non-impulsive source signal and limited earthquake and instrument distribution. Having an array that is effectively deployed to record seismic activity would greatly increase the capability to gather Vs data. Double-difference relocation requires seismic waveforms with pickable arrivals and Vp and Vs models but would provide a means of potentially increasing event location accuracy. Attenuation tomography would be worth pursuing with a more event-rich dataset. Focal mechanisms of induced/triggered earthquakes could provide more information about the stress and fault geometry in the reservoir.

Using both DAS and geophone data is quite important in the future. Joint inversion methods such as using the horizontal and vertical components provided by three-component geophones with the dispersion curve provided by DAS will be useful. For a full-scale study, a horizontal surface deployment of a DAS system as the sole seismic receiver array would require a prohibitively large amount of fiber optic cable to be able to image more than the shallow surface. But DAS deployed vertically down a well or horizontally at depth in a directional borehole would be an effective substitute to downhole geophones if properly coupled to the casing and surrounding substrate.

In order to be able to carry on synthetic calculations to validate models or for full waveform adjoint inversion approaches, it is important to consider an access to a 3D density model. To improve the resolution of prior velocity models using a full waveform inversion approach such as adjoint method, it would be recommended to use a source with a wider range of low frequencies. This would allow the use of a classical strategy for full waveform inversion which consists in starting at low frequencies, resolving longer wavelengths, then increasing the frequency content during subsequent iterations to increase the resolution of the model. In order to carry direct data and synthetic waveforms comparison, individual instrument response for seismometers need to be accessible.

If there were multiple wells with DAS or downhole geophone arrays, several additional means of analysis would be worth consideration. 3D vertical seismic profiling (VSP) would provide more information at depth by using sources at depth in at least one well. Active sources at the surface near wells could be repeated over time to look for temporal changes. Alternatively, cross-borehole ambient noise would provide information at depth without requiring active sources. Borehole stations could also be correlated to surface stations for vertically arriving ambient noise to image body waves or horizontal surface waves.

Section 6. Geodesy

A. Results

The following results have been excerpted from a paper (Reinisch et al., 2018) as well a manuscript in preparation, entitled “Time Series Analysis of Volume Change at Brady Hot Springs, Nevada, USA, Using Geodetic Data” by Elena C. Reinisch and others.

Data Collection

Both interferometric synthetic aperture radar (InSAR) and Global Positioning System (GPS) data were collected at Brady. InSAR data was acquired with a wavelength of approximately 30 mm by the TerraSAR-X (TSX) satellite mission operated the German Space Agency, DLR (Pitz & Miller 2010). We have scenes from tracks 53 (strip_008R), 167 (strip_014R), and 91 (strip_006R). To cover years before TSX was operational, we also work with data from Japan Aerospace Exploration Agency’s Advanced Land Observing Satellite (ALOS) tracks 215 and 216 and the European Space Agency’s second European Remote-Sensing Satellite (ERS-2) track 485. The PALSAR radar sensor aboard the ALOS satellite used a wavelength of about 240 mm (Rosenqvist et al., 2007). The ERS-2 satellite mission carried a radar sensor with a C-band wavelength of roughly 57 mm (Francis et al., 1995). These data are archived by the Western North America InSAR (WInSAR) Consortium. Satellite statistics and temporal coverage for our dataset are shown in Table 6.1.

Platform	Track	Repeat Cycle (days)	Wavelength (mm)	First Epoch YYYYMMDD	Last Epoch YYYYMMDD	Number of Pairs
ALOS	T215	46	240	20071217	20101109	7
ALOS	T216	46	240	20061231	20110226	16
ERS-2	T485	35	57	20030427	20090823	10
TSX	T53	11	30	20111121	20181002	89
TSX	T167	11	30	20110924	20170213	36
TSX	T91	11	30	20120723	20160929	40

Table 6.1. SAR Platform Statistics for InSAR Dataset

We produce interferograms using the open source processing software GMSTAR, which utilizes Generic Mapping Tools (GMT) for creation and visualization of interferometric pairs (Sandwell et al., 2011a,b). Noise is removed by applying an adaptive Goldstein filter that depends on spatial coherence (Goldstein & Werner, 1997; Baran et al., 2003; Sandwell et al., 2011b). We use the ‘statistical-cost, network-flow phase-unwrapping algorithm’ (Chen & Zebker 2000) to unwrap pairs. Both the pairs and the digital elevation model (DEM) used to create these pairs are available publicly (Reinisch & U. of Wisconsin, 2017). We work with unwrapped range change rates (i.e., rate of change of displacement along line of sight of the radar) (**Figure 6.1**). Far-field effects are removed by averaging the observed data in the NW portion of the interferogram, where we expect no deformation, and subtracting the result from all the observed range change rates. There are two regions where phase discontinuities are known to occur in interferograms at Brady. We exclude these regions from analysis because unwrapping fails at these discontinuities.

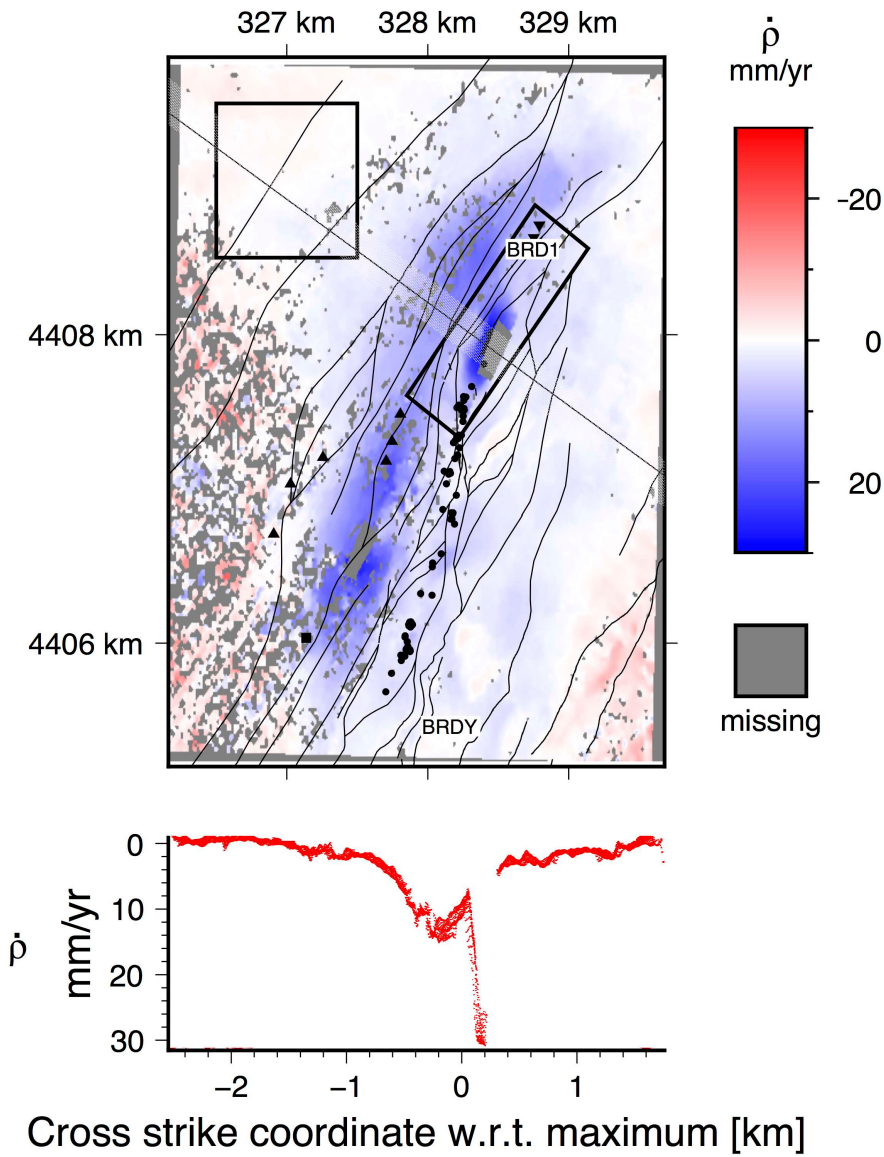


Figure 6.1. Figure 1 from Reinisch, et al. (2018) “(a) Deformation field measured by InSAR data, showing observed rates of change in range $\dot{\rho}$ between 2016 July 22 and 2017 August 22, in map view (a) and profile (b). Blue regions denoting an increase in range indicate subsidence. The two regions of phase discontinuities masked from analysis are shown as grey patches. The rectangle in the NW corner outlines the region used for estimating far-field deformation. The rectangle in the NE outlines the study area for the PoroTomo experiment. GPS stations are labelled in white. Injection wells are shown as inverted triangles, production wells are upright triangles and the stimulation well 15-12 is denoted as a solid black square. Faults from Jolie et al. (2015) are shown with thick black lines. Fumaroles from Coolbaugh et al. (2004) are shown with filled circles. The black line bisecting the study area shows the profiled region. Coordinates are easting and northing in the Universal Transverse Mercator (UTM) projection on the WGS84 ellipsoid zone 11 N (Snyder, 1987).”

In addition to InSAR data, we have GPS data from three continuous stations in the MAGNET network. Data from these stations have been analyzed using standard procedures and have time-series of relative position which are publicly available (Blewitt et al., 2013; Kreemer & U. of Wisconsin, 2018). GPS station BRD1 was installed on the head of Well 18-1, within the subsiding bowl, on March 10, 2016 as part of the PoroTomo project. Stations BRAD and BRDY were already operational prior to Deployment. BRAD is located to the located to the Northwest. Station BRDY is located to the southeast of the subsiding area and is used to estimate the far-field range change for the GPS measurements. We use GPS measurements of displacement at BRD1 with respect to BRDY converted to range change estimates to validate the range change found from InSAR (Figure 6.2).

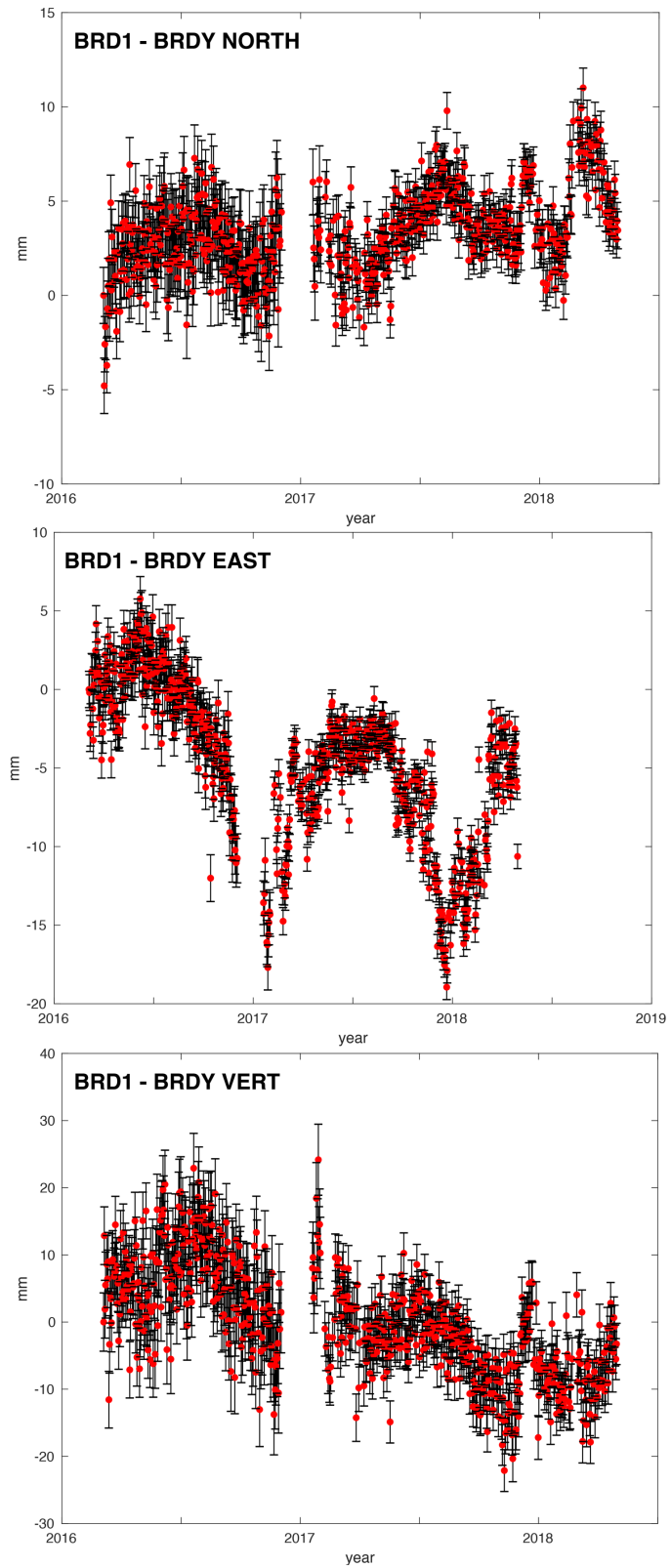


Figure 6.2. Raw GPS time series for BRD1 from 2016 to 2018.

Data Error Analysis

We use GPS to analyze the accuracy of the InSAR measurements. The uncertainty for the range change estimated from GPS is derived from measurement uncertainty at each station. We use the standard error of the mean as an estimate of uncertainty for the range changes observed using InSAR. We find the difference between the mean range change from InSAR for TSX T53 pair spanning from July 22, 2016 to August 22, 2017 and the range change measured from GPS suggests that the realistic 1σ uncertainty is less than 5 mm in range change for the InSAR data set (Reinisch et al., 2018). We derive a spatial covariance function for the InSAR data using semivariogram analysis with an exponential model and the results from the accuracy test using GPS (Reinisch et al., 2018).

Deformation Modeling

Our objective for the geodetic portion of the PoroTomo project was to characterize the mechanism for the observed subsidence. To do so, we define a “multi-cube” parameterization where each cube represents a sink with an initial volume of $V_0 = W^3$, with $W = 100 \text{ m}$ as the length of one edge. We can then represent volume change of the cube by $\Delta V = -3U_3W^2$, where $-U_3$ is the (uniform) slip element describing contraction of the cube (**Figure 6.3**).

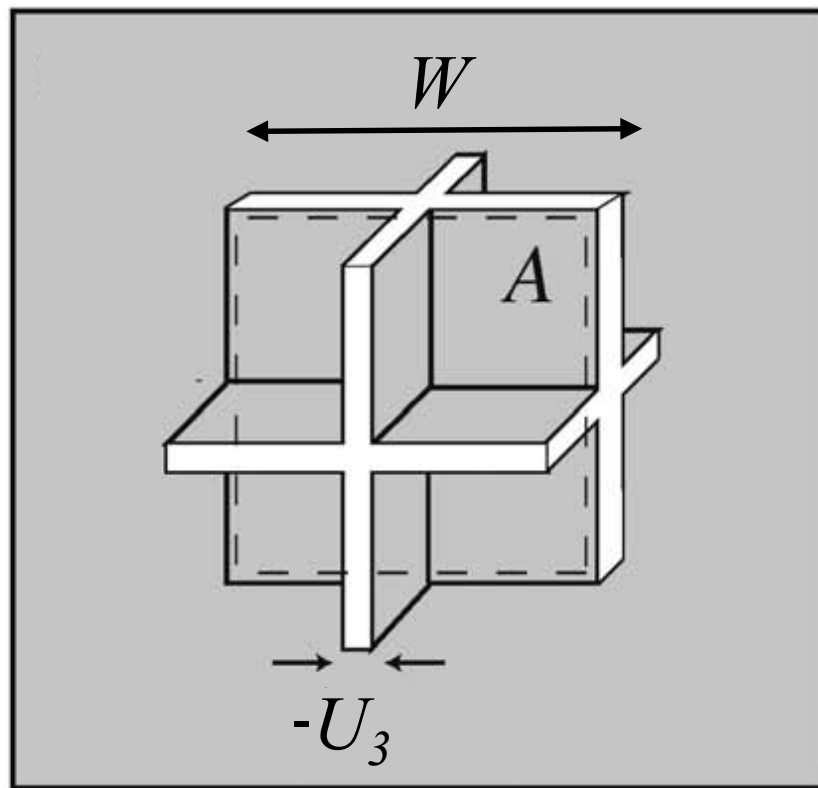


Figure 6.3. Figure 2 from Reinisch, et al. (2018): “Sketch of the cubic sink model, showing three orthogonal, planar dislocations. The width W represents the dimension of each orthogonal square patch, A represents the surface area of each patch and $-U_3$ represents the tensile closing of each patch. The sketch is modified from Bonafede & Ferrari (2009), their fig. 2(iii).”

We perform a checkerboard test for 100-meter resolution to determine if we meet the target of 250 m or the “beyond target” resolution of 100 m with this model. Results are shown in

Figure 6.4. There is overall good agreement between the input model and the recovered model, with only slight smearing in bottom and top right corners of the recovered model. Using a Two-tailed Student’s T test (e.g., Wackerly et al., 2007), we find no significant difference between the input model and the recovered model at 99 percent confidence. Thus, we conclude that we meet the “beyond target” metric for resolution.

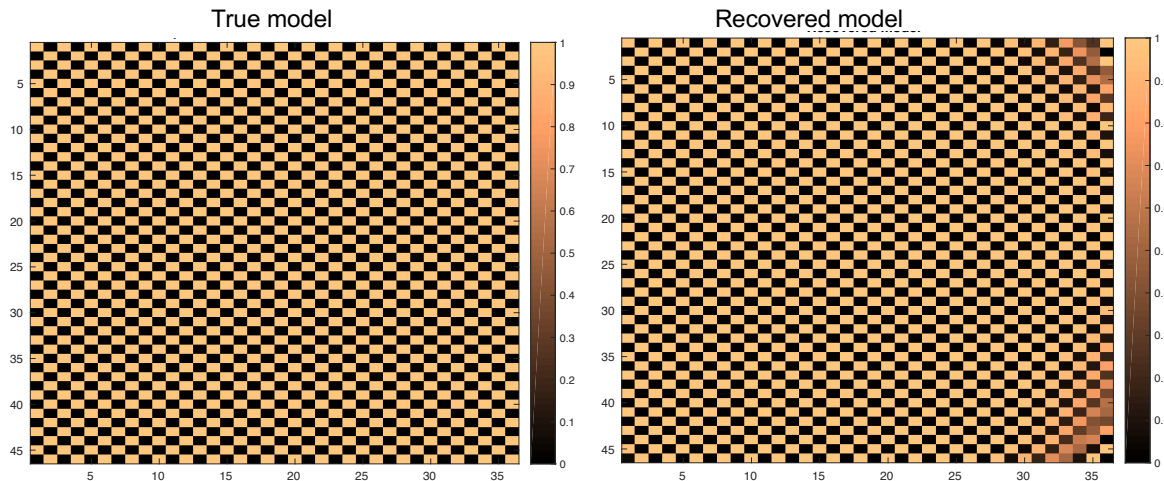


Figure 6.4. Results from checkerboard test at 100-meter resolution. (Left) True model at $(100 \text{ m})^3$ voxel size. (Right) Recovered model.

Single Pair Analysis

We apply our “multi-cube” parameterization to a single TSX T53 pair spanning from July 22, 2016 to August 22, 2017 (Reinisch et al., 2018). **Figure 6.5** shows the deformation fields from this analysis. These results are found using a temperature-defined prior model, which will be discussed in further detail in Section V.A.5 “Hypothesis Testing”. The observed subsidence is along strike of the faulting system; the modeled deformation field follows this trend. We note that the residual (observed minus modeled) values of range change rate are less than the uncertainty in the data, leading us to conclude that the model fits the data well. We quantify a misfit of the model to the data using the square of the reduced χ^2 test statistic

$$\sqrt{\chi_{v,obs}^2} = 1.5 \quad (6.1)$$

(Strang & Borre, 1997, p. 334; Aster et al., 2013, p. 29).

We further analyze our results in terms of estimates per cube. **Figure 6.6** shows the parameterization’s gridded layer where each cube has an estimate of volumetric strain rate. In

this specific case using a temperature defined prior model, the strain rates are interpreted as thermal volumetric strain rates. To approximate the volume of the modeled reservoir we consider areas of significant cooling, where

$$\dot{V}^{(T)} < -2\sigma(\dot{V}|\dot{T}) \quad \text{with} \quad \sigma(\dot{V}|\dot{T}) = 82.7 \text{ m}^3 \text{yr}^{-1}. \quad (6.2)$$

We calculate the volume of the modeled reservoir to be $1.2 \times 10^8 \text{ m}^3$ and the resulting volume change rate of the cubes in the modeled reservoir to be $\dot{V}^{(T)} = (-2.9 \pm 0.3) \times 10^4 \text{ m}^3 \text{yr}^{-1}$. We note that the areas of significant cooling occur between the injection and production wells, which is consistent with our key concept that highly permeable conduits along faults channel fluids from shallow aquifers to the deep reservoir tapped by the production wells.

We also consider our estimates in terms of rate of change of thermal energy. We assume that the volume of rock that is cooling is the same as the volume of rock that is shrinking (Ali *et al.* 2016). Using the estimated rates of cooling and values of specific heat of the rock $c_{rock} = 948 \text{ JK}^{-1} \text{kg}^{-1}$ and a range of values for uniform rock density $\rho_{rock} \in [1900, 2800] \text{ kg/m}^3$, we calculate the 95 percent confidence interval for the rate of change of thermal energy for the reservoir to be $\dot{E}_{est} \in [-53, -79] \text{ MW}$. Given the power plant's capacity of [10,26] MW (e.g. Faulds *et al.* 2010; Cardiff *et al.* 2017), this indicates an efficiency on the order of 20 percent.

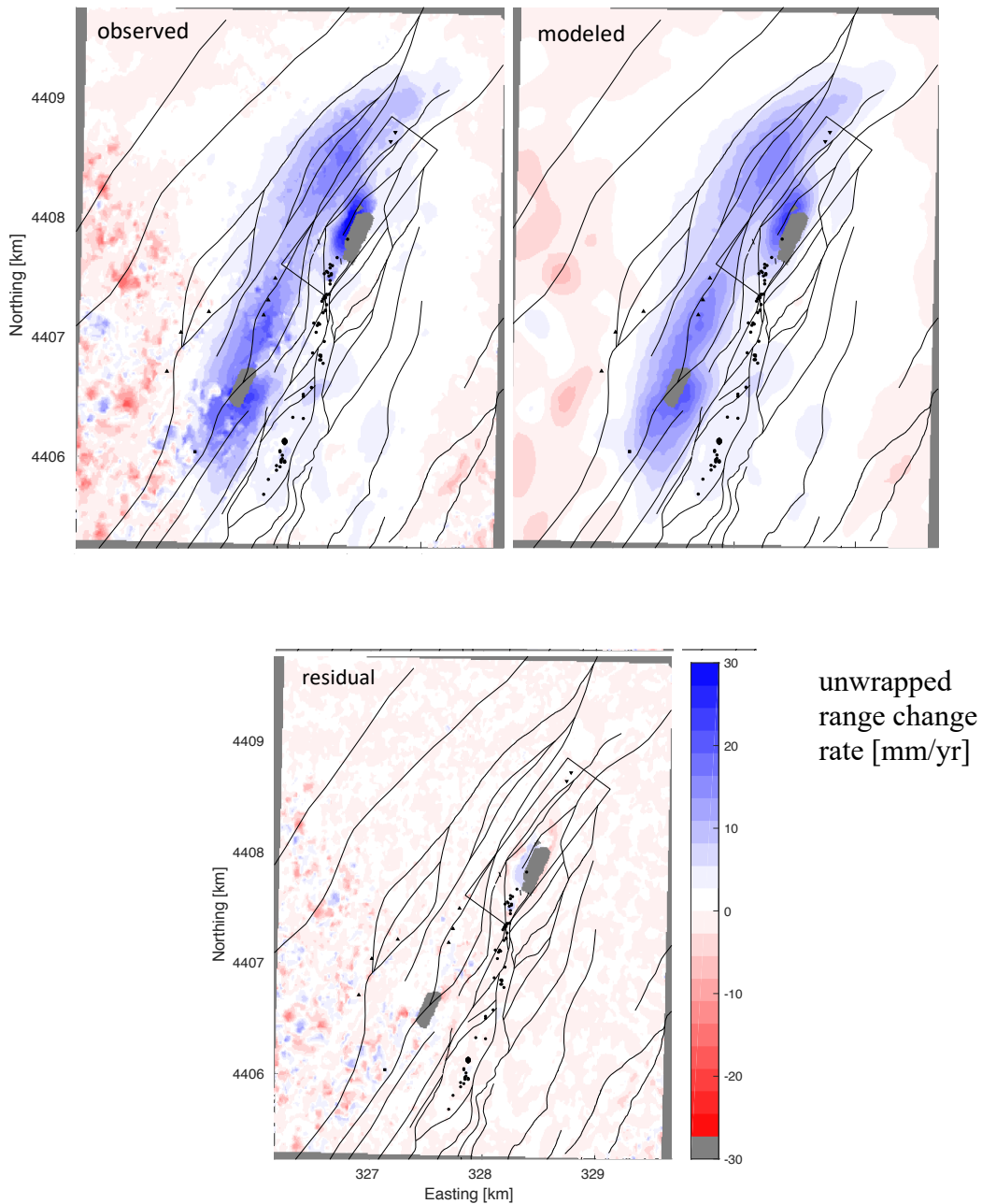


Figure 6.5. Figure 6 from Reinisch, et al. (2018) “Maps of deformation fields for linear, geostatistical inversion with a prior model defined in terms of thermal contraction. The observed deformation field with nuisance effects removed spans from 2016 July 22 to 2017 August 22 and is plotted as rate of range change. Modelled values of range change rate are calculated from best-fitting estimates using a temperature-defined prior model. Residual values are shown as observed minus modelled values.” [The blocked rectangular region represents the study area for the PoroTomo experiment. Injection wells are shown as inverted triangles, production wells are upright triangles and the stimulation well is denoted as a square. Faults are shown with black lines. Fumarole locations are denoted with circles. We use the UTM coordinate system.]

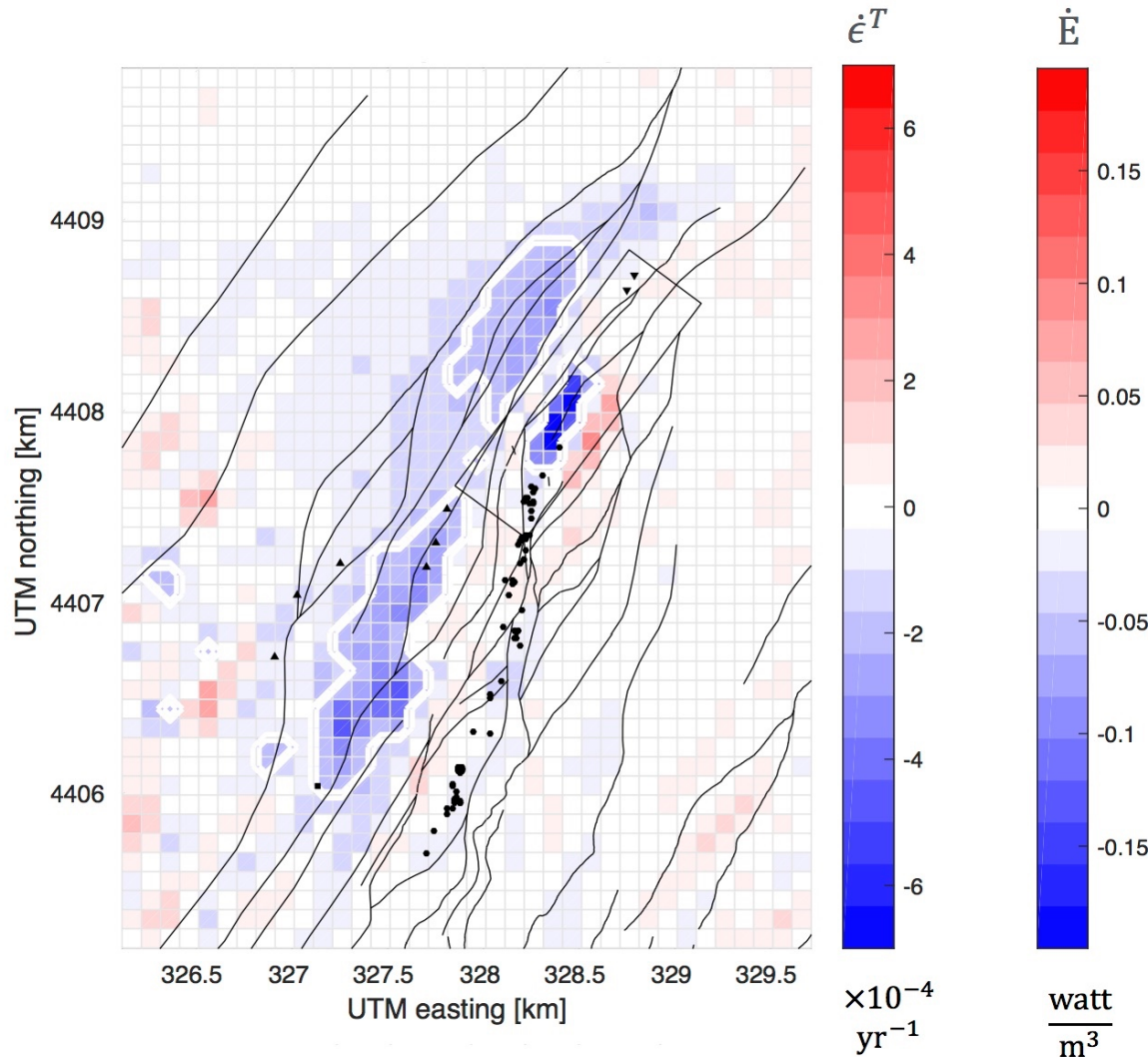


Figure 6.6. Figure 7 from Reinisch, et al. (2018) “Map of parameters estimated from a linear, geostatistical inversion using a prior model defined in terms of thermal contraction. The color of each square denotes the rate of change in a cube (with width $W = 100$ m) in the model. Estimates of $\dot{\epsilon}^{(T)}$ are shown in yr^{-1} . Estimates for thermal energy change rate \dot{E} are shown assuming $c_{\text{rock}} = 948 \text{ JK}^{-1}\text{kg}^{-1}$ and $\rho_{\text{rock}} = 2800 \text{ kgm}^{-3}$.” The white line bounds the region of the reservoir with a significant rate of contraction, as defined by equation (6.2). Other plotting conventions as in previous figure.

Hypothesis Testing

One benefit of the “multi-cube” parameterization is that it allows for direct characterization of subsidence in terms of volume change. Our goal with the “multi-cube” parameterization was to take this characterization further by defining what is the mostly likely driving mechanism for the observed subsidence. To do so, we performed our modeling using geostatistical inversion in a Bayesian framework (Reinisch et al., 2018). We hypothesize three different dominant geophysical mechanisms driving the observed subsidence: (1) thermal contraction of the rock

matrix, (2) a decrease in pore fluid pressure, or (3) a linear combination of (1) and (2). In the case of a decrease in pore fluid pressure, we interpret volume change in terms of a pressure change and thus the resulting volumetric strain rates are characterized as poroelastic volumetric strain rates. In the case of thermal contraction, volume change is related to temperature change and the resulting volumetric strain rates are thermal volumetric strain rates. The linear combination of thermal contraction and a decrease in pore fluid pressure results in volumetric strain rates that have both poroelastic and thermal contributions.

To determine the most reasonable interpretation of the observed volume change, we set prior models for each proposed type of volumetric strain rate based on prior studies. The prior uncertainties define the model covariance in each case, which is then used in the geostatistical inversion. After find best-fitting (posterior) estimates for each case of volumetric strain rate, we compare the posterior estimates to the corresponding prior model. If the hypothesized model agrees with the data, then the prior and posterior confidence bounds should overlap.

The results for our three interpretations of volumetric strain rate are shown as histograms in **Figure 6.7**. In the temperature-defined prior model, we see clear overlap between the prior and posterior models. This suggests that the observed volumetric strain rates at Brady may be reasonably interpreted as due to thermal contraction of the rock matrix. However, we see no overlap between the prior and posterior models in the case of the pressure-defined prior model. Moreover, the posterior model shows values much larger than what we considered to be reasonable values of poroelastic volumetric strain rates at Brady in our prior model. This suggests that the volumetric strain rates derived from the observed subsidence are too large to be attributed to a decrease in pore fluid pressure. We quantify these results through model comparison using Bayes Factor guidelines set by Kass & Raftery (1995). We find that Bayesian inference favors with “very strong evidence” thermal contraction over a decrease in pore fluid pressure as the dominant, driving mechanism of volume change.

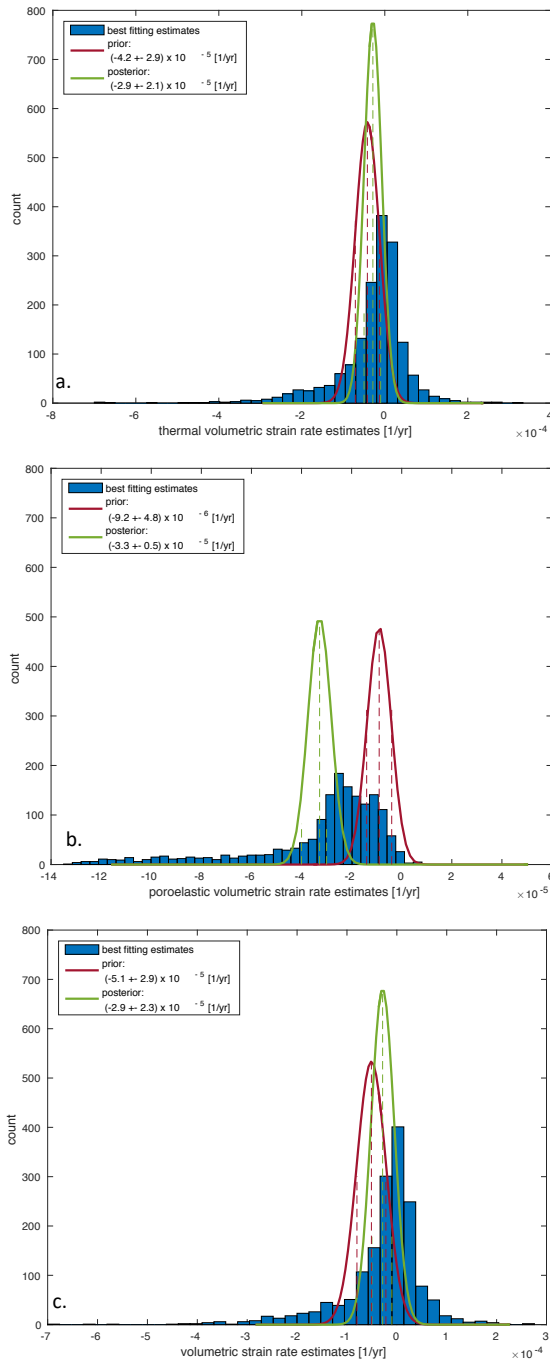


Figure 6.7. Figure 5 from Reinisch, et al. (2018) “Histogram of best-fitting estimates of volumetric strain rates for (a) temperature-defined prior, (b) pressure-defined prior and (c) prior combining temperature and pressure. Overlaid are posterior probability densities for both the prior (red) and posterior (green) models.”

Spatial and Temporal Analysis of Multiple Pairs

We expand on our deformation modeling by applying the “multi-cube” parameterization to a data set of pairs spanning from 2003 through 2018, as detailed in Section V.A.1. We select this data set by applying a minimum spanning tree (MST) algorithm using orbital separation as the weighting criterion (e.g., Reinisch et al., 2016). The resulting minimum spanning forest (MSF) dataset has 198 pairs. We then apply the “multi-cube” parameterization to arrive at estimates of thermal volumetric strain rates at Brady through 2018. Using temporal adjustment techniques (e.g., Reinisch et al., 2016), we perform time series analysis on each of the 1,656 cubes in the model, allowing for 1,656 separate time series of thermal volumetric strain at Brady. We consider different temporal parameterizations and find that while areas outside of the deforming region are suitably characterized by a single rate for entire time period, areas inside the deforming region require a piecewise-linear parameterization to capture the change in deformation rate during site shutdowns as determined using an F-test at 95 percent confidence (e.g., Wackerly et al., 2007).

Focus on Site Shutdowns

We also focus on detecting differences in deformation during Stages 2 and 3 of Deployment as well as February 22, 2018 to May 1, 2018, when the site was shutdown. We supplement with paired daily estimates of GPS data to increase coverage between satellite repeat times and perform a joint inversion of volume change rate estimates from both GPS and InSAR. We arrive at single estimates of volume change rate from InSAR pairs by summing individual volume change rate estimates for each cube that is in an area defined by rectangle at the center of the study region and oriented along strike with dimensions 3000 m long and 1000 m wide. This area includes the area of observed deformation (and significant volumetric strain rate). GPS estimates of volume change rate come from a cuboid parameterization where the cuboid has the same dimensions and location of rectangular region and has depth and height equal to the “multi-cube” parameterization used to model the InSAR data (100 m depth to the center of the cuboid with 100 m thickness). We perform temporal adjustment on the volume change rates estimated from GPS and InSAR using a piece-wise linear parameterization with breaks denoting the beginning and end of when well operations deviated from normal (Stages 2 and 3 of the Deployment period, February 22, 2018, and May 1, 2018). Results are shown in Figure 6.8 and Figure 6.9. We find a misfit of $\chi^2_{v,obs} = 2.5$. Using a Student’s T test at 95 percent confidence (e.g., Wackerly et al., 2007), we determine that there is a significant difference between volume change rates of consecutive stages with 95 percent confidence. Moreover, both shutdown periods show an increase in volume change, and the rates from Deployment period are consistent with concept of thermal contraction of the rock matrix as the dominant driving mechanism of the observed deformation.

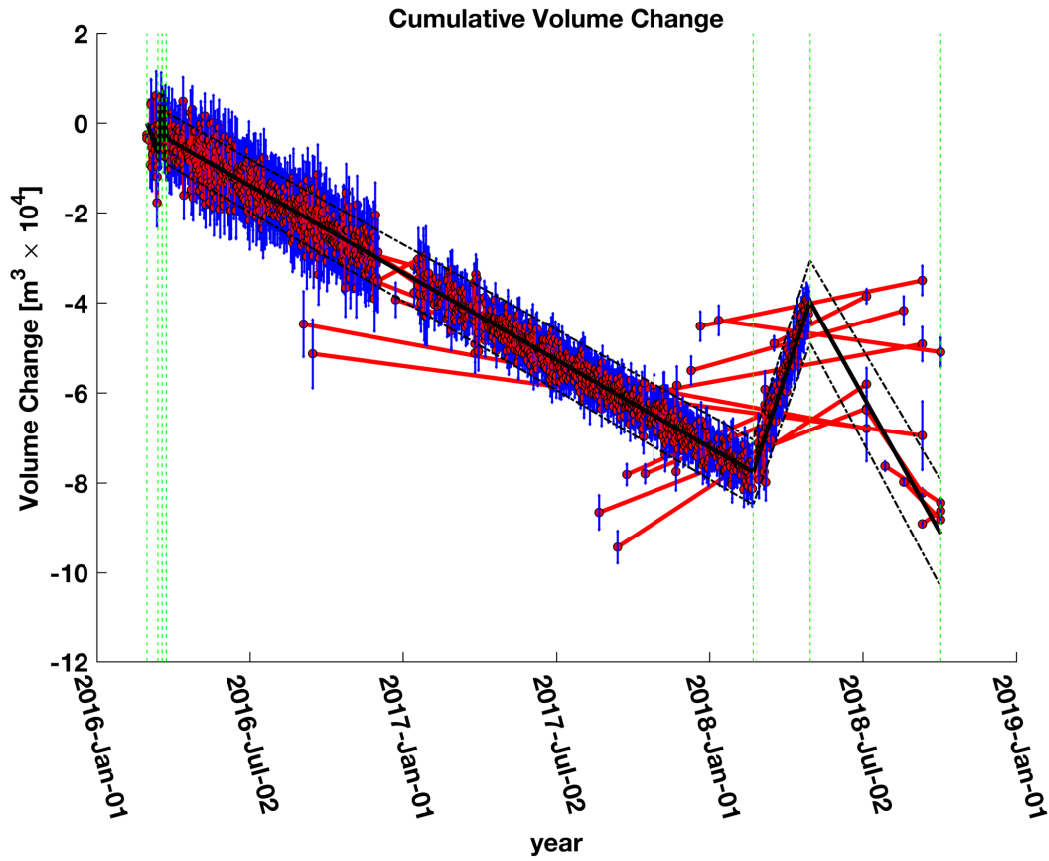


Figure 6.8. Time series covering the March 2016 deployment period and 2018 shutdown showing cumulative volume change over time from temporal adjustment of volume change rates estimated from InSAR and GPS data. Black lines show the modeled volume change with 68 percent confidence intervals (dashed lines) as estimated by temporal adjustment with a piecewise-linear temporal function with breaks at the start of each deployment stage. Red segments indicate measurements of observed volume change derived from individual geodetic pairs. For each pair, the volume change at the mid-point of each time interval is plotted to fall on the modeled curve and the vertical blue bars denote 1σ -measurement uncertainty, after scaling by the square root of the variance scale factor $\sqrt{\chi^2_{v,obs}} = 2.5$.

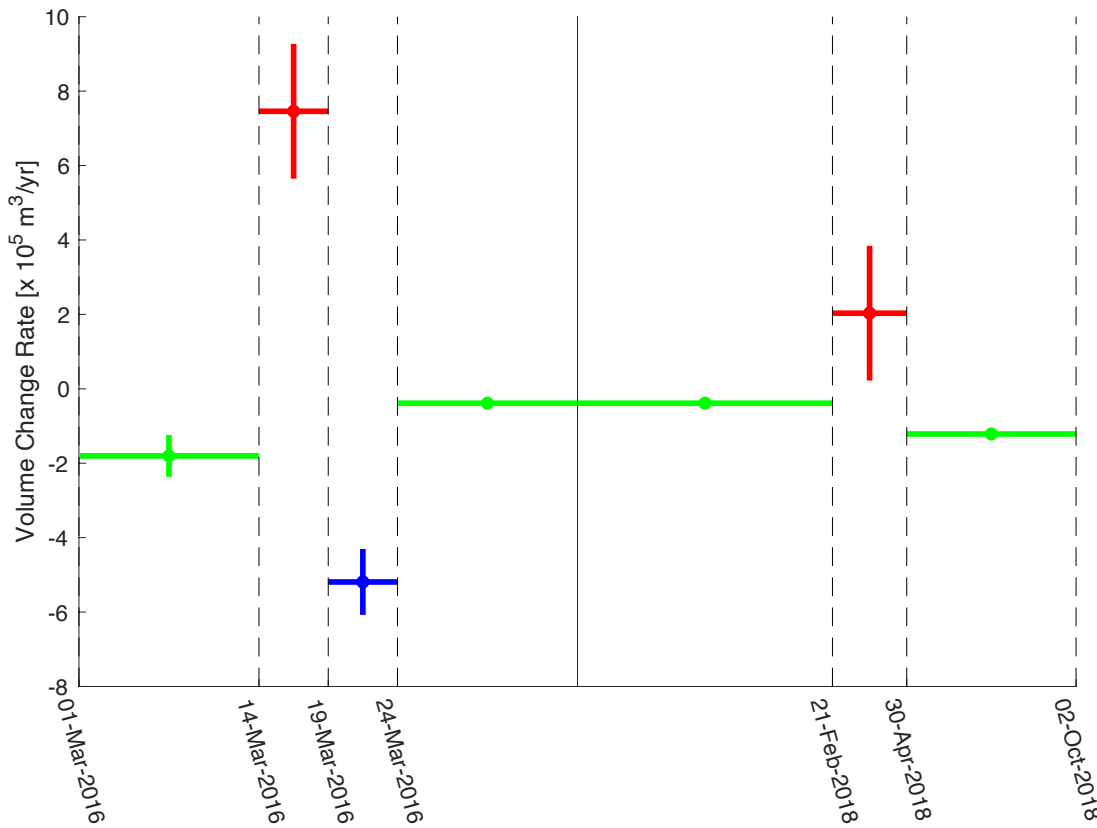


Figure 6.9. Estimated rates of volume change from the start of the March 2016 deployment period to 2018 October 2 after temporal adjustment of InSAR and GPS data using a piecewise-linear parameterization with breaks at the stage of each deployment stage and the 2018 shutdown. Rate estimates are shown as dots with vertical and horizontal bars denoting the uncertainty and duration of the stage, respectively. Dashed black lines denote breaks in the parameterization. Normal operations stages are shown in green. Red denotes when the site was shutdown (Stage 2 and the 2018 shutdown). Stage 3, when there was increased infield injection and pulsing, is shown in blue. The solid grey line denotes a break in the x axis.

B. Discussion

We found InSAR to be a valuable managing resource for Brady, similar to other studies at other geothermal sites (e.g., Eneva et al., 2018). It allows for long-term spatial and temporal coverage of the study area and can be acquired without visiting the field. While InSAR can only recover transient signals longer than 11 days (or the repeat cycle of the satellite in question), this limitation can be mitigated by supplementing with continuous GPS data. GPS data is also useful for validating the observed unwrapped range change rates from InSAR. Working with (unwrapped) range change rates and our “multi-cube” parameterization, we were able to directly interpret observed subsidence in terms of volume change. To mitigate the effect of unwrapping errors, we do not include range change values where the phase gradient is steep. In terms of deformation modeling, geostatistical inversion with a Bayesian approach helped us identify a dominant driving mechanism for subsidence and thus helped to further characterize subsurface processes at Brady. In addition to this spatial analysis, we found that performing time series analysis on results from our “multi-cube” modeling lead to a better understanding of temporal trends in subsidence and the concluded dominant driving mechanism of such subsidence.

C. Recommendations

The methods mentioned above are applicable to other geothermal sites after minor modifications. A GPS station in the actively deforming area is required for calibration and useful to illuminate transient deformation signals that InSAR cannot recover. SAR images provide the required spatial resolution for deformation modeling, with X-band (e.g., TerraSAR-X) data providing the clearest interferograms. While C-band (e.g., ERS-1, ERS-2) signals are still adequate, SCANSAR images (e.g., Sentinel-1 (Torres et al. (2012))) degrade the spatial resolution too much to be useful for analyzing geothermal processes in the subsurface. It is also useful to have a satellite with a short revisit time to capture transient signals. In addition, a large dataset of interferometric pairs is useful to allow for long time series analysis of deformation trends. The “multi-cube” parameterization can be adjusted in cube size and grid layer for spatial scalability. Spatial correlation parameters and prior models corresponding to the Bayesian, geostatistical inversion are also easily updated to reflect conditions at the site in question.

Section 7. Hydrology

A. Results

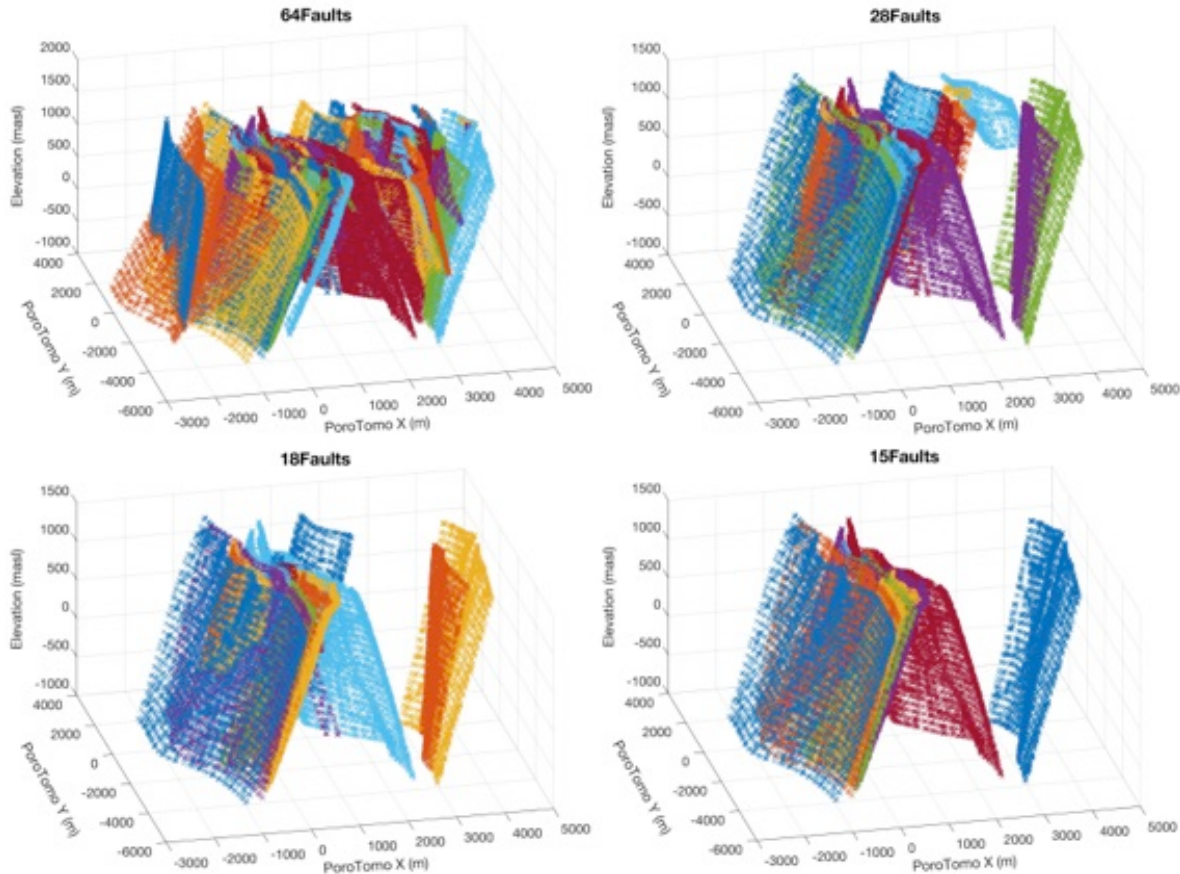
Hydrology research as part of PoroTomo focused on the analysis of down-hole pressure and temperature data to assess the hydraulic and thermal properties of the Brady reservoir. In addition, hydrology research focused on the correlation between observed reservoir pressure changes and other reservoir changes, such as temperature measured along distributed temperature sensing (DTS) fiber-optic cable, and the prevalence of micro-seismicity measured with both traditional geophones and distributed acoustic sensing (DAS) fiber-optic cable. Briefly, the results of these hydrogeologic investigations are as follows, and are discussed in further detail below:

1. *Characterization of Hydraulic Conductivity (K) Structure:* Through a combination of detailed pumping rate records provided by ORMAT, and the use of pressure sensors in multiple observational wells, we were able to select site conceptual models of K heterogeneity that are most consistent with observed data.
2. *Characterizing Rock Thermal Properties via DTS:* Through analysis of thermal recovery behavior following an injection of cold water into a Brady well, we were able to show how thermal properties of surrounding host rock can be characterized.
3. *Demonstrating DTS as a proxy measurements of wellbore flow and water level height:* Through a joint analysis of pressure data from traditional down-hole sensors and DTS temperature data, we were able to show how DTS data can be used both to assess water level height in a well, and to show dynamic processes such as flow along and out of the borehole.
4. *Assessing mechanisms for generating micro-seismic events during plant shutdowns:* By combining pressure data with measurements and timing of micro-seismicity before and throughout the PoroTomo experiment, we were able to describe a physical mechanism by which geothermal plant shutdowns can make micro-seismicity more likely. Similarly, our mechanism implies that long-term pumping at geothermal reservoir reduces seismicity while the site is operational, and improves predictability of seismic events.

Characterization of Hydraulic Conductivity (K) Structure:

At Brady, the availability of both flowrate data (i.e., hydraulic “sources”) and pressure measurements at multiple locations (i.e., hydraulic “receivers”) allowed us to apply heterogeneous numerical modeling to assess the likelihood of different “structured” models. The structural models investigated included cases where heterogeneous porous media flow dominated, cases where the contrast between fault zones and surrounding host rock represented the main source of heterogeneity, and cases where complex fault architecture consisted of fault cores surrounded by damage zone embedded in unfractured host rock.

Based on application of each of these conceptual models, we were able to discern that some of the structural models were not able to adequately reproduce the available pressure data from 3 wells. Based on the investigation of multiple model types, our best fit conceptual model for flow at Brady consists of complex fault zones consisting of 15 “Primary” faults, with both a central fault core and a surrounding rock damage zone. Our analysis (**Figure 7.1**) was able to show that conceptual models that included greater numbers of faults were not able to fit existing pressure data within the measurement error tolerance of ~1 m H₂O.



All Faults (64 Faults)			
Well	56A-1	81B-1	SP-2
MAE [m]	3.2	2.3	1.8
Φ [m^2]		142.8	
Primary, Secondary, and Tertiary Faults (28 Faults)			
Well	56A-1	81B-1	SP-2
MAE [m]	2.7	2.4	1.9
Φ [m^2]		144.4	
Primary and Secondary Faults (18 Faults)			
Well	56A-1	81B-1	SP-2
MAE [m]	4	2	1.4
Φ [m^2]		181.8	
Primary Faults (15 Faults)			
Well	56A-1	81B-1	SP-2
MAE [m]	1.4	0.4	1.4
Φ [m^2]		27.2	

Figure 7.1. Several conceptual models for fault networks at Brady (top), and associated misfit (Mean Absolute Error, MAE) to pressure data from individual wells. Adapted from Patterson (2018)

The hydraulic characterization at Brady was aided substantially by existing structural information supplied by field geologists. In cases where few observation locations for pressure observations are available, this “structural” approach to characterization is most likely to result in realistic images of hydraulic parameter heterogeneity. However, if more detailed and comprehensive measurements of pressure within a reservoir are available, truly “tomographic” methods, i.e. hydraulic tomography, can be applied in which hydraulic data is used to image heterogeneity within an unstructured model. This type of characterization was demonstrated, for example, based on data from the Boise Hydrogeophysical Research Site (Cardiff et al. 2012).

Given the immense parameter space for hydraulic conductivity variations (roughly 13 orders of magnitude), and its drastic influence on the shape and connectivity of subsurface conduits for heat flow, investing more heavily in instrumentation to detect pressure changes at multiple points within a reservoir (e.g., via packer strings within monitoring wells) represents a prime opportunity for improving characterization of geothermal sites.

Characterizing Rock Thermal Properties via DTS

Installation of the vertical DTS cable in a well at Brady required that cold water be added to the well for safety. Wellbore response following this cold-water injection was closely watched and was used to analyze the thermal properties of surrounding host rock. Because the wellbore was cased throughout the interval analyzed, the primary mechanism for heating of the wellbore is thermal diffusion from the surrounding formation. By analyzing this data on an elevation-by-elevation basis, we were able to estimate thermal diffusivity for the surrounding host rock, which helps to constrain how effectively heat can transmit through the host rocks at Brady. **Figure 7.2** displays the raw DTS temperature data from Brady as well as the associated parameter estimation results, demonstrating that changes in thermal diffusivity largely corresponded with changes in rock type (Patterson et al., 2017).

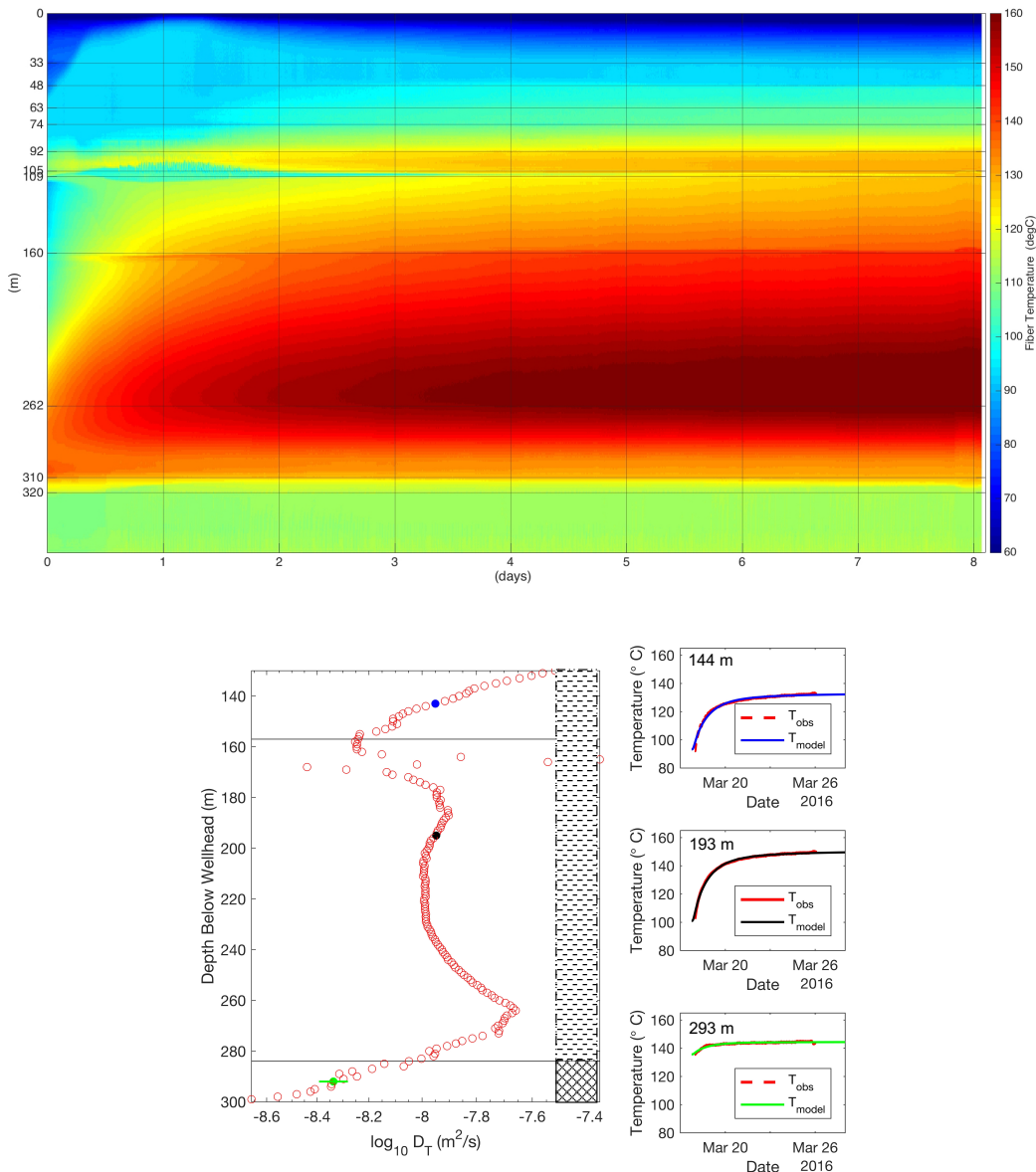


Figure 7.2. DTS data from Brady and associated parameter estimation. Top: Warming of borehole following injection of cooled water is apparent throughout the testing period. Data from individual depths was fit by estimating local rock thermal diffusivities. Bottom: Parameter estimation results showing thermal diffusivity estimates (left) and example fits between field data and numerical model (right). Adapted from Patterson et al. (2017).

Demonstrating DTS as a proxy measurement of wellbore flow and water table height

Some segments of the vertical DTS (DTSV) data collected showed interesting “pulsing” behavior that occurred only during the time period when the Brady site was online. Through comparison with hydraulic data sources, we were able to show that pulsing and temperature changes represent water exiting the cased wellbore through its screened bottom, which led to a

drop in the well water level. An example comparison demonstrating how DTS data can show signatures of water level changes is shown in **Figure 7.3**.

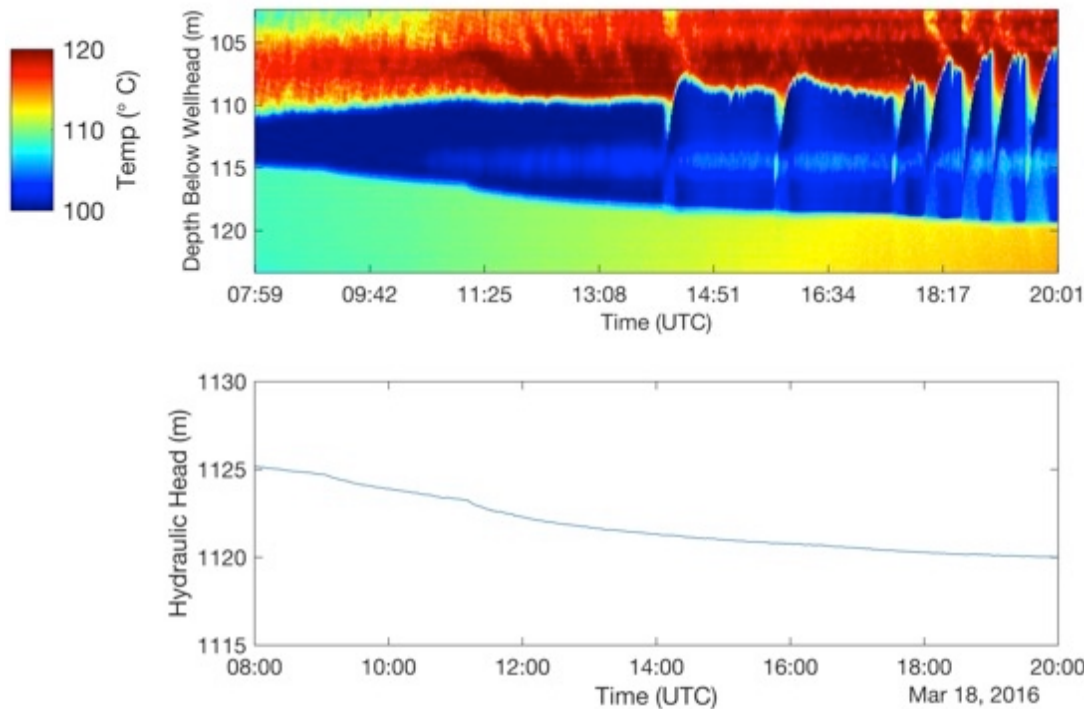


Figure 7.3. Comparison between DTS temperature record (near 110 m depth) and measurements of pressure (head) changes at another nearby observation well. The response of the temperature interface at 115-120 m depth closely mirrors the observed pressure changes during the testing period.

Assessing mechanisms for generating micro-seismic events during plant shutdowns

Long-term records of extraction rates and micro-seismicity at Brady had shown a significant correspondence between times when the site was shut-down and timing of micro-seismicity (**Figure 7.4**). Locations of micro-seismicity measured via these long-term records also indicated that the micro-seismicity tended to occur near faults penetrated by pumping (extraction) wells, and at similar depths (**Figure 7.5, left**). Still, to date no mechanism had been suggested for the cause of these microseismic events.

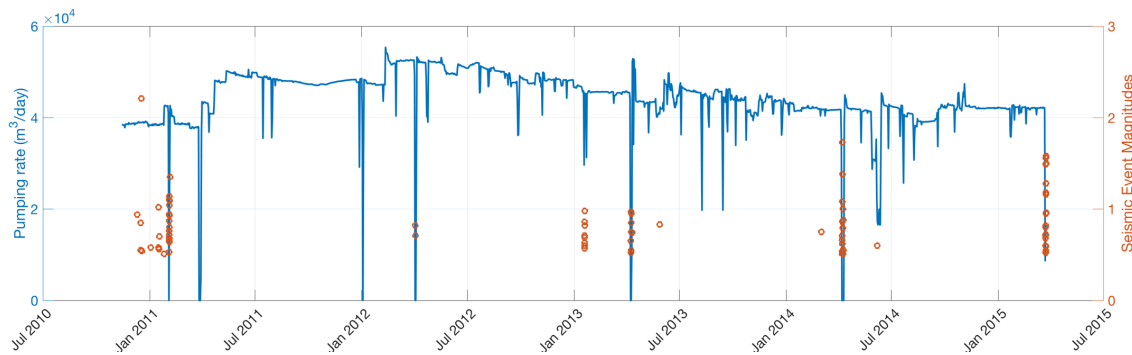


Figure 7.4. Correlation between pumping rate (blue curve) and microseismic events (red points). Most microseismic events correspond with periods when the plant is shutdown.

Locations of seismic events likewise indicated that they occurred primarily in the vicinity of the depths of extraction wells (Cardiff et al., 2018).

Several small micro-seismic events were detected during the period of the PoroTomo study (the purple points in **Figure 7.5**, left) Based on the hydraulic characterization data, and estimates of reservoir flow parameters, we were able to model the propagation of pressure changes within the Brady reservoir following site shut-downs, using a simplified analytic model. These models demonstrated that, at the times of the micro-seismic events, site shutdowns would lead to pressure increases along faults penetrated by pumping wells, with a magnitude of roughly 0.1 MPa (**Figure 7.5**, right). Given that pressure changes of this magnitude have often been discussed as “triggering thresholds” for induced seismicity, the increase in overall pressure following the cessation of pumping represents a plausible triggering mechanism for seismic events. Conversely, the long-term pumping at Brady can be seen as restricting seismicity, and the ability to predict micro-seismic stress releases during site shutdowns may help limit any risk associated with these small events (Cardiff et al., 2018).

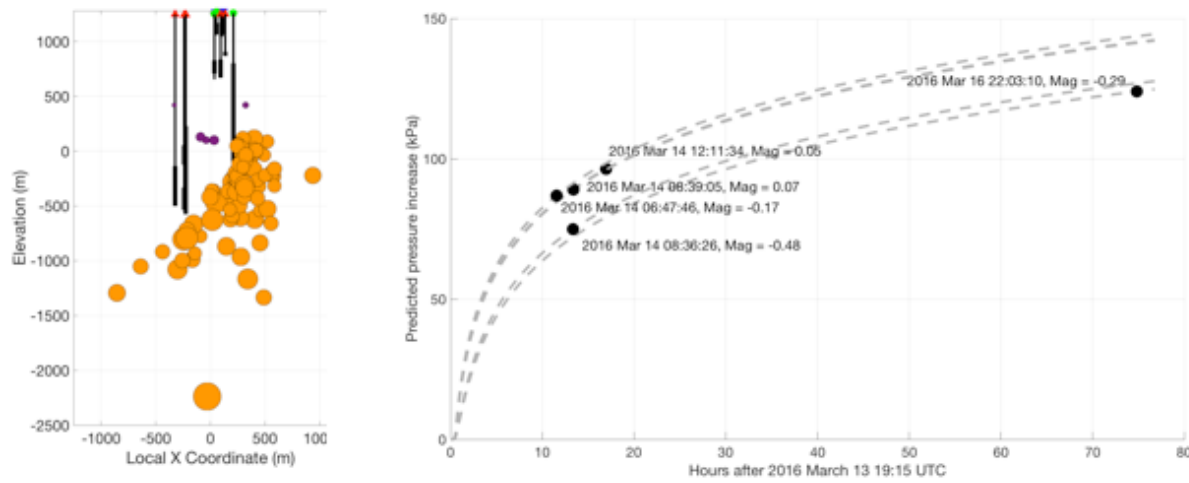


Figure 7.5. (Left) Long-term seismic event catalog showing seismic events recorded at Brady before (orange circles) and during (purple circles) the PoroTomo experiment. (Right) Simulation of pressure changes following site shutdowns based on estimated flow-rate changes and aquifer hydraulic parameters. Adapted from Cardiff et al. (2018).

B. Discussion

The ability of hydraulic measurements (i.e., measurements of flowrates, pressures and temperatures) to provide information about critically-important reservoir properties – including permeability, porosity, and thermal properties – has been used by site managers often to allow basic initial characterization of geothermal resources. Often, this is done through basic single-well tests that can assess the overall / average hydraulic properties of a site. Commonly, these tests are analyzed using simple analytical models that assume homogeneous reservoir properties and do not take into account reservoir structure measured via other methods.

In this project, we used more modern numerical methods in order to develop a site conceptual model that explicitly includes heterogeneity in these key properties. In addition, pressure data was collected jointly alongside other measurements and examined within a spatio-temporally consistent database. This allowed a more in-depth evaluation of reservoir properties, while also allowing us to assess processes that resulted from interacting physical phenomena (e.g., induced micro-seismicity).

C. Recommendations

In the case of the PoroTomo project, hydraulic data provided a critical resource in that it: 1) provides independent information on reservoir hydraulic and thermal properties as a baseline against which other geophysical inversion results can be assessed; and 2) allows investigation and explanation of “multi-physics” coupled processes that occur in geothermal reservoirs (e.g. thermal/hydraulic coupling associated with movement of heat in wellbores, and hydraulic/mechanical coupling associated with induced microseismicity). Indeed, any assessment of the value of geophysical information strongly benefits from detailed hydraulic characterization data be collected alongside, to provide validation of geophysical imaging or predictions.

We suggest that in future investigations, the following actions be taken in order to improve hydraulic characterization of geothermal reservoirs.

1. *Changes & Improvements to hydraulic monitoring via detailed records, packer use, and DTS:* More accurate and more detailed hydraulic data, via both measurements of sources of hydraulic changes (i.e., well records), and novel monitoring (multi-level pressure installations, DTS)
2. *Multi-frequency oscillating pumping tests to improve resolution of hydraulic parameters:* Expanding the use of oscillating pumping to take advantage of characterization information associated with multi-frequency pumping.

We expand on these suggestions below.

Changes & Improvements to hydraulic monitoring via detailed records, packer use, and DTS

During future geothermal investigations, the amount and quality of hydraulic data collected can be improved by:

- Detailed coordination before any changes to site operations such that pumping flowrates and temperatures are recorded: 1) at all wells; 2) continuously throughout the site history; and 3) with high accuracy. In particular, long-term extraction records are vital for modeling the continuous process of heat propagation within the geothermal reservoir.
- Gaining the most possible information from available (expensive) wells by using packer strings to collect vertical pressure information.
- Instrumenting multiple wells with distributed temperature sensing (DTS) equipment such that water level changes and within-wellbore flow can be assessed spatially.

Multi-frequency oscillating pumping tests to improve resolution of hydraulic parameters

Oscillating pumping tests can take place via many methods – either by alternately injecting and extracting water from a reservoir, or by slightly perturbing long-term flowrates upwards and downwards (as was done during the PoroTomo field campaign). While oscillatory changes to flowrates were detectable during the PoroTomo experiment, their benefit as a characterization method has not yet been fully realized in geothermal characterization.

Oscillatory changes to flowrates, as one type of periodic stimulation, are extraordinarily non-invasive to perform (simply alter flowrates above and below long-term average pumping that is desired), and similarly produce highly identifiable signals that are valuable in noisy, operational sites such as active commercial geothermal reservoirs.

As is clear in many other geophysical fields, the value of information from many frequencies of stimulation (e.g., a spectrum of seismic wave frequencies) is greater than that from only a single frequency. Recent research has similarly demonstrated the degree to which oscillatory pumping tests over multiple different frequencies can improve characterization of reservoir heterogeneity across various scales. Because of the short duration of the “flooding” stage of the PoroTomo experiment, only one frequency of 12-hour pumping oscillations was implemented. In longer-term operations, several pumping frequencies can be implemented which has been shown to improve resolution of hydraulic properties.

Section 8. Value of Information

A. Results

Value of Information (VOI) theory provides a powerful framework for determining the utility of additional information when making decisions with uncertain outcomes. The VOI metric can be the potential to be extremely useful for subsurface characterization, since new data collection is often expensive and its efficacy is uncertain. The Value of Information focused on the vertical distributed acoustic sensing (DAS) data. A synthetic analysis, which did not incorporate data, was performed to evaluate if DASH could supplement the geophones, which were sparsely spaced for reverse-time migration (RTM) modeling. The VOI method accounts for this uncertainty through the reliability,

$$Pr(\Theta = \theta_i | \Theta^{int} = \theta_j) = \frac{Pr(\Theta = \theta_i) Pr(\Theta^{int} = \theta_j | \Theta = \theta_i)}{Pr(\Theta^{int} = \theta_j)} \quad i, j = F, NF \quad 8.1$$

where Θ can represent the actual occurrence of a structure in the subsurface and Θ^{int} represents the interpreted structure from the proposed (geophysical) data. For the purposes of our VOI problem definition, the fault locations are the decision variable Θ . Specifically, for the PoroTomo example, the reliability will quantify how often the interpretations of faults θ_j^{int} align with the actual presence of faults $\theta_{i=F}$ and vice versa. Faults are important structures for geothermal systems: they often provide fluid conduits for both upward and downward circulation, allowing for production and recharge of geothermal fluids (Folsom et al., 2018). Therefore, at each location within a migrated image, there would be either a fault (F) or absence of a fault (NF). The reliability is a conditional, or posterior, probability which summarizes how frequently the interpretations from geophysical information align correctly or incorrectly with actuality and can be thought of as capturing the "imperfection" of the information being considered.

Value of information calculates the difference of two expected values: the average utility of the decision made with only the current information (the prior value V_{prior}) and the average utility of the decision made with the additional, yet imperfect, information: value with imperfect information

$$V_{imperfect} = \sum_{j=N,NF} Pr(\Theta^{int} = \theta_j) \max_a \left[\sum_{i=F,NF} Pr(\Theta = \theta_i | \Theta = \theta_j) v_a(\theta_i) \right] \quad 8.2$$

where the reliability (Equation 8.1) acts as a weight on utility outcomes (v) from different decision alternatives (a , e.g. drill or don't drill), as represented by $v_a(\theta_i)$ (Trainor-Guitton et al., 2015). To observe if there is value to using DAS, reliabilities (Equation 8.1) would need to be calculated to get $V_{imperfect}$'s. The focus of our work is to quantify the reliability or the posterior probability for seismic images created with DAS, not on the utility outcomes (v) or possible alternatives (a), although these can greatly influence $V_{imperfect}$ as well.

A geologic model of Brady Natural Laboratory (**Figure 8.1**) was used as an a priori fault location model (Siler et al., 2016). Imaging of both synthetic and field data was performed to analyze if certain fault dips and strikes would be detectable given the geometric configuration of seismic sources and receivers. Reverse time migration was utilized to construct a 3D model of reflectivity from the observed DASV data. All migration algorithms (reverse time migration here) image single scattering events, either reflections or diffractions. These algorithms are based

on the Born approximation and decompose the medium into a background model responsible for travel time (i.e. velocity), and a perturbation model responsible for the reflections and diffractions (i.e. reflectivity) (Woodward, 1992).

Coherent structures exist within the images that are consistent with three faults: the fault farthest from the DAS well at distance of 750 m to the northeast, and two Western-dipping faults below the well that contains the DAS. Convolution Neural Networks (CNN) were used to obtain an agnostic, quantitative measure of the reliability of detecting faults from images derived from DAS. A transfer learning approach utilized layers of convolutional neural networks trained on the ImageNet repository.

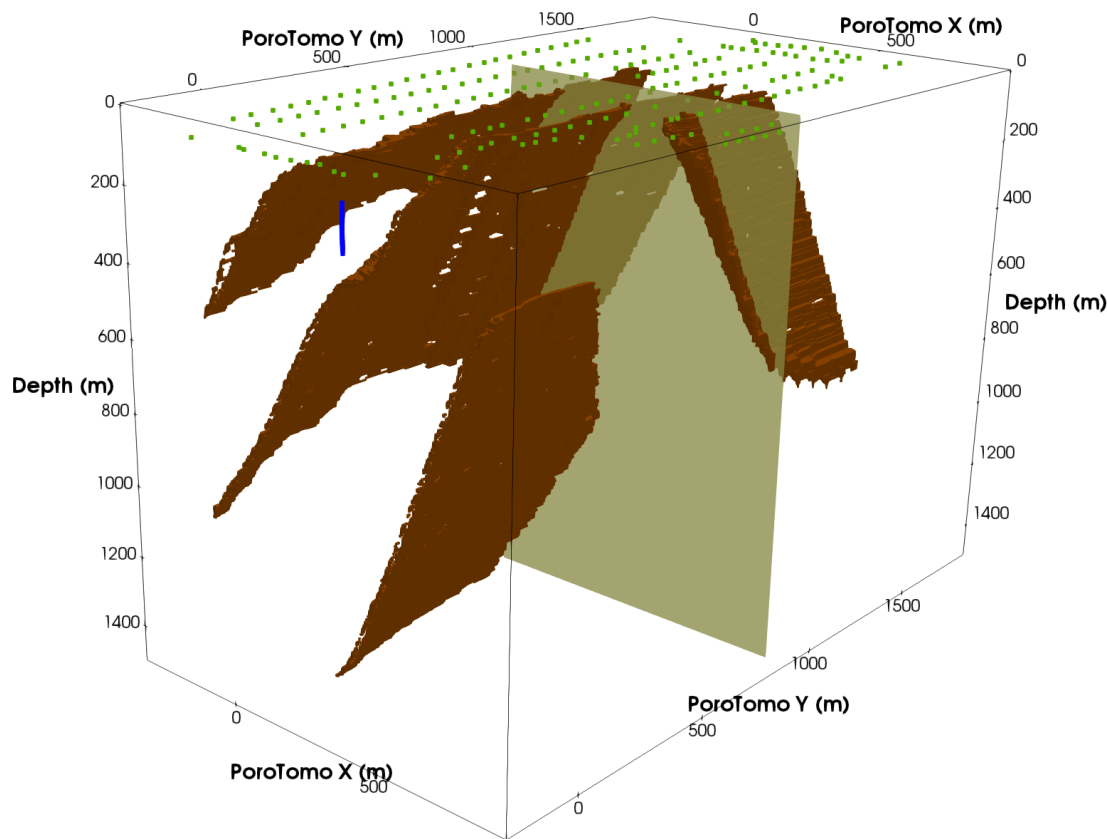


Figure 8.1. Fault model from Siler et al. (2016) with DASV (blue) and sources (green) locations.

Three PS (P-wave velocity for down-going and S-wave velocity for up-going) images (**Figure 8.2**) discern the middle of the Western-dipping and the far Eastern-dipping faults (~1 km away). The first image utilizes the receiver wavefield from the synthetic model, the second is the actual DASV observed data from PoroTomo and the last uses pure noise. The pure noise result confirms that the structure that is consistent with the middle west dipping fault is not migration artifacts.

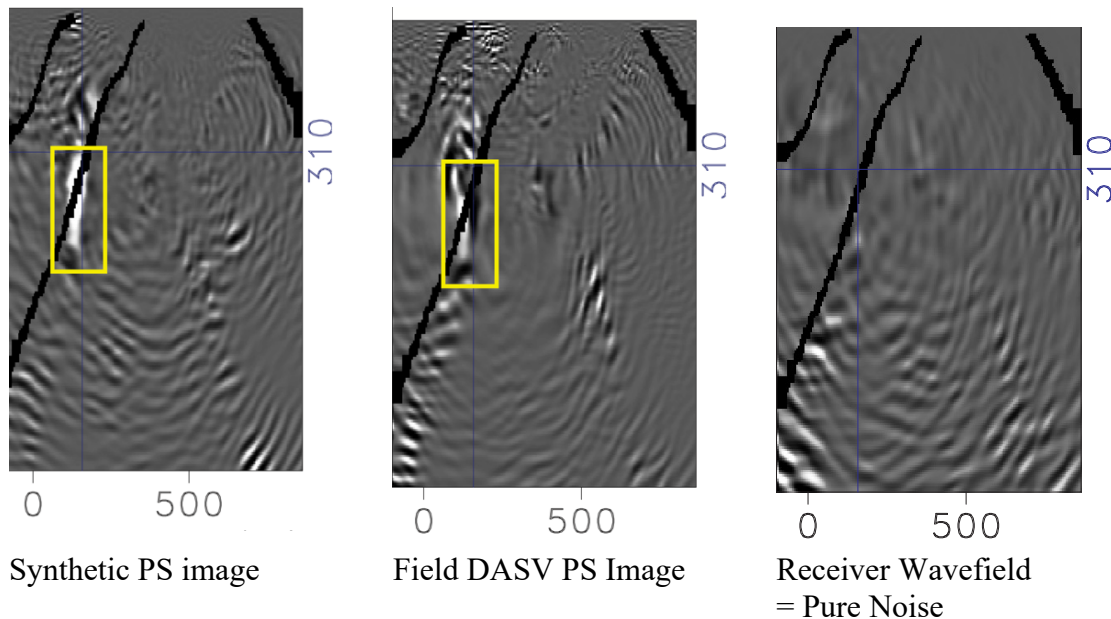


Figure 8.2. Slices of RTM's at intersection with Well 56-A1 (Trainor-Guitton et al., 2018a, 2018b). The slice is the same slice as in Figure 8.1.

We used the Inception-v3, a pre-trained CNN model, on our fault imaging application to obtain Bayesian statistics of the information content (Szegedy et al., 2015). We can take advantage of the CNN to detect edges, shapes, and other high-level features to help with classifying fault versus not fault in our noisy images. To add training and testing images specific to this classification problem, 2D slices were scanned with a 10 by 10 template but then resampled to the size (299x299) expected by the Inception-v3 software. Using the Brady fault model, the training data were classified as fault or no fault.

Figure 8.3 is the Bayesian confusion matrix of the synthetic DASV. This is the “best possible” fault detection statistics given the acquisition geometry since there are no noise sources and RTM was performed using the right velocity model.

		Predicted (<i>Interpreted</i>) Θ_j	
		Fault	No Fault
	Fault	470 (70.0%)	616 (34.8 %)
	No Fault	201 (30.0%)	1,155 (65.2%)

Figure 8.3. “Best” confusion matrix given source-receiver geometry, assuming Siler et al. (2016) as correct labels

B. Discussion

This imaging combined with CNN modeling was applied to the DASH scenario, to assess if the horizontal DAS could add value to sparse geophones (Jreij et al., 2018). This study used purely numerical modeling of the PoroTomo geometry and not the DASH data because the

DASH data were challenged by statics. Expertise and resources were not available to process this data sufficiently.

For DASV, the training sets were generated by comparing locations of the “fault” and the collocated patterns in the RTM image. For thick “faults”, the middle of the fault does not present any contrast or reflectivity, and thus will not produce a coherent event in the RTM image. However, this location will be classified as a fault. Thus, to improve this training, a gradient of the reflectivity should be used instead. This may align better in space with the RTM events that are consistent with fault reflectivity. Future work will improve the classification, and also investigate the inline 2D sections of the Brady fault scenario.

It’s remarkable but not unheard of that the uncoupled cable is able to pick up signal from fault almost 1 km from Well 56-A1. Lindsey et al. (2017) demonstrated how earthquakes are detectable by fiber imperfectly coupled to the subsurface.

C. Recommendations

Forward modeling of wave fields in combination with convolutional neural networks classification would optimize the locations of source and receiver in a proposed deployment.

Deploying DAS vertically in a borehole avoids the issue of “statics” encountered when analyzing images from a DAS array deployed horizontally.

To best use imaging methods, the project budget and personnel should include resources for noise removal and processing. Doing so would improve the quality of the images calculated from the vertical DAS images and increase the usefulness of the horizontal DAS data.

Images calculated from DAS data may be even better with cable coupling devices installed (e.g., Munn et al., 2017)

Section 9. Fiber Optic Technologies

A. What Is DAS/DTS?

DAS is Distributed Acoustic Sensing. In DAS continuous analyses of local variations of the (Rayleigh) backscattered signal from successive incident pulses generate a continuous dynamic strain recording along the fiber.

DTS is Distributed Temperature Sensing. In DTS the forward propagating light generates inelastic (Raman) backscattered light at two distinct wavelengths. The temperature profile is calculated from the ratio of intensities of the two wavelengths.

B. DAS vs Traditional Seismic Instruments

Regional Earthquake Recordings

In general, the physics of ground motion measured by DAS and geophones were confirmed (Wang et al., 2018). Both DAS and geophones showed highly similar P- and S- waveform traces from the $M_L = 4.3$ Hawthorne earthquake whose epicenter was 150 km away (**Figure 9.1**). However, the signal-to-noise ratio (SNR) of a single DAS channel was generally lower by a factor of two when compared to geophones at earthquake body-wave frequencies of a few hertz. The SNRs of both DAS and geophones varied with local geological heterogeneity. The SNRs measured for the Hawthorne earthquake at Brady were better than observed for active sources.

The Hawthorne earthquake was also recorded by cable in Well 56-1 (Miller et al. 2018). The coherent signal is clear only in the interval from 160 m to 300 m (**Figure 9.2**). The apparent velocity (2 km/sec) is consistent with propagation seen in near-offset recordings of active-source (Vibroseis) signals.

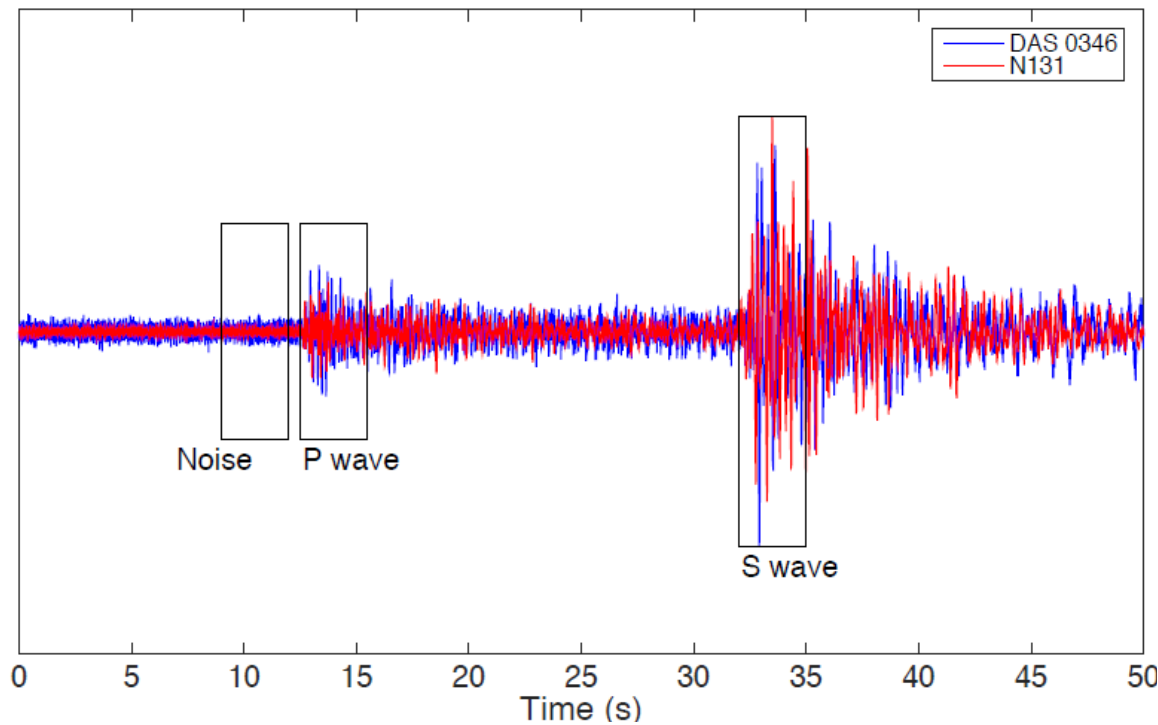


Figure 9.1. Example comparison of normalized DAS strain rate (blue) and raw geophone coil-case velocity (red) records for March 21, 2016 Hawthorne earthquake. Boxes show the two-second time windows that were used to obtain noise and signal for P and S-wave arrivals. The geophone record was scaled to match its peak amplitude to that of DAS.

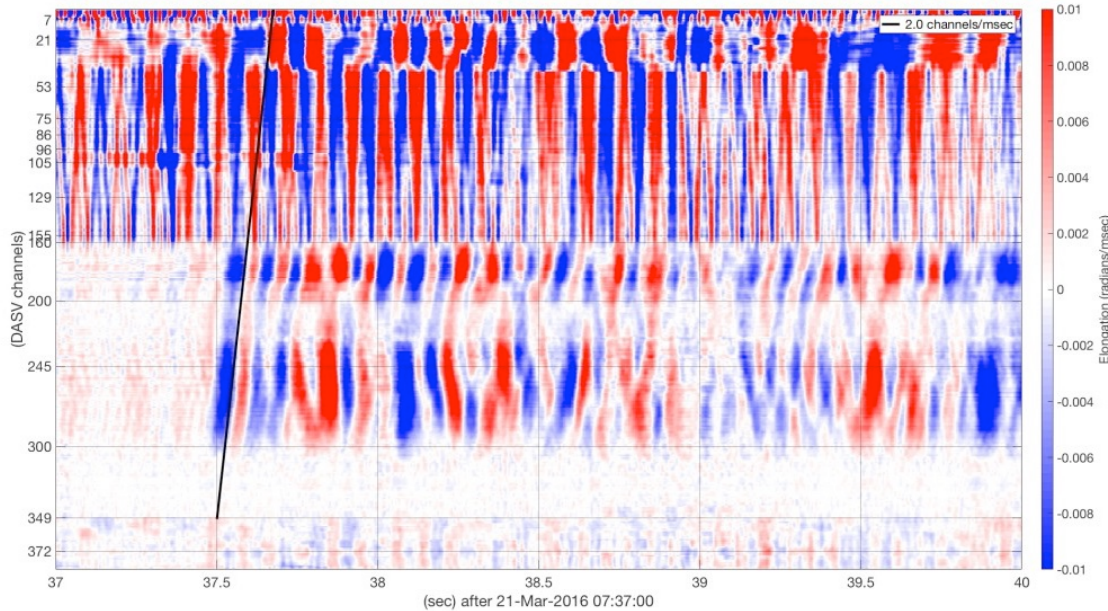


Figure 9.2. Hawthorne earthquake arrival on DAS cable hanging in Well 56-1.

Local Site Heterogeneity

DAS amplitude theoretically varies as the cosine squared of the angle between the particle motion and the cable direction. However, the high correlation between its amplitude and contours of the SNR of the east component of geophones (**Figure 9.3**) rather than with cable direction implies that DAS amplitude is controlled mostly by site effects (Wang et al., 2018). Variation of coupling of cable with ground motion is likely present as well.

Figure 9.4 shows waveforms that are the result of correlating the recorded source sweep with DAS strain recorded in Well 56-1 and averaging over repeat sweeps at the same location using 1D P- and S-wave velocity models (Miller et al., 2018). The PS reflection is strongly evident for SP 125 and absent for SP 199. It is possible that the strong downgoing event that is about 100 ms after the indicated direct S is the “true” direct S and that the label matches a downgoing shear converted at a near-vertical interface (fault or fracture) that more strongly affects SP 125 than SP 199.

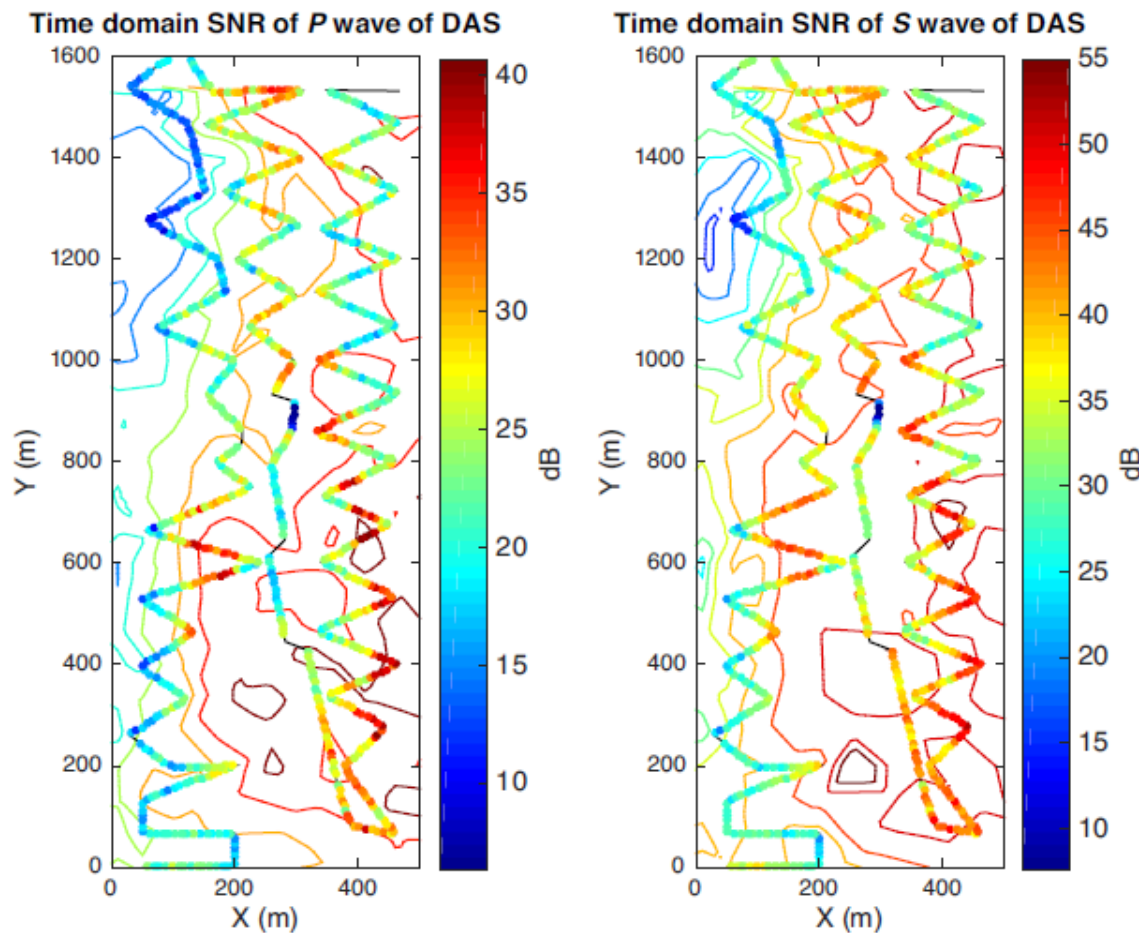


Figure 9.3. Time-domain DAS and geophone SNR map for (a) P-wave arrival and (b) S-wave arrival. Dots are the SNR of every 10th DAS channel and contours are based on the SNR of the east component of geophones, which is a good approximation of site effects.

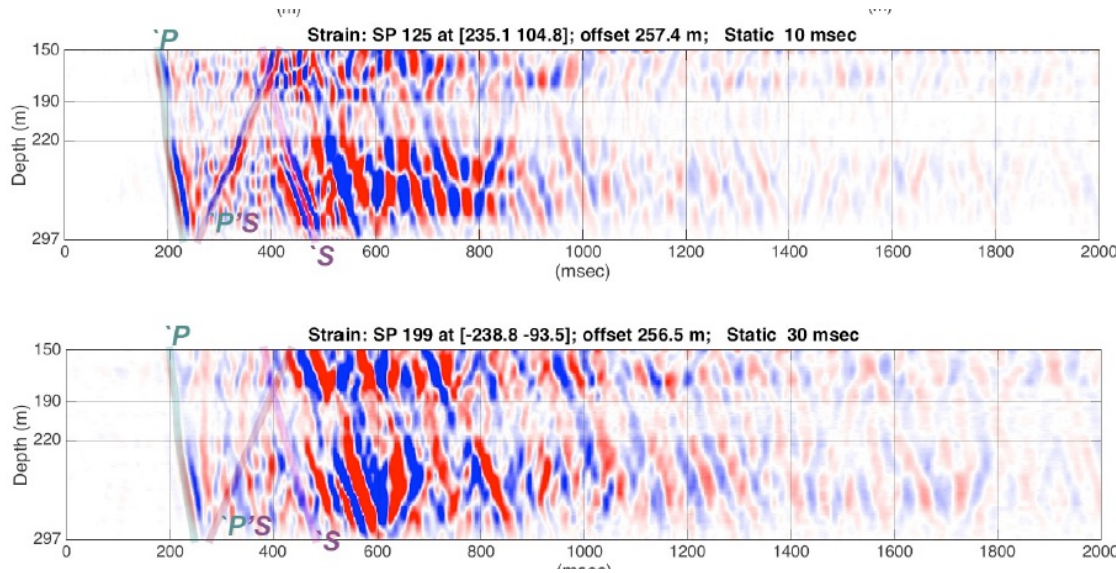


Figure 9.4. Processed DAS strain recorded in the vertical fiber-optic cable in Well 56-1 for Shot Points (SP) 125 and 199 at similar offsets but on opposite sides of Well 56-1. Each data panel is annotated with direct (downgoing) P, direct (downgoing) S as well as a PS reflection from an interface at 320 m. The coordinate system for shot points is centered at the 56-1 wellhead.

Synthetic Strain Seismograms

Synthetic strain seismograms can be a useful tool to provide a controlled baseline for first-order comparisons (Wang et al., 2018). Synthetic strain seismograms were computed from Green's functions for the moment tensor solution for the Hawthorne event. Comparisons of DAS and geophone waveforms were made for a segment of fiber that is approximately aligned with the back azimuth to the earthquake (Figure 9.5). The comparison shows that DAS has significant potential for contributing to seismic array analysis of regional earthquakes.

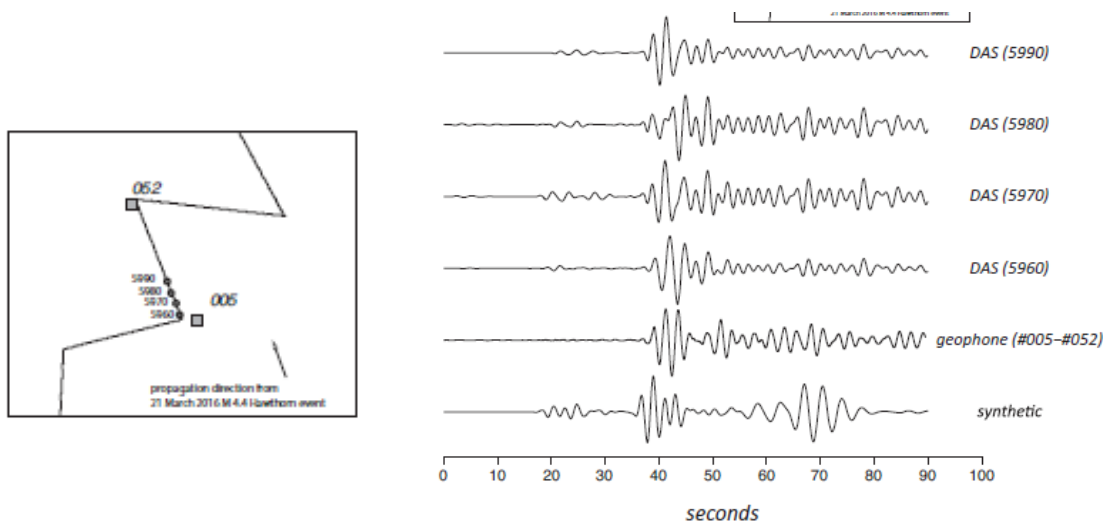


Figure 9.5. Comparison of synthetic strain seismogram, DAS channels, and geophones. Waveforms from four DAS channels were selected and integrated to yield strain. Waveforms from two geophones, which are approximately co-located at the ends of the cable segment, were rotated and integrated with respect to time to obtain displacement and differenced with respect to space to provide a strain estimate.

C. Traffic Monitoring

The distributed nature of DAS arrays allows for the monitoring of long pieces of infrastructure (e.g., road, railways, pipelines). We used data collected in the deployment at Garner Valley and at Brady Hot Spring to evaluate the capability of DAS and its high-density sensor configuration to passively monitor traffic (Lancelle 2016; Fratta et al. 2017) and to actively use traffic as a source of seismic waves for near-surface imaging (Zheng et al. 2017).

Figure 9.6 shows the location and configuration of the array DAS array deployed in Garner Valley, CA. This site host the Garner Valley Downhole Array operated by University of California Santa Barbara. The deployed 750-m long array had one length of fiber parallel (just South of the right of way) to California Highway 74. We used this section to monitor traffic and speed of the passing vehicles. Using the response of the channels in the straight section, we were able to track both the speed and the direction of the vehicles (**Figure 9.7**; Lancelle, 2016). The figure plots the DAS-captured signals of five passing vehicles in both directions. The slopes formed by the vehicles following the traffic moveout were used to calculate the speed of the vehicles (shown with red dashed lines). Note that the signals from the vehicle traveling in the East-West direction appear with lower strain rates amplitudes than the signal going in the West-East direction. Also, the traces presented in the 630-640 seconds time interval are longer than the other traces. These data appear to indicate that the longer signal corresponds to two vehicles traveling close together in the same direction. These results hint at the capability of DAS for the monitoring of traffic and traffic patterns.

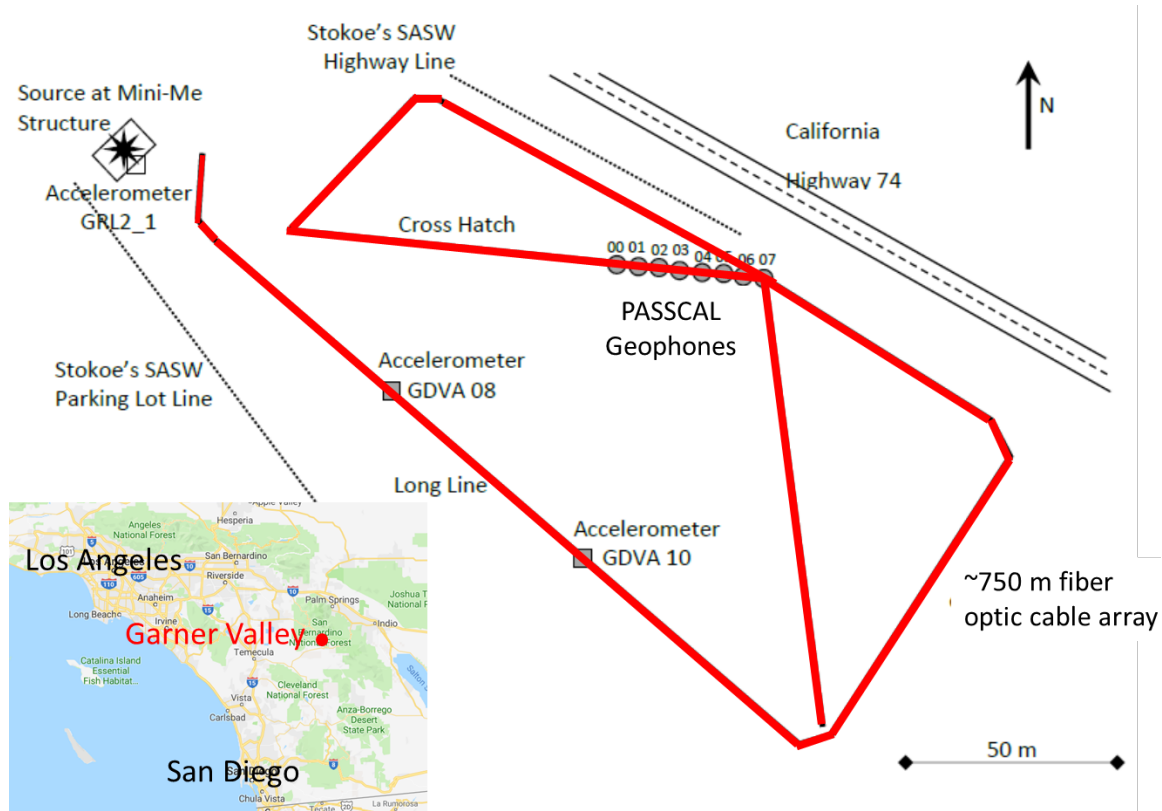


Figure 9.6. Location and configuration of the DAS array (in the red line) in Garner Valley, CA.

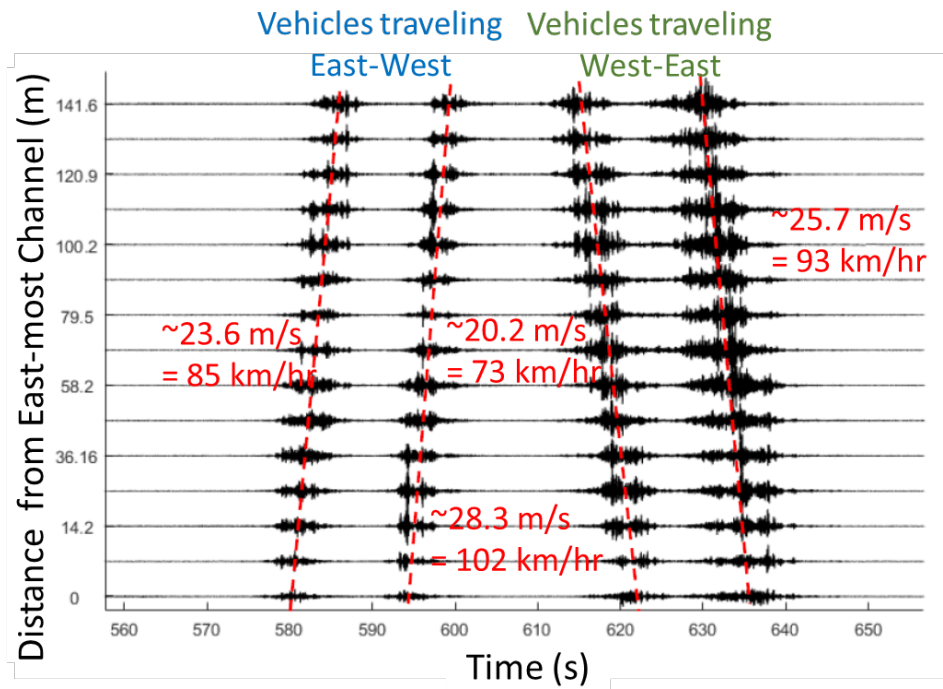


Figure 9.7. DAS array response for the monitoring of traffic speed and direction in a section of California Highway 74 in Garner Valley, CA.

The ability of DAS to monitoring the type of vehicles was tested with the fiber-optic cable at Brady Hot Spring that PoroTomo deployed for the imaging of the Natural Laboratory. The whole array and the sections of the array used in the traffic monitoring study are presented in **Figure 9.8**. The color scale shown in the figure represents the seismic energy captured by the DAS array during one night in March 2016. That energy distribution captures two different effects. First the high vibration energy created by the traffic along interstate I-80 (NW corner of the array) and the heterogeneity of the near subsurface sediments at the site. While the array zigzags parallel to the interstate highway, the captured energy decreases across the array from the N to the SW.

Traffic actively was monitored during the 6 AM to 7 AM “rush” hour for vehicles traveling along the service road to a quarry for diatomaceous earth. Cameras were set up to image the traffic and validate the interpretation of the captured DAS signals. The results presented in **Figure 9.9** correspond to one morning along two DAS channels along a section perpendicular to the service road (the service road was selected due to the light, single-vehicle traffic pattern). The DAS channel closest to the service road was located about 10 m from the center lane. It is apparent from each of the traces that there are differences between the amplitude and length of the traces for cars, SUVs and tractor trailers. The differences in these signatures provide an alternative for the identification of different types of vehicles (and even potentially the loaded/unloaded nature of the passing trucks) for monitoring road operation and degradation.

Vehicular traffic was also used as a source of seismic energy for ambient noise tomography. Zheng et al. (2017) used DAS recordings to obtain dispersion curves and image the spatial distribution of S-wave velocity. S-wave velocity estimated from DAS data are presented in **Figure 9.10**. The results at different horizontal slices show the heterogeneous distribution of sediment stiffness in three dimensions. These results have implication for the earthquake-

resistance design of the infrastructure along with the interpretation of the near-surface geology. The estimated shear-wave velocity is listed as model M06 in the Table of Material Properties.

These types of data, analyses, and interpretation are possible because of the distributed nature of DAS arrays.

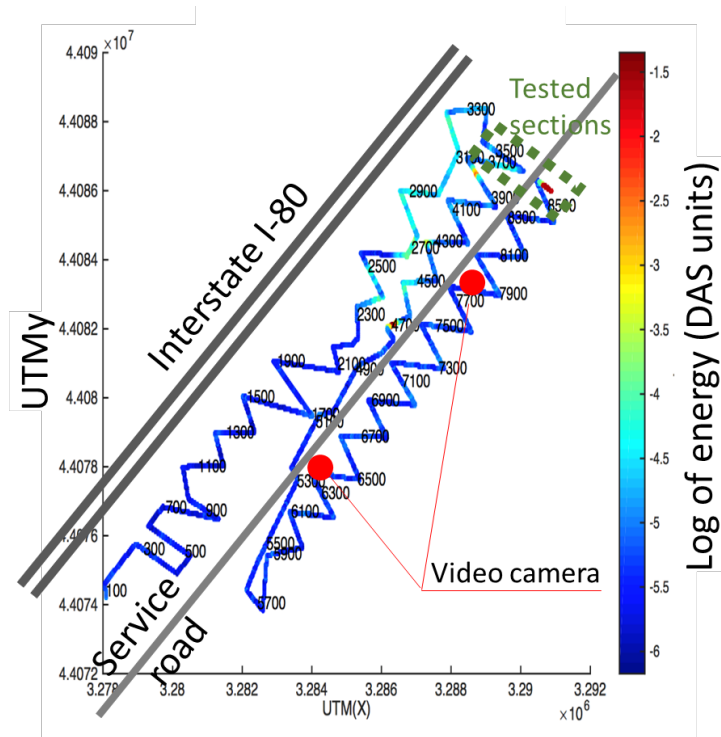


Figure 9.8. DAS array in Brady Hot Springs, NV. The rectangle labeled “Tested sections” on the NE of the array show the section of DAS used in the traffic monitoring study.

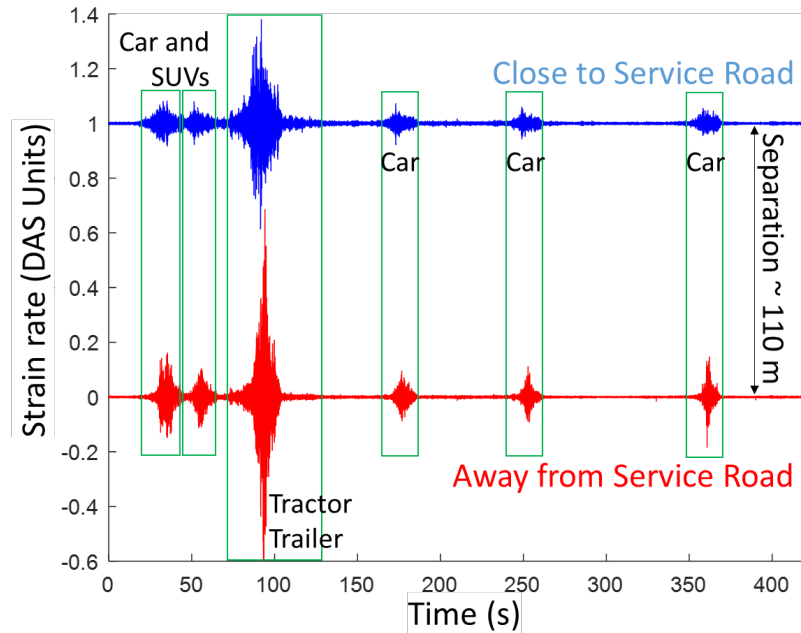


Figure 9.9. Signals capture with DAS section perpendicular to the service road (refer to Figure 9.8; Fratta et al., 2017)

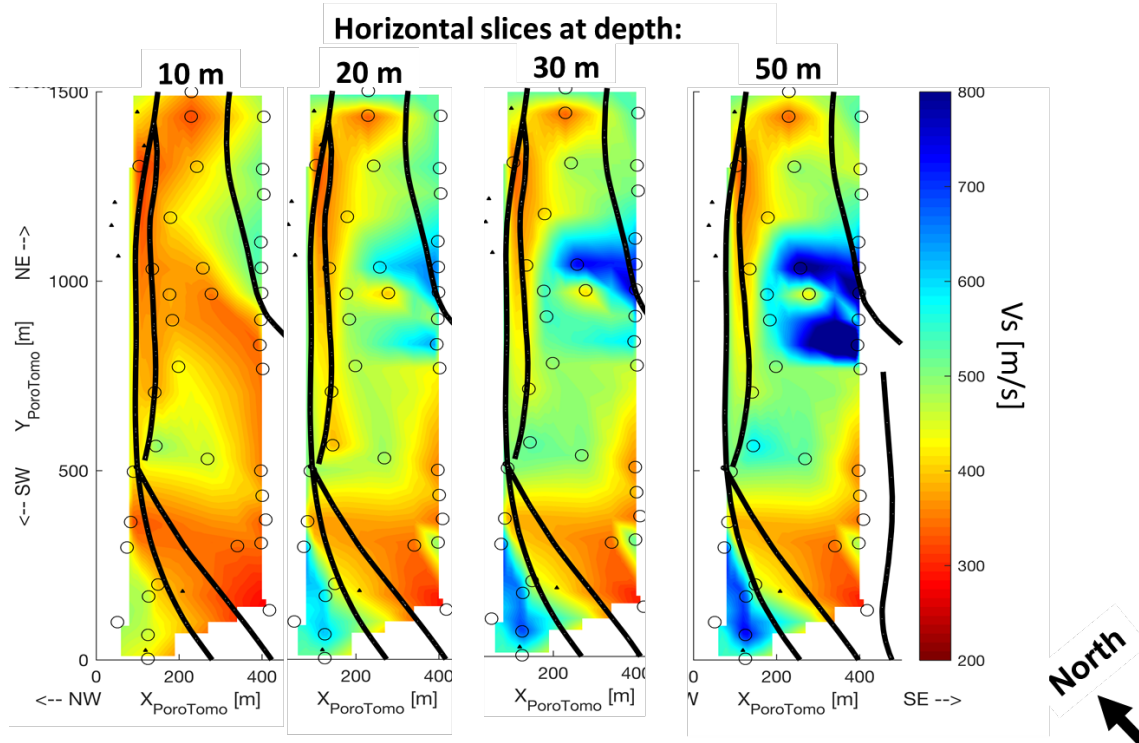


Figure 9.10. Ambient noise tomography images results for the shear-wave velocity estimated from DAS data at several depths.

D. Fiber Longevity

A follow-up to the DTS measurements made in Brady observation well 56-1 during the 2016 PoroTomo field experiment was conducted on August 24, 2018 by CTEMPS personnel. Over an approximately 20-hour period, measurements were made with a Silixa XT DTS interrogator configured to make continuous sixty-second readings on a single channel with a bottom hole U-bend. The spatial sampling interval was 25 cm with a temperature resolution of approximately 0.03°C. Most thermal boundaries observed in the original 2016 experiment still persist with the exception of the isothermal thermal cap that extends over a broader interval (**Figure 9.11**).

Figure 9.12 and **Figure 9.13** show a temperature time series comparison of the 2016 and the 2018 data.

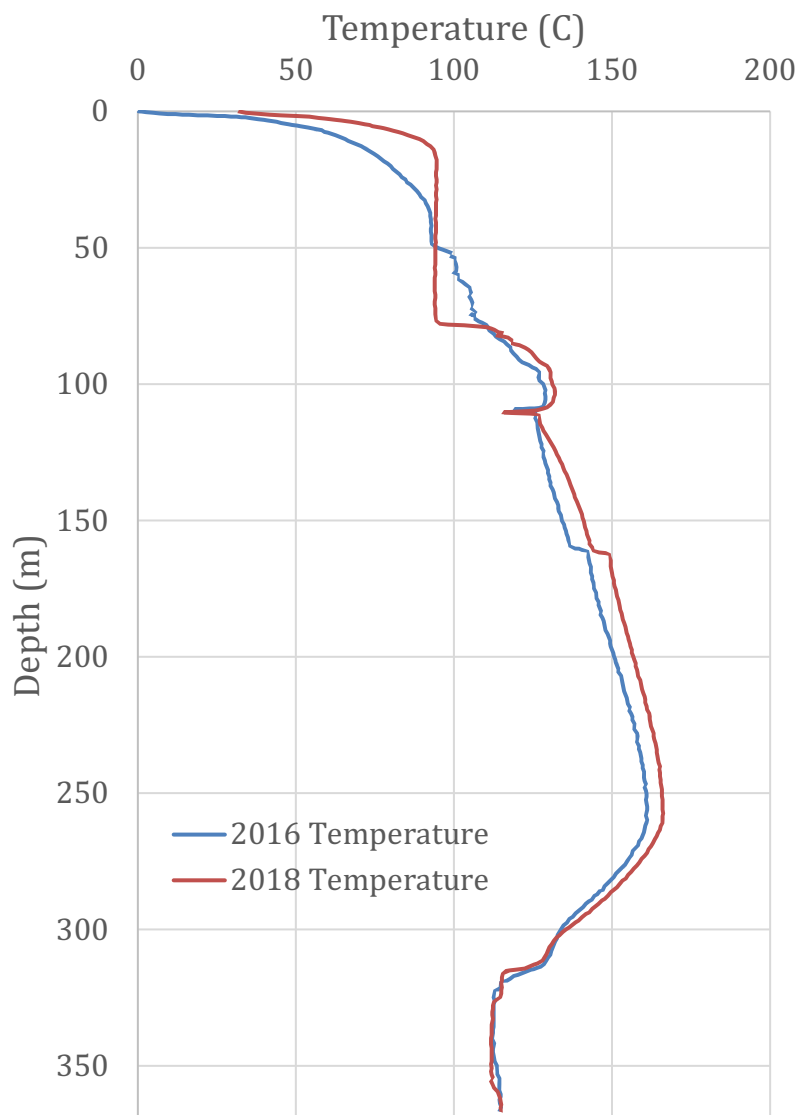


Figure 9.11. Thermal profiles in Well 56-1 in March 2016 and August 2018.

In the 2016 survey, thermal boundaries at 109 m, 160 m, and near 312 m show fluctuations that are correlated with changes in reservoir pressure resulting from a plant shutdown on 24 March 2016. No fluctuation is seen at these depths in the 2018 data, suggesting that the irregularities are stable under normal plant operations, as was the case during the 2018 recording period.

The 2018 data shows a larger zone of constant temperature (93°C) between 14 m and 80 m, presumably related to steam condensation. This zone appears to respond to the surface temperature and the state fluids outside the well casing (Patterson et al., 2017). Most notable is a quasi-regular repeating thermal exchange process that is evident in both recordings between 325 m and 367 m (roughly the perforated zone). In 2016 the repetition period was (eventually) stable at about 30 min/cycle. In 2018 there are 20 cycles during the 20-hour recording. Miller et al. (2018) compared DTS with DAS recordings and found a local acoustic signal. We interpret this acoustic signature to be a result of fluid flowing in the oscillatory process.

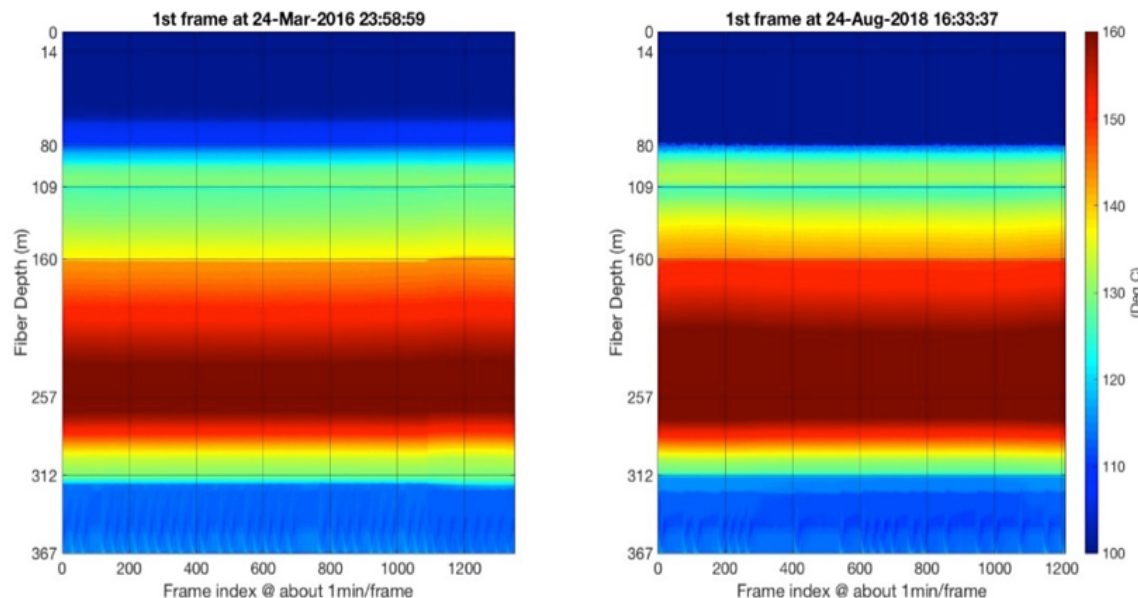


Figure 9.12. Thermal profiles in Well 56-1 in March 2016 and August 2018 versus time over approximately 20 hours (1200 minutes).

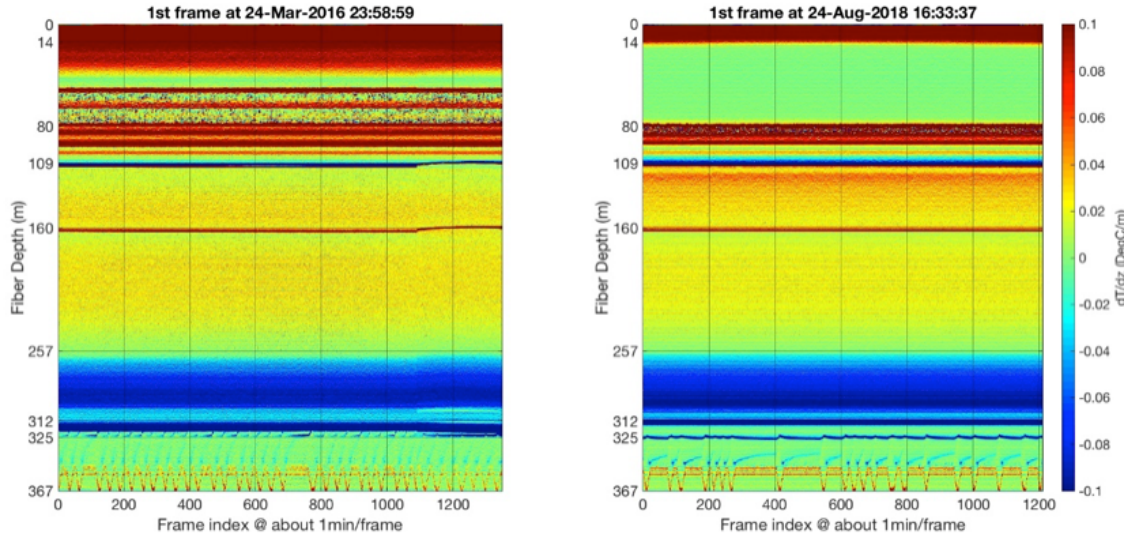


Figure 9.13. Thermal gradient profiles in Well 56-1 in March 2016 and August 2018 versus time over approximately 20 hours (1200 minutes).

These data demonstrate the durability of fiber in metal tube (FIMT) cable in a high-temperature environment for extended deployments. In fact, the cable has been exposed to temperatures in excess of its 150°C rating. Cables suitable for downhole deployments are available rated to up to 300°C with constructions optimized for survival in corrosive environments like geothermal wells.

E. Recommendations

Coupling is the most important consideration for DAS deployments. The particle motion needs to be coupled through the formation, to the cable structure, and into the fiber itself. There are several methods of coupling (**Figure 9.14**). Frictional coupling (as in the Well 56-1 configuration) is typical when deploying with pre-existing infrastructure. When installing new infrastructure, it is straightforward to clamp the cable to the casing as it goes into the well and then cement it in place. This provides significantly improved coupling when compared to frictional coupling alone.

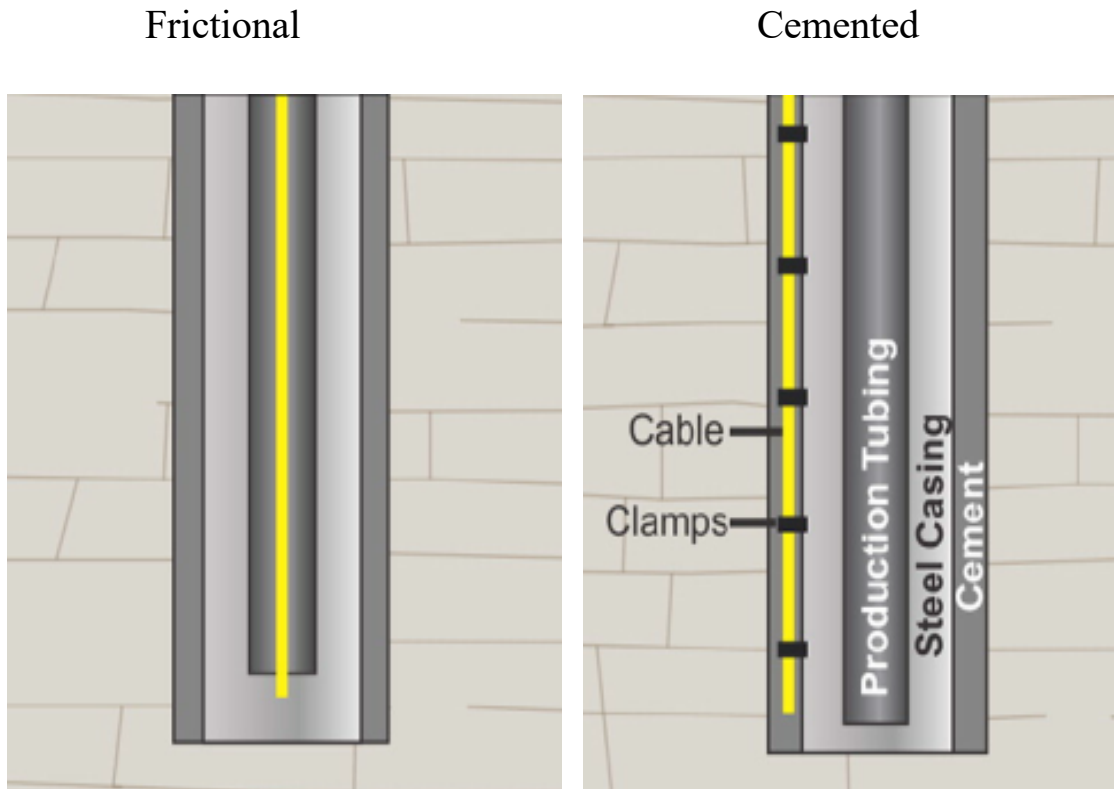


Figure 9.14. Schematics of different coupling methods (Modified from Munn et al. 2017).

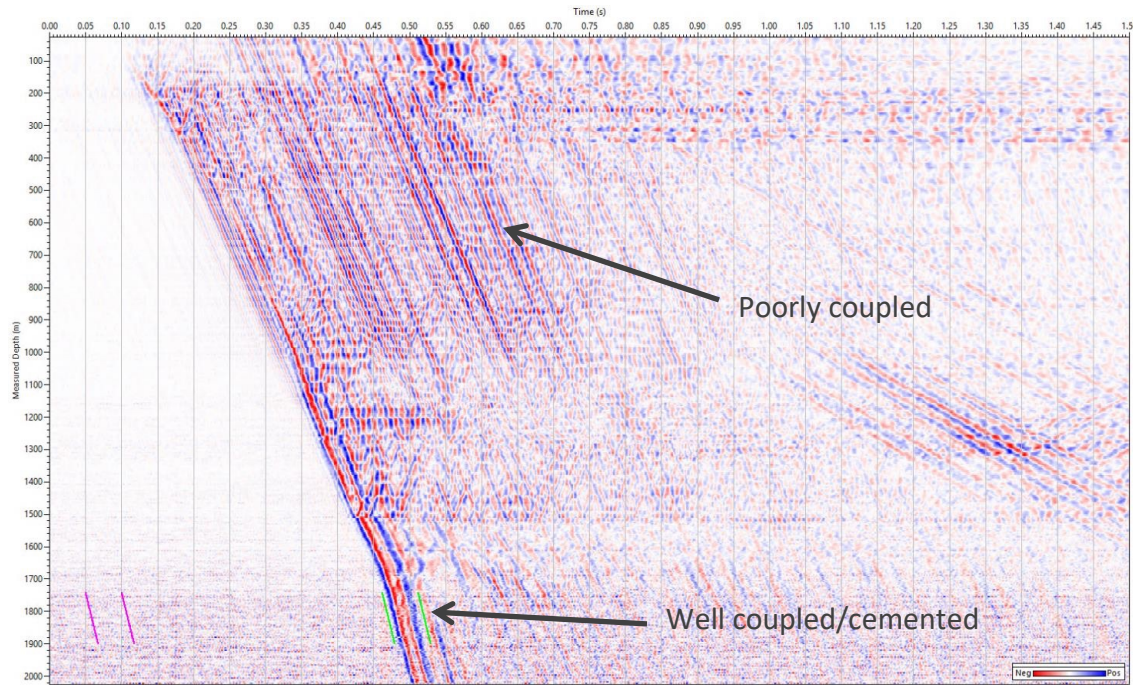


Figure 9.15. Figure demonstrating the difference in DAS signal along a cable that is partially cemented. The upper section, which is not cemented and is poorly coupled section, displays strong cable/casing ringing compared to the lower section, which is cemented. This data set is not from Brady. Figure provided by Silixa LLC.

Permanently emplacing cable in wells can present challenges when the casing is perforated, as may be the case for geothermal production wells. In these cases, there is technology available that can transmit the location and orientation of the cable. Cable orientation beacons (**Figure 9.16**) can be attached to the fiber optic cable underneath the casing clamps and use the cable to acoustically communicate with the surface. This information makes it possible to avoid the cable when perforating the casing.



Figure 9.16. Cable orientation beacon setup. Figure provided by Silixa LLC.

While DAS technology is not as precise as geophones, there have been significant advances since the PoroTomo deployment. **Figure 9.17** shows a comparison. The DAS data shown in green (panels g and k) from an interrogator configuration similar to that used by the 2016 PoroTomo deployment at Brady. The data shown in magenta (panels f and j) is from the latest Carina DAS system developed by Silixa. While the Carina data has a lower SNR than the geophone data (blue in panels e and i), it is two orders of magnitude greater than the older DAS system. The sensitivity allows for measuring strain on the picostrain scale and can be sensitive enough to measure the dilation and contraction of fractures directly in-situ.

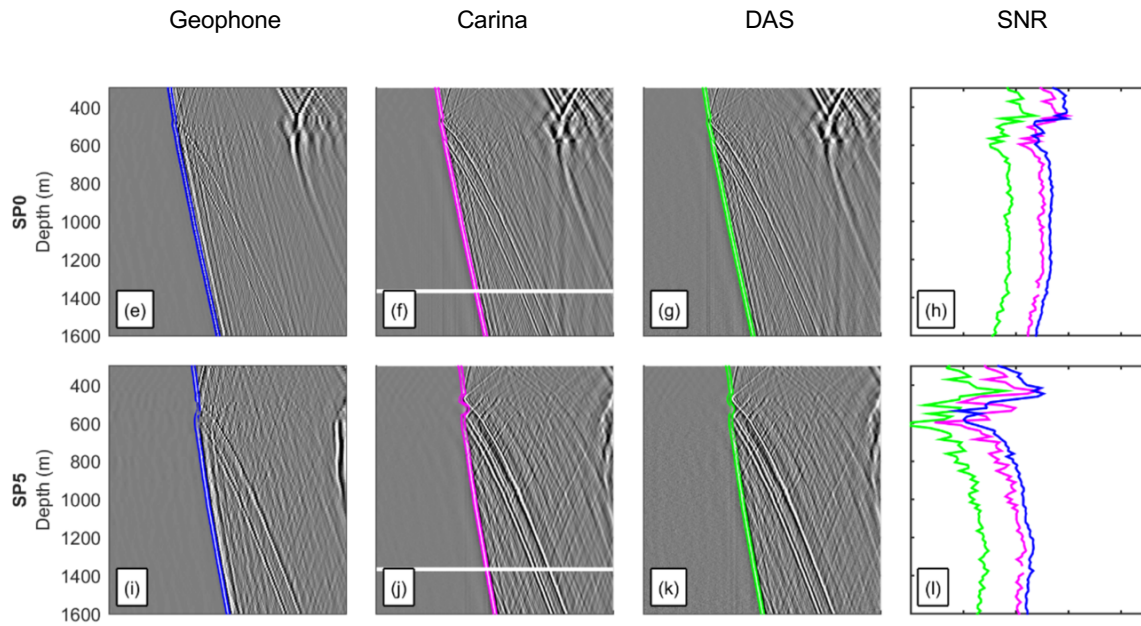


Figure 9.17. Comparison of geophone and DAS records from an offset vertical seismic profile survey in Otway, Australia (modified from Correa et al. 2017).

In conclusion, fiber optic distributed sensing can be effective tools for geothermal sites with cable technology suitable for harsh downhole environments. The cables are capable of surviving for extended periods in a geothermal reservoir if designed appropriately. By cementing cable into wells behind the casing, the increased coupling provides improved data quality and a permanent installation that can provide dense datasets for enhanced characterization and long-term monitoring of wells and the surrounding reservoir. This installation can also accommodate plans for perforating the casing. Significant improvements have brought the technology close to having SNR on par with traditional geophones and wouldn't require perturbing the well for permanent cable installations behind casing.

Section 10. Feasibility of Coupled Inversion of Three Data Types

A. Results

The PoroTomo team has completed inverse modeling of the three data sets (seismology, geodesy, and hydrology) individually, as described previously. We have registered the estimated values of the material properties on a three-dimensional grid with a spacing of 25 meters between nodes. The material properties are listed in Table 10.1.

Slices showing the material properties in a horizontal slices at 49 meters depth appear in **Figure 10.1** and **Figure 10.2**. Vertical slices in a plane perpendicular to the dominant strike of the fault system appear in **Figure 10.3**. Vertical slices in a plane parallel to the dominant strike of the fault system appear in **Figure 10.4**. An Excel file containing all of these values has been submitted to the GDR.

The results agree on the following points. The material is unconsolidated and/or fractured, especially in the shallow layers. The structural trends follow the fault system in strike and dip. The geodetic measurements favor the hypothesis of thermal contraction. Temporal changes in pressure, subsidence rate, and seismic amplitude are associated with changes in pumping rates during the four stages of the deployment in 2016. The modeled hydraulic conductivity is high in fault damage zones. All the observations are consistent with the conceptual model: highly permeable conduits along faults channel fluids from shallow aquifers to the deep geothermal reservoir tapped by the production wells.

ID	Material property
M00	Density from Witter et al. [kg/m ³]
M01	P-wave velocity from Matzel's sweep interferometry [m/s]
M02	S-wave velocity from Matzel's sweep interferometry [m/s]
M03	Poisson's ratio from Matzel's sweep interferometry [.]
M04	Young's modulus from Matzel's sweep interferometry [Pa]
M05	P-wave velocity from body-wave tomography geophone only [m/s]
M06	Shear-wave velocity Multiscale Analysis of Surface Waves [m/s]
M07	Quality factor Qp from Matzel's sweep interferometry [.]
M08	Quality factor Qs from Matzel's sweep interferometry [.]
M10	P-wave velocity from body-wave tomography Thurber20171123 [.]
M11	Quality factor ratio Qs/Qp Matzel sweep interferometry [.]
M12	Temperature from a HT model [degC]
M15	Siler lithology [numbered unit]
M16	Strain rates in voxels from Reinisch et al. [picostrain/s]
M23	Pressure from H-T modeling [Pa]
M24	Areal fault density (area per unit volume) [m ² /m ³]
M25	Hydraulic Conductivity from [m/s]

Table 10.1. Identification codes of material properties.

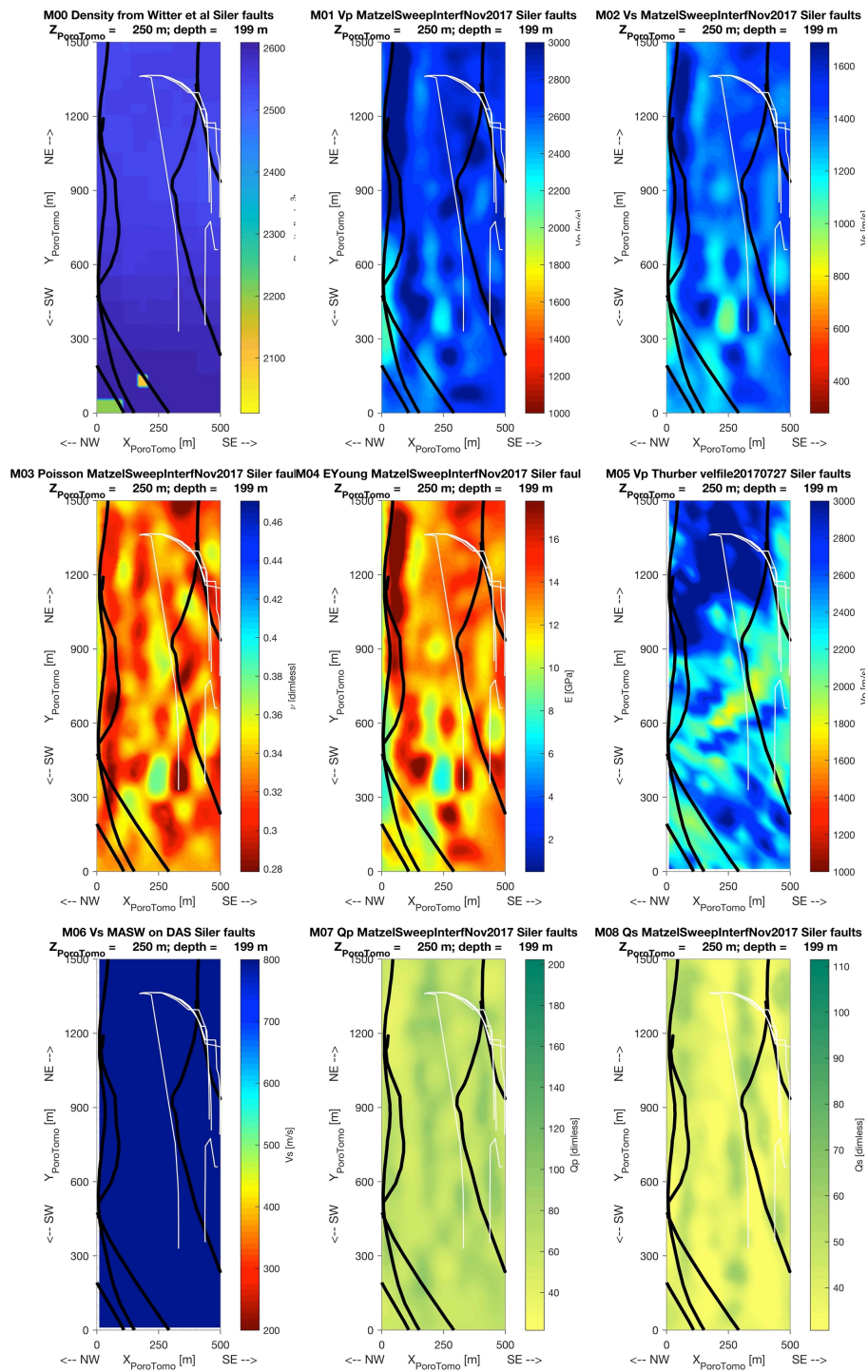


Figure 10.1. Horizontal slices showing material properties at a depth of 49 m below the mean elevation of the surface. Faults (black lines) are from Siler et al. 2016. Coordinates are in the rotated PoroTomo coordinate system. Models of material properties are identified in Table 10.1..

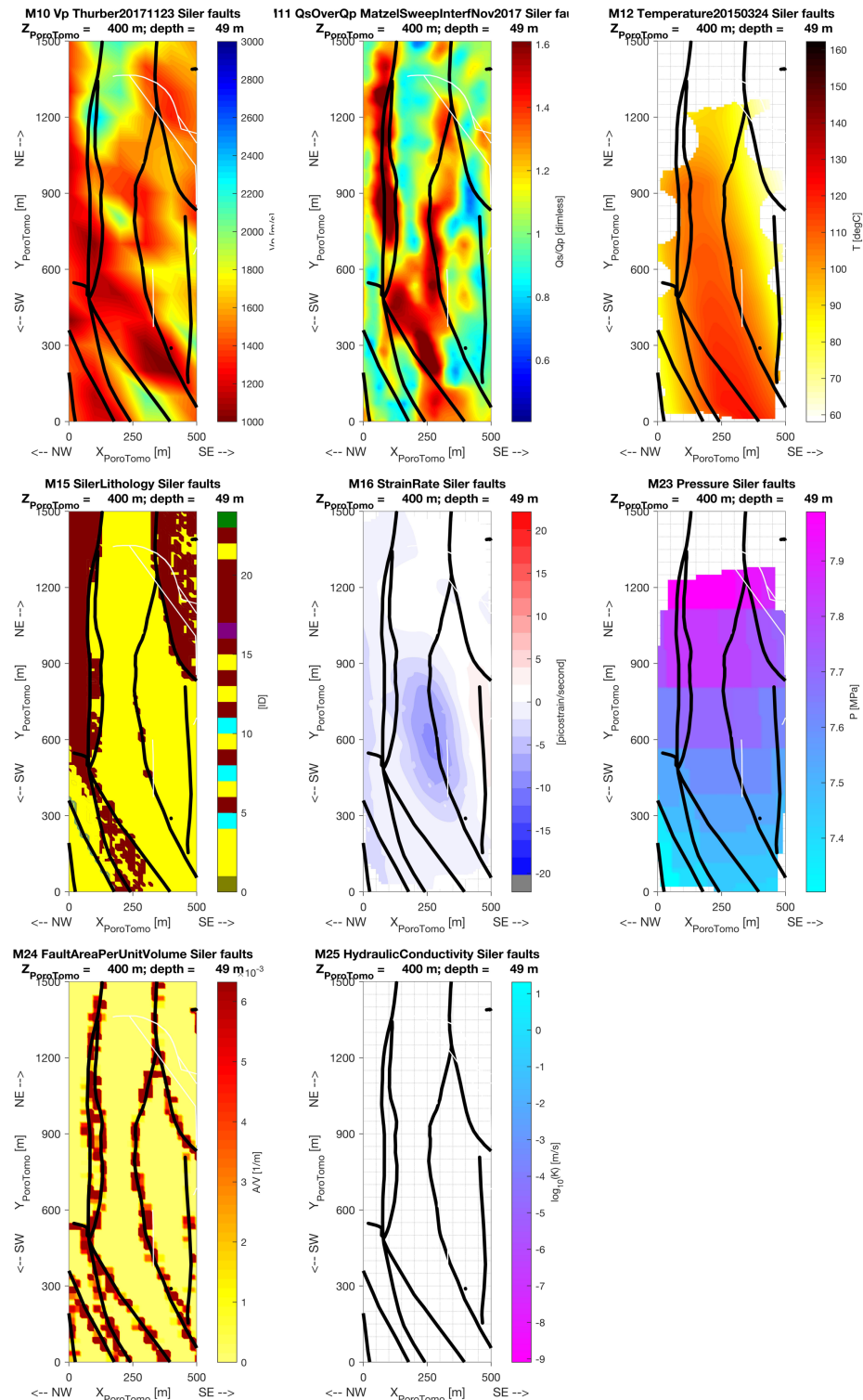


Figure 10.2. Horizontal slices showing material properties at a depth of 49 m below the mean elevation of the surface. Faults (black lines) are from Siler et al. 2016. Coordinates are in the rotated PoroTomo coordinate system. Models of material properties are identified in Table 10.1

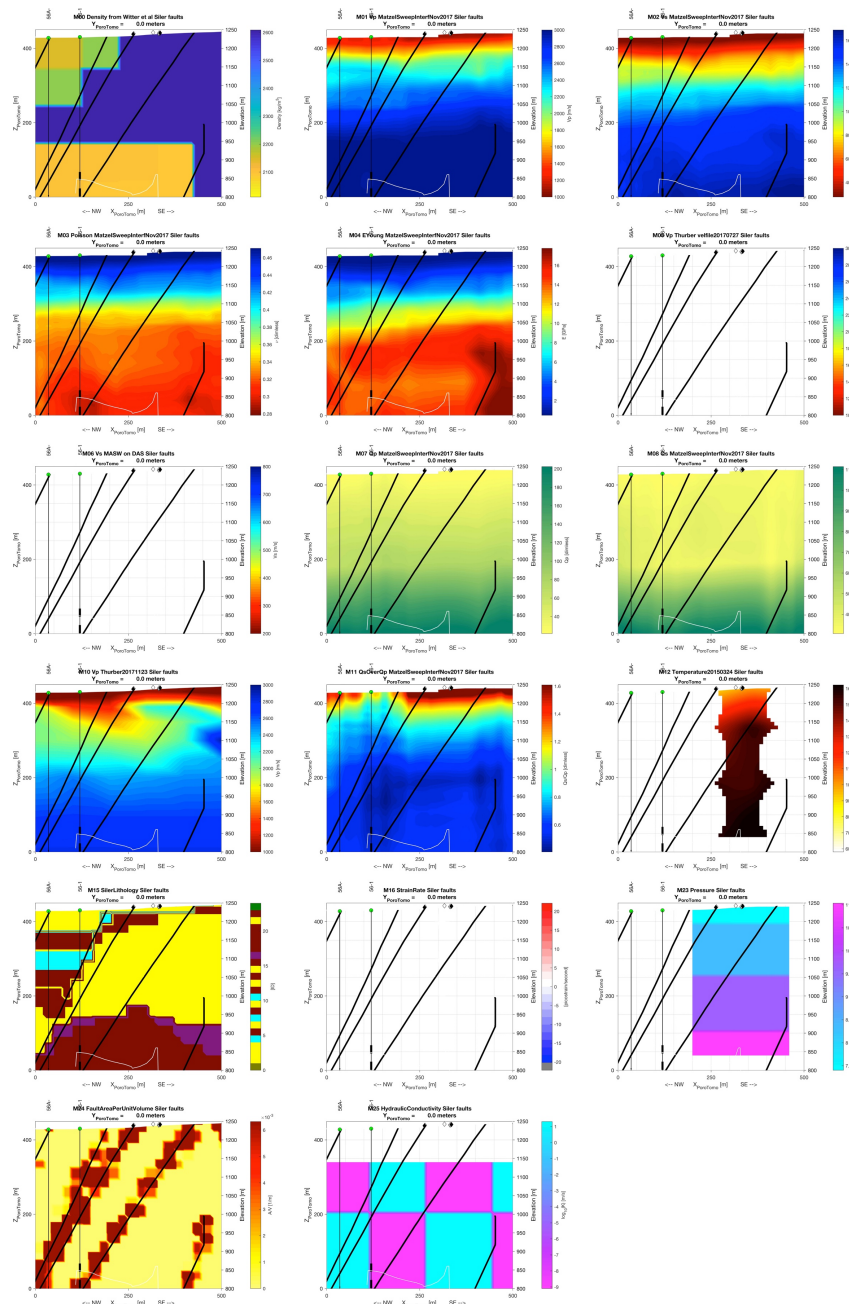


Figure 10.3. Vertical slices showing material properties in a plane perpendicular to the dominant strike of the normal fault system.. Faults (black lines) are from Siler et al. 2016. Coordinates are in the rotated PoroTomo coordinate system. Models of material properties are identified in Table 10.1

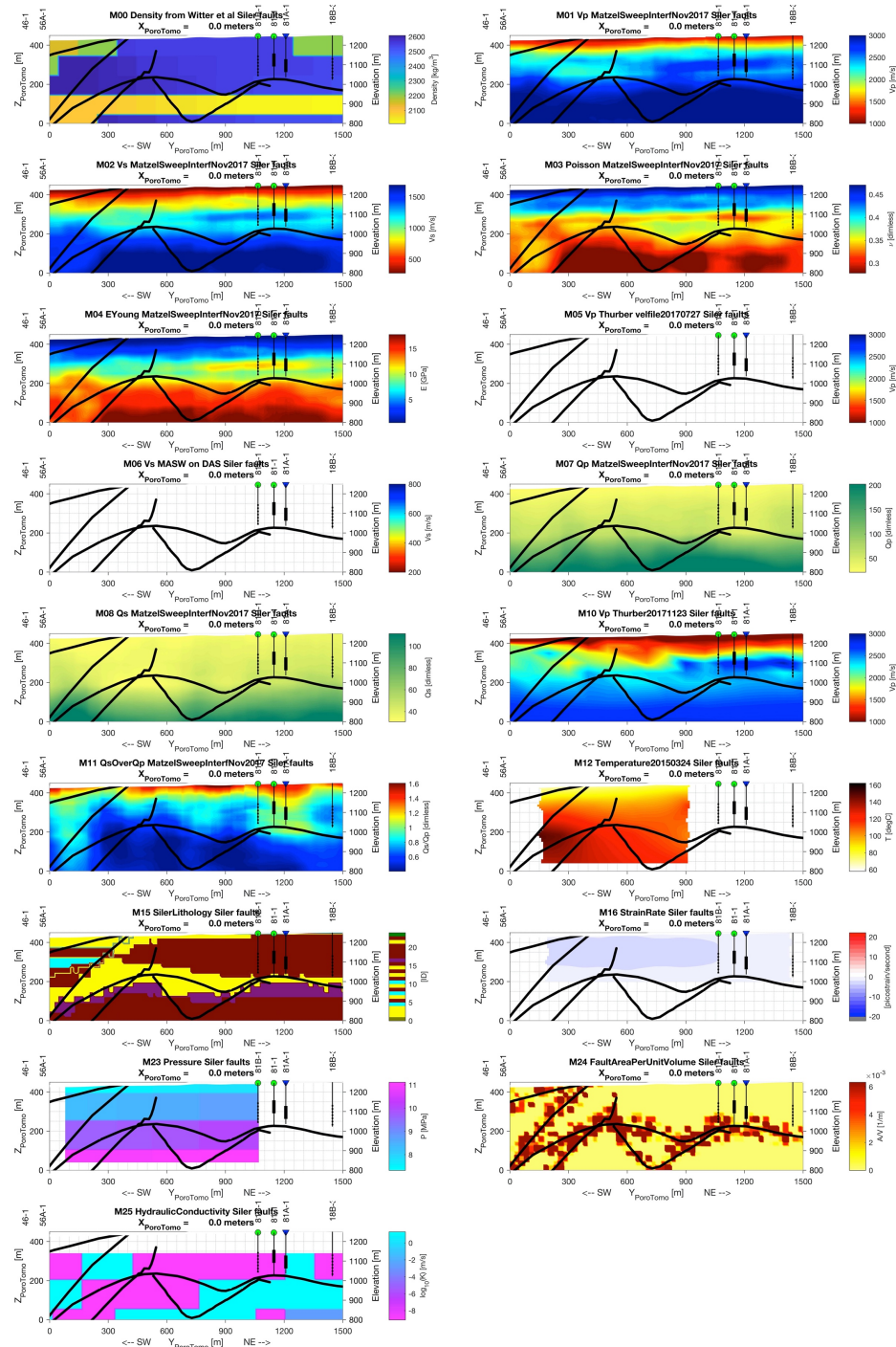


Figure 10.4. Vertical slice showing material properties in a plane parallel to the dominant strike of the normal fault system.. Faults (black lines) are from Siler et al. 2016. Coordinates are in the rotated PoroTomo coordinate system. Models of material properties are identified in Table 10.1.

Details on estimated values of material properties

M00 Density from Witter et al. [kg/m^3]

Model M00 shows density in kilograms per cubic meter from the study by Witter et al. (2016), for which the abstract follows. Values have been interpolated to the PoroTomo mesh with 25-meter spacing between points.

Witter, J. B., D. L. Siler, J. E. Faulds, and N. H. Hinz (2016), 3D geophysical inversion modeling of gravity data to test the 3D geologic model of the Bradys geothermal area, Nevada, USA, Geotherm Energy, 4, 14.

<http://dx.doi.org/10.1186/s40517-016-0056-6>

Three-dimensional geophysical inversion modeling of gravity data has been performed to test the validity of a 3D geologic model constructed for the Bradys geothermal area. Geophysical modeling was implemented in three different ways: (1) fully unconstrained (i.e., no geologic data included); (2) constrained by the 3D geologic model using homogeneous rock unit densities, and (3) constrained by the 3D geologic model using heterogeneous rock unit densities. We show that the existing 3D geologic model of the Bradys area is broadly consistent with the gravity data. At a more detailed level, however, our analysis suggests that some adjustments to the Bradys 3D geologic model would improve agreement between the observed gravity and the calculated gravity response. The results of the geophysical inversion modeling are important as they serve as a guide to show where and how the boundaries of the 3D geologic model may need to be adjusted to address density excesses and deficiencies. A 3D geologic model that has been independently tested prior to drilling (using a method such as that described in this paper) will be more robust and have less uncertainty than those which have not been tested. Such an approach will facilitate a reduction in drilling risk, lead to more successful drilling programs, and provide valuable geologic input to improve the accuracy of reservoir models.

1 P-wave velocity from Matzel's sweep interferometry [m/s]

Model M01 contains the P-wave velocity in meters per second estimated using “sweep interferometry” as described by Matzel et al. (2017a; 2017b), for which the abstracts are listed in Project Output as products 22 and 27.

Matzel, E., X. Zeng, C. Thurber, Y. Luo, C. Morency, and PoroTomo_Team (2017), Seismic Interferometry Using the Dense Array at the Brady Geothermal Field (abstract SGP-TR-212), paper presented at Stanford Geothermal Workshop, Stanford University.

Matzel, E., X. Zeng, C. Thurber, C. Morency, K. Feigl, and PoroTomo_Team (2017), Using Virtual Earthquakes to Characterize the Material Properties of the Brady Hot Springs, Nevada paper presented at Geothermal Research Council Transactions, Salt Lake City. <https://www.osti.gov/scitech/servlets/purl/1399706>.

2 S-wave velocity from Matzel's sweep interferometry [m/s]

Model M02 contains the shear-wave velocity in meters per second estimated using “sweep interferometry” as described by Matzel et al. (2017a; 2017b).

3 Poisson's ratio from Matzel's sweep interferometry [.]

Model M03 contains the (dimensionless) Poisson ratio calculated from the ratio of P-wave velocity Vp to S-wave velocity Vs, each estimated using “sweep interferometry” as described by Matzel et al. (2017a; 2017b). The relevant formula is:

```
%https://en.wikipedia.org/wiki/Elastic_modulus
VpOverVs = Vp ./ Vs;
Poisson = 0.5*((VpOverVs.^2) - 2)./( (VpOverVs.^2)-1);
```

4 Young's modulus from Matzel's sweep interferometry [Pa]

Model M04 contains the Young's modulus calculated from the P-wave velocity Vp and the S-wave velocity Vs, each estimated using “sweep interferometry” as described by Matzel et al. (2017a; 2017b). The density is from the study by Witter et al. (2016). The relevant formulae are:

```
% https://en.wikipedia.org/wiki/P-wave_modulus
% In linear elasticity, the P-wave modulus Mp, also
% known as the longitudinal modulus or the constrained modulus, is one of
% the elastic moduli available to describe isotropic homogeneous materials.
Mp = Density_kg_per_m3 .* (Vp).^2;
% Young's modulus
EYoung = Mp .* (1 + Poisson) .* (1 - 2*Poisson) ./ (1 - Poisson);
```

M05 P-wave velocity from body-wave tomography geophone only [m/s]

Model M05 contains the P-wave velocity in meters per second estimated using body-wave tomography. This preliminary result used a set of travel times picked from the seismograms recorded by Fairfield Nodal geophones only. In other words, no data from distributed acoustic sensing (DAS) were included in this inversion.

M06 Shear-wave velocity Multiscale Analysis of Surface Waves [m/s]

Model M06 contains shear-wave velocity in meters per second, as estimated by Zeng et al. (2017), the abstract for which is listed in Project Output as product 34.

Zeng, X., C. H. Thurber, H. F. Wang, D. Fratta, and Porotomo_Team (2017), 3D shear wave velocity structure revealed with ambient noise tomography on a DAS array (abstract #S33F-06), in Fall Meeting Amer. Geophys. Un., edited, New Orleans.

M07 Quality factor Qp from Matzel's sweep interferometry [.]

Model M07 contains the quality factor Q for P waves estimated using “sweep interferometry” as described by Matzel et al. (2017a; 2017b). Lower values of Q imply more attenuation of seismic waves.

M08 Quality factor Qs from Matzel's sweep interferometry [.]

Model M08 contains the quality factor Q for S waves estimated using “sweep interferometry” as described by Matzel et al. (2017a; 2017b). Lower values of Q imply more attenuation of seismic waves.

M10 P-wave velocity from body-wave tomography Thurber20171123 [m/s]

Model M10 contains the P-wave velocity in meters per second estimated using body-wave tomography, as described by Parker et al., (2018), for which the abstract follows. This inversion contains travel times picked from Fairfield Nodal geophones, horizontal DAS, and vertical DAS.

M11 Quality factor ratio Qs/Qp Matzel sweep interferometry [.]

Model M11 contains the ratio of the quality factor Qs for S waves to the quality factor Qp for P waves, each estimated using “sweep interferometry” as described by Matzel et al. (2017a; 2017b). Qualitatively, lower values of Qs/Qp may be interpreted as material that has lower fluid saturation and/or is more compact.

M12 Temperature from a HT model [degC]

Model M12 contains temperature in degrees Celsius as calculated in a simulation. The calculation couples the hydrologic flow (Darcy's Law) with simple thermodynamics. The epoch of validity is 24 March 2015. Values have been interpolated from a data set that is available on GDR as: <https://dx.doi.org/10.15121/1369075>.

15 Siler lithology [numbered unit]

Model M15 contains lithologic units as identified in the geologic model of Siler et al. (2016), for which the abstract follows.

Siler, D. L., N. H. Hinz, J. E. Faulds, and J. Queen (2016), 3D analysis of geothermal fluid flow favorability: Brady's, Nevada, USA, paper presented at PROCEEDINGS, 41st Workshop on Geothermal Reservoir Engineering Stanford University, Stanford, California, February 22-24, 2016 SGP-TR-209.

<https://pangea.stanford.edu/ERE/pdf/IGAstandard/SGW/2016/Siler.pdf>

Geothermal circulation requires heat, permeability and fluids. Fracture permeability along discrete fault zones provides the pathways for fluid convection. Within individual faults, however, fluid flow zones can have variable character, size, and spatial distribution, representing a significant challenge to exploration and evaluation of geothermal resources. A comprehensive and validated methodology for quantitatively identifying the character, extent, and location of most likely fluid upflow zones within a resource area does not exist. Here, we present a methodology for evaluating favorability for geothermal fluid flow in 3D, an application of this technique to the Brady's geothermal system, Nevada, USA, and a preliminary evaluation of the results based on data from the production field. A variety of data types, including 2D seismic reflection data, downhole lithologic data, and geologic map data are integrated in 3D space in order to develop a 3D geologic model of the Brady's geothermal system. From this geologic model, the stress state of modeled faults, the density of fault intersections, and the inferred fluid flow characteristics of the various stratigraphic intervals are evaluated as proxies for permeability and geothermal fluid flow. Integration of these results with temperature data reveals locations within the geothermal field where the collocation of probable fracture permeability and high temperatures indicates a high likelihood for hosting geothermal fluid circulation. These results are consistent with the locations of injection, production, and non-productive wells within the Brady's field. Validation of these results with data from the well field suggests that these techniques do indeed shed light on specific details of the fluid flow systematics in geothermal systems. Though Brady's is a relatively data-rich system, this methodology can be adapted and applied to exploration and resource assessment not only in mature production fields, but also in blind, greenfield and otherwise data-poor geothermal areas.

Lithologic units are coded using the following identification numbers. The color table groups similar lithologies together.

ID, Symbol, Lithology

1,	Q, Quaternary sediments, undifferentiated
2,	Tsy, Tertiary sediments
3,	Ts16, Tertiary lacustrine sediments
4,	Ts15, Tertiary lacustrine sediments
5,	Tls3, Tertiary limestone
6,	Tbo7, Tertiary basalt flows
7,	Ts14, Tertiary lacustrine sediments
8,	Tls2, Tertiary limestone
9,	Tbo6, Tertiary basalt flows
10,	Ts13, Tertiary lacustrine sediments
11,	Tls1, Tertiary limestone
12,	Tbo5, Tertiary basalt flows
13,	Ts12, Tertiary lacustrine sediments
14,	Tbo4, Tertiary basalt flows
15,	Ts11, Tertiary lacustrine sediments
16,	Tbo3, Tertiary basalt flows

- 17, Tpd, Tertiary Porphrytic (hornblende-biotite) dacite to rhyodacite flows and domes
- 18, Tbo2, Tertiary basalt flows
- 19, Tlr, Tertiary rhyolite lavas and lesser tuffs
- 20, Tbo1, Tertiary basalt flows
- 21, Tda, Tertiary andesite to dacite lavas
- 22, Tslo, Tertiary lacustrine sediments
- 23, Trt, Tertiary (Oligocene) ash-flow tuffs
- 24, Mzu, Mesozoic undifferentiated

16 Strain rates in voxels from Reinisch et al. [1/s]

Model M16 shows the volumetric strain rate estimated from InSAR data in a model of thermal contraction, as described by Reinisch et al. (2018), for which the abstract is listed in Project Output as product 62.

Reinisch, E. C., M. Cardiff, and K. L. Feigl (2018), Characterizing Volumetric Strain at Brady Hot Springs, Nevada, USA Using Geodetic Data, Numerical Models, and Prior Information, *Geophys. J. Int.*, 1501–1513. <http://dx.doi.org/10.1093/gji/ggy347>

23 Pressure from H-T modeling [Pa]

Model M23 contains fluid pressure in Pa as calculated in a simulation. The calculation couples the hydrologic flow (Darcy's Law) with simple thermodynamics. The epoch of validity is 24 March 2015. Values have been interpolated from a data set that is available on GDR as: <https://dx.doi.org/10.15121/1369075>.

24 Areal fault density (area per unit volume) [m²/m³]

Model M24 contains the surface area of faults per unit volume as identified in the geologic model of Siler et al. (2016). Starting with 3-dimensional coordinates of each fault, we found the best-fitting plane and defined a mesh surface using a Delaunay triangulation. We then calculated the locus of points defined by the intersection of the fault surface with each of the six faces of a cube with volume (25 m)³. The surface area of the polygon is then normalized by the volume of the cube to give the fault density in square meters per cubic meter.

25 Hydraulic Conductivity [m/s]

Model M25 shows hydraulic conductivity in meters per second as estimated from hydrogeologic modeling by Jeremy Patterson and Mike Cardiff. The details are described above in Section 6 in the sub-section entitled, "Characterization of Hydraulic Conductivity (K) Structure". More information can be found in Patterson's Master's Thesis, entitled, "Understanding Constraints on Geothermal Sustainability Through Reservoir Characterization at Brady Geothermal Field, Nevada."

Coupled Inversion

As described in the SOPO, Subtask 9.4 planned to assess the feasibility of coupled inversion of three data types (seismology, geodesy, and hydrology). The first step toward such a coupled inversion is to determine the relative weighting for each of the three data sets. Although we have not (yet) accomplished this task, we have explored the correlations between the sets of material

properties. For example, **Figure 10.5** shows the correlation between two different estimates of P-wave velocity.

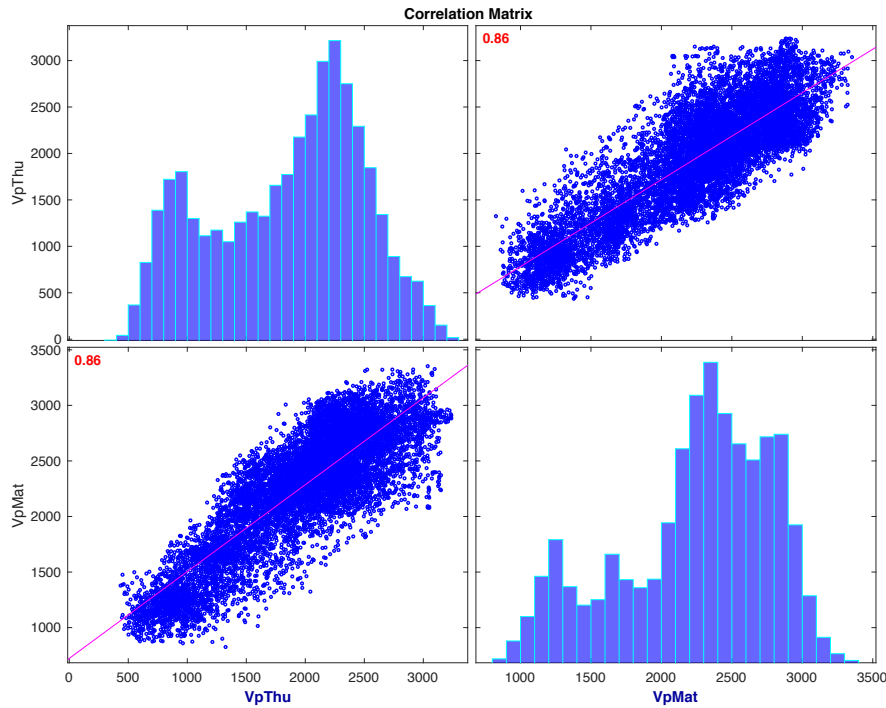


Figure 10.5. Correlation between two estimates of P-wave velocity, M1 and M13, showing values in meters per second. The panels on the diagonal show histograms of each variable individually. The off-diagonal panels show scatter plots of each variable with respect to another, with the best-fitting straight line shown in red. Its slope equals the Pearson's linear correlation coefficient in the upper left corner of a scatter plot indicates. It is printed in red if the correlation is statistically different from zero with 95 percent confidence.

Section 11. Conclusions and Recommendations

Overall, the PoroTomo project achieved its objective of assessing “an integrated technology for characterizing and monitoring changes in an EGS reservoir in three dimensions”. The technology performance metric of (spatial) resolution was assessed using checkerboard tests, as shown in Table 11.1. For the material property of P-wave velocity estimated using body-wave, travel-time tomography, the spatial resolution of the model is 100 m over most of the study area at a depth of 200 m. The P-wave and S-wave velocity models estimated from sweep interferometry were combined with a model of density to calculate the material properties of Poisson’s ratio and Young’s modulus with the same level of resolution. The 100-meter resolution achieved using the data from seismology represents a 2-fold improvement over the models existing at Brady before the PoroTomo project began and meets the minimum requirement specified in the SOPO.

	Seismology	Seismology	Geodesy	Hydrology	Combined
Estimated parameter	P-wave velocity Vp [m/s]	S-wave velocity Vs [m/s]	volumetric strain rate $d\varepsilon/dt = d(\Delta V/V)/dt$ [1/s]	hydraulic conductivity K [m/s]	
Resolution at Brady in 2014	200 m	200 m	~500 m		
Minimum requirement: improve resolution to	100 m ✓	100 m ✓	500 m ✓	500 m ✓	100 m ✓
Target: improve resolution to	50 m	50 m	250 m ✓	250 m	50 m
Beyond (“over”) target: improve resolution to	25 m	25 m	100 m ✓	100 m	25 m
Combined with	Vs, Density	Vp	T, P, Q	porosity	geology
Useful for inferring	Poisson’s ratio, Young’s modulus	Poisson’s ratio	cooling rate dT/dt Thermal dE/dt	fluid flow permeability	porosity permeability

Table 11.1. Spatial resolution achieved for estimating various parameters.

Using data from geodesy, the PoroTomo team was able to estimate the volumetric strain rate in the shallow aquifer with a spatial resolution of 100 m in a layer at depths of 50-150 m, thus going beyond the target resolution of 250 m specified in the SOPO. The rate of volumetric strain rate $d\varepsilon/dt$ can be used to infer the rate of cooling dT/dt and the rate of change in thermal energy dE/dt in the shallow parts of the field.

Using data from hydrology, the PoroTomo team was able to estimate the hydraulic conductivity K with a spatial resolution of 500 m, thus meeting the minimum requirement specified in the SOPO. These estimates of hydraulic conductivity K have been used to simulate the flow paths within the geothermal field at Brady. If estimates of porosity were available, then

they could be combined with the hydraulic conductivity K to calculate permeability and thus further constrain models of fluid flow.

Using the information from seismology, geodesy, and hydrology, the PoroTomo team achieved a spatial resolution of 100 m, thus meeting the minimum requirement specified in the SOPO.

The following three paragraphs were updated in July 2019 in response to a query from DOE.

Before starting the PoroTomo project, the methods for analyzing each of the three types of data individually were at Technology Readiness Level TRL 2 (“technology concept formulated”) or TRL 3 (“proof of concept”), as stated in the SOPO. Following the deployment of a prototype in the field at Brady Hot Springs in 2016, each of these methods has increased to TRL 5 (“component validation in relevant environment”). Since the individual methods for analyzing the three types of data (seismology, hydrology, and geodesy), were already proven concepts before the start of the project, they do not constitute “subject inventions”.

The integrated technology, analyzing all three data types, is now at TRL 3 (“proof of concept”). The “integrated technology” is a method for combining the estimated values of the 17 various material properties (e.g., density) into a single three-dimensional mesh with 17 such values for each hexahedral element (i.e. “voxel”). To do so, the method uses standard methods of interpolation that have been published previously⁴. For example, to calculate the Young’s modulus, the method uses a mathematical formula available on Wikipedia⁵ to combine the density derived from gravity modeling with the P-wave velocity derived from seismology. The software for performing the interpolation is available as open-source software at the GitHub repository: <https://github.com/feigl/PoroTomo>

Therefore, the integrated technology does not constitute a “subject invention”.

Recommendations

Looking forward, the PoroTomo team can offer several recommendations that apply to other experiments, such as those planned for the Frontier Observatory for Research in Geothermal Energy (FORGE) site in Utah. The technical recommendations are discussed above in the relevant sections. In terms of approach, our most important recommendation is to emphasize teamwork. A multi-disciplinary team, including researchers from universities, industry and national laboratories contributed to the success of the PoroTomo project at Brady Hot Springs, Nevada. Critical discussions, including fortnightly teleconferences and yearly reviews, as well as conferences such as the Stanford Geothermal Workshop, the Geothermal Resource Council, and the American Geophysical Union, were essential to analyzing the PoroTomo data sets. The same type of critical discussions also took place when the PoroTomo team participated in meetings, including the initial kick-off meeting, two stage gate reviews, and a final review, as well as two peer reviews conducted by the Department of Energy’s Geothermal Technologies Office (GTO). Throughout this process, the PoroTomo team benefitted by interacting with its Technical

⁴ For example, the Matlab interpolation function named “scatteredInterpolant” refers to the following publication. Amidror, Isaac. “Scattered data interpolation methods for electronic imaging systems: a survey.” *Journal of Electronic Imaging*. Vol. 11, No. 2, April 2002, pp. 157–176.

⁵ https://en.wikipedia.org/wiki/Elastic_modulus

Management Team (TMT) and GTO staff. The PoroTomo project has led to collaborations at other geothermal sites, including Raft River, Idaho; Coso California; San Emidio, Nevada; Fallon, Nevada; and Milford, Utah.

Section 12. Data Management Plan

The members of the project are committed to meeting the goal of “making all research data displayed in publications resulting from the proposed work digitally accessible at the time of publication”⁶.

This includes data that are displayed in charts, figures, images, etc. In addition, the underlying digital research data used to generate the displayed data should be made as accessible as possible in accordance with the principles stated above. This requirement could be met by including the data as supplementary information to the published article, or through other means. The published article should indicate how these data can be accessed.”⁶

Databases accessible to all team members were created and maintained. For each subtask, the responsible team member submitted the data to the DOE Geothermal Data Registry (GDR) as described in the Data Management Plan submitted at the start of the project. Data sets were submitted in three levels of analysis: (1) meta-data description, (2) “raw” data before analysis, and (3) “processed” data after preliminary analysis for quality control. These data sets are listed in

Per an agreement between Ernest Majer (LBNL) and Arlene Anderson, DOE GTO program manager for GDR, data from all of the EGS networks including Brady’s are archived at the Northern California Earthquake Data Center (NCEDC) at the University of California Berkeley, and not at GDR. GDR queries for the data will be redirected to NCEDC.

We have released all of the PoroTomo data sets to the public. Since several of the data sets exceed the storage capacity of the GDR, they are stored on a file server at the University of Wisconsin-Madison. The files stored there can be accessed via FTP at <ftp://roftp.ssec.wisc.edu/porotomo>. Descriptions and metadata for these data sets have been submitted to the GDR with URLs (“links”) pointing to the file server.

We are currently working with Jon Weers (NREL) to transfer the entire PoroTomo data set from UW-Madison to the GDR using ESNET and FTP. Once this operation is completed, the links pointing to the server will need to be updated.

The following submissions were made to the DOE GDR⁷. The DOI for each submission is listed if one was assigned.

⁶ Funding Opportunity Announcement DE-FOA-0000842 <https://eere-exchange.energy.gov>

⁷ <https://gdr.openei.org>

Submission Name	DOI
Active Source 3D Seismic Tomography of Brady Hot Springs Geothermal Field, Nevada	
Analysis of Existing Data from a Distributed Acoustic Sensing Experiment at Garner Valley, California	https://dx.doi.org/10.15121/1177103
Analysis of Existing InSAR Data Brady Hot Springs Geothermal Area	https://dx.doi.org/10.15121/1169016
Analyzed Boise Data for Oscillatory Hydraulic Tomography	https://dx.doi.org/10.15121/1196281
Analyzed DTS Data, Guelph, ON Canada	https://dx.doi.org/10.15121/1196286
BRAD and BRDY GPS Station RINEX Files 03-26-2014	https://dx.doi.org/10.15121/1176866
BRAD BRDY BRD1 GPS Station RINEX Files 01-18-2017	
BRAD BRDY BRD1 GPS Station RINEX Files 04-14-2017	
BRAD BRDY BRD1 GPS Station RINEX Files 07-17-2017	
BRAD BRDY BRD1 GPS Station RINEX Files 1-19-2018	
BRAD BRDY BRD1 GPS Station RINEX Files 10-18-2016	
BRAD BRDY BRD1 GPS Station RINEX Files 10-30-2017	
BRAD GPS Station Time-Series Data 01/30/2004 - 05/02/2017	
Brady 1D Seismic Velocity Model Ambient Noise Prelim	https://dx.doi.org/10.15121/1148801
Brady Geothermal 1D Seismic Velocity Model	
Brady Geothermal Field Borehole Pressure Data	
Brady Geothermal Field Well Lithologies	https://dx.doi.org/10.15121/1196280
Brady Well Coordinates and Observation Sensor Depths	https://dx.doi.org/10.15121/1261986
Brady's Field GPS RINEX Files	
Brady's Field GPS Time-Series Data	
Brady's Geothermal Field - Analysis of Pressure Data	https://dx.doi.org/10.15121/1367912

Brady's Geothermal Field - DTS Raw Data	https://dx.doi.org/10.15121/1367868
Brady's Geothermal Field - List of Sentinel-1A InSAR Images	https://dx.doi.org/10.15121/1368177
Brady's Geothermal Field - Map of DAS, Nodal, Vibroseis and Reftek Station Deployment	https://dx.doi.org/10.15121/1368198
Brady's Geothermal Field - March 2016 Vibroseis SEG-Y Files and UTM Locations	https://dx.doi.org/10.15121/1367891
Brady's Geothermal Field - Metadata for DTS and DAS Surveys	https://dx.doi.org/10.15121/1261983
Brady's Geothermal Field - Metadata for InSAR Holdings	https://dx.doi.org/10.15121/1287499
Brady's Geothermal Field - Updated Vibroseis Source Locations	https://dx.doi.org/10.15121/1368358
Brady's Geothermal Field Active Source Seismic Survey MetaData	https://dx.doi.org/10.15121/1261982
Brady's Geothermal Field DAS and DTS Surface and Borehole Array Metadata	https://dx.doi.org/10.15121/1261907
Brady's Geothermal Field DAS Earthquake Data	https://dx.doi.org/10.15121/1334285
Brady's Geothermal Field DAS Vibroseis Data	https://dx.doi.org/10.15121/1367869
Brady's Geothermal Field DASH Resampled in Time	
Brady's Geothermal Field Distributed Temperature Sensing Data	https://dx.doi.org/10.15121/1377901
Brady's Geothermal Field InSAR Raw Data	https://dx.doi.org/10.15121/1261931
Brady's Geothermal Field Nodal Seismometer Active Source Data Sample	https://dx.doi.org/10.15121/1367556
Brady's Geothermal Field Nodal Seismometer Data	
Brady's Geothermal Field Nodal Seismometer Earthquake Data	https://dx.doi.org/10.15121/1334284
Brady's Geothermal Field Nodal Seismometers Metadata	https://dx.doi.org/10.15121/1261984
Brady's Geothermal Field PoroTomo Laboratory Deployment Map	https://dx.doi.org/10.15121/1261980
Brady's Geothermal Field Reftek Seismometer Data	
Brady's Geothermal Field Reftek Seismometer Metadata	https://dx.doi.org/10.15121/1261985
Brady's Geothermal Field Sample Interferogram in HDF5 Format	https://dx.doi.org/10.15121/1223853

Brady's Geothermal Field Seismic Network Metadata	https://dx.doi.org/10.15121/1166944
Brady's Geothermal Field Well Pumping Data During Deployment	https://dx.doi.org/10.15121/1334283
Bradys Geothermal Field MEQ Relocations 3D Velocity Models	https://dx.doi.org/10.15121/1196282
Bradys Hot Springs Ambient Noise Correlation functions (Initial Waveforms)	https://dx.doi.org/10.15121/1196283
Bradys Hot Springs Geothermal Area Build FEM Configuration	https://dx.doi.org/10.15121/1196284
BRDY BRAD BRD1 GPS Station RINEX Files 09-17-2015	https://dx.doi.org/10.15121/1254458
BRDY GPS Station Time-Series Data 01/28/2012 - 05/01/2017	
Distributed Acoustic Sensing Experiment Data from Garner Valley, California	https://dx.doi.org/10.15121/1261941
DTS Raw Data Guelph, ON Canada	https://dx.doi.org/10.15121/1176865
Filenames of Data from the Distributed Acoustic Sensing Experiment at Garner Valley, California	
Garner Valley DAS Metadata	https://dx.doi.org/10.15121/1169012
Graph Theory for Analyzing Pair-wise Data: Application to Interferometric Synthetic Aperture Radar Data	
Guelph, ON Canada DTA Metadata	https://dx.doi.org/10.15121/1169014
Instructions for Downloading Brady Seismic Network Raw Waveform Data from NCECDC	
Poroelastic References	https://dx.doi.org/10.15121/1169009
PoroTomo - Distributed Temperature Sensing (DTS) Measurements made in Brady Observation Well 56-1	
PoroTomo Natural Laboratory Horizontal Distributed Acoustic Sensing Data	
PoroTomo Project: Brady's Field, Station BRDY	https://dx.doi.org/10.15121/1254453
PoroTomo Project: Brady's Geothermal Field, Station BRAD	https://dx.doi.org/10.15121/1254454
PoroTomo Project: Brady's Geothermal Field, Subtask 3.5: GPS Data Analysis	https://dx.doi.org/10.15121/1254452
PoroTomo Project: Brady's Geothermal Field: GPS station deployment and data analysis	https://dx.doi.org/10.15121/1261972
PoroTomo: Brady Geothermal Field InSAR Data	

Pressure-Temperature Simulation at Brady Hot Springs	https://dx.doi.org/10.15121/1369075
Raw Pressure Data from Boise Hydrogeophysical Research Site (BHRS)	https://dx.doi.org/10.15121/1176944
Raw Pressure Data from Observation Wells at Brady's Hot Springs	https://dx.doi.org/10.15121/1334282
Sample data from a Distributed Acoustic Sensing Experiment at Garner Valley, California	https://dx.doi.org/10.15121/1177104
Temperature and Pressure Data Brady Monitoring Well SP-2	https://dx.doi.org/10.15121/1176860
Triggered MEQ Events on LBNL Permanent Seismic Array, Brady's EGS, March 2016	
Understanding Constraints on Geothermal Sustainability Through Reservoir Characterization at Brady Geothermal	
UTM Well Coordinates for the Boise Hydrogeophysical Research Site (BHRS)	https://dx.doi.org/10.15121/1169015
Value of Information References	https://dx.doi.org/10.15121/1166943
Material Properties for Brady Hot Springs Nevada USA from PoroTomo Project	https://dx.doi.org/10.15121/1501544

Table 12.1. List of data sets submitted to Geothermal Data Repository.

Section 13. Project Output

A. Presentations (chronological order by date of presentation)

1. Ali, S. T., N. C. Davatzes, K. L. Feigl, H. F. Wang, W. Foxall, R. J. Mellors, J. Akerley, E. Zemach, and P. Spielman (2015), Deformation at Brady Hot Springs geothermal field measured by time series analysis of InSAR data [SGP-TR-204], paper presented at Proceedings, 40th Workshop on Geothermal Reservoir Engineering Stanford University, Stanford, California, January 26-28, 2015, 6p. We analyze interferometric synthetic aperture radar (InSAR) data acquired between 2004 and 2014, by multiple satellite missions, to measure and characterize time-dependent deformation at the Brady Hot Springs geothermal field in western Nevada. Results from inverse modeling suggest that the deformation is a result of volumetric contraction in shallow units, likely associated with damaged regions where fault segments interact mechanically and that the rate of deformation is decreasing linearly over time.
2. Feigl, Kurt L., Syed Hammad Ali, John Akerley, Elena C. Reinisch, Michael A. Cardiff, Nicholas Christopher Davatzes, William Foxall, Dante Fratta, Corne Kreemer, Robert J. Mellors, Janice Lopeman, Paul Spielman, and Herb F Wang (2015), Time-Dependent Deformation at Brady Hot Springs Geothermal Field (Nevada) Measured With Interferometric Synthetic Aperture Radar and Modeled with Multiple Working Hypotheses of Coupled Behavior, *American Geophysical Union Fall Meeting 2015*.
To measure time-dependent deformation at the Brady Hot Springs geothermal field in western Nevada, we analyze interferometric synthetic aperture radar (InSAR) data acquired between 2004 and 2014 by five satellite missions, including: ERS-2, Envisat, ALOS, TerraSAR-X, and TanDEM-X. The resulting maps of deformation show an elliptical subsiding area that is ~4 km by ~1.5 km. Its long axis coincides with the strike of the dominant normal-fault system at Brady. Within this bowl of subsidence, the interference pattern shows several smaller features with length scales of the order of ~1 km. This signature occurs consistently in all of the well-correlated interferometric pairs spanning several months. Results from inverse modeling suggest that the deformation is a result of volumetric contraction in shallow units, no deeper than 600 m, that are probably associated with damaged regions where faults interact via thermal (T), hydrological (H), mechanical (M), and chemical (C) processes. Such damaged zones are expected to extend downward along steeply dipping fault planes, providing high-permeability conduits to the production wells. Using time series analysis, we test the hypothesis that geothermal production drives the observed deformation. We find a good correlation between the observed deformation rate and the rate of production in the shallow wells. We explore first-order models to calculate the time-dependent deformation fields produced by coupled processes, including: thermal contraction of rock (T-M coupling), decline in pore pressure (H-M coupling), and dissolution of minerals over time (H-C-M coupling). These processes are related to the heterogeneity of hydro-geological and material properties at the site.

3. Lancelle, Chelsea, Dante Fratta, Neal E. Lord, Herbert F. Wang, and Athena Chalari (2015), Active Travel-Time Tomography using a Distributed Acoustic Sensing Array, *American Geophysical Union Fall Meeting 2015*.

Distributed acoustic sensing (DAS) is a sensor array used for monitoring ground motion by utilizing the interaction of light pulses with sections of a fiber-optic cable. In September 2013 a field test was conducted at the NEES@UCSB Garner Valley field site in Southern California incorporating DAS technology. A 762-meter-long fiber-optic cable was trenched to a depth of about 0.3 m in a rectangular design with two interior diagonal segments. The fiber was excited by a number of sources, including a 45 kN shear shaker and a smaller 450 N portable mass shaker, both of which were available through NEES@UCLA. In addition to these sources, signals were recorded from a minivib source and hammer blows on a steel plate, as well as 8 hours of overnight ambient noise recording. One goal of the field test was to evaluate the use of DAS for tomographic studies. The large number of measurement points inherent to DAS lends itself well to this type of study. Tomograms were constructed using two of the active-sources at multiple locations. There were 8 minivib locations within the array and 13 hammer locations along the boundary of the array. Travel-time data were collected with the DAS array. Two-dimensional velocity tomograms were constructed for different resolutions from the two active sources and compared. In all the images, the lowest velocities lie near the center of the array with higher velocities surrounding this area. The impact results, however, may contain an artifact due to multiple propagation modes.

4. Lim, David, Warren Barrash, and Michael Cardiff (2015) Oscillatory Hydraulic Tomography at the Field Scale: Boise Hydrogeophysical Research Site, *American Geophysical Union Fall Meeting 2015*.

The use of sinusoidal or periodic testing for field-scale tomography of aquifer parameters (conductivity / storativity) is a novel, minimally-invasive method for aquifer characterization between boreholes. Previous results have demonstrated the effectiveness of this method, which we name Oscillatory Hydraulic Tomography (OHT), through both numerical and laboratory experiments. However, implementation and analysis of field-scale OHT testing has not been achieved to-date, and thus the technique remains unproven for application in real-world aquifers. We present an evaluation of OHT at the field scale here through application at the Boise Hydrogeophysical Research Site (BHRs), a field-scale (~20m diameter x 20m thickness) research site. Through Bayesian inversion, we assess issues such as data quality impacts and resolution of obtained tomographic images. We discuss issues associated with both data collection and data processing, and based on our experiences suggest a workflow for OHT performance at other field sites. The advantages of OHT, relative to “traditional” hydraulic tomography with constant rate pumping tests, include the ability to test across a range of stimulation frequencies (obtaining increased heterogeneity information), very high signal-to-noise ratios. Additionally, we examine the impact of nonlinear effects – such as water table boundary conditions – and their impact on OHT analysis algorithms.

5. Lord, Neal E., Herb F. Wang, Dante Fratta, Chelsea Lancelle, and Athena Chalari (2015), Garner Valley Vibroseis Data Processing Using Time-Frequency Filtering Techniques to Remove Unwanted Harmonics and External Noise, *American Geophysical Union Fall Meeting 2015*.

Time-frequency filtering techniques can greatly improve data quality when combined with frequency swept seismic sources (vibroseis) recorded by seismic arrays by removing unwanted source harmonics or external noise sources (e.g., cultural or ambient noise). A source synchronous filter (SSF) is a time-frequency filter which only passes a specified width frequency band centered on the time varying frequency of the seismic source. A source delay filter (SDF) is a time-frequency filter which only passes those frequencies from the source within a specified delay time range. Both of these time-frequency filters operate on the uncorrelated vibroseis data and allow separate analysis of the source fundamental frequency and each harmonic. In either technique, the time-frequency function of the source can be captured from the source encoder or specified using two or more time-frequency points.

SSF and SDF were both used in the processing of the vibroseis data collected in the September 2013 seismic experiment conducted at the NEES@UCSB Garner Valley field site. Three vibroseis sources were used: a 45 kN shear shaker, a 450 N portable mass shaker, and a 26 kN vibroseis truck. Seismic signals from these sources were recorded by two lines of 1 and 3 component accelerometers and geophones, and the Silixa Ltd's intelligent Distributed Acoustic Sensing (iDASTM) system connected to 762 m of trenched fiber optical cable in a larger rectangular area. SSF and SDF improved vibroseis data quality, simplified data interpretation, and allowed new analysis techniques.

6. Parker, Lesley, Robert J. Mellors, Clifford H. Thurber, Herb F. Wang, and Xiangfang Zeng (2015), Phase Velocity and Full-Waveform Analysis of Co-located Distributed Acoustic Sensing (DAS) Channels and Geophone Sensor, *American Geophysical Union Fall Meeting 2015*.

A 762-meter Distributed Acoustic Sensing (DAS) array with a channel spacing of one meter was deployed at the Garner Valley Downhole Array in Southern California. The array was approximately rectangular with dimensions of 180 meters by 80 meters. The array also included two subdiagonals within the rectangle along which three-component geophones were co-located. Several active sources were deployed, including a 45-kN, swept-frequency, shear-mass shaker, which produced strong Rayleigh waves across the array. Both DAS and geophone traces were filtered in 2-Hz steps between 4 and 20 Hz to obtain phase velocities as a function of frequency from fitting the moveout of travel times over distances of 35 meters or longer. As an alternative to this traditional means of finding phase velocity, it is theoretically possible to find the Rayleigh-wave phase velocity at each point of co-location as the ratio of DAS and geophone responses, because DAS is sensitive to ground strain and geophones are sensitive to ground velocity, after suitable corrections for instrument response (Mikumo & Aki, 1964). The concept was tested in WPP, a seismic wave propagation program, by first validating and then using a 3D synthetic, full-waveform seismic model to simulate the effect of increased levels of noise and uncertainty as data go from ideal to more realistic. The results obtained from this study provide a better understanding of the DAS response and its potential for being combined with traditional seismometers for obtaining phase velocity at a single location.

7. Trainor-Guitton, Whitney, Chelsea Lancelle, Herb Wang, and Kurt L. Feigl, (2015), Value of Information: comparing surface-wave dispersion curves estimated from conventional seismometers versus distributed acoustic sensing, *American Geophysical Union Fall Meeting 2015*
The efficacy of geophysical data to estimate key subsurface parameters is difficult to quantify given the complexity of both the signal and the earth, among many other factors. To address this, we utilize a metric from decision analysis known as the value of information (VOI). We analyze the uncertainty of surface-wave dispersion curves derived from travel times recorded by two types of seismological sensors: 3-component seismometers and Distributed Acoustic Sensing (DAS), a technique for measuring longitudinal strain in fiber-optic cables. Both data types were recorded at the Garner Valley test site in California. A 45 kN shear-shaker source produced a swept-frequency input from a few Hz to 10 Hz and back over 60 seconds. The geophone and DAS traces were filtered to remove harmonics from the source, traffic and other external noise. Source-Synchronous Filtering (Lord et al., AGU 2015) was applied to obtain waveforms. To measure the travel time from the source to the sensor, multiple zero-crossings are picked for frequencies between 4 and 20 Hz. These picks are used to estimate phase velocities as a function of frequency for both data types by plotting the travel times versus the distance of the sensor from the source. The slope of the best-fitting line provides an estimate of the phase velocity at a given frequency. To assess its uncertainty, we use a nonparametric bootstrap procedure [Efron & Tibshirani, 1986]. The resulting distributions of phase velocities describe the precision of the estimates for each data type. We then plot the phase velocities as a function of their frequency to generate many dispersion curves. These dispersion curves are inverted to estimate the posterior distribution of shear wave velocity with depth for each type of data. We hypothesize that this information is used to make a decision (e.g. how to develop a geothermal field), and therefore the VOI technique can be applied. This approach provides a metric for evaluating the VOI of each of the two data types.
8. Zeng, Xiangfang Chelsea Lancelle, Clifford H. Thurber, Dante Fratta, Herbert F. Wang, Athena Chalari, and Andy Clarke (2015), Properties of Noise Correlation Functions Obtained from a Distributed Acoustic Sensing (DAS) Array at Garner Valley, California, *American Geophysical Union Fall Meeting 2015*
The field test of Distributed Acoustic Sensing (DAS) conducted at Garner Valley, California on September 11-12, 2013 provided a continuous overnight record of ambient noise. The DAS array recorded ground motions every one meter of optical cable that was arranged approximately in the shape of a rectangle with dimensions of 160 m by 80 m. The long dimension of the array was adjacent to a state highway. Three hours of record were used to compute noise cross-correlation functions (NCFs) in one-minute windows. The trace from each sensor channel was pre-processed by downsampling to 200 Hz, followed by normalization in the time-domain and bandpass filtering between 2 and 20 Hz (Bensen et al., 2007). The one-minute NCFs were then stacked using the time-frequency domain phase-weighted stacking method (Schimmel & Gallart, 2007). The NCFs between channels were asymmetrical reflecting the direction of traffic noise. The group velocities were found using the frequency-time analysis method. The energy was concentrated between 5 and 15 Hz, which falls into the typical traffic noise frequency band. The resulting velocities were between 100 and 300 m/s for frequencies between 10 and 20 Hz, which are in the same range as described in the results for surface-wave dispersion obtained using an active source for the same site (Lancelle et al., 2015). The group velocity starts to decrease for frequencies greater than ~10 Hz, which was expected on the basis of a previous shear-wave velocity model (Steidl et al., 1996). Then, the phase velocity was calculated using the multichannel analysis of surface wave technique (MASW - Park et al., 1999) with 114 NCFs spaced one meter apart. The resulting dispersion curve between 5 and 15 Hz gave phase velocities that ranged from approximately 170 m/s at 15 Hz to 250 m/s at 5 Hz. These results are consistent with other results of active-source DAS and seismometer records obtained at the Garner Valley site (e.g., Stokoe et al. 2004).

9. Ali, Tabrez, John Akerley, Elena C. Baluyut, Nicholas C Davatzes, Janice Lopeman, Joseph Moore, Mitchell Plummer, Paul Spielman, Ian Warren and Kurt L. Feigl (2016), Geodetic Measurements and Numerical Models of Deformation: Examples from Geothermal Fields in the Western United States, Paper presented at PROCEEDINGS, 41st Workshop on Geothermal Reservoir Engineering Stanford University, Stanford, California, February 22-24, 2016, 7 p.
- Interferometric Synthetic Aperture Radar (InSAR) is an indispensable tool for measuring crustal deformation due to tectonic and anthropogenic processes. It provides unsurpassed spatial sampling, very good precision, and a useful observation cadence. By analyzing the temporal evolution and spatial pattern of the deformation, we can gain insight into the subsurface processes. Here, we use InSAR data acquired by the ERS-1, ERS-2, Envisat, ALOS, ALOS-2, TerraSAR-X, and TanDEM-X satellite missions to measure time-dependent deformation at a number of producing geothermal fields in the Western United States: including Raft River in Idaho, Coso and East Mesa in California, as well as Brady Hot Springs and Dixie Valley in Nevada. Although most of these sites exhibit subsidence, at least one shows transient uplift. We use the geodetic observations to constrain numerical models of the reservoir. We explore several different hypotheses for the processes driving subsidence, including poroelastic compaction and/or thermoelastic contraction.
10. Ali, S. T. (23 Sept 2016), Geodetic Measurements and Numerical Models of Deformation: Examples from Geothermal Fields in the Western United States, presentation at the Friday Informal Seminar Hour within the Earth Resources Laboratory at the Massachusetts Institute of Technology (MIT).
- Interferometric Synthetic Aperture Radar (InSAR) is a geodetic technique for measuring crustal deformation that provides very good precision, unsurpassed spatial sampling, and a useful observation cadence. By analyzing the temporal evolution and spatial pattern of deformation, and combining them with numerical models, we can gain insight into underlying geophysical processes and estimate parameters of interest. In this talk, I will show how geodetic observations of surface deformation, made at producing geothermal fields in the Western United States, combined with fully coupled numerical models can provide insight into the geometry and geomechanical properties of reservoirs. I will discuss the relative roles of thermal and hydraulic processes in driving transient deformation. I will also give a brief overview of Defmod (<https://bitbucket.org/stali/defmod/>), a small, yet fully unstructured, parallel finite element code for modeling crustal deformation over time scales of seconds to centuries.
11. Ali, Tabrez, Elena C. Reinisch, Kurt L. Feigl, and Nicholas Christopher Davatzes (2016), Geodetic Measurements and Numerical Models of Deformation at Coso Geothermal Field, California, USA, *American Geophysical Union Fall Meeting 2016*
- We measure transient deformation at the Coso geothermal field in south-central California using interferometric synthetic aperture data acquired between 2004 and 2016 by the Envisat and Sentinel-1A satellite missions. All well-correlated interferometric pairs show subsidence, with rates as high as ~30 mm/year, over a large ~75 km² circular area surrounding the field below which most of the seismicity associated with geothermal production is located. The deformation signature remains in the same location throughout the ~12 year interval. Time-series analysis of multiple interferometric pairs reveals continuous subsidence. A decrease in the subsidence rate after 2010 corresponds to a decrease in the net production rate. Using three-dimensional, fully numerical, multiphysics models, we explore the coupling between deformation and geothermal production. We seek to distinguish between two possible mechanisms: (i) decreasing pore-pressure following net extraction of fluids, or (ii) decrease in temperature of presumably fractured reservoir rock. Irrespective of the mechanism, a contracting ellipsoidal reservoir located at a depth of ~2 km, with a volume of 80 km³ or less is required to explain the geodetic observations. Almost ~90% of the seismicity beneath the field occurs within this 80 km³ ellipsoid.

12. Feigl, Kurt L., Michael A. Cardiff, Xiangfang Zeng, Neal Edward Lord, Chelsea Lancelle, Lesley Parker, Elena C. Reinisch, David Lim, Syed Tabrez Ali, Dante Fratta, Clifford H. Thurber, Herbert F. Wang, Michelle Robertson, Janice Lopeman, Corné Kreemer, Christina Morency, Nicholas Christopher Davatzes, PoroTomo Team, Thomas Coleman, and Douglas E Miller (2016), Overview and Preliminary Results from the PoroTomo project at Brady Hot Springs, Nevada: Poroelastic Tomography by Adjoint Inverse Modeling of Data from Seismology, Geodesy, and Hydrology, *American Geophysical Union Fall Meeting 2016*

In the geothermal field at Brady Hot Springs, Nevada, highly permeable conduits along faults appear to channel fluids from shallow aquifers to the deep geothermal reservoir tapped by the production wells. Subsidence occurs over an elliptical area that is ~4 km by ~1.5 km. Results from inverse modeling suggest that the deformation is a result of volumetric contraction in units with depth less than 600 m. (S. Tabrez Ali et al., *Geothermics*, 2016).

Characterizing such structures in terms of their rock mechanical properties is essential to successful operations of Enhanced Geothermal Systems (EGS). The goal of the PoroTomo project is to assess an integrated technology for characterizing and monitoring changes in the rock mechanical properties of an EGS reservoir in three dimensions with a spatial resolution better than 50 meters. The targeted rock mechanical properties include: saturation, porosity, Young's modulus, Poisson's ratio, and density, all of which are "critically important" characteristics of a viable EGS reservoir.

In March 2016, we deployed the integrated technology in a 1500-by-500-by-400-meter volume at Brady. The 15-day deployment included 4 distinct time intervals with intentional manipulations of the pumping rates in injection and production wells. The data set includes: active seismic sources, fiber-optic cables for Distributed Acoustic Sensing (DAS) and Distributed Temperature Sensing (DTS) arranged vertically in a borehole to ~400 m depth and horizontally in a trench 8700 m in length and 0.5 m in depth; 244 seismometers on the surface, 3 pressure sensors in observation wells, continuous geodetic measurements at 3 GPS stations, and 7 InSAR acquisitions. To account for the mechanical behavior of both the rock and the fluids, we are developing numerical models for the 3-D distribution of the material properties.

13. Fratta, Dante, Xiangfang Zeng, Neal Edward Lord, Lesley Parker, Herbert F Wang, Clifford H Thurber, Fan-Chi Lin, Kurt L Feigl and PoroTomo Team (2016), Horizontal-to-Vertical Spectral Ratio for Estimating Thickness of Sedimentary Deposits across the PoroTomo site in Brady Hot Springs, Nevada (USA), *American Geophysical Union Fall Meeting 2016*

During March 2016, the PoroTomo research team deployed more than 8700 m of DAS and DTS cable in horizontal and vertical sensing arrays, 244 three-component surface geophones, InSAR images, pressure transducers, and a vibroseis truck to actively and passively image the response of a geothermal field in Brady Hot Springs, Nevada. During the imaging period the geothermal field was manipulated to change the pore pressure in the formation. The objective of the study is to invert for poroelastic parameters within a 1500 m by 500 m by 400 m volume using tomographic techniques. Among the different imaging techniques, the research team is using passive horizontal-to-vertical spectral ratio data captured with the three-component geophones to estimate the thickness of the sedimentary deposits across the PoroTomo site. The interpretation of the inverted data is complicated due the heterogeneity in the near surface deposits at the site. These deposits include diatomaceous earth, sandy/silty layers, and hardened silica associated with the presence of fumaroles. In spite of the challenges associated with deposits of very different stiffness, the mapping of sediment thickness across the Natural Laboratory helps constrain the inversion of Multiple Channel Analysis of Surface Waves to improve the quality of the solution images.

14. Lord, Neal Edward, Xiangfang Zeng, Dante Fratta, Kurt L. Feigl, Herbert F. Wang, and PoroTomo Team (2016), Multispectral Analysis of Surface Wave (MASW) Analysis of Near-Surface Structure at Brady Hot Springs from Active Source and Ambient Noise Using a 8700-meter Distributed Acoustic Sensing (DAS) Array, *American Geophysical Union Fall Meeting 2016*
The PoroTomo research team deployed 8700-meters of Distributed Acoustic Sensing (DAS) cable in a shallow trench on the surface and 400 meters down a borehole at Brady Hot Springs, Nevada in March 2016. The goal of the experiment was to detect changes in geophysical properties associated with hydrologic changes. The DAS cable occupied a natural laboratory of 1500-by-500-by-400-meters overlying a commercial, geothermal field operated by Ormat Technologies. The DAS cable was laid out in three parallel zig-zag lines with line segments approximately 120-meters in length. A large Vibroseis truck (T-Rex) provided the seismic source with a sweep frequency between 5 and 80 Hz over 20 seconds. Over the 15 days of the experiment, the Vibroseis truck re-occupied approximately 250 locations outside and within the array days while changes were made in water reinjection from the power plant into wells in the field. At each source location, one vertical and two orthogonal horizontal modes were excited. Dispersion curves were constructed using MASW and a Vibroseis source location approximately in line with each DAS cable segment or from ambient noise correlation functions. Representative fence diagrams of S-wave profiles were constructed by inverting the dispersion curves obtained for several different line segments.
15. Pai, Henry, Jonathan Burnett, Chris Sladek, Michael Wing, Kurt L Feigl, John S. Selker, Scott Tyler, and PoroTomo Team (2016), Analyzing the Potential for Unmanned Aerial Systems (UAS) Photogrammetry in Estimating Surface Deformations at a Geothermal Field, *American Geophysical Union Fall Meeting 2016*
UAS systems equipped with a variety of spectral imaging devices are increasingly incorporated in spatial environmental assessments of continental surfaces (e.g., digital elevation maps, vegetative coverage classifications, surface temperatures). This presented work performed by the UAS team at the Center for Transformative Environmental Monitoring Programs (AirCTEMPS) examines the potential to measure small (sub-cm) deformation from a geothermal injection experiment at Brady's geothermal field in western Nevada (USA). Areal mapping of the 700 x 270 m area of interest was conducted with a nadir pointing Sony A5100 digital camera onboard an autopiloted quadcopter. A total of 16 ground control points were installed using a TopCon GR3 GPS receiver. Two such mapping campaigns were conducted with one before and one after an anticipated surface deformation event. A digital elevation map (DEM) for each time period was created from over 1500 images having 80% overlap/sidelap by using structure from motion (SfM) via Agisoft Photoscan software. The resulting DEM resolution was 8 mm/pixel with residual aerial triangulation errors was < 5 mm. We present preliminary results from an optimized workflow which achieved errors and average differential DEM heights between campaigns at the cm-scale which is broader than the maximum expected deformation. Despite the disconnect between error and deformation severity, this study presents a unique application of sub-cm UAS-based DEMs and further distinguishes itself by comparing results to concurrent Interferometric Synthetic Radar (InSAR). The intent of our study and presentation of results is to streamline, cross-validate, and share methods to encourage further adoption of UAS imagery into the standard toolkit for environmental surface sensing across spatial scales.

16. Parker, Lesley, Xiangfang Zeng, Clifford H. Thurber, and PoroTomo Team (2016), Assessing Multiple Methods for Determining Active Source Travel Times in a Dense Array, *American Geophysical Union Fall Meeting 2016*
238 three-component nodal seismometers were deployed at the Brady Hot Springs geothermal field in Nevada to characterize changes in the subsurface as a result of changes in pumping conditions. The array consisted of a 500 meter by 1600 meter irregular grid with 50 meter spacing centered in an approximately rectangular 1200 meter by 1600 meter grid with 200 meter spacing. A large vibroseis truck (T-Rex) was deployed as an active seismic source at 216 locations. Over the course of 15 days, the truck occupied each location up to four times. At each location a swept-frequency source between 5 and 80 Hz over 20 seconds was produced using three vibration modes: longitudinal S-wave, transverse S-wave, and P-wave. Seismic wave arrivals were identified using three methods: cross-correlation, deconvolution, and Wigner-Ville distribution (WVD) plus the Hough Transform (HT). Surface wave arrivals were clear for all three modes of vibration using all three methods. Preliminary tomographic models will be presented, using the arrivals of the identified phases.
17. Reinisch, Elena C., Syed Tabrez Ali, Michael A. Cardiff, Christina Morency, Corné Kreemer, Kurt L. Feigl, and PoroTomo Team (2016), Analysis of Interferometric Synthetic Aperture Radar Phase Data at Brady Hot Springs, Nevada, USA Using Prior Information, *American Geophysical Union Fall Meeting 2016*
Time-dependent deformation has been observed at Brady Hot Springs using interferometric synthetic aperture radar (InSAR) [Ali et al. 2016, <http://dx.doi.org/10.1016/j.geothermics.2016.01.008>]. Our goal is to evaluate multiple competing hypotheses to explain the observed deformation at Brady. To do so requires statistical tests that account for uncertainty. Graph theory is useful for such an analysis of InSAR data [Reinisch, et al. 2016, <http://dx.doi.org/10.1007/s00190-016-0934-5>]. In particular, the normalized edge Laplacian matrix calculated from the edge-vertex incidence matrix of the graph of the pair-wise data set represents its correlation and leads to a full data covariance matrix in the weighted least squares problem. This formulation also leads to the covariance matrix of the epoch-wise measurements, representing their relative uncertainties. While the formulation in terms of incidence graphs applies to any quantity derived from pair-wise differences, the modulo- 2π ambiguity of wrapped phase renders the problem non-linear. The conventional practice is to unwrap InSAR phase before modeling, which can introduce mistakes without increasing the corresponding measurement uncertainty. To address this issue, we are applying Bayesian inference. To build the likelihood, we use three different observables: (a) wrapped phase [e.g., Feigl and Thurber 2009, <http://dx.doi.org/10.1111/j.1365-246X.2008.03881.x>]; (b) range gradients, as defined by Ali and Feigl [2012, <http://dx.doi.org/10.1029/2012GC004112>]; and (c) unwrapped phase, i.e. range change in mm, which we validate using GPS data. We apply our method to InSAR data taken over Brady Hot Springs geothermal field in Nevada.

18. Wang, Herbert F., Dante Fratta, Neal Edward Lord, Chelsea Lancelle, Clifford H. Thurber, Xiangfang Zeng, Lesley Parker, Athena Chalari, Douglas Miller, Kurt L. Feigl, and PoroTomo Team (2016), Ground Motion Analysis of Co-Located DAS and Seismometer Sensors, *American Geophysical Union Fall Meeting 2016*
The PoroTomo research team deployed 8700-meters of Distributed Acoustic Sensing (DAS) cable in a shallow trench and 400-meters in a borehole at Brady Hot Springs, Nevada in March 2016 together with an array of 246, three-component geophones. The seismic sensors occupied a natural laboratory 1500 x 500 x 400 meters overlying the Brady geothermal field. The DAS cable was laid out in three parallel zig-zag lines with line segments approximately 100-meters in length and geophones were spaced at approximately 50-m intervals. In several line segments, geophones were co-located within one meter of the DAS cable. Both DAS and the conventional geophones recorded continuously over 15 days. A large Vibroseis truck (T-Rex) provided the seismic source at approximately 250 locations outside and within the array. The Vibroseis protocol called for excitation in one vertical and two orthogonal horizontal directions at each location. For each mode, three, 5-to-80-Hz upsweeps were made over 20 seconds. In addition, a moderate-sized earthquake with a local magnitude of 4.3 was recorded on March 21, 2016. Its epicenter was approximately 150-km away. Several DAS line segments with co-located geophone stations were used to test relationships between the strain rate recorded by DAS and ground velocity recorded by the geophones.
19. Zeng, Xiangfang, Clifford H. Thurber, Yan Luo, Eric Matzel, and PoroTomo Team (2016), High-resolution shallow structure revealed with ambient noise tomography on a dense array, *American Geophysical Union Fall Meeting 2016*
A dense seismic array was deployed by the PoroTomo research team at Brady Hot Springs, Nevada in March 2016. The array consisted of 238 short-period three-component geophones (5-Hz corner frequency) with about 60 m spacing. Over the 15 day deployment, the array recorded over 6,000 active source signals (vibroseis sweeps) and ambient noise that was dominated by traffic noise. We adopted the one-bit method to better reduce the effect of the active source. Spectral whitening was performed between 0.5 and 2 Hz. The continuous record was chopped into 1 minute segments. The 1-minute cross-correlation functions were initially stacked linearly, and then the phase-weighted stacking method was applied to improve signal quality. More than two million noise correlation functions (NCFs) have been obtained. The Rayleigh wave group velocity was measured on the symmetric component of the NCFs with the frequency-time analysis method. The average group velocity is about 400 m/s at 4 Hz, which is consistent with preliminary active source result. To avoid mis-picking possible precursors, the arrival time was picked at the peak in a two-second time window predicted with the average group velocity of the fundamental mode. The quality of the arrival measurements is defined by the signal-to-noise ratio. We were able to pick reliable arrivals at about 35% of the station-pairs. Since the straight-ray assumption may not be valid in a strongly heterogeneous medium, the wave path was traced with a finite difference scheme and the LSQR method was utilized to invert group velocity. The heterogeneous features of the group velocity map are consistent with a local geologic map.

20. Feigl, Kurt L. and PoroTomo Team (2017), Overview and Preliminary Results from the PoroTomo project at Brady Hot Springs, Nevada: Poroelastic Tomography by Adjoint Inverse Modeling of Data from Seismology, Geodesy, and Hydrology, Paper presented at PROCEEDINGS, 42nd Workshop on Geothermal Reservoir Engineering Stanford University, Stanford, California, February 13-15, 2017, 15 p. In the geothermal field at Brady Hot Springs, Nevada, subsidence occurs over an elliptical area that is ~4 km by ~1.5 km. Highly permeable conduits along faults appear to channel fluids from shallow aquifers to the deep geothermal reservoir tapped by the production wells. Results from inverse modeling suggest that the deformation is a result of volumetric contraction in units with depth less than 600 m [Ali et al., 2016]. Characterizing such structures in terms of their rock mechanical properties is essential to successful operations of Enhanced Geothermal Systems (EGS). The goal of the PoroTomo project is to assess an integrated technology for characterizing and monitoring changes in the rock mechanical properties of an EGS reservoir in three dimensions with a spatial resolution better than 50 meters. The targeted rock mechanical properties include: saturation, porosity, Young's modulus, Poisson's ratio, and density, all of which are "critically important" characteristics of a viable EGS reservoir. In March 2016, we deployed the integrated technology in a 1500-by-500-by-400-meter volume at Brady Hot Springs. The 15-day deployment included four distinct time intervals with intentional manipulations of the pumping rates in injection and production wells. The data set includes: active seismic sources, fiber-optic cables for Distributed Acoustic Sensing (DAS) and Distributed Temperature Sensing (DTS) arranged vertically in a borehole to ~400 m depth and horizontally in a trench 8700 m in length and 0.5 m in depth; 244 seismometers on the surface, three pressure sensors in observation wells, continuous geodetic measurements at three GPS stations, and seven InSAR acquisitions. To account for the mechanical behavior of both the rock and the fluids, we are developing numerical models for the 3-dimensional distribution of the material properties.
21. Liu, Fang, Pengcheng Fu, Robert J. Mellors, Mitchell Plummer, Tabrez Ali, Elena C. Reinisch, Qi Liu, and Kurt L. Feigl (2017), Inferring geothermal reservoir processes at the Raft River Geothermal Field, Idaho, USA through modeling InSAR-measured surface deformation, Paper presented at PROCEEDINGS, 42nd Workshop on Geothermal Reservoir Engineering Stanford University, Stanford, California, February 13-15, 2017, 11 p. Ground surface deformations detected with Interferometric Synthetic Aperture Radar (InSAR) provide valuable information for inferring subsurface reservoir processes that are difficult to observe directly. This study aims at building a reservoir model that honors the available geological, hydrological and geo-mechanical data and also produces ground surface deformation consistent with InSAR measurements. In our coupled thermo-hydro-mechanical (THM) model, the reservoir deforms as a result of the rock's poroelastic response to changes in hydrologic pressure and thermal expansion/contraction. The computations are performed using a massively parallel multi-physics code (GEOS) at the scale of the geothermal field. At Raft River, the results indicate that the observed deformation cannot be caused solely by pressure changes in the deep production reservoir, and that pressure increase in a shallower reservoir that accommodates the injected fluid (likely in the Salt Lake Formation) must be involved. The rising pressure in the shallow reservoir generates strong uplift at ground surface. The combination of this uplift with surface subsidence around the production wells creates a complex pattern of surface deformation in which the center of subtle subsidence significantly deviates from the location of the production wells. The net pressure in the shallow reservoir may gradually diffuse into the moderately permeable layer underneath, resulting in additional slow deformation. Therefore, the surface deformation captured by InSAR represents a combination of multiple mechanisms acting over different time scales. A parametric study suggests that the Bridge Fault Zone is likely a barrier, impeding laterally flow cross the fault, although the fault could serve as a fast flow path along the strike direction. The surface deformation data appear to be insensitive to the presence of the Narrows Structure (i.e., a poorly defined northeast-southwest trending structure within the deep geothermal reservoir), since removing the Narrows Structure from the model does not substantially change the modeled deformation pattern at the surface. A flow barrier likely exists to the east of the site, where the surface uplift forms a band striking from north to south. This case study demonstrates the utility of a forward model that honors available known information and THM coupled processes in understanding geothermal reservoir characteristics.

22. Matzel, Eric, Xiangfang Zeng, Clifford Thurber, Yan Luo, Christina Morency, and PoroTomo Team (2017), Seismic Interferometry Using the Dense Array at the Brady Geothermal Field, Paper presented at *PROCEEDINGS, 42nd Workshop on Geothermal Reservoir Engineering Stanford University, Stanford, California, February 13-15, 2017*, 4 p.
- In March 2016, as part of the Poroelastic Tomography experiment, a large seismic array was deployed over the geothermal field at Brady's Hot Springs in Nevada. This array recorded more than two weeks of continuous data, including several local and regional earthquakes, vibroseis sweeps, and local traffic noise, as well as the ambient seismic wavefield. In this study, we use several methods of seismic interferometry to investigate the site. We focus on three techniques: Shot interferometry uses the energy from the vibroseis sweeps as sources of high frequency energy. Coda interferometry isolates the energy from the scattered wavefield of distant earthquakes. Ambient noise correlation uses the energy of the ambient background field. In each case, the data recorded at one seismometer are correlated with the data recorded at another to obtain an estimate of the Green's function between the two. The 240 geophones, concentrated over a 1.5 square-kilometer area, allow us to calculate nearly 30,000 paths, which we use to characterize the site and measure the localized wavefield.
23. Zeng, Xiangfang, Clifford Thurber, Herb Wang, Dante Fratta, Eric Matzel, and PoroTomo Team (2017), High-resolution Shallow Structure Revealed with Ambient Noise Tomography on a Dense Array, Paper presented at *PROCEEDINGS, 42nd Workshop on Geothermal Reservoir Engineering Stanford University, Stanford, California, February 13-15, 2017*, 5 p.
- In March 2016, the PoroTomo Team deployed a dense seismic array to image the structure of the Brady Hot Springs geothermal reservoir in Nevada. At this site, a 4 km by 1.5 km elliptical subsidence area was observed by analyzing InSAR images (Ali et al., 2016). The array was composed of 244 short-period, three-component geophones and ~8,600 m of distributed acoustic sensing (DAS) fiber-optic cable installed in surface trenches plus ~350 m installed in a borehole. The geophone array provided about 60 m spatial sampling whereas sampling of the surface DAS was nominally 1 m. The acquisition system provided 15 days of continuous records that were used to calculate noise cross-correlation functions (NCFs). NCF cans be treated as empirical Green's functions and used in ambient noise tomography. The surface wave dispersion curves were obtained from the NCFs between geophones pairs and pairs of DAS channels. The dispersion curves were inverted for shear wave velocity profiles in different locations of the array. A low velocity zone is associated with the area of subsidence obtained from InSAR.
24. Feigl, Kurt L. and The PoroTomo Team, including Michael A. Cardiff, Xiangfang Zeng, Neal E. Lord, Chelsea Lancelle, David D. Lim, Lesley Parker, Elena C. Reinisch, S. Tabrez Ali, Dante Fratta, Clifford H. Thurber, Herbert F. Wang, Michelle Robertson, Thomas Coleman, Douglas E. Miller Janice Lopeman, Paul Spielman, John Akerley, Corné Kreemer, Christina Morency, Eric Matzel, Whitney Trainor-Guitton, Samir Jreij, and Nicholas C. Davatzes (26 May 2017), Coupled processes and material properties at Brady Hot Springs, Nevada: Overview of the PoroTomo project (Poroelastic Tomography by Adjoint Inverse Modeling of Data from Seismology, Geodesy, and Hydrology), presented at the Seismological Laboratory at the California Institute of Technology in Pasadena

25. Thurber, C. X. Zeng, L. Parker, N. Lord, D. Fratta, H. Wang, E. Matzel, M. Robertson, K. L. Feigl, and PoroTomo Team (2017), Imaging Seismic Structure of Geothermal Reservoir with Large N Array at Brady Hot Springs, Nevada, *Seismological Society of America 2017 Annual Meeting*

In March 2016, we deployed a dense seismic array to image the structure of the Brady Hot Springs geothermal reservoir in Nevada, where a 4 km * 1.5 km elliptical subsidence area was observed with InSAR (Ali et al., 2016). The array was composed of 244 short-period, three-component geophones and 9,000 m of distributed acoustic sensing (DAS) fiber-optic cable installed in surface trenches plus 400 m installed in a borehole. The geophone array provided about 60 m spatial sampling while sampling of the surface DAS was about 1 m. The acquisition system provided 15 days of continuous records including active source and ambient noise signals.

A large vibroseis truck (T-Rex) was operated at 191 locations to excite a swept-frequency signal from 5 to 80 Hz over 20 seconds using three vibration modes. The cross-correlation method was utilized to retrieve waveforms from the geophone records. The first arrivals (P-wave) were automatically picked from the cross-correlation functions and the travel times were used to invert the P-wave velocity structure.

Multichannel analysis of surface waves was used on the DAS records to measure phase velocity of Rayleigh waves between 5 and 20 Hz, providing S-wave velocity structure information.

The ambient noise tomography method was also applied to the continuous geophone and DAS records. The geophone array provided more than twenty thousand noise cross-correlation functions. The group velocity dispersion curves of Rayleigh and Love waves were measured between 2 and 4 Hz using the frequency-time analysis method. The average group velocity is about 400 m/s, which is consistent with preliminary active source results. A low velocity zone is also observed in the area of greatest subsidence.

26. Jreij, Samir, Whitney Trainor-Guitton, and Douglas Miller (2017), Field data comparison of 3D horizontal distributed acoustic sensing and geophones. *SEG Technical Program Expanded Abstracts 2017*, 6 p.

<https://doi.org/10.1190/segam2017-17793499.1>

The use of surface horizontal DAS fiber to characterize reservoirs has not been thoroughly studied previously. This study focuses on a comparison between horizontal DAS and multicomponent geophone data using common receiver gather data. The east-component of a geophone was rotated to align with a section of DAS data. Then, synthetic modeling was conducted to discuss conversion between DAS strain to particle velocity data in order to create a comparison between the two datasets. The DAS broadside sensitivity is present when comparing the two common receiver gathers as it is not able to resolve certain waves that the east-component of the geophone is able to. Although the DAS data do not resolve all events that the geophone is able to, there is still coherent reflection events that encourage further studies of horizontal distributed systems. A reverse time migration of all the geophone data using a rudimentary velocity model shows coherent reflectors. It is expected that DAS will show equivalent levels of data quality when the data are migrated.

27. Matzel, Eric, Xiangfang Zeng, Cliff Thurber, Christina Morency, Kurt Feigl, and PoroTomo Team (2017), Using Virtual Earthquakes to Characterize the Material Properties of the Brady Hot Springs, Nevada, *GRC Transactions* **41**, 7 p.

<https://e-reports-ext.llnl.gov/pdf/883964.pdf>

In this study, we demonstrate the power of seismic interferometry for use in imaging and monitoring the Brady geothermal field. Two types of interferometry are compared, ambient noise correlation (ANC), and interferometry of active vibroseis sweep sources (SI). When applied to the large, dense array of seismometers that were deployed at the site, these techniques allow detailed measurements of the physical characteristics, in particular, seismic velocity and attenuation.

28. Cronin, Shane Patrick, Whitney Trainor-Guitton, PoroTomo Team, Andrew Pare, Semir Jreij, and Hayden Powers (2017), Integration of DAS (distributed acoustic sensing) vertical seismic profile and geostatistically modeled lithology data to characterize an enhanced geothermal system, *American Geophysical Union Fall Meeting 2017*

In March 2016, a 4-week field data acquisition took place at Brady's Natural Lab (BNL), an enhanced geothermal system (EGS) in Fallon, NV. During these 4 weeks, a vibe truck executed 6,633 sweeps, recorded by nodal seismometers, horizontal distributed acoustic sensing (DAS) cable, and 400 meters of vertical DAS cable. DAS provides lower signal to noise ratio than traditional geophones but better spatial resolution. The analysis of DAS VSP included Fourier transform, and filtering to remove all up-going energy. Thus, allowing for accurate first arrival picking. We present an example of the Gradual Deformation Method (GDM) using DAS VSP and lithological data to produce a distribution of valid velocity models of BNL. GDM generates continuous perturbations of prior model realizations seeking the best match to the data (i.e. minimize the misfit). Prior model realizations honoring the lithological data were created using sequential Gaussian simulation, a commonly used noniterative geostatistical method. Unlike least-squares-based methods of inversion, GDM readily incorporates a priori information, such as a variogram calculated from well-based lithology information. Additionally, by producing a distribution of models, as opposed to one optimal model, GDM allows for uncertainty quantification. This project aims at assessing the integrated technologies ability to monitor changes in the water table (possibly to one meter resolution) by exploiting the dependence of seismic wave velocities on water saturation of the subsurface.

29. Feigl, Kurt L., Jeremy Patterson, Lesley Parker, Elena C. Reinisch, Xiangfang Zeng, Michael A. Cardiff, Dante Fratta, Neal E. Lord, Clifford H. Thurber, Herb F. Wang, Michelle Robertson, Douglas E. Miller, John Akerley, Corné Kreemer, Christina Morency, Nicholas Christopher Davatzes, and PoroTomo Team (2017), Characterization of Material Properties at Brady Hot Springs, Nevada by Inverse Modeling of Data from Seismology, Geodesy, and Hydrology, *American Geophysical Union Fall Meeting 2017*

The PoroTomo project consists of poroelastic tomography by adjoint inverse modeling of data from seismology, geodesy, and hydrology. The goal of the PoroTomo project is to assess an integrated technology for characterizing and monitoring changes in the rock mechanical properties of an enhanced geothermal system in 3 dimensions with a spatial resolution better than 50 meters. In March 2016, we deployed the integrated technology in a 1500-by-500-by-400-meter volume at Brady. The 15-day deployment included 4 distinct time intervals with intentional manipulations of the pumping rates in injection and production wells. The data set includes: active seismic sources, fiber-optic cables for Distributed Acoustic Sensing (DAS) and Distributed Temperature Sensing (DTS) arranged vertically in a borehole to ~400 m depth and horizontally in a trench 8700 m in length and 0.5 m in depth; 244 seismometers on the surface, 3 pressure sensors in observation wells, continuous geodetic measurements at 3 GPS stations, and 7 InSAR acquisitions.

To account for the mechanical behavior of both the rock and the fluids, we are developing numerical models for the 3-D distribution of the material properties. We present an overview of results, including: 1) Tomographic images of P-wave velocity estimated from seismic body waves [Thurber et al., this meeting]. 2) Tomographic images of phase velocity estimated from ambient noise correlation functions [Zeng et al., this meeting]. 3) Models of volumetric contraction to account for subsidence observed by InSAR and GPS [Reinisch et al., this meeting]. 4) Interpretation of pressure and temperature data [Patterson et al., this meeting].

Taken together, these results support a conceptual model of highly permeable conduits along faults channeling fluids from shallow aquifers to the deep geothermal reservoir tapped by the production wells.

30. Fratta, Dante, Chelsea Lancelle, Esra Ak, Neal E. Lord, Herb F. Wang, and PoroTomo Team (2017), Distributed Acoustic Sensing (DAS) Array near a Highway for Traffic Monitoring and Near-Surface Shear-Wave Velocity Profiles, *American Geophysical Union Fall Meeting 2017*
Monitoring traffic is important for many technical reasons. It allows for better design of future roads and assessment of the state of current roads. The number, size, weight, and speed of vehicles control deterioration rate. Also, real-time information supplies data to intelligent information systems to help control traffic. Recently there have been studies looking at monitoring traffic seismically as vibrations from traffic are not sensitive to weather and poor visibility. Furthermore, traffic noise can be used to image S-wave velocity distribution in the near surface by capturing and interpreting Rayleigh and Love waves (Nakata, 2016; Zeng et al. 2016). The capability of DAS for high spatial sampling (1 m), temporal sampling (up to 10 kHz), and distributed nature (tens of kilometers) allows for a closer look at the traffic as it passes and how the speed of the vehicle may change over the length of the array. The potential and difficulties of using DAS for these objectives were studied using two DAS arrays. One at Garner Valley in Southern California (a 700-meter array adjacent to CA Highway 74) and another in Brady Hot Springs, Nevada (an 8700-meter array adjacent to Interstate 80). These studies experimentally evaluated the use of DAS data for monitoring traffic and assessing the use of traffic vibration as non-localized sources for seismic imaging. DAS arrays should also be resilient to issues with lighting conditions that are problematic for video monitoring and it may be sensitive to the weight of a vehicle. This study along a major interstate provides a basis for examining DAS' potential and limitations as a key component of intelligent highway systems.
31. Patterson, Jeremy, Michael A. Cardiff, David Lim, Thomas Coleman, Herb F. Wang, Kurt L. Feigl, and PoroTomo Team (2017), Characterization of Hydrologic and Thermal Properties at Brady Geothermal Field, NV, *American Geophysical Union Fall Meeting 2017*
Understanding and predicting the temperature evolution of geothermal reservoirs is a primary focus for geothermal power plant operators ensuring continued financial sustainability of the resource. Characterization of reservoir properties - such as thermal diffusivity and hydraulic conductivity - facilitates modeling efforts to develop a better understanding of temperature evolution. As part of the integrated "PoroTomo" experiment, borehole pressure measurements were collected in three monitoring wells of various depths under varying operational conditions at the Brady Geothermal Field near Reno, NV. During normal operational conditions, a vertical profile of borehole temperature to 330 m depth was collected using distributed temperature sensing (DTS) for a period of 5 days. Borehole pressure data indicates 2D flow and shows rapid responses to changes in pumping /injection rates, likely indicating fault-dominated flow. The temperature data show that borehole temperature recovery following cold water slug injection is variable with depth. Late time vertical temperature profiles show the borehole following a shallow geotherm to a depth of approximately 275 meters, below which the temperature declines until a depth of approximately 320 meters, with a stable zone of cold water forming below this, possibly indicating production-related thermal drawdown. A validated heat transfer model is used in conjunction with the temperature data to determine depth-dependent reservoir thermal properties. Hydraulic reservoir properties are determined through inversion of the collected pressure data using MODFLOW. These estimated thermal and hydraulic properties are synthesized with existing structural and stratigraphic datasets at Brady.

32. Reinisch, Elena C., Kurt L. Feigl, Michael A. Cardiff, Christina Morency, Corné Kreemer, John Akerley, and PoroTomo Team (2017), Characterizing Volumetric Strain at Brady Hot Springs, Nevada, USA Using Geodetic Data, Numerical Models, and Prior Information, *American Geophysical Union Fall Meeting 2017* Time-dependent deformation has been observed at Brady Hot Springs using data from the Global Positioning System (GPS) and interferometric synthetic aperture radar (InSAR) [e.g., Ali et al. 2016, <http://dx.doi.org/10.1016/j.geothermics.2016.01.008>]. We seek to determine the geophysical process governing the observed subsidence. As two end-member hypotheses, we consider thermal contraction and a decrease in pore fluid pressure. A decrease in temperature would cause contraction in the subsurface and subsidence at the surface. A decrease in pore fluid pressure would allow the volume of pores to shrink and also produce subsidence. To simulate these processes, we use a dislocation model that assumes uniform elastic properties in a half space [Okada, 1985]. The parameterization consists of many cubic volume elements (voxels), each of which contracts by closing its three mutually orthogonal bisecting square surfaces. Then we use linear inversion to solve for volumetric strain in each voxel given a measurement of range change. To differentiate between the two possible hypotheses, we use a Bayesian framework with geostatistical prior information. We perform inversion using each prior to decide if one leads to a more geophysically reasonable interpretation than the other.
33. Thurber, Clifford H., Lesley Parker, Peng Li, Dante Fratta, Xiangfang Zeng, Kurt L. Feigl, Esra Ak, Neal Lord, and PoroTomo Team (2017) Active-Source Seismic Tomography at Bradys Geothermal Field, Nevada, with Dense Nodal and Fiber-Optic Seismic Arrays, *American Geophysical Union Fall Meeting 2017*
We deployed a dense seismic array to image the shallow structure in the injection area of the Brady Hot Springs geothermal site in Nevada. The array was composed of 238 5 Hz, three-component nodal instruments and 8,700 m of distributed acoustic sensing (DAS) fiber-optic cable installed in surface trenches plus about 400 m installed in a borehole. The geophone array had about 60 m instrument spacing in the target zone, whereas DAS channel separations were about 1 m. The acquisition systems provided 15 days of continuous records including active source and ambient noise signals. A large vibroseis truck (T-Rex) was operated at 196 locations, exciting a swept-frequency signal from 5 to 80 Hz over 20 seconds using three vibration modes. Sweeps were repeated up to four times during different modes of geothermal plant operation: normal operation, shut-down, high and oscillatory injection and production, and normal operation again.
The cross-correlation method was utilized to remove the sweep signal from the geophone records. The first P arrivals were automatically picked from the cross-correlation functions using a combination of methods, and the travel times were used to invert for the 3D P-wave velocity structure. Models with 100 m and 50 m horizontal node spacing were obtained, with vertical node spacing of 10 to 50 m. The travel time data were fit to about 30 ms, close to our estimated picking uncertainty. We will present our 3D V_p model and the result of our search for measurable temporal changes, along with preliminary results for a 3D V_s model.

34. Zeng, Xiangfang, Clifford H. Thurber, Herb F. Wang, Dante Fratta, and Porotomo Team (2017), 3D shear wave velocity structure revealed with ambient noise tomography on a DAS array, *American Geophysical Union Fall Meeting 2017*

An 8700-m Distributed Acoustic Sensing (DAS) cable was deployed at Brady's Hot Springs, Nevada in March 2016 in a 1.5 by 0.5 km study area. The layout of the DAS array was designed with a zig-zag geometry to obtain relatively uniform areal and varied angular coverage, providing very dense coverage with a one-meter channel spacing. This array continuously recorded signals of a vibroseis truck, earthquakes, and traffic noise during the 15-day deployment. As shown in a previous study (Zeng et al., 2017), ambient noise tomography can be applied to DAS continuous records to image shear wave velocity structure in the near surface. To avoid effects of the vibroseis truck operation, only continuous data recorded during the nighttime was used to compute noise cross-correlation functions for channel pairs within a given linear segment. The frequency band of whitening was set at 5 to 15 Hz and the length of the cross-correlation time window was set to 60 second. The phase velocities were determined using the multichannel analysis of surface waves (MASW) methodology. The phase velocity dispersion curve was then used to invert for shear wave velocity profiles. A preliminarily velocity model at Brady's Hot Springs (Lawrence Livermore National Laboratory, 2015) was used as the starting model and the sensitivity kernels of Rayleigh wave group and phase velocities were computed with this model. As the sensitivity kernel shows, shear wave velocity in the top 200 m can be constrained with Rayleigh wave group and phase velocities in our frequency band. With the picked phase velocity data, the shear wave velocity structure can be obtained via Occam's inversion (Constable et al., 1987; Lai 1998). Shear wave velocity gradually increases with depth and it is generally faster than the Lawrence Livermore National Laboratory (2015) model. Furthermore, that model has limiting constraints at shallow depth. The strong spatial variation is interpreted to reflect the different sediments and sediment thicknesses in the near surface. Shear wave velocities in the northeast corner of the tested area is high whereas loose soil reduces shear wave velocities in the central part of the tested area. This spatial variation pattern is very similar to the results obtained with the ambient noise tomography using the 238-geophone array used the experiment.

35. Akerley, John Feigl, Kurt L. Feigl, Michael A. Cardiff, Patrick Walsh, and Sam Batzli (2018), Analysis of a Long-Term Test by Inverse Modeling Surface Deformation as Measured by InSAR, Paper presented at *PROCEEDINGS, 43rd Workshop on Geothermal Reservoir Engineering Stanford University, Stanford, California, February 12-14, 2018*, 9 p.

Following the completion of a production well and an injection well at an undeveloped geothermal field in Nevada, a long-term flow test was conducted to measure and understand reservoir characteristics. Measurements were made several times daily of variables including: volumetric flow rate of injection, volumetric flow rate of production, downhole pressure in production wells and wellhead pressure in the injection well. To better understand reservoir flow paths, a chemical tracer was also injected in the injection well. To measure the deformation, we use Interferometric Synthetic Aperture Radar (InSAR). Interferometric pairs of SAR images acquired every 11 days during the test show uplift around the injection well. To interpret the deformation field, we perform inverse modeling using the General Inversion of Phase Technique (GIPhT). This study demonstrates the value of combining InSAR data with conventional data to constrain models of reservoir characteristics and rock properties. For example, the modeled volume change estimated from the InSAR data is comparable to the value measured at the wellhead. Similarly, by matching the modeled pressure value to the measured value, we expect to be able to constrain the bulk modulus at the field scale.

36. Feigl, Kurt L. and PoroTomo Team (2018), Overview and Preliminary Results from the PoroTomo project at Brady Hot Springs, Nevada: Poroelastic Tomography by Adjoint Inverse Modeling of Data from Seismology, Geodesy, and Hydrology, Paper presented at *PROCEEDINGS, 43rd Workshop on Geothermal Reservoir Engineering Stanford University, Stanford, California, February 12-14, 2018*, 13 p.
- In the geothermal field at Brady Hot Springs, Nevada, subsidence occurs over an elliptical area that is ~4 km by ~1.5 km. Highly permeable conduits along faults appear to channel fluids from shallow aquifers to the deep geothermal reservoir tapped by the production wells. Results from inverse modeling suggest that the deformation is a result of volumetric contraction in units with depth less than 600 m [Ali et al., 2016]. Characterizing such structures in terms of their rock-mechanical properties is essential to successful operations of Enhanced Geothermal Systems (EGS). The goal of the PoroTomo project is to assess an integrated technology for characterizing and monitoring changes in the rock-mechanical properties of an EGS reservoir in three dimensions with a spatial resolution better than 50 meters. In March 2016, we deployed the integrated technology in a 1500-by-500-by-400-meter volume at Brady Hot Springs. The data set includes: active seismic sources, fiber-optic cables for Distributed Acoustic Sensing (DAS) and Distributed Temperature Sensing (DTS) arranged vertically in a borehole to ~400 m depth and horizontally in a trench 8700 m in length and 0.5 m in depth, 244 seismometers on the surface, three pressure sensors in observation wells, continuous geodetic measurements at three GPS stations, and seven InSAR acquisitions. The deployment consisted of four distinct time intervals ("stages"). Between each measurement interval, the hydrological conditions were intentionally manipulated by modifying the rates of pumping in the injection and production wells. To account for the mechanical behavior of both the rock and the fluids, we are developing numerical models for the 3-dimensional distribution of the material properties. In this paper, we provide a snapshot of work in progress, including the highlights listed in the Conclusions below.
37. Jreij, Samir F., Whitney J. Trainor-Guitton, James L. Simmons, and PoroTomo Team (2018), Improving Point-Sensor Image Resolution with Distributed Acoustic Sensing at Brady's Enhanced Geothermal System, Paper presented at *PROCEEDINGS, 43rd Workshop on Geothermal Reservoir Engineering Stanford University, Stanford, California, February 12-14, 2018*, 12 p.
- To date, investigations into the deployment and ability of surface horizontal distributed acoustic sensing (DAS) fiber to characterize reservoirs has been lacking compared to borehole DAS configurations, which has been more prevalent for well diagnostics and vertical seismic profiles. Existence of three-component (3C) geophones and surface DAS fiber at Brady's enhanced geothermal system motivates this study. We review principles of compressional wave (P-wave) and shear wave (S-waves; SV and SH) particle motion and how these waves are recorded on horizontal DAS fiber as a function of their emergent angle. Note that vertical (P-wave) and orthogonal horizontal (S-wave) vibrators were used at Brady's making the consideration of S-waves potentially important. We then use elastic synthetic prestack modeling and prestack elastic Reverse-Time-Migration (RTM) to explore the joint use of geophone and DAS data for subsurface seismic imaging. In particular, we use different combinations of the geophone and DAS data as input to RTM, and then document the extent to which the Brady fault model geometry is recovered by the imaging. The migrated images demonstrate that surface DAS can improve imaging resolution over that obtained from sparse geophones alone.

38. Miller, Douglas E., Thomas Coleman, Xiangfang Zeng, Jeremy R. Patterson, Elena C. Reinisch, Michael A. Cardiff, Herbert F. Wang, Dante Fratta, Whitney Trainor-Guitton, Clifford H. Thurber, Michelle Robertson, Kurt Feigl, and The PoroTomo Team (2018), DAS and DTS at Brady Hot Springs: Observations about Coupling and Coupled Interpretations, Paper presented at *PROCEEDINGS, 43rd Workshop on Geothermal Reservoir Engineering Stanford University, Stanford, California, February 12-14, 2018*, 13 p.
- In March 2016 an extensive integrated survey was performed at the geothermal field at Brady Hot Springs, Nevada, where highly permeable conduits along faults appear to channel fluids from shallow aquifers to the deep geothermal reservoir tapped by the production wells. The 15-day deployment included 4 distinct time intervals with intentional manipulations of the pumping rates in injection and production wells. The data set included, fiber-optic cables for Distributed Acoustic Sensing (DAS) and Distributed Temperature Sensing (DTS) arranged vertically in a borehole to ~400 m depth and horizontally in a trench 8700 m in length. The vertical installation in well 56-1 was organized quickly after an initial deployment in well 55-1 failed when an in-well calcification collapsed under the weight of sand which was intended to improve coupling between the fiber cable and borehole wall. Well 56-1 was drilled to 732m in 1991 and completed with a cemented production casing to 314m and a slotted liner between 314m and 369m. (All depths referenced to KB 6.7m above ground level.) 369m of 3.2mm (1/8 in) optical fiber in metal tube (FIMT) cable was deployed into the well. It contained both single-mode and multi-mode fibers with optical U-bends at the bottom. Silixa DTS and DAS interrogators were operated to continuously monitor the installation for 8 days. In addition to providing active and passive seismic waveform data, the DAS was processed to extract fiber slow strain at a rate comparable to the DTS (2 samples/min). Material will be presented that reviews and discusses observable phenomena that supplement and constrain processing algorithms and interpretations.
39. Patterson, Jeremy R., Michael Cardiff, Thomas Coleman, Herb Wang, Kurt L. Feigl, John Akerley, and Paul Spielman (2018), Geothermal Reservoir Characterization Using Distributed Temperature Sensing at Brady Geothermal Field, Nevada, Paper presented at *PROCEEDINGS, 43rd Workshop on Geothermal Reservoir Engineering Stanford University, Stanford, California, February 12-14, 2018*, 6 p.
- Distributed temperature sensing (DTS) systems provide near real-time data collection that captures borehole spatiotemporal temperature dynamics. Temperature data were collected in an observation well at an active geothermal site for a period of eight days under geothermal production conditions. Collected temperature data showcase the ability of DTS systems to detect changes to the location of the steam-water interface, visualize borehole temperature recovery - following injection of a cold-water slug - and identify anomalously warm and/or cool zones. The high sampling rate and spatial resolution of DTS data also shows borehole temperature dynamics that are not captured by traditional pressure-temperature survey tools. Inversion of thermal recovery data using a finite-difference heat-transfer model produces a thermal-diffusivity profile that is consistent with laboratory-measured values and correlates with identified lithologic changes within the borehole. Used alone or in conjunction with complementary data sets, DTS systems are useful tools for developing a better understanding of both reservoir rock thermal properties as well as within and near borehole fluid movement.

40. Trainor-Guitton, Whitney, Antoine Guitton, Samir Jreij, Hayden Powers, C. Bane Sullivan, James Simmons, and PoroTomo Team (2018), 3D Imaging from vertical DAS fiber at Brady's Natural Laboratory, Paper presented at *PROCEEDINGS, 43rd Workshop on Geothermal Reservoir Engineering Stanford University, Stanford, California, February 12-14, 2018*, 10 p.
- Faults play an important role in geothermal fluid transport and can also present a contrast in acoustic impedance such that seismic methods can approximately locate their presence in the subsurface. In March 2016, a continuous active seismic survey collected 184 three-component shots while a vertical DAS cable was in place 150 to 280 meters below surface. First forward modeling was performed to understand the volume of illumination given the location of the vertical DAS cable and the geometry of the vibe shot. Reverse time migration (RTM), a prestack depth migration was used. The modeling domain is 1560m by 915m by 1500m in x, y, and z respectively. Two horizontal reflectors that extended through the entire modeling domain at depths 700m and 1,100m respectively were used demonstrate how much of the image could be accounted for the illumination and not migration artifacts, using the most current velocity model for the area (Matzel et al., 2017). It was confirmed given approximately 30 meters of reliable fiber in the well and the geometry of the vibe shots, a 300 by 100 by 500 m (depth) volume can successfully recover the 2 horizontal reflectors. Next, imaging of the current fault model of Brady's (Siler and Faulds, 2013) was performed to analyze if certain fault dips and strikes would be detectable given the shot geometry. The final reflectivity model indicated faults passing through the well and as far away as 1km could be imaged with well-processed data, assuming the velocity model well represents the true subsurface. Finally, the real data was migrated to analyze the resolving power of the DAS cable. Some shots present stronger P to S reflections than P-P. Thus, a P to S migration was performed additionally using the Vp for the down-going waves and Vs for the up-going.
41. Matzel, E., C. Morency, K. Feigl, and C. Thurber (2018), Imaging Seismic Attenuation at the Brady Geothermal Field Using Interferometry, *Seismological Association of America: 2018 Seismology of the Americas*
- The Poroelastic Tomography experiment (PoroTomo) was conducted in March 2016 at Brady Hot Springs in Nevada. A key goal of the experiment is to understand how fluids travel from shallow aquifers, through faults and fractures, to deep geothermal reservoirs. As part of the effort, seismic, geodetic, and hydraulic technologies were tested and developed to fully characterize the rock mechanical properties. This abstract focuses on the application of seismic interferometry to image variations in seismic attenuation at the site. During the experiment, a large seismic array was deployed and recorded more than two weeks of continuous data, active vibroseis sweeps, local traffic noise, and the ambient seismic wavefield. In this study, we use several methods of seismic interferometry to investigate the site. We focus on two techniques: sweep interferometry uses the energy from the vibroseis sweeps as sources of high frequency energy; ambient noise correlation uses the energy of the ambient background field. In each case, the data recorded at one seismometer are correlated with the data recorded at another to obtain an estimate of the Green function between the two. The 238 geophones, concentrated over a 1.5 square-kilometer area, allow us to calculate nearly 30,000 paths, which we use to characterize the site and measure the localized wavefield. In collaboration with Ormat, pressures were changed during four stages of operation, including shutdown, followed by increased injection and pulsing. These changes caused measurable differences in the material properties beneath the site including the attenuation of seismic energy. We use two methods to study the changes in seismic attenuation at the site. The simplest is to measure the normalized amplitudes of the Green functions and to compare the values during each stage of operation. The second is to model the full waveform of the data, separating out contributions of Qs and Qp. Because P and S have different sensitivity to fluids in fractures and pores, the ratio of Qs/Qp is highly sensitive to the fluid saturation. We see anomalously high values of Qs/Qp at depth at the injection site and following fault boundaries. Over the course of the experiment, we observe large changes in attenuation across the site, bounded by structural features.

42. Nayak, Avinash, Clifford Thurber, Lesley Parker, Peng Li, Dante Fratta, Xiangfang Zeng, Esra Ak, Kurt Feigl, Neal Lord, and PoroTomo Team (2018), Seismic Tomography at Brady Geothermal Field, Nevada, with Dense Nodal and Fiber-Optic Seismic Arrays, *Seismological Society of America 2018 Annual Meeting*
We deployed dense seismic arrays to image the shallow structure in the injection area of the Brady Hot Springs geothermal site in Nevada. The arrays were composed of 238 5 Hz, three-component nodal instruments and ~9,000 m of distributed acoustic sensing (DAS) fiber-optic cable installed in surface trenches plus ~400 m installed in a borehole. The geophone array had an instrument spacing of about 60 m in the target zone, whereas DAS channel separations were about 1 m, with a 10 m averaging (gauge) length. The acquisition systems provided 15 days of continuous data including active source and ambient noise signals. A large vibroseis truck was operated at 191 locations, exciting a swept-frequency signal from 5 to 80 Hz over 20 seconds using three vibration directions. Sweeps were repeated up to four times during different stages of geothermal plant operation: initial normal operation, shut-down, high and oscillatory injection and production, and final normal operation again. After removing the sweep signals, the first P-wave arrivals were automatically picked using a combination of methods. The resulting travel times were used to invert for the 3D P-wave velocity structure. Models with 100 m and 50 m horizontal node spacing were obtained, with vertical node spacing of 10 to 50 m. The travel time data were fit to about 30 ms, close to our estimated picking uncertainty. However, many automatic picks were of poor quality, and parts of the 3D model were not well resolved due to a lack of picks for some nodes and vibe points. We are carrying out a second round of automatic picking using trace-to-trace correlation, with high-quality, reviewed picks as the master traces for the correlations. We will present our updated 3D P-wave velocity model along with comparisons to other existing information for the structure at the Brady site. We will also present preliminary results from a search for temporal changes in P-wave travel times caused by the changes in fluid injection and production.
43. Jreij, Samir F., Whitney J. Trainor-Guitton, and James L. Simmons (2018), Determining the Added Value of Surface Distributed Acoustic Sensors in Sparse Geophone Arrays using Transfer Learning in a Convolutional Neural Network, *SEG Technical Program Expanded Abstracts 2018*, 4693-4697
<https://library.seg.org/doi/abs/10.1190/segam2018-2997965.1>
Distributed sensors have widely been used in boreholes and their added value is apparent in these environments. Surface acquisitions with distributed sensors have not been quite as successful due to the limited understanding of the types of waves that the instrument records. This paper discusses experiments to identify if there is any added value to using distributed acoustic sensors with sparse geophone arrays in 2-D surface acquisition. The results qualitatively show that 2-D surface DAS arrays are able to recover migrated images similar to sparse, multi-component geophone arrays. Quantitative analysis was also performed using transfer learning in a convolutional neural network. The quantitative analysis shows that adding distributed sensors for this experiment only helped in decreasing false negatives and increasing the true negatives in identifying reflectors. This paper provides the framework for future quantitative analysis in the geophysics field using machine learning.

44. Trainor-Guitton, Whitney, Samir Jreij, Antoine Guitton, and James Simmons (2018), Fault Classification from 3D Imaging of a Vertical DAS Profile, *SEG Technical Program Expanded Abstracts 2018*, 4664-4668
<https://library.seg.org/doi/abs/10.1190/segam2018-2989447.1>
Faults play an important role in geothermal fluid transport and can also present a contrast in acoustic impedance such that seismic methods can approximately locate their presence in the subsurface. Brady Natural Lab is a geothermal reservoir that has numerous faults that allow for both recharge and deep-to-shallow heat exchange via subsurface fluids. In March 2016 at Brady, a continuous active seismic survey collected 191 3-mode vibe points, while a vertical DAS cable was in place 150 to 280 meters below surface. Imaging of both synthetic and field data was performed to analyze if certain fault dips and strikes would be detectable given the shot geometry. Coherent structures exist that are consistent with 3 faults: the fault farthest from the DAS well at distance of 750m to the northeast, and two Western-dipping faults below the well that contains the DAS. Lastly, convolution neural networks were used to obtain an agnostic, quantitative measure of the reliability of detecting faults from images derived from DAS. A transfer learning approach utilized layers of convolutional neural networks trained on the ImageNet repository.
45. Feigl, Kurt L. and PoroTomo Team (2018b), Overview of Results and Lessons Learned from the PoroTomo project at Brady Hot Springs, Nevada: Poroelectric Tomography by Adjoint Inverse Modeling of Data from Seismology, Geodesy, and Hydrology, *GRC Transactions*, p 599-622
In the geothermal field at Brady Hot Springs, Nevada, subsidence occurs over an elliptical area that is ~4 km by ~1.5 km. Highly permeable conduits along faults appear to channel fluids from shallow aquifers to the deep geothermal reservoir tapped by the production wells. Results from inverse modeling suggest that the deformation is a result of volumetric contraction in units with depth less than 600 m (Ali et al., 2016). Characterizing such structures in terms of their rock-mechanical properties is essential to successful operations of Enhanced Geothermal Systems (EGS). The goal of the PoroTomo project is to assess an integrated technology for characterizing and monitoring changes in the rock-mechanical properties of an EGS reservoir in three dimensions with a spatial resolution better than 50 meters. In March 2016, we deployed the integrated technology in a 1500-by-500-by-400-meter volume at Brady Hot Springs. The integrated technology analyzes data from multiple arrays of sensors, including: active seismic sources, fiber-optic cables for Distributed Acoustic Sensing (DAS) and Distributed Temperature Sensing (DTS) arranged vertically in a borehole to ~400 m depth and horizontally in a trench 8700 m in length and 0.5 m in depth, 246 three-component seismometers on the surface, three pressure sensors in observation wells, continuous geodetic measurements at three GPS stations, and seven satellite images using Synthetic Aperture Radar (SAR). The deployment consisted of four distinct time intervals ("stages"). Between each measurement interval, the hydrological conditions were intentionally manipulated by modifying the rates of pumping in the injection and production wells. To account for the mechanical behavior of both the rock and the fluids, we are developing numerical models for the 3-dimensional distribution of the material properties. In this paper, we summarize the highlights of the project, emphasizing the lessons learned that will apply to experiments at the FORGE site.

46. Fratta, Dante, Esra Ak, Lesley Parker, Clifford H. Thurber (2018), Particle Velocity Polarization for the Evaluation of Body and Surface Waves in the Brady Hot Springs Geothermal Site in Northwest Nevada, *American Geophysical Union Fall Meeting 2018*

As part of the PoroTomo Project, active and passive seismic data were collected with a three-dimensional seismogram array in order to image petrophysical properties of a 1500-m by 500-m by 400-m volume in a geothermal field in Brady Hot Springs, Nevada. We intended to use the arrival of multiple phases including P-, S-, Rayleigh, and Love waves to invert for the distribution of Young's modulus, shear modulus, Poisson's ratio and density with an expected resolution of 50 m or better at a depth of up to 200 m. Since the determination of arrival times of S- and surface waves is challenging, we are using Wigner-Ville Distribution decomposition plus the Hough Transform and polarization techniques to interpret waves triggered by a vibroseis and captured by a three-dimensional Nodal seismographs. The determination of body and surface waves travel time arrivals were masked by the changes in the expected particle velocity polarizations caused by anisotropy and heterogeneity of the formation. In spite of these challenges the obtained results provide constraints and a-priori information for autopickers. These results can then be used in the overall interpretation of travel times for the tomographic images of the Brady Hot Springs geothermal volume.

47. Feigl, Kurt L, Lesley Parker, Jeremy R. Patterson, Elena C. Reinisch, Avinash Nayak, Xiangfang Zeng, Michael A. Cardiff, Neal E. Lord, Dante Fratta, Clifford H. Thurber, Herbert F. Wang, Michelle Robertson, Thomas Coleman, Douglas E. Miller, John Akerley, Corne Kreemer, Christina Morency, Eric Matzel, Whitney Trainor-Guitton, Nicholas C. Davatzes (2018), Overview of Results and Lessons Learned from the PoroTomo project at Brady Hot Springs, Nevada: Poroelastic Tomography by Adjoint Inverse Modeling of Data from Seismology, Geodesy, and Hydrology, *American Geophysical Union Fall Meeting 2018*

In the geothermal field at Brady Hot Springs, Nevada, subsidence occurs over an elliptical area that is ~4 km by ~1.5 km. Characterizing such structures in terms of their rock-mechanical properties is essential to successful operations of Enhanced Geothermal Systems (EGS). The goal of the PoroTomo project is to assess an integrated technology for characterizing and monitoring changes in the rock-mechanical properties of an EGS reservoir in 3 dimensions with a spatial resolution better than 50 meters. In March 2016, we deployed the integrated technology in a 1500-by-500-by-400-meter volume at Brady Hot Springs. The data set includes: active seismic sources, fiber-optic cables for Distributed Acoustic Sensing (DAS) and Distributed Temperature Sensing (DTS) arranged vertically in a borehole to ~400 m depth as well as horizontally in a trench 8700 m in length and 0.5 m in depth, 246 seismometers on the surface, 3 pressure sensors in observation wells, continuous geodetic measurements at three GPS stations, and 7 InSAR acquisitions. The deployment consisted of four distinct time intervals ("stages"). Between each measurement interval, the hydrological conditions were intentionally manipulated by modifying the rates of pumping in the injection and production wells. To account for the mechanical behavior of both the rock and the fluids, we are developing numerical models for the 3-dimensional distribution of the material properties. Overall, the data sets collected at Brady Hot Springs support a conceptual model of highly permeable conduits along faults channeling fluids from shallow aquifers to the deep geothermal reservoir tapped by the production wells.

48. Matzel, Eric, Christina Morency, Clifford H. Thurber, Kurt L. Feigl (2018), Observing Changes in fluid Pressure at the Brady Geothermal field using Seismic Interferometry, *American Geophysical Union Fall Meeting*

The Poroelastic Tomography experiment (PoroTomo) was conducted in March 2016 at Brady Hot Springs in Nevada. A key goal of the experiment is to understand how fluids travel from shallow aquifers, through faults and fractures, to deep geothermal reservoirs. As part of the effort, seismic, geodetic, and hydraulic technologies were tested and developed to fully characterize the rock mechanical properties.

During the experiment, a large seismic array was deployed and recorded more than two weeks of continuous data, active vibroseis sweeps, local traffic noise, and the ambient seismic wavefield. In this study, we use several methods of seismic interferometry to investigate the site. We focus on two techniques: sweep interferometry uses the energy from the vibroseis sweeps as sources of high frequency energy. Ambient noise correlation uses the energy of the ambient background field. In each case, the data recorded at one seismometer are correlated with the data recorded at another to obtain an estimate of the Green function between the two. The 238 geophones, concentrated over a 1.5 square-kilometer area, allow us to calculate nearly 30,000 paths, which we use to characterize the site and measure the localized wavefield.

In collaboration with Ormat, pressures were changed during four stages of operation, including shutdown, followed by increased injection and pulsing. These changes caused measurable differences in the material properties beneath the site, including the attenuation of seismic energy. We see fault-bounded variations in attenuation from one stage to the next, with areas undergoing subsidence becoming more seismically efficient.

We use two methods to study the changes in seismic attenuation at the site. The simplest is to measure the normalized amplitudes of the Green functions and to compare the values during each stage of operation. The second is to waveform model the data, separating out contributions of Qs and Qp. Because P and S have different sensitivity to fluids in fractures and pores, the ratio of Qs/Qp is highly sensitive to the fluid saturation. We see anomalously high values of Qs/Qp at depth at the injection site and following fault boundaries.

B. Technologies/Techniques:

Software for performing interpolation, as well as other utility functions are available as open-source software at: <https://github.com/feigl/PoroTomo>

C. Status Reports:

- Research Performance Progress Report for Q1 (2014/10/01 – 2014/12/31)
- Research Performance Progress Report for Q2 (2015/01/01 – 2015/03/31)
- Research Performance Progress Report for Q3 (2015/04/01 – 2015/06/30)
- Research Performance Progress Report for Q4 (2015/07/01 – 2015/09/31)
- Research Performance Progress Report for Q5 (2015/10/01 – 2015/12/31)
- Research Performance Progress Report for Q6 (2016/01/01 – 2016/03/31)
- Research Performance Progress Report for Q7 (2016/04/01 – 2016/06/30)
- Research Performance Progress Report for Q8 (2016/07/01 – 2016/09/31)
- Research Performance Progress Report for Q9 (2016/10/01 – 2016/12/31)
- Research Performance Progress Report for Q10 (2017/01/01 – 2017/03/31)
- Research Performance Progress Report for Q11 (2017/04/01 – 2017/06/30)
- Research Performance Progress Report for Q12 (2017/07/01 – 2017/09/31)
- Research Performance Progress Report for Q13 (2017/10/01 – 2017/12/31)
- Research Performance Progress Report for Q14 (2018/01/01 – 2018/03/31)
- Research Performance Progress Report for Q15 (2018/04/01 – 2018/06/30)
- Research Performance Progress Report for Q16 (2018/07/01 – 2018/09/31)

Research Performance Progress Report for Q17 (2018/10/01 – 2018/12/31)

D. Media Reports:

Gordon, S. (2015), Better data tools for a bigger geothermal future

<https://www.engr.wisc.edu/better-data-tools-for-a-bigger-geothermal-future/>

E. Invention Disclosures:

None.

F. Patent Applications:

None.

G. Licensed Technologies:

None.

H. Networks/Collaborations Fostered:

Research into the suitability of DAS as a seismic instrument at Garner Valley produced several products in collaboration with PoroTomo team members. These include:

Baldwin, Jonathan A. (2015), Developing a Multichannel Analysis of Surface Waves (MASW) Method for Application to Distributed Acoustic Sensing (DAS) Array and Co-Located Seismometers at Garner Valley, California, M.S. Thesis, University of Wisconsin, Madison, 50 p.

Since its introduction by Park, et. al. (1999) Multichannel Analysis of Surface Waves has been an invaluable geophysical technique for geotechnical site investigation. The technique is primarily used to develop the velocity profile of shear waves passing through the subsurface at shallow depths. Traditionally this method relies on a series or array of geophones or other sensors. In recent years, a new technology has been developed known as Distributed Acoustic Sensing (DAS) that can be used to measure ground motion at high spatial resolutions. The purpose of this paper is to develop a technique for MASW investigation, utilizing a seismometer array, which can be used to examine the results from DAS relative to traditional sensors. Data were collected at the George E. Brown Jr. Network for Earthquake Engineering Simulation's Garner Valley Downhole Array, run by University of California Santa-Barbara using arrays of vertically oriented seismometers and accelerometers placed around the site. Various techniques, including Time-Frequency Filtering (TFF) and Moving Window Cross Correlations (MWCC) were used to extract surface wave dispersion results from these measurements. An SASW site investigation of the GVDA by Stokoe et al. (2004) was used as a comparison for the dispersion curves to validate the technique. Preliminary DAS results collected at the site and processed using the same methods by collaborators on the project are also compared with the seismometer results. Final seismometer results are then inverted to develop shear-wave velocity profiles of the GVDA using the Surface Wave Modal Inversion (SWAMI) tool, created by Lai and Rix (1998).

Baldwin, A., D. Fratta, H. Wang, N. Lord, A. Chalari, B. Nigbor, E. Castongia, and C. Lancelle (2014), Using Distributed Acoustic Sensing (DAS) for Multichannel Analysis of Surface Waves (MASW) to Evaluate Ground Stiffness, *American Geophysical Union Fall Meeting 2014*.

Since its introduction by Park et al. (1999), Multichannel Analysis of Surface Waves (MASW) has become an invaluable geophysical technique for geotechnical site investigation. The technique is primarily focused on developing 2-D and 3-D shear stiffness vs. depth images of the near surface. MASW involves measuring surface waves of various frequencies produced by a seismic source, such as a sledgehammer or vibroseis source, which is evaluated to determine the velocity of the shear waves propagating through the subsurface at shallow depths. Traditionally, this technique relies on a long string of geophones as receivers. However, our study utilized a Distributed Acoustic Sensor array to detect ground motion caused by passing surface waves at a spatial resolution of one meter. The purpose of this investigation is to compare the effectiveness of using a DAS array for MASW data collection instead of traditional geophones. Data were collected at the Network for Earthquake Engineering Simulation's Garner Valley Downhole Array site (NEES's GVDA). Various time-frequency filtering and moving window cross correlation (MWCC) techniques were examined for extracting the surface wave dispersion. The results were found to be in good agreement with those previously obtained by Stokoe et al. (2004).

Lancelle, C., N. Lord, H. Wang, D. Fratta, R. Nigbor, A. Chalari, R. Karaulanov, J. Baldwin, and E. Castongia (2014), Directivity and Sensitivity of Fiber-Optic Cable Measuring Ground Motion using a Distributed Acoustic Sensing Array (abstract # NS31C-3935), American Geophysical Union Fall Meeting 2014

Distributed acoustic sensing (DAS) is a relatively recent development for measurement of ground motion by using a fiber-optic cable itself as the sensor. In September 2013 a field test was conducted at the NEES@UCSB Garner Valley field site in Southern California incorporating DAS technology. A 762 meter long fiber-optic cable was trenched to a depth of about 0.3 m in a rectangular design with two interior diagonal segments. Existing instruments at the field site include the Garner Valley Downhole Array (GVDA) surface and borehole accelerometers and pore pressure transducers. A PASSCAL seismometer array and four NEES@UCLA tri-axial accelerometers were also deployed along the two interior diagonal segments. These sensors also recorded most of the source events. One goal of the field test was to study the response of the fiber-optic cable to various vibration sources, including a 45 kN shear shaker and a smaller 450 N portable mass shaker, both of which were available through NEES@UCLA. In addition to the shear sources, signals were recorded from a mini-Vibe source and hammer blows on a steel plate. The focus of this study is on the directivity and the sensitivity of the fiber-optic cable and the distributed acoustic sensor. Preliminary results indicate that the fiber-optic cable is most effective if oriented in the direction of maximum strain. Even with the directional response, signals were recorded throughout the array for different cable orientations at distances up to two-hundred meters. Move-out of different phases could be seen over several meters of traces recorded one-meter apart. Sensitivity of the fiber-optic cable relative to the other instruments is also presented.

Lord, N., H. Wang, D. Fratta, C. Lancelle, A. Baldwin, B. Nigbor, A. Chalari, and E. Castongia (2014), Surface Wave Dispersion Analysis Using Time-Frequency Filtering and an Interactive Normal Move Out (NMO) Tool with Uncorrelated Garner Valley Vibroseis Data, *American Geophysical Union Fall Meeting 2014*

Frequency swept seismic sources (vibroseis) recorded by seismic arrays can be used to directly measure the surface wave apparent velocity as a function of frequency. Time-frequency filtering (TFF) passes only a narrow frequency band centered on the time varying frequency of the seismic source. This greatly improves the quality of the uncorrelated seismic data by removing noise outside of the narrow band filter. Sources of noise include traffic, harmonics generated by the seismic source and the propagating seismic waves. TFF also allows the separate analysis of the source fundamental frequency and each harmonic. The filtered data is used with an interactive normal move out (NMO) tool to adjust the time and apparent velocity parameters to extract a surface wave dispersion curve. This technique was used on the vibroseis data collected in the September 2013 seismic experiment conducted at the NEES@UCSB Garner Valley field site. Three vibroseis sources were used: a 45 KN shear shaker, a 450 N portable mass shaker, and a 26 KN vibroseis truck. They were recorded by two lines of 1 and 3 component accelerometers and geophones, and a Distributed Acoustic Sensor (Silixa-iDAS™) system connected to 762 m of trenched fiber optical cable in a larger rectangular area.

Wang, H., N. Lord, A. Chalari, C. Lancelle, J. Baldwin, E. Castongia, D. Fratta, R. Nigbor, and R. Karaulanov (2014), Field Trial of Distributed Acoustic Sensing Using Active Sources at Garner Valley, California (abstract # NS41C-07), *American Geophysical Union Fall Meeting 2014*

An optical fiber Distributed Acoustic Sensor array was deployed in a shallow trench at the site of the Garner Valley Downhole Array (GVDA) in southern California. The site was operated as a collaborator of the Network for Earthquake Engineering Simulation (NEES) by UCSB. The fiber-optic cable layout approximated a rectangle whose dimensions were roughly 160 meters by 80 meters. The layout included two subdiagonals to provide a variety of orientations of the cable relative to source locations. The study included different seismic sources deployed at a number of surveyed positions: a 45 kN shear shaker operated at the site by NEES@UCLA, a portable 450 N shaker, a small Vibroseis truck, and hammer blows on a steel plate to map cable locations. Several dozen separate tests were recorded in which each test typically included ten repeats. The data were utilized for several studies. First, the characteristics of the recorded signals were analyzed for directivity and sensitivity of the cable response (Lancelle et al., 2014, this meeting). The DAS system recorded dynamic ground events in the direction of the cable and hence comparisons with geophones required signal processing. The one-meter spacing of DAS traces could be well correlated over distances of a few meters. Second, swept-sine sources were used to obtain surface-wave velocity dispersion to determine near-surface shear-wave velocity distribution using Multispectral Analysis of Surface Waves (MASW) (Baldwin et al., 2014, this meeting). The results were in good agreement with previous Vibroseis results at the site (Stokoe et al. 2004). Third, a new method for time-frequency filtering was developed for extracting the surface-wave phase velocities from uncorrelated receiver traces (Lord et al., 2014, this meeting).

Following discussions at the Stanford Geothermal workshops and the GTO Peer Review in 2015, we collaborated with researchers studying the Raft River geothermal field in Idaho. The resulting studies were published in peer-reviewed journals:

Ali, S. T., E. C. Reinisch, J. Moore, M. Plummer, I. Warren, N. C. Davatzes, and K. L. Feigl (2018), Geodetic measurements and numerical models of transient deformation at Raft River geothermal field, Idaho, USA, *Geothermics*, 74, 106-111. <http://dx.doi.org/10.1016/j.geothermics.2018.02.007>

We perform synthetic aperture radar interferometry using data acquired between 2004 and 2016 by the Envisat, and ALOS-2 satellite missions to measure transient deformation at the Raft River geothermal field in Cassia County in Southern Idaho where geothermal production began in late 2007. Time-series analysis of multiple interferometric pairs indicates uplift at an exponentially decaying rate, over an ~8 km-by-5 km area centered near three injection wells that recycle produced brine. Similarly, subsidence at an exponentially decaying rate is observed in a 4 km-by-4 km area west of the production wells. These two signatures remain in the same location in all of the well-correlated Envisat interferometric pairs spanning the time interval between 2007 and 2010. The boundary separating the uplifting and subsiding areas is associated with the steeply dipping Bridge fault zone. Using two-dimensional numerical models, we explore first-order, bi-directional coupling between hydrological and mechanical processes. Our results suggest that: (i) most of the deformation occurs due to pore pressure changes following the start of geothermal production, (ii) the rate of deformation decays to zero over a time scale on the order of ~5 years as the system reaches steady state, and (iii) a reservoir-scale permeability of the order of $\sim 10^{-14} \text{ m}^2$ is required to explain the transient deformation.

Liu, F., P. Fu, R. J. Mellors, M. A. Plummer, S. T. Ali, E. C. Reinisch, Q. Liu, and K. L. Feigl (2018), Inferring Geothermal Reservoir Processes at the Raft River Geothermal Field, Idaho, USA, Through Modeling InSAR-Measured Surface Deformation, *Journal of Geophysical Research: Solid Earth*, 123, 3645-3666. <https://doi.org/10.1029/2017JB015223>

Ground surface deformations detected with interferometric synthetic aperture radar provide valuable information for inferring subsurface reservoir processes that are difficult to observe directly. This study aims at building a reservoir model that honors the available geological, hydrological, and geomechanical data and also produces ground surface deformation consistent with interferometric synthetic aperture radar measurements at the Raft River Geothermal Field. In the thermo-hydro-mechanical coupled model developed, the reservoir deforms as a result of the rock's poroelastic response to changes in hydrologic pressure and thermal expansion/contraction. The results indicate that the observed deformation is the result of pressure decrease in the deep production reservoir and pressure increase in a shallower reservoir that accommodates the injected fluid (likely in the Salt Lake Formation). The combination of the uplift around injection wells with subsidence around the production wells, affected by the Bridge Fault as a flow barrier, creates a complex pattern of surface deformation in which the center of subtle subsidence significantly deviates from the location of the production wells. A parametric study suggests that (a) the Bridge Fault Zone is likely a flow barrier, (b) the surface deformation appears to be insensitive to the presence of the Narrows Structure, and (c) additional flow barriers likely exist to shape the flow system. This case study demonstrates the utility of a high-fidelity forward model that honors available known information and thermo-hydro-mechanical coupled processes in understanding geothermal reservoir characteristics.

We collaborated with two researchers, Jim Faulds and Nicholas Hinz, at the Nevada Bureau of Mines and Geology (NBMG) on the campus of the University of Nevada, Reno. Building on work by Dr. Drew Siler (now at LBL), they developed a sophisticated 3-D geologic model of the Brady Natural Laboratory using the EarthVision software. We communicated with Jeff Waggoner (LLNL) about using the EarthVision software. His expertise is considerable and appreciated.

Our collaborator Scott Tyler and his group at University of Nevada, Reno flew several flights of an Uninhabited Autonomous Vehicle (UAV) over the Natural Laboratory at Brady Hot Springs, Nevada during the PoroTomo deployment in March 2016. The UAV operations were performed by the Center for Transformative Environmental Monitoring Programs (CTEMPs <http://ctemps.org/>) at no cost to DOE.

We have shared the DAS data set collected during the PoroTomo deployment in March 2016 with Zhongwen Zhan at the California Institute of Technology. As a result, he submitted an abstract and published a paper, as follows.

Muir, J. B., and Z. Zhan (2017), S33B-0867: Reconstructing the Seismic Wavefield using Curvelets and Distributed Acoustic Sensing Wednesday, 13 December 2017, 13:40 - 18:00, New Orleans Ernest N. Morial Convention Center - Poster Hall D-F, in *Fall Meeting American Geophysical Union*, edited, New Orleans. Distributed Acoustic Sensing (DAS) offers an opportunity to produce cost effective and uniquely dense images of the surface seismic wavefield - DAS also produces extremely large data volumes that require innovative methods of data reduction and seismic parameter inversion to handle efficiently. We leverage DAS and the super-Nyquist sampling enabled by compressed sensing of the wavefield in the curvelet domain to produce accurate images of the horizontal velocity within a target region, using only short (~1-10 minutes) records of either active seismic sources or ambient seismic signals. Once the wavefield has been fully described, modern "tomographic" techniques, such as Helmholtz tomography or Wavefield Gradiometry, can be employed to determine seismic parameters of interest such as phase velocity. An additional practical benefit of employing a wavefield reconstruction step is that multiple heterogeneous forms of instrumentation can be naturally combined - therefore in this study we also explore the addition of three component nodal seismic data into the reconstructed wavefield. We illustrate these techniques using both synthetic examples and data taken from the Brady Geothermal Field in Nevada during the PoroTomo (U. Wisconsin Madison) experiment of 2016.

Li, Z., and Z. Zhan (2018), Pushing the limit of earthquake detection with distributed acoustic sensing and template matching: a case study at the Brady geothermal field, *Geophys. J. Int.*, 215, 1583-1593.
<http://dx.doi.org/10.1093/gji/ggy359>

Template matching has been widely applied in the detection of earthquakes and other seismic events due to its power in detecting weak signals. Recent studies using synthetics have shown that application of template matching to large-N arrays can potentially detect earthquakes substantially below the noise level. Here we apply template matching to the distributed acoustic sensing (DAS) data recorded in the Brady Hot Springs geothermal field, Nevada. Using 5 catalogued events, we detect 116 events and find 68 of them well below the noise level. We confirm 112 events are true earthquakes by examining the patterns of their sensor-to-sensor cross-correlation sections. This demonstrates that the combination of DAS and template matching has capability to detect microseismicity below the noise level, which is unusual for conventional seismic arrays and methods. With the updated catalogue, we observe a surge of earthquakes during the shutdown of a geothermal power plant nearby. In addition, the rapid increases in the downhole pressure record coincide with intense swarms of earthquakes. These observations show a strong correlation between the seismicity frequencies and the downhole pressure changes. Finally, we investigate several factors that may affect the detection performance and compare different strategies for spatial down-sampling, in order to provide helpful insights for future large-N design and data processing.

Similarly, PoroTomo team member Xiangfang Zeng collaborated with Lina Zhang of the Xiamen Seismic Survey Research Center to apply the noise-correlation methodology that he refined at Brady to estimate the three-dimensional shear wave velocity structure in Fujian Province, China. As a result, they submitted the following abstract.

Zhang, L., and X. Zeng (2017), T43C-0706: Three-dimensional shear wave velocity structure in Fujian Province, China, Thursday, 14 December 2017, 13:40 - 18:00, New Orleans Ernest N. Morial Convention Center - Poster Hall D-F in Fall Meeting American Geophysical Union, edited, New Orleans.

The permanent regional seismic network that consist of 100 broadband and 100 short period stations covers the Fujian Province with ~20 km spacing. During the west Taiwan Strait seismic experiment, 94 portable broadband stations were deployed in the coast region, which provides denser coverage. Combining two datasets, we utilized the ambient noise tomography technique to image shear wave velocity structure in Fujian province. The one-month continuous records of the vertical component were used to compute noise cross-correlation function (NCF). The Rayleigh wave signal between 1 and 20 seconds clearly emerges on most NCFs. The group velocity dispersion curve was obtained by the time-frequency analysis technique from symmetrical component of NCF. To reduce error of straight ray-path assumption in 2D tomography of group velocity map, the travel-time field was computed with a finite-difference scheme and the ray-path was tracing on the travel-time field. The checkerboard test suggests the resolution of 2D tomography is up to 40 km. With group velocity maps, the shear wave velocity structure of each inversion node was obtained by a linear inversion and was assembled to the final three-dimensional shear wav velocity structure. The Fuzhou and Zhangzhou basins are imaged as low velocity bodies at shallow depth. The general pattern of our model in middle crust is also consistent with geological units in this region.

On Dec 9, 2018, as part of the 2018 AGU Annual Meeting, PoroTomo team member Herb Wang collaborated with Scott Tyler and Xavier Comas to host a workshop on DAS:

Distributed Acoustic Sensing: Principles and Case Studies

The DAS workshop is patterned after many years of successful Distributed Temperature Sensing (DTS) workshops offered by the Center for Transformative Environmental Monitoring Programs (CTEMPs) the weekend before the Fall AGU meeting. The workshop will provide an overview of the technology and its principles. The technology overview will be followed by a variety of case histories that illustrate applications that include Vertical Seismic Profiling (VSP), near-surface characterization, infrastructure monitoring, mine monitoring, earthquake seismology, and CO₂ sequestration and geothermal reservoir monitoring. An opportunity is provided for vendors to describe their equipment and services as well for national laboratories to inform the workshop of their development efforts. Finally, the workshop will close with an open discussion of the future of DAS for the AGU community.

The workshop had 58 attendees, including 23 presenters.

I. Websites Featuring Project Work or Results:

A brief description of the PoroTomo project, including objectives and participants, is available on the web site of the Department of Geoscience at the University of Wisconsin-Madison: <http://geoscience.wisc.edu/geoscience/people/faculty/feigl/porotomo/>

The data sets collected and analyzed by the PoroTomo team were made available at:
<ftp://roftp.ssec.wisc.edu/>

J.1 Other Products – Theses:

49. Lancelle, Chelsea (2016), Distributed Acoustic Sensing for Imaging Near-Surface Geology and Monitoring Traffic at Garner Valley, California, PhD Thesis, University of Wisconsin, Madison, 98 p.

Distributed Acoustic Sensing (DAS) is a relatively new technology that uses a fiber-optic cable as a sensor. DAS got its start in the energy industry for borehole monitoring and more recently has started being used in horizontal arrays. The DAS technique senses strain rates every 1 m over distances of up to 100 km of cable length with sampling rates as fast as 100 kHz. This dissertation uses a horizontal DAS array in Southern California to evaluate the use of DAS for imaging near-surface geology and monitoring traffic. The first chapter uses Multichannel Analysis of Surface Waves to evaluate the response of DAS to surface waves. Dispersion curves from the DAS array match well with results from 1) other instruments at the site, 2) ambient noise correlation functions using the same DAS array, and 3) previous studies at the site. The second chapter uses the DAS array to create 2D tomographic images of the site for a number of nodal separations and the directional sensitivity of DAS is discussed. The third chapter explores the possibility of using DAS for traffic monitoring. Vehicle counts, relative amplitudes, and velocities are identified and prove DAS could be used for traffic monitoring.

50. Lim, David (2016), Investigations of approximations for modeling periodic flow in phreatic aquifers (Master's Thesis), University of Wisconsin, Madison, 77 p.
- Sinusoidal variations in the stage of a river, pumping, and other forcings can cause periodic flow in near-surface, unconfined aquifers. Modeling these continuously variable groundwater flow characteristics can be extremely time-consuming if the standard approach of using transient, two-dimensional (2D) nonlinear groundwater flow models is pursued. In this thesis, I investigate the accuracy of linearized approaches for modeling these flows in phreatic aquifers by comparing nonlinear and linear flow simulations—with varying degrees of physical accuracy and mathematical complexity—via application to archetypal conceptual models and frequency-dependent parameter estimation.
- In the first section of this thesis, using model inter-comparisons, I gain a general insight into the ability of different linearized models to accurately simulate periodic flow in unconfined aquifers. This study utilizes a 2D nonlinear variably saturated Richards-based flow model developed in COMSOL as a “baseline” for realistic flow simulations. I then perform comparisons between this model and physically less realistic, 2D nonlinear fully saturated, one-dimensional (1D) weakly nonlinear, and 1D fully linear flow models in terms of 1) the ability of less realistic models to mimic Richards' Equation; and 2) their computational efficiency. Through these model inter-comparisons, I further develop existing guidelines for when linearized models, used for simulating unconfined periodic groundwater flow, may be considered reasonable.
- In the second section of this thesis, I assess the ability of 2D linear numerical flow models to mimic more realistic, 2D nonlinear Richards-based numerical models when simulating field-scale oscillatory pumping tests in a phreatic aquifer. More specifically, both nonlinear and linear flow models were created in COMSOL and were calibrated toward data, collected at the Boise Hydrogeophysical Research Site (BHRS), for parameter estimation. Estimates of hydraulic conductivity and specific storage were obtained from each modeling approach and were compared. Estimates from both approaches had overall good agreement with estimates obtained from prior testing at the site. I find that the errors induced of using a linear, saturated model introduces a small amount of bias in this case, though neither nonlinear nor linear modeling approaches to estimating parameters is unreasonable. In addition quantifying effects from using linearized models in parameter estimation, a frequency dependence, which has been noted in the literature, in parameter estimates was also investigated. Both models showed some consistent trends in frequency dependence in both the effective hydraulic conductivity and effective diffusivity.
51. Reinisch, Elena (2016), Graph Theory for Analyzing Pair-wise Data: Application to Interferometric Synthetic Aperture Radar Data (Master's Thesis), University of Wisconsin, Madison, 82 p.
- Graph theory is useful for estimating time-dependent model parameters via weighted least-squares using interferometric synthetic aperture radar (InSAR) data. Plotting acquisition dates (epochs) as vertices and pair-wise interferometric combinations as edges defines an incidence graph. The edge-vertex incidence matrix and the normalized edge Laplacian matrix are factors in the covariance matrix for the pair-wise data. Using empirical measures of residual scatter in the pair-wise observations, we estimate the variance at each epoch by inverting the covariance of the pair-wise data. We evaluate the rank deficiency of the corresponding least-squares problem via the edge-vertex incidence matrix. We implement our method in a MATLAB software package called GraphTreeTA available on GitHub (<https://github.com/feigl/gipt>). We apply temporal adjustment to the data set described in Lu et al. (2005) at Okmok volcano, Alaska, which erupted most recently in 1997 and 2008. The data set contains 44 differential volumetric changes and uncertainties estimated from interferograms between 1997 and 2004. Estimates show that approximately half of the magma volume lost during the 1997 eruption was recovered by the summer of 2003. Between June 2002 and September 2003, the estimated rate of volumetric increase is $(6.2 \pm 0.6) \times 10^6 \text{ m}^3/\text{yr}$. Our preferred model provides a reasonable fit that is compatible with viscoelastic relaxation in the five years following the 1997 eruption. Although we demonstrate the approach using volumetric rates of change, our formulation in terms of incidence graphs applies to any quantity derived from pair-wise differences, such as wrapped phase or wrapped residuals.

52. Parker, Lesley M. (2017), Active Source 3D Seismic Tomography of Brady Hot Springs Geothermal Field, Nevada, M.S. Thesis, University of Wisconsin, Madison, 56 p.

We deployed a dense seismic array to image the shallow structure in the injection area of the Brady Hot Springs geothermal site in Nevada. The array was composed of 238 5 Hz, three-component nodal instruments and 8,700 m of distributed acoustic sensing (DAS) fiber-optic cable installed in surface trenches plus 400 m installed in a borehole. The geophone array had about 60 m instrument spacing in the target zone, whereas DAS channel separations were about 1 m. The acquisition systems provided 15 days of continuous records including active source and ambient noise signals. A large vibroseis truck (T-Rex) was operated at 196 locations exciting a swept-frequency signal from 5 to 80 Hz over 20 seconds using three vibration modes. Sweeps were repeated up to four times during different modes of geothermal plant operation: normal operation, shutdown, high and oscillatory injection and production, and normal operation again. The cross-correlation method was utilized to remove the sweep signal from the geophone records. The first P arrivals were automatically picked from the cross-correlation functions using a combination of methods, and the travel times were used to invert for the 3D P-wave velocity structure.

Models with 50 m horizontal node spacing were obtained, with vertical node spacing of 10 to 50 m. The travel time data were fit to about 30 ms, close to our estimated picking uncertainty. Boundaries between high and low velocity zones agree with previous surveys of local faults and low velocity zones near the surface correspond to fumarole locations. A rapid increase in velocity at about 50 m depth fits with borehole data on the depth of the Quaternary sediments. There is some evidence for changes in the P-wave velocity during the experiment with slower travel times at the beginning of the experiment.

53. Jreij, Samir F. (2018), The feasibility of using distributed acoustic sensors in surface seismic, M.S. Thesis, Colorado School of Mines, 92 p.

In this thesis, an imaging technique that utilizes sparsely sampled, multi-component geophone data and a dense surface distributed acoustic sensor (DAS) acquisition is proposed. The PoroTomo survey at Brady's Natural Lab consisted of 238 multi-component geophones that are spaced anywhere from 60 meters to 150 meters apart. This proves to be a difficult migration problem with such sparse spacing. Fortunately, the PoroTomo survey also included 9 km of surface DAS fiber placed in a variety of orientations. DAS, however, can only record particle motion in the direction that it is oriented. After a broad literature review, it has been found that previous surface DAS surveys have come to be inconclusive regarding the feasibility of using the fiber by itself. These studies, however, only utilize a vertical source in short offsets. Assuming a flat-layered Earth, a P-wave reflection will not show data on a DAS fiber as the particle motion is not polarized properly. The PoroTomo survey utilized a 3-C source that allowed for the testing and proof of this hypothesis.

Both 2-D and 3-D numerical experiments are performed to test the feasibility of using multi-component geophone and DAS data together. In 2-D, a reflectivity model is created from the local fault model in the PoroTomo Survey. This provided a variety of structural dips to test the imaging technique. It was found that using an S-source rather than a P-source with these models produced a much sharper resulting image. A quantitative analysis is further performed to provide an unbiased perspective on the results. The quantitative analysis utilized both energy norm image filtering and a convolutional neural network to prove that distributed sensors add value to imaging efforts with sparsely-sampled, multicomponent geophones. The 2-D example is an idealized experiment. A more extreme example is performed in 3-D to confirm the conclusions made in 2-D. A methodology to model DAS data in 3-D is presented prior to showing examples of utilizing the two data types together for imaging. The resulting images in 3-D are low frequency due to the velocity model and stability limitations. Quantitative analysis is also required for an unbiased perspective on the results. The quantitative analysis utilized only the energy norm image filtering technique in 3-D as the machine learning algorithm is not able to achieve a reasonable cross-validation accuracy. The results from energy norm image filtering show that utilizing DAS in surface surveys with a sparse multi-component geophone acquisition proves to be useful in reducing the number of false positives by a small fraction. This experiment, however, is still considered inconclusive in regards to identifying if DAS can add value to sparsely sampled geophone data because the geometry of the DAS acquisition is so unique. A more regular experiment must be performed prior to making such conclusions, so 2-D lines of fiber were utilized instead of the PoroTomo acquisition geometry. The 2-D DAS acquisition increases identifying the true positives significantly.

54. Patterson, Jeremy (2018), Understanding Constraints on Geothermal Sustainability Through Reservoir Characterization at Brady Geothermal Field, Nevada (Master's Thesis), University of Wisconsin, Madison, 129 p.

The vast supply of geothermal energy stored throughout the Earth and the exceedingly long time required to dissipate that energy makes the world's geothermal energy supply nearly limitless. As such, this resource holds the potential to provide a large supply of the world's energy demands; however, like all natural resources, it must be utilized in an appropriate manner if it is to be sustainable. Understanding sustainable use of geothermal resources requires thorough characterization efforts aimed at better understanding subsurface properties. The goal of this work is to understand which critical subsurface properties exert the most influence on sustainable geothermal production as a means to provide targeted future resource characterization strategies.

Borehole temperature and reservoir pressure data were analyzed to estimate reservoir thermal and hydraulic properties at an active geothermal site. These reservoir properties then served as inputs for an analytical model which simulated net power production over a 30-year period. The analytical model was used to conduct a sensitivity analysis to determine which parameters were most critical in constraining the sustainability of a geothermal reservoir. Modeling results reveal that the number of preferential flow pathways (i.e. fractures) used for heat transport provides the greatest impact on geothermal reservoir sustainability. These results suggest that early and pre-production geothermal reservoir exploration would achieve the greatest benefit from characterization strategies which seek to delineate the number of active flow pathways present in the system.

J.2 Other Products – Papers published in peer-reviewed journals

55. Ali, S.T., J. Akerley, E.C. Baluyut, M. Cardiff, N.C. Davatzes, K.L. Feigl, W. Foxall, D. Fratta, R.J. Mellors, P. Spielman, H.F. Wang, and E. Zemach (2016), Time-series analysis of surface deformation at Brady Hot Springs geothermal field (Nevada) using interferometric synthetic aperture radar, *Geothermics*, 61, 114-120 <https://doi.org/10.1016/j.geothermics.2016.01.008>.

We analyze interferometric synthetic aperture radar (InSAR) data acquired between 2004 and 2014, by the ERS-2, Envisat, ALOS and TerraSAR-X/TanDEM-X satellite missions to measure and characterize time-dependent deformation at the Brady Hot Springs geothermal field in western Nevada due to extraction of fluids. The long axis of the ~4 km by ~1.5 km elliptical subsiding area coincides with the strike of the dominant normal fault system at Brady. Within this bowl of subsidence, the interference pattern shows several smaller features with length scales of the order of ~1 km. This signature occurs consistently in all of the well-correlated interferometric pairs spanning several months. Results from inverse modeling suggest that the deformation is a result of volumetric contraction in shallow units, no deeper than 600 m, likely associated with damaged regions where fault segments mechanically interact. Such damaged zones are expected to extend downward along steeply dipping fault planes, providing a high permeability conduit to the production wells. Using time series analysis, we test the hypothesis that geothermal production drives the observed deformation. We find a good correlation between the observed deformation rate and the rate of production in the shallow wells. We also explore mechanisms that could potentially cause the observed deformation, including thermal contraction of rock, decline in pore pressure and dissolution of minerals over time.

56. Cardiff, Michael, David D. Lim, Jeremy R. Patterson, John Akerley, Paul Spielman, Janice Lopeman, Patrick Walsh, Ankit Singh, William Foxall, Herbert F. Wang, Neal E. Lord, Clifford H. Thurber, Dante Fratta, Robert J. Mellors, Nicholas C. Davatzes, and Kurt L. Feigl (2018), Geothermal production and reduced seismicity: Correlation and proposed mechanism, *Earth and Planetary Science Letters*, 482, 470-477, <https://doi.org/10.1016/j.epsl.2017.11.037>.
At Brady Hot Springs, a geothermal field in Nevada, heated fluids have been extracted, cooled, and re-injected to produce electrical power since 1992. Analysis of daily pumping records and catalogs of microseismicity between 2010 and 2015 indicates a statistically significant correlation between days when the daily volume of production was at or above its long-term average rate and days when no seismic event was detected. Conversely, shutdowns in pumping for plant maintenance correlate with increased microseismicity. We hypothesize that the effective stress in the subsurface has adapted to the long-term normal operations (deep extraction) at the site. Under this hypothesis, extraction of fluids inhibits fault slip by increasing the effective stress on faults; in contrast, brief pumping cessations represent times when effective stress is decreased below its long-term average, increasing the likelihood of microseismicity.
57. Castongia, Ethan, Herbert F. Wang, Neal Lord, Dante Fratta, Michael Mondanos, and Athena Chalari (2017), An Experimental Investigation of Distributed Acoustic Sensing (DAS) on Lake Ice, *Journal of Environmental and Engineering Geophysics*, 22(2), 167-176, <http://dx.doi.org/10.2113/JEEG22.2.167>.
A vibration-sensitive, Distributed Acoustic Sensor (DAS) array, using fiber-optic cables, was deployed in a triangularly shaped geometry on the frozen surface of Lake Mendota in Madison, Wisconsin, USA. The purpose of the array and testing program was to analyze the DAS response and to utilize the high spatial density of the distributed array for system response characterization in a well-constrained, small, surface array. A geophone array was also deployed to provide a reference system. The design of the array allowed us to assess the response of DAS with respect to distance from the seismic sources, the degradation of the response with length of the cable, the directivity of the fiber response with respect of the direction of the particle motion, and the quality of the signal with respect to cable type. The DAS array was examined for different cable constructions and orientations relative to the source propagation direction. Tight-buffered and loose-tube fiber-optic cable constructions were used, with both having good signal responses when well-coupled to the ice. In general, the tight-buffered cable was better suited for DAS applications. Directional sensitivity of the DAS was also inspected for several directions of wave propagation and particle motion. The results showed that the strongest DAS signals were recorded when the direction of the fiber was oriented parallel to the direction of particle motion. Finally, the DAS and geophone data sets were examined together to qualitatively determine, in conjunction with established DAS best practices, how the high spatial density offered by DAS could improve results over traditional point sensor arrays in certain situations.

58. Coleman, T. I., B. L. Parker, C. H. Maldaner, and M. J. Mondanos (2015), Groundwater flow characterization in a fractured bedrock aquifer using active DTS tests in sealed boreholes, *Journal of Hydrology*, 528, 449-462. <http://www.sciencedirect.com/science/article/pii/S0022169415004746>
In recent years, wireline temperature profiling methods have evolved to offer new insight into fractured rock hydrogeology. Important advances in wireline temperature logging in boreholes make use of active line source heating alone and then in combination with temporary borehole sealing with flexible impervious fabric liners to eliminate the effects of borehole cross-connection and recreate natural flow conditions. Here, a characterization technique was developed based on combining fiber optic distributed temperature sensing (DTS) with active heating within boreholes sealed with flexible borehole liners. DTS systems provide a temperature profiling method that offers significantly enhanced temporal resolution when compared with conventional wireline trolling-based techniques that obtain a temperature-depth profile every few hours. The ability to rapidly and continuously collect temperature profiles can better our understanding of transient processes, allowing for improved identification of hydraulically active fractures and determination of relative rates of groundwater flow. The advantage of a sealed borehole environment for DTS-based investigations is demonstrated through a comparison of DTS data from open and lined conditions for the same borehole. Evidence for many depth-discrete active groundwater flow features under natural gradient conditions using active DTS heat pulse testing is presented along with high resolution geologic and geophysical logging and hydraulic datasets. Implications for field implementation are discussed.
59. Lord, Neal, Herbert Wang, and Dante Fratta (2016), A source-synchronous filter for uncorrelated receiver traces from a swept-frequency seismic source, *Geophysics*, 81(5), P47-P55
<https://doi.org/10.1190/geo2015-0324.1>.
We have developed a novel algorithm to reduce noise in signals obtained from swept-frequency sources by removing out-of-band external noise sources and distortion caused from unwanted harmonics. The algorithm is designed to condition nonstationary signals for which traditional frequency-domain methods for removing noise have been less effective. The source synchronous filter (SSF) is a time-varying narrow band filter, which is synchronized with the frequency of the source signal at all times. Because the bandwidth of the filter needs to account for the source-to-receiver propagation delay and the sweep rate, SSF works best with slow sweep rates and moveout-adjusted waveforms to compensate for source-receiver delays. The SSF algorithm was applied to data collected during a field test at the University of California Santa Barbara's Garner Valley downhole array site in Southern California. At the site, a 45 kN shaker was mounted on top of a one-story structure and swept from 0 to 10 Hz and back over 60 s (producing useful seismic waves greater than 1.6 Hz). The seismic data were captured with small accelerometer and geophone arrays and with a distributed acoustic sensing array, which is a fiber-optic-based technique for the monitoring of elastic waves. The result of the application of SSF on the field data is a set of undistorted and uncorrelated traces that can be used in different applications, such as measuring phase velocities of surface waves or applying convolution operations with the encoder source function to obtain traveltimes. The results from the SSF were used with a visual phase alignment tool to facilitate developing dispersion curves and as a prefilter to improve the interpretation of the data.

60. Parker, L. M., C. H. Thurber, X. Zeng, N. E. Lord, D. O. Fratta, H. F. Wang, M. C. Robertson, A. M. Thomas, M. S. Karplus, A. Nayak, and K. L. Feigl (2018), Active-Source Seismic Tomography at the Brady Geothermal Field, Nevada, with Dense Nodal and Fiber-Optic Seismic Arrays, *Seismological Research Letters*, 89(5), 1629–1640, <https://doi.org/10.1785/0220180085>.
We deployed a dense seismic array to image the shallow structure in the injection area of the Brady Hot Springs geothermal power plant in western Nevada. The array was composed of 238 three-component, 5 Hz nodal instruments, 8700 m of distributed acoustic sensing (DAS) fiber-optic cable (FOC) installed horizontally in surface trenches, and 400 m of FOC installed vertically in a borehole. The geophone array had about 60 m instrument spacing in the target zone, whereas DAS channel separations were about 1 m with an averaging (gauge) length of 10 m. The acquisition systems provided 15 days of continuous records, including active-source and ambient noise signals. A large vibroseis truck was operated at 196 locations, exciting a swept-frequency signal from 5 to 80 Hz over 20 s using three vibration modes (vertical, longitudinal, and transverse), with three sweeps per mode at each site. Sweeps were repeated up to four times at each site during four different stages of power plant operation: normal operation, shutdown, high and oscillatory injection and production, and normal operation. After removal of the sweep signal from the raw data, the first P-wave arrivals were automatically picked using a combination of methods. The travel times were then used to invert for the 3D P-wave velocity structure. Models with 100 m horizontal and 20–50 m vertical node spacing were obtained, covering an area 2000 m by 1300 m, with acceptable resolution extending to about 250 m below surface. The travel-time data were fit to a root mean square (rms) misfit of 31 ms, close to our estimated picking uncertainty. Lateral boundaries between high and low velocity zones agree relatively well with the location of local faults from previous studies, and low near-surface velocities are associated with faults and fumarole locations. A sharp increase in velocity from < 1500 to > 2000 m/s at approximately 50 m below the ground surface in many parts of the study area may indicate a shallower water table than expected for the region.
61. Patterson, Jeremy R., Michael Cardiff, Thomas Coleman, Herb Wang, Kurt L. Feigl, John Akerley, and Paul Spielman (2017), Geothermal reservoir characterization using distributed temperature sensing at Brady Geothermal Field, Nevada, *The Leading Edge*, 36(12), 1024a1–1024a7, <https://doi.org/10.1190/tle36121024a1.1>.
Distributed temperature sensing (DTS) systems provide near real-time data collection that captures borehole spatiotemporal temperature dynamics. Temperature data were collected in an observation well at an active geothermal site for a period of eight days under geothermal production conditions. Collected temperature data showcase the ability of DTS systems to detect changes to the location of the steam-water interface, visualize borehole temperature recovery — following injection of a cold-water “slug” — and identify anomalously warm and/or cool zones. The high sampling rate and spatial resolution of DTS data also shows borehole temperature dynamics that are not captured by traditional pressure-temperature survey tools. Inversion of thermal recovery data using a finite-difference heat-transfer model produces a thermal-diffusivity profile that is consistent with laboratory-measured values and correlates with identified lithologic changes within the borehole. Used alone or in conjunction with complementary data sets, DTS systems are useful tools for developing a better understanding of both reservoir rock thermal properties as well as within and near borehole fluid movement.

62. Reinisch, Elena C., Michael Cardiff, and Kurt L. Feigl (2018), Characterizing Volumetric Strain at Brady Hot Springs, Nevada, USA Using Geodetic Data, Numerical Models, and Prior Information, *Geophysical Journal International*, 215(2), 1501-1513, <https://doi.org/10.1093/gji/ggy347>.
The geothermal field at Brady Hot Springs, Nevada has subsided over the past decade. Between 2004 and 2014, the rate of downward-vertical displacement was on the order of 10 mm yr⁻¹, as measured by two independent geodetic techniques: interferometric synthetic aperture radar (InSAR) and Global Positioning System. The observed deformation field forms an approximately elliptical bowl that is 4 km long and aligned with the trace of the NNE striking normal fault system. We use modeling to estimate the plausibility of pressure changes or thermal contraction as the cause of the observed subsidence. As a result, Bayesian inference favors with ‘very strong evidence’ thermal contraction over other hypotheses as the dominant driving mechanism for the observed subsidence. Using InSAR data spanning from 2016 July 22 to 2017 August 22, we estimate the volume change rate in the significantly deforming volume to be (-29 ± 3) thousand m³ yr⁻¹ and the total rate of change in thermal energy between -53 and -79 MW. We infer the total volume of cubes where the estimated volumetric strain rate is significantly different from zero with 95 per cent confidence to be 119 million m³. We find that the main region of significant cooling occurs between the injection and production well locations. This result supports the idea that highly permeable conduits along faults channel fluids from shallow aquifers to the deep reservoir tapped by the production wells.
63. Wang, Herbert F., Xiangfang Zeng, Douglas E. Miller, Dante Fratta, Kurt L. Feigl, Clifford H. Thurber, and Robert J. Mellors (2018), Ground motion response to an ML 4.3 earthquake using co-located distributed acoustic sensing and seismometer arrays, *Geophysical Journal International*, 213(3), 2020-2036, <https://doi.org/10.1093/gji/ggy182>.
The PoroTomo research team deployed two arrays of seismic sensors in a natural laboratory at Brady Hot Springs, Nevada in March 2016. The 1500 m (length) \times 500 m (width) \times 400 m (depth) volume of the laboratory overlies a geothermal reservoir. The distributed acoustic sensing (DAS) array consisted of about 8400 m of fiber-optic cable in a shallow trench and 360 m in a well. The conventional seismometer array consisted of 238 shallowly buried three-component geophones. The DAS cable was laid out in three parallel zig-zag lines with line segments approximately 100 m in length and geophones were spaced at approximately 60 m intervals. Both DAS and conventional geophones recorded continuously over 15 d during which a moderate-sized earthquake with a local magnitude of 4.3 was recorded on 2016 March 21. Its epicentre was approximately 150 km south-southeast of the laboratory. Several DAS line segments with co-located geophone stations were used to compare signal-to-noise ratios (SNRs) in both time and frequency domains and to test relationships between DAS and geophone data. The ratios were typically within a factor of five of each other with DAS SNR often greater for P-wave but smaller for S-wave relative to geophone SNR. The SNRs measured for an earthquake can be better than for active sources because the earthquake signal contains more low-frequency energy and the noise level is also lower at those lower frequencies.
Amplitudes of the sum of several DAS strain-rate waveforms matched the finite difference of two geophone waveforms reasonably well, as did the amplitudes of DAS strain waveforms with particle-velocity waveforms recorded by geophones. Similar agreement was found between DAS and geophone observations and synthetic strain seismograms. The combination of good SNR in the seismic frequency band, high-spatial density, large N and highly accurate time control among individual sensors suggests that DAS arrays have potential to assume a role in earthquake seismology.

64. Zeng, Xiangfang, Chelsea Lancelle, Clifford Thurber, Dante Fratta, Herb Wang, Neal Lord, Athena Chalaris, and Andy Clarke (2017), Properties of Noise Cross-Correlation Functions Obtained from a Distributed Acoustic Sensing Array at Garner Valley, California, *Bulletin of the Seismological Society of America* 107(2), 603-610, <http://dx.doi.org/10.1785/0120160168>.
A field test that was conducted at Garner Valley, California, on 11 and 12 September 2013 using distributed acoustic sensing (DAS) to sense ground vibrations provided a continuous overnight record of ambient noise. The energy of ambient noise was concentrated between 5 and 25 Hz, which falls into the typical traffic noise frequency band. A standard procedure (Bensen et al., 2007) was adopted to calculate noise cross-correlation functions (NCFs) for 1-min intervals. The 1-min-long NCFs were stacked using the time-frequency domain phase-weighted-stacking method, which significantly improves signal quality. The obtained NCFs were asymmetrical, which was a result of the nonuniform distributed noise sources. A precursor appeared on NCFs along one segment, which was traced to a strong localized noise source or a scatterer at a nearby road intersection. NCF for the radial component of two surface accelerometers along a DAS profile gave similar results to those from DAS channels. We calculated the phase velocity dispersion from DAS NCFs using the multichannel analysis of surface waves technique, and the result agrees with active-source results. We conclude that ambient noise sources and the high spatial sampling of DAS can provide the same subsurface information as traditional active-source methods.

J.3 Other Products: Publications in Progress

Song, Zhenghong, Xiangfang Zeng, Clifford H Thurber, Herbert F. Wang, and Dante Fratta (submitted), Imaging shallow structure with active-source surface wave signal recorded by distributed acoustic sensing arrays, *Earthquake Science*
Zeng, Xiangfang, Clifford H. Thurber, Herbert F. Wang, Dante Fratta, and Kurt L. Feigl (submitted), High-resolution Shallow Structure at Brady Hot Springs Using Ambient noise Tomography on a trenched DAS Array, *AGU DAS*
Reinisch, Elena C., Michael Cardiff, John Akerley, Corné Kreemer, and Kurt L. Feigl (expected submission March 2019), Time-series Analysis of Volume Change at Brady Hot Springs, Nevada, USA using Geodetic Data, *Journal of Geophysical Research - Solid Earth*

K. Awards, Prizes, and Recognition:

UW graduate student Chelsea Lancelle received the Outstanding Student Paper Award⁸ at the 2014 Fall Meeting of the American Geophysical Union for a presentation entitled, “Directivity and Sensitivity of Fiber-Optic Cable Measuring Ground Motion using a Distributed Acoustic Sensing Array”. This work is listed as the 2nd presentation under Section V.A. The e-poster is available through AGU’s archive of meeting abstracts on their website.

⁸ <http://ospa.agu.org/ospa/2014-fall-meeting-ospa-winners/>

References

- Akram, J., and D. W. Eaton (2016). A review and appraisal of arrival-time picking methods for downhole microseismic data. *Geophysics*, **81**, KS67-KS87.
- Ali, S. T., J. Akerley, E. C. Baluyut, M. Cardiff, N. C. Davatzes, K. L. Feigl, W. Foxall, D. Fratta, R. J. Mellors, P. Spielman, H. F. Wang, and E. Zemach (2016). Time-series analysis of surface deformation at Brady Hot Springs geothermal field (Nevada) using interferometric synthetic aperture radar. *Geothermics*, **61**, 114–120. doi:10.1016/j.geothermics.2016.01.008
- Ali, S. T. & University of Wisconsin. (2015a). Brady Geothermal Field InSAR Raw Data [data set]. Retrieved from <http://gdr.openei.org/submissions/482>. doi:10.15121/1261931
- Ali, S. T., & Feigl, K. L. (2012). A new strategy for estimating geophysical parameters from InSAR data: application to the Krafla central volcano in Iceland. *Geochemistry, Geophysics, Geosystems*, **13**(6), 18 p. doi:10.1029/2012GC004112
- Ali, S. T., J. Akerley, E. C. Baluyut, N. C. Davatzes, J. Lopeman, J. Moore, M. Plummer, P. Spielmann I. Warren, and K. L. Feigl (2016a). Geodetic measurements and numerical models of deformation: examples from geothermal fields in the western United States. *PROCEEDINGS*, 41st Workshop on Geothermal Reservoir Engineering, Stanford University, Stanford, California, February 22-24, 2016, 7 p.
- Ali, S. T., N. C. Davatzes, K. L. Feigl, H. F. Wang, W. Foxall, R. J. Mellors, J. Akerley, P. Spielman, and E. Zemach (2014). Deformation at Brady Hot Springs (Nevada) geothermal field measured by time series analysis of InSAR data. presented at American Geophysical Union Fall Meeting 2014, San Francisco.
- Ali, S. T., N. C. Davatzes, K. L. Feigl, H. F. Wang, W. Foxall, R. J. Mellors, J. Akerley, E. Zemach, and P. Spielman (2015). Deformation at Brady Hot Springs geothermal field measured by time series analysis of InSAR data. *PROCEEDINGS*, 40th Workshop on Geothermal Reservoir Engineering, Stanford University, Stanford, California, January 26-28, 2015, 5 p.
- Ali, S. T., N. C. Davatzes, R. J. Mellors, W. Foxall, P. S. Drakos, E. Zemach, C. Kreemer, H. F. Wang, and K. L. Feigl (2013). InSAR measurements and numerical models of deformation at Brady Hot Springs geothermal field (Nevada), 1995-2012. presented at American Geophysical Union Fall Meeting 2013, San Francisco.
- Ali, S. T. and K. L. Feigl (2012). A new strategy for estimating geophysical parameters from InSAR data: Application to the Krafla central volcano in Iceland. *Geochemistry, Geophysics, Geosystems*, **13**(6), 18 p., <http://dx.doi.org/10.1029/2012GC004112>.
- Ali, S.T., J. Akerley, E.C. Baluyut, M. Cardiff, N.C. Davatzes, K.L. Feigl, W. Foxall, D. Fratta, R.J. Mellors, P. Spielman, H.F. Wang, and E. Zemach (2016). Time-series analysis of surface deformation at Brady Hot Springs geothermal field (Nevada) using interferometric synthetic aperture radar. *Geothermics*, **61**, 114–120, <https://doi.org/10.1016/j.geothermics.2016.01.008>.
- Aster, R. C., B. Borchers, and C. H. Thurber (2013). *Parameter Estimation and Inverse Problems*. Boston: Elsevier Academic Press.
- Baldwin, A., D. Fratta, H. Wang, N. Lord, A. Chalari, B. Nigbor, E. Castongia, and C. Lancelle (2014). Using Distributed Acoustic Sensing (DAS) for Multichannel Analysis of Surface Waves (MASW) to Evaluate Ground Stiffness. presented at American Geophysical Union Fall Meeting 2014, San Francisco.
- Baran, I., M. P. Stewart, B. M. Kampes, Z. Perski, and P. Lilly (2003). A modification to the Goldstein radar interferogram filter. *IEEE Transactions on Geoscience and Remote Sensing*, **41**(9), 2114–2118. doi:10.1109/TGRS.2003.817212
- Bensen, G. D., M. H. Ritzwoller, M. P. Barmin, A. L. Levshin, F. Lin, M. P. Moschetti, N. M. Shapiro, and Y. Yang (2007). Processing seismic ambient noise data to obtain reliable broad-band surface wave dispersion measurements. *Geophysical Journal International*, **169**(3), 1239-1260. <https://doi.org/10.1111/j.1365-246X.2007.03374.x>.
- Berryman, J. G., and H. F. Wang (1998). Double-porosity modeling in elastic wave propagation for reservoir characterization. *SPIE Proceedings*, **3453**, 58-69. <https://doi.org/10.1117/12.323295>
- Blewitt, G., C. Kreemer, W. C. Hammond, and J. M. Goldfarb (2013). Terrestrial reference frame NA12 for crustal deformation studies in North America. *Journal of Geodynamics*, **72**, 11–24. doi:10.1016/j.jog.2013.08.004
- Bonafede, M. and C. Ferrari (2009). Analytical models of deformation and residual gravity changes due to a Mogi source in a viscoelastic medium. *Tectonophysics*, **471**(1), 4–13. doi:10.1016/j.tecto.2008.10.006
- Bourbié, T., and O. Coussy (1987). *Acoustics of Porous Media*. Paris: Éditions Technip.
- Cardiff, M., D. D. Lim, J. R. Patterson, J. Akerley, P. Spielman, J. Lopeman, ..., and K. L. Feigl (2017). Geothermal production and reduced seismicity: correlation and proposed mechanism. *Earth and Planetary Science Letters*, **482**, 470–477. doi:10.1016/j.epsl.2017.11.037
- Cardiff, M., W. Barrash, B. Malama, and M. Thoma (2011). Information content of slug tests for estimating hydraulic properties in realistic, high-conductivity aquifer scenarios. *Journal of Hydrology*, **403**, 66-82.
- Cardiff, M., W. Barrash and P. K. Kitanidis (2012). A field proof-of-concept of aquifer imaging using 3-D transient hydraulic tomography with modular, temporarily-emplaced equipment. *Water Resources Research*, **48**, 18 p. doi:10.1029/2011WR011704
- Chen, C.W., and H. A. Zebker (2000). Network approaches to two-dimensional phase unwrapping: intractability and two new algorithms. *Journal of Optical Society of America A*, **17**(3), 401–414. doi:10.1364/JOSAA.17.000401

- Coleman, T. (2013). A novel technique for depth discrete flow characterization: fibre optic distributed temperature sensing within boreholes sealed with flexible underground liners (Master's thesis). University of Guelph, Canada.
- Coleman, T. I., B. L. Parker, C. H. Maldaner, and M. J. Mondanos (2015). Groundwater flow characterization in a fractured bedrock aquifer using active DTS tests in sealed boreholes. *Journal of Hydrology*, **528**, 449-462.
- Constable, S. C., R. L. Parker, and G. G. Constable (1987). Occam's inversion: a practical algorithm for generating smooth models from electromagnetic sounding data. *Geophysics*, **52**(3), 289-300. <https://doi.org/10.1190/1.1442303>
- Coolbaugh, M.F., C. Sladek, C. Kratt, and G. Edmondo (2004). Digital mapping of structurally controlled geothermal features with GPS units and pocket computers. *GRC Transactions*, **28**, 321–325.
- Correa, J., A. Egorov, K. Tertyshnikov, A. Bona, R. Pevzner, T. Dean, B. Freifeld, and S. Marshall (2017). Analysis of signal to noise and directivity characteristics of DAS VSP at near and far offsets — A CO2CRC Otway Project data example. *The Leading Edge*, **36**(12), 994a1-994a7. <https://doi.org/10.1190/tle36120994a1.1>
- Dziewonski A.M., S. Bloch, and M. Landisman (1969). A technique for the analysis of transient seismic signals. *Bulletin of the Seismological Society of America*, **59**, 427–444.
- Efron, B. and R. Tibshirani (1986). Bootstrap Methods for Standard Errors, Confidence Intervals, and Other Measures of Statistical Accuracy. *Statistical Science*, **1**(1), 54-77. <https://doi.org/10.1214/ss/1177013817>.
- Eneva, M., Barbour, A., Adams, D., Hsiao, V., Blake, K., Falorni, G., & Locatelli, R. (2018). Satellite Observations of Surface Deformation at the Coso Geothermal Field, California, *GRC Transactions*, **42**.
- Faulds, J.E., Coolbaugh, M.F., Benoit, D., Oppiger, G., Perkins, M., Moeck, I. & Drakos, P. (2010). Structural controls of geothermal activity in the northern Hot Springs Mountains, western Nevada: the tale of three geothermal systems (Brady's, Desert Peak, and Desert Queen). *GRC Transactions*, **34**, 675–683.
- Faulds, J. E., A. R. Ramelli, M. F. Coolbaugh, N. H. Hinz, L. J. Garside, and J. H. Queen (2017). Preliminary geologic map of the Bradys geothermal area, Churchill County, Nevada (Open-File Rept. 2017-04). Nevada Bureau of Mines and Geology.
- Feigl, Kurt L. and Clifford H. Thurber (2009). A method for modelling radar interferograms without phase unwrapping: application to the M 5 FawnSkin, California earthquake of 1992 December 4. *Geophysical Journal International*, **176**(2), 491-504. <https://doi.org/10.1111/j.1365-246X.2008.03881.x>
- Feigl, K. L., Ali, S. T., Akerley, J., Baluyut, E., Cardiff, M. A., Davatzes, N. C., ... & Lopeman, J. (2015). Time-Dependent Deformation at Brady Hot Springs Geothermal Field (Nevada) Measured With Interferometric Synthetic Aperture Radar and Modeled with Multiple Working Hypotheses of Coupled Behavior. presented at American Geophysical Union Fall Meeting 2014, San Francisco.
- Folsom, M., J. Lopeman, D. Perkin, and M. Sophy (2018). Imaging shallow Outflow Alteration to Locate Productive Faults in Ormat's Brady's and Desert Peak Fields Using CSAMT. *PROCEEDINGS*, 43rd Workshop on Geothermal Reservoir Engineering, Stanford University, Stanford, California, February 12-14, 2018, 11 p.
- Foxall, W. (2016). Brady Geothermal Field Microearthquake Relocations 3D Velocity Models (data set). Retrieved from: <https://gdr.openei.org/submissions/493>.
- Francis, C., Graf, G., Edwards, P., McCraig, M., McCarthy, C., Lefebvre, A., ... Weschler, F. (1995). The ERS-2 spacecraft and its payload. *ESA Bulletin*, **83**.
- Fratta, D., Lancelle, C., Ak, E., Lord, N. E., Wang, H. F., and Porotomo Team (2017). Distributed Acoustic Sensing (DAS) Array near a Highway for Traffic Monitoring and Near-Surface Shear-Wave Velocity Profiles. presented at American Geophysical Union Fall Meeting 2017, New Orleans.
- Goldstein, R. & Werner, C. (1997). Radar ice motion interferometry, in 3rd ERS Symposium on Space at the Service of Our Environment, Florence, Italy, pp. 969–972.
- Hampshire, J.B., II, and J. O'Donnell (2013, June). The Seismic Hammer: a .16 MJoule Seismic Source with Flat Output Spectrum from 10s to 250 Hz. Presented at the Seismic Instrumentation Technology Symposium, Albuquerque, New Mexico. <https://www.iris.edu/hq/files/workshops/2013/06/posters/Hampshire.pdf>
- Herrmann, R. B. (2013). Computer programs in seismology: An evolving tool for instruction and research. *Seismological Research Letters*, **84**, 1081-1088.
- Johannessen, K., B. Drakeley, and M. Farhadiroushan (2012). Distributed Acoustic Sensing - a new way of listening to your well/reservoir (SPE 149602). abstract presented at SPE Intelligent Energy International Utrecht, The Netherlands, 27–29 March 2012.
- Jolie, E., Moeck, I. & Faulds, J.E. (2015). Quantitative structural–geological exploration of fault-controlled geothermal systems—a case study from the Basin-and-Range Province, Nevada (USA). *Geothermics*, **54**, 54–67. doi:10.1016/j.geothermics.2014.10.003
- Jones, K. R. (2014). *Infrasound Generation from the HH Seismic Hammer*. Sandia Report, SAND2014-19350, Sandia National Laboratories, Albuquerque, New Mexico, 51 p.
- Jreij, S., W. Trainor-Guitton, and J. Simmons (2018). Improving Point-Sensor Image Resolution with Distributed Acoustic Sensing at Brady's Enhanced Geothermal System. *PROCEEDINGS*, 43rd Workshop on Geothermal Reservoir Engineering, Stanford University, Stanford, California, February 12-14, 2018, 12 p.
- Kass, R.E. & Raftery, A.E. (1995). Bayes factors. *Journal of the American Statistical Association*, **90**(430), 773–795.
- Kreemer, C. and U. of Wisconsin (2018). *BRAD BRDY and BRD1 GPS Station RINEX Files 01-19-2018* (data set). Retrieved from: <https://gdr.openei.org/submissions/999>.

- Lai, C. G. (1998). *Simultaneous inversion of Rayleigh phase velocity and attenuation for near-surface site characterization* (Ph. D. Dissertation). Georgia Institute of Technology.
- Lai, C. G. & Rix, G. J. (1998). *Simultaneous inversion of Rayleigh phase velocity and attenuation for near-surface site characterization* (Report No. GIT-CEE/GEO-98-2). School of Civil and Environmental Engineering, Georgia Institute of Technology.
- Lancelle, C. (2016). *Distributed Acoustic Sensing for Imaging Near-Surface Geology and Monitoring Traffic at Garner Valley, California* (PhD Dissertation). University of Wisconsin-Madison.
- Lancelle, C., N. Lord, H. Wang, D. Fratta, R. Nigbor, A. Chalari, R. Karaulanov, J. Baldwin, and E. Castongia (2014). Directivity and Sensitivity of Fiber-Optic Cable Measuring Ground Motion using a Distributed Acoustic Sensing Array. presented at American Geophysical Union Fall Meeting 2014, San Francisco.
- Lancelle, Chelsea, Dante Fratta, Neal E. Lord, Herbert F. Wang, and Athena Chalari (2015). Active Travel-Time Tomography using a Distributed Acoustic Sensing Array. presented at American Geophysical Union Fall Meeting 2015, San Francisco.
- Lim, David, Warren Barrash, and Michael Cardiff (2015) Oscillatory Hydraulic Tomography at the Field Scale: Boise Hydrogeophysical Research Site. presented at American Geophysical Union Fall Meeting 2015, San Francisco.
- Linsey, N. J., E. R. Martin, D. S. Dreger, B. Freifeld, S. Cole, S. R. James, B. L. Biondi, and J. B. Ajo-Franklin (2017). Fiber-Optic Network Observations of Earthquake Wavefields. *Geophysical Research Letters*, **44**, 11,792-11,799. doi: 10.1002/2017GL075722
- Lord, N., H. Wang, D. Fratta, C. Lancelle, A. Baldwin, B. Nigbor, A. Chalari, and E. Castongia (2014). Surface Wave Dispersion Analysis Using Time-Frequency Filtering and an Interactive Normal Move Out (NMO) Tool with Uncorrelated Garner Valley Vibroseis Data. presented at American Geophysical Union Fall Meeting 2014, San Francisco.
- Lord, Neal E., Herb F. Wang, Dante Fratta, Chelsea Lancelle, and Athena Chalari (2015). Garner Valley Vibroseis Data Processing Using Time-Frequency Filtering Techniques to Remove Unwanted Harmonics and External Noise. presented at American Geophysical Union Fall Meeting 2015, San Francisco.
- Lord, Neal, Herbert Wang, and Dante Fratta (2016). A source-synchronous filter for uncorrelated receiver traces from a swept-frequency seismic source. *Geophysics*, **81**(5), P47-P55. https://doi.org/10.1190/geo2015-0324.1
- Lu Z., T. Masterlark, and D. Dzurisin (2005). Interferometric synthetic aperture radar study of Okmok volcano, Alaska, 1992–2003: Magma supply dynamics and postplacement lava flow deformation. *Journal of Geophysical Research: Solid Earth*, **110**(B2). https://doi.org/10.1029/2004JB003148.
- Maggi, Alessia, Carl Tape, Min Chen, Daniel Chao, Jeroen Tromp (2009). An automated time-window selection algorithm for seismic tomography. *Geophysical Journal International*, **178**(1), 257–281. https://doi.org/10.1111/j.1365-246X.2009.04099.x
- Matzel, Eric, Xiangfang Zeng, Clifford Thurber, Yan Luo, Christina Morency, and PoroTomo Team (2017a). Seismic Interferometry Using the Dense Array at the Brady Geothermal Field, PROCEEDINGS, 42nd Workshop on Geothermal Reservoir Engineering, Stanford University, Stanford, California, February 13-15, 2017, 3-6.
- Matzel, E., X. Zeng, C. Thurber, C. Morency, K. Feigl, and PoroTomo_Team (2017b), Using Virtual Earthquakes to Characterize the Material Properties of the Brady Hot Springs, Nevada paper presented at Geothermal Research Council Transactions, Salt Lake City. https://www.osti.gov/scitech/servlets/purl/1399706.
- McLeod, I.H., Cumming, I.G., Seymour, M.S. (1998). Envisat ASAR data reduction: Impact on SAR interferometry. *IEEE Transactions on Geoscience and Remote Sensing*, **36**(2), 589–602. doi:10.1109/36.662741
- Mikumo, T., & Aki, K. (1964). Determination of local phase velocity by intercomparison of seismograms from strain and pendulum instruments. *Journal of Geophysical Research*, **69**(4), 721–731.
- Miller, D., T. Coleman, and The PoroTomo Team (2018). DAS and DTS at Brady Hot Springs: Observations about Coupling and Coupled Interpretations. *PROCEEDINGS*, 43rd Workshop on Geothermal Reservoir Engineering, Stanford University, Stanford, California, February 12-14, 2018.
- Morency, C., and J. Tromp (2008). Spectral-element simulations of wave propagation in porous media. *Geophysical Journal International*, **175**(1), 301-345. http://gji.oxfordjournals.org/content/175/1/301.abstract
- Munn, J.D., T. I. Coleman, B. L. Parker, M. J. Mondanos, and A. Chalari (2017). Novel cable coupling technique for improved shallow distributed acoustic sensor VSPs. *Journal of Applied Geophysics*, **138**, 72–79, doi: 10.1016/j.jappgeo.2017.01.007.
- Nakata, N., et al. (2011). Shear wave imaging from traffic noise using seismic interferometry by cross-coherence. *Geophysics*, **76**(6), SA97-SA106. https://doi.org/10.1190/geo2010-0188.1.
- Nathwani, J., E. Majer, K. Boyle, D. Rock, J. Peterson, and S. Jarpe (2011). DOE real-time seismic monitoring at enhanced geothermal system sites. *PROCEEDINGS*, Thirty-sixth workshop on Geothermal Reservoir Engineering, Stanford University, Stanford, California, January 31- February 2, 2011, 6 p.
- Okada, Yoshimitsu (1985). Surface deformation due to shear and tensile faults in a half-space. *Bulletin of the Seismological Society of America*, **75**(4), 1135-1154.
- Okada, Y. (1992). Internal deformation due to shear and tensile faults in a half-space. *Bulletin of the Seismological Society of America*, **82**(2), 1018–1040.
- Onyango, E. A., L. L. Worthington, R. E. Abbott, and L. A. Preston (2018). Dense Array Seismic Study of a Legacy Underground Nuclear Test at the Nevada National Security Site. presented at American Geophysical Union Fall Meeting 2018, Washington, D.C.

- Park, Choon B., Richard D. Miller, and Jianghai Xia (1999). Multichannel analysis of surface waves. *Geophysics*, **64**(3), 800-808. <https://doi.org/10.1190/1.1444590>.
- Park, C. and Carnevale, M. (2010). Optimum MASW survey-revisit after a decade of use. *GeoFlorida 2010: Advances in Analysis, Modeling and Design*, ASCE Conference Proceedings, 20-24 February 2010, West Palm Beach, FL. [https://doi.org/10.1061/41095\(365\)130](https://doi.org/10.1061/41095(365)130)
- Park, C. B., R. D. Miller, J. Xia, and J. Ivanov (2007). Multichannel analysis of surface waves (MASW)—active and passive methods. *The Leading Edge*, **32**, 656-662. doi:10.1190/tle32060656.1.
- Parker, L. M., C. H. Thurber, X. Zeng, N. E. Lord, D. Fratta, H. F. Wang, M. C. Robertson, A. M. Thomas, M. S. Karplus, A. Nayak, and K. L. Feigl (2018). Active-source seismic tomography at the Brady Geothermal Field, Nevada, with dense nodal and fiber-optic seismic arrays. *Seismological Research Letters*, **89**, 1629-1640, doi:10.1785/0220180085.
- Patterson, J., M. Cardiff, T. Coleman, H. Wang, K. Feigl, J. Akerley, and P. Spielman (2017). Geothermal reservoir characterization using distributed temperature sensing at Brady Geothermal Field, Nevada. *Leading Edge*, **36**(12), 1024a1–1024a7. doi: 10.1190/tle36121024a1.1.
- Patterson, Jeremy, Michael A. Cardiff, David Lim, Thomas Coleman, Herb F. Wang, Kurt L. Feigl, and PoroTomo Team (2017). Characterization of Hydrologic and Thermal Properties at Brady Geothermal Field, NV. presented at American Geophysical Union Fall Meeting 2017, New Orleans.
- Patterson, Jeremy (2018). Understanding Constraints on Geothermal Sustainability Through Reservoir Characterization at Brady Geothermal Field, Nevada (Master's Thesis), University of Wisconsin, Madison, 129 p.
- Pitz, W. & Miller, D. (2010). The TerraSAR-X satellite, *IEEE Transactions on Geoscience and Remote Sensing*, **48**(2), 615–622. doi:10.1109/TGRS.2009.2037432.
- Pride, S. R., and J. G. Berryman (2003b). Linear dynamics of double-porosity dual-permeability materials. I. Governing equations and acoustic attenuation. *Physical Review E*, **68**, 036603. <http://link.aps.org/doi/10.1103/PhysRevE.68.036603>
- Reinisch, E., and University of Wisconsin. (2017). *PoroTomo: Brady Geothermal Field InSAR Data* (data set). Retrieved from <http://gdr.openei.org/submissions/941>.
- Reinisch, Elena C., Michael Cardiff, Kurt L. Feigl (2016). Graph theory for analyzing pair-wise data: application to geophysical model parameters estimated from interferometric synthetic aperture radar data at Okmok volcano, Alaska. *Journal of Geodesy*, **91**(1), 9-24. <http://dx.doi.org/10.1007/s00190-016-0934-5>.
- Reinisch, Elena C., Kurt L. Feigl, Michael A. Cardiff, Christina Morency, Corné Kreemer, John Akerley, and PoroTomo Team (2017). Characterizing Volumetric Strain at Brady Hot Springs, Nevada, USA Using Geodetic Data, Numerical Models, and Prior Information. presented at American Geophysical Union Fall Meeting 2017, New Orleans.
- Reinisch, E. C., Cardiff, M., & Feigl, K. L. (2018). Characterizing Volumetric Strain at Brady Hot Springs, Nevada, USA Using Geodetic Data, Numerical Models, and Prior Information. *Geophysical Journal International*, **215**(2), 1501–1513. doi:10.1093/gji/ggy347
- Rosenqvist, A., Shimada, M., Ito, N., & Watanabe, M. (2007). ALOS PALSAR: A pathfinder mission for global-scale monitoring of the environment. *IEEE Transactions on Geoscience and Remote Sensing*, **45**(11), 3307–3316. doi:10.1109/TGRS.2007.901027
- Sandwell, D., Mellors, R., Tong, X., Wei, M. & Wessel, P. (2011a). Open radar interferometry software for mapping surface Deformation. *EOS, Transactions, American Geophysical Union*, **92**(28), 234–234. doi:10.1029/2011EO280002
- Sandwell, D., Mellors, R., Tong, X., Wei, M. & Wessel, P. (2011b). *GMTSAR: an InSAR Processing system based on generic mapping tools*. Technical Report, Scripps Institution of Oceanography. doi:10.2172/1090004
- Schimmel, M. and J. Gallart (2007). Frequency-dependent phase coherence for noise suppression in seismic array data. *Journal of Geophysical Research*, **112**, B04303. <https://doi.org/10.1029/2006JB004680>.
- Siler, D. L., and J. E. Faulds (2013). Three-Dimensional Geothermal Fairway Mapping: Examples From the Western Great Basin, USA. *GRC Transactions*, **42**, 327-332.
- Siler, D. L., N. H. Hinz, J. E. Faulds, and J. Queen (2016). 3D analysis of geothermal fluid flow favorability: Brady's, Nevada, USA, *PROCEEDINGS*, 41st Workshop on Geothermal Reservoir Engineering Stanford University, Stanford, California, February 22-24, 2016, 10 p. <https://pangea.stanford.edu/ERE/db/GeoConf/papers/SGW/2016/Siler.pdf>
- Snyder, J.P. (1987). *Map projections—a working manual* (Professional Paper 1395). US Government Printing Office.
- Steidl, Jamison H., Alexei G. Tumarkin, and Ralph J. Archuleta (1996). What Is a Reference Site?, *Bulletin of the Seismological Society of America*, **86**(6), 1733-1748.
- Stokoe, K. H., E. M. Rathje, C. R. Wilson, B. L. Rosenblad, and F.-Y. Menq (2004). Development of the NEES large-scale mobile shakers and associated instrumentation for in situ evaluation of nonlinear characteristics and liquefaction resistance of soils. presented at 13th World Conference on Earthquake Engineering, Vancouver, British Columbia, 1–6 August 2004.
- Strang, G., and K. Borre (1997). *Linear Algebra, Geodesy, and GPS*. Wellesley, MA: Wellesley-Cambridge Press.
- Szegedy, C., V. Vanhoucke, J. Shlens, and Z. Wojna (2015). Rethinking the Inception Architecture for Computer Vision. *Computer Vision and Pattern Recognition*, doi: 10.1109/CVPR.2016.308.
- Thurber, C., and D. Eberhart-Phillips (1999). Local earthquake tomography with flexible gridding, *Computers & Geosciences*, **25**, 809-818.
- Thurber, Clifford H., Lesley Parker, Peng Li, Dante Fratta, Xiangfang Zeng, Kurt L. Feigl, Esra Ak, Neal Lord, and PoroTomo Team (2017). Active-Source Seismic Tomography at Bradys Geothermal Field, Nevada, with Dense Nodal and Fiber-Optic Seismic Arrays. presented at American Geophysical Union Fall Meeting 2017, New Orleans.

- Torres, R., Snoeij, P., Geudtner, D., Bibby, D., Davidson, M., Attema, E., ... Rostan, F. (2012). GMES Sentinel-1 mission. *Remote Sensing of Environment*, **120**, 9–24. doi:10.1016/j.rse.2011.05.028
- Trainor-Guitton, W. J., G. M. Hoversten, G. Nordquist, and R. G. Intani (2015). Value of information analysis using geothermal field data: accounting for multiple interpretations & determining new drilling locations. *Society of Exploration Geophysics Technical Program Expanded Abstracts 2015*, 1996–2000. <https://doi.org/10.1190/segam2015-5733829.1>
- Trainor-Guitton, W., A. Guitton, S. Jreij, H. Powers, C. B. Sullivan, and PoroTomo Team (2018a). 3D Imaging from vertical DAS fiber at Brady's Natural Laboratory. *PROCEEDINGS, 43rd Workshop on Geothermal Reservoir Engineering*, Stanford University, Stanford, California, February 12-14, 2018, 11 p.
- Trainor-Guitton, W., S. Jreij, A. Guitton, and J. Simmons (2018b). Fault Classification from 3D Imaging of a Vertical DAS Profile. *Society of Exploration Geophysics Technical Program Expanded Abstracts 2018*, 4664–4668.
- Wackerly, D., Mendenhall, W. & Scheaffer, R. (2007). *Mathematical Statistics with Applications*. Belmont, CA: Cengage Learning.
- Wang, H., N. Lord, A. Chalari, C. Lancelle, J. Baldwin, E. Castongia, D. Fratta, R. Nigbor, and R. Karaulanov (2014). Field Trial of Distributed Acoustic Sensing Using Active Sources at Garner Valley, California. presented at American Geophysical Union Fall Meeting 2014, San Francisco.
- Wang, H.F., X. Zeng, D.E. Miller, D. Fratta, K.L. Feigl, C.H. Thurber, R. Mellors (2018). Ground Motion Response to a ML 4.3 Earthquake Using Co-Located Distributed Acoustic Sensing and Seismometer Arrays. *Geophysical Journal International*, **213**(3), 2020–2036. <https://doi.org/10.1093/gji/ggy102>.
- Witter, J. B., Siler, D. L., Faulds, J. E., and Hinz, N. H. (2016). 3D geophysical inversion modeling of gravity data to test the 3D geologic model of the Bradys geothermal area, Nevada, USA. *Geothermal Energy*, **4**(14), 21 p. <https://doi.org/10.1186/s40517-016-0056-6>
- Wohletz, K., and G. Heiken (1992). *Volcanology and Geothermal Energy*. Berkeley, California: University of California Press. <http://ark.cdlib.org/ark:/13030/ft6v19p151/>
- Woodward, M. J. (1992). Wave-equation tomography. *Geophysics*, **57**, 15–26.
- Zeng, Xiangfang, Clifford H. Thurber, Yan Luo, Eric Matzel, and PoroTomo Team (2016). High-resolution shallow structure revealed with ambient noise tomography on a dense array. presented at American Geophysical Union Fall Meeting 2016, San Francisco.
- Zeng, X., C. Thurber, H. Wang, D. Fratta, E. Matzel, and The PoroTomo Team (2017). High-resolution Shallow Structure Revealed with Ambient Noise Tomography on a Dense Array. *PROCEEDINGS, 42nd Workshop on Geothermal Reservoir Engineering*, Stanford University, Stanford, California, February 13-15, 2017, 5 p.
- Zeng, X., C. Lancelle, C. Thurber, D. Fratta, H. Wang, N. Lord, A. Chalari, and A. Clarke (2017). Properties of noise cross-correlation functions obtained from a distributed acoustic sensing array at Garner Valley, California. *Bulletin of the Seismological Society of America*, **107**(2), 603–610. <https://doi.org/10.1785/0120160168>.
- Zeng, Xiangfang, Clifford H. Thurber, Herb F. Wang, Dante Fratta, and Porotomo Team (2017). 3D shear wave velocity structure revealed with ambient noise tomography on a DAS array. presented at American Geophysical Union Fall Meeting 2017, New Orleans.